



Technische Universität München
TUM School of Natural Sciences

Lattice Dynamics in LuVO_3 and Nested Mirror Optics

Christoph Anton Herb, M. Sc.

Vollständiger Abdruck der von der TUM School of Natural Sciences der Technischen Universität München zur Erlangung eines

Doktors der Naturwissenschaften (Dr. rer. nat.)

genehmigten Dissertation.

Vorsitz: Prof. Dr. Michael Knap
Prüfer der Dissertation: 1. Prof. Dr. Peter Böni
2. Priv.-Doz. Dr. Sebastian Mühlbauer

Die Dissertation wurde am 31.01.2024 an der Technischen Universität München eingereicht und durch die TUM School of Natural Sciences am 29.02.2024 angenommen.

Abstract

Neutron scattering is an essential tool for investigating the physical properties of condensed matter systems across a wide range of temporal and spatial scales. This thesis provides a two-fold exploration of this broad topic, on the one hand emphasizing the potential of inelastic neutron scattering for the investigation of lattice dynamics and, on the other hand, exploring current issues in neutron optics and potential avenues to overcome them.

Within the first part, we elucidated a phonon softening in the Jahn-Teller active compound LuVO_3 . This softening coincided with a monoclinic-to-orthorhombic structural phase transition at 82.5 K, accompanied by a change in orbital and spin order. Utilizing inelastic neutron scattering at several three-axis spectrometers (EIGER, PUMA, and MIRA-2), we systematically examined the lattice dynamics of a single crystal of LuVO_3 along various high-symmetry directions, observing the expected longitudinal and transverse acoustic phonon modes. A single transverse acoustic phonon branch was found to reproducibly express a phonon softening close to the zone boundary. When cooling below 82.5 K, we observed a small but significant discontinuous reduction of the phonon energy by 0.3 meV, corresponding to 3% of the total phonon energy of about 10 meV.

This softening was explored in the context of elastic anomalies due to structural phase transitions. An improper ferroelastic transition has been identified to optimally predict the observed discontinuity in energy. Further exploration of the compound with supersonic measurements, an investigation of the order of the transition, and studying the system's reaction to pressure are envisioned for a deeper understanding of the underlying lattice dynamics.

The second part of the thesis addresses current challenges in neutron optics by introducing nested mirror optics as an innovative solution to overcome under-illumination issues during neutron extraction from compact sources. Nested mirror optics are, in essence, laterally nested reflective surfaces that enable efficient neutron transport and the recovery of the initial volume of neutron phase space at a specific point. Their favorable characteristics have been validated through analytic calculations, Monte Carlo simulations, and neutron measurements. Those measurements encompassed neutron imaging and experiments with position-sensitive detectors to explore the transport characteristics of parabolic and elliptic nested mirror optics, demonstrating a high efficiency of transport and the expected preservation of the neutron phase space. Additionally, we utilized two orthogonal planar elliptic nested mirror optics to image one- and two-dimensional intensity distributions.

Despite engineering challenges, including deformations of the thin silicon substrates due to the neutron supermirror coatings applied on one side only, nested mirror optics exhibit promising potential in beam extraction, long-distance neutron transport, and sample focusing. Considering the results presented here, we strongly recommend the incorporation of nested mirror optics into the toolbox of neutron optics and beamline design, especially for future compact high-brilliance neutron sources.

Zusammenfassung

Die Neutronenstreuung ist ein wichtiges und vielfältiges Instrument zur Untersuchung der physikalischen Eigenschaften von Systemen der kondensierten Materie über einen weiten Bereich von zeitlichen und räumlichen Skalen hinweg. In dieser Arbeit behandeln wir dieses umfassende Thema auf zweierlei Weise, indem wir einerseits das Potenzial der inelastischen Neutronenstreuung zur Erforschung von Gitterdynamiken hervorheben und andererseits einige der gegenwärtigen Herausforderungen der Neutronenoptik und Ansätze zu deren Überwindung behandeln.

Im ersten Teil untersuchen wir die Gitterdynamik eines Jahn-Teller-aktiven Einkristalls LuVO_3 , wobei wir eine Energieänderung eines transversalen Phononenzweigs in der Nähe eines strukturellen Phasenüberganges bei 82.5 K feststellten, welcher mit einer Änderung der Orbital- und Spinordnung einhergeht. Mithilfe inelastischer Neutronenstreuung an verschiedenen Drei-Achsen-Spektrometern (EIGER, PUMA und MIRA-2) haben wir die Gitterdynamik in LuVO_3 entlang mehrerer hochsymmetrischer Richtungen untersucht und dabei die erwarteten longitudinalen und transversalen Phononenmoden beobachtet. Nur in einem einzigen transversalen, akustischen Phononenzweig beobachteten wir eine Energieänderung in der Nähe der Zonengrenze. Sobald der Kristall unter 82.5 K abgekühlt wird, stellen wir hier reproduzierbar eine kleine, aber signifikante Reduzierung der Phononenenergie um 0.3 meV fest. Dies entspricht etwa 3 % der Phononenenergie von 10 meV.

Diese sprunghafte Energieänderung wurde im Zusammenhang mit elastischen Anomalien bei strukturellen Phasenübergängen diskutiert. Das beobachtete Verhalten lässt sich durch einen “improper ferroelastic” Phasenübergang am besten erklären. Weitere Untersuchungen hinsichtlich der Ordnung des Übergangs und der Reaktion des Systems auf Druck werden Teil zukünftiger Forschung sein, die unser Verständnis der Gitterdynamik in LuVO_3 weiter vertiefen wird.

Der zweite Teil der Arbeit befasst sich mit aktuellen Herausforderungen der Neutronenoptik und stellt verschachtelte Spiegeloptiken als neuartigen Ansatz zur Überwindung von Unterausleuchtungsproblemen bei der Neutronenextraktion aus kompakten Quellen vor. Diese Optiken basieren auf verschachtelten reflektierenden Oberflächen, die einen effizienten Neutronentransport zwischen zwei Punkten ermöglichen, ohne den an der Quelle emittierten Neutronenphasenraum unwiederbringlich zu verdünnen. Die vorteilhaften Eigenschaften der Optiken wurden durch analytische Berechnungen, Monte-Carlo-Simulationen und Neutronenmessungen verifiziert. Unter anderem wurden Neutronenbildgebung und positionssensitive Detektoren verwendet, um die Eigenschaften von parabolischen und elliptischen verschachtelten Spiegeloptiken zu untersuchen. Hierbei wurden eine hohe Transporteffizienz und die Beibehaltung des Neutronenphasenraums nachgewiesen. Zusätzlich wurde die Abbildung von ein- und zweidimensionalen Intensitätsstrukturen realisiert.

Die Optiken zeigen großes Potenzial für die Quellextraktion, den Transport über große Entfernungen und die Fokussierung von Neutronen auf die Probe, und erweitern dadurch den Baukasten der Neutronenoptik gerade im Hinblick auf kompakte, hochbrillante Quellen.

Contents

1	Introduction	1
2	Theory of Neutron Scattering	5
2.1	Properties of the Neutron	5
2.2	Properties of a Neutron Beam	6
2.3	Scattering Theory	7
2.3.1	Nuclear Elastic Scattering	10
2.3.2	Nuclear Coherent Elastic Scattering	12
2.3.3	Nuclear Coherent Inelastic Scattering	13
3	Instrumentation	15
3.1	Triple-Axis Spectroscopy	15
3.1.1	Monochromator and Analyzer	15
3.1.2	Scan Modes	17
3.1.3	Enhancing Beam Quality with Filters and Collimators	18
3.1.4	Monitors	19
3.1.5	Cold Triple-Axis Spectrometer MIRA-2, FRM-II, DE	19
3.1.6	Thermal Triple-Axis Spectrometer EIGER, PSI, CH	19
3.1.7	Thermal Triple-Axis Spectrometer PUMA, FRM-II, DE	20
3.2	Neutron Imaging	20
3.2.1	Spatially Resolving Neutron Detection Systems	20
3.2.2	Data Evaluation	23
3.2.3	Imaging Beamline BOA, PSI, CH	25
4	Lattice Dynamics in LuVO_3	27
4.1	Properties of $R\text{VO}_3$	27
4.1.1	Crystal Structure of $R\text{VO}_3$	27
4.1.2	Electronic Structure of $R\text{VO}_3$	29
4.2	Properties of LuVO_3	31
4.3	Experimental Details	35
4.3.1	Single Crystal of LuVO_3	36
4.3.2	Measurement Strategy	36
4.4	Phonon Dispersions	39
4.5	Discussion	43
4.5.1	Lattice Dynamics and Elastic Constants	44
4.5.2	Variations of Elastic Constants	46
4.5.3	Elastic Anomalies due to Structural Phase Transitions	47
4.5.4	Elastic Properties Distant from Phase Transitions	51
4.6	Conclusion and Outlook	53
5	Theory of Nested Mirror Geometries	55
5.1	The History of Neutron Guides	55

5.2	Long Guides with Rectangular Cross Section	62
5.2.1	Straight guides	62
5.2.2	Large Guides and Compact Sources – Under-illumination	63
5.3	Long Elliptic Guides	64
5.4	Elliptic Nested Mirror Optics	72
5.5	Parabolic Nested Mirror Optics	78
5.6	Two-Dimensional Nested Mirror Optics	81
5.7	McStas Simulations of Nested Mirror Optics	82
6	Characterization of NMO Prototypes	85
6.1	Investigation of the Polarizing Elliptic NMO at MIRA-2	85
6.1.1	Measurement Geometry at MIRA-2	86
6.1.2	Alignment of the Elliptic NMO	87
6.1.3	Efficiency of Transport	89
6.1.4	Preservation of Beam Shape	92
6.1.5	Comparison to Simulations	94
6.2	Investigation of NMOs at BOA	98
6.2.1	Double-Planar Parabolic NMO	98
6.2.2	Polarizing Elliptic NMO	107
6.2.3	Non-Polarizing Double-Planar Elliptic NMO	109
6.3	Investigation of Mirror Deformations	115
7	Applications of Nested Mirror Optics	123
7.1	Beam Extraction	123
7.1.1	Integrated Brilliance Transfer by Elliptic NMOs	125
7.1.2	Extraction into a Low-Divergence Beam with Parabolic NMOs	128
7.2	Focusing and Magnification	132
7.3	Summary of Nested Mirror Optics	133
8	Conclusion and Outlook	139
A	Inelastic TAS data obtained for LuVO₃	171
B	Derivation of Snell’s law	177
C	Geometric Aberrations in Elliptic Guides	179
D	Analytic Derivation of $p_{R_2}(r_2)$ in Elliptic Guides	181
E	Derivation of $p_Z(z)$	183
F	Numerical Approximation of $p_{R_2}(r_2)$ in Elliptic Guides	187
G	Design of Elliptic NMOs	189

1. Introduction

Neutron scattering is a powerful and versatile technique often utilized at the forefront of experimental solid-state physics. Our exploration of this topic within this work is dual; on the one hand, we utilized inelastic neutron scattering to investigate the softening of a transversal phonon branch in the rare-earth vanadate (REV) LuVO_3 , and on the other hand, we propose nested mirror optics (NMO) as an addition to the toolkit of contemporary neutron optics to enhance the efficiency of neutron extraction from compact sources and to facilitate the transport of neutrons to various scattering experiments.

Constituting the first part of this thesis, we used inelastic triple-axis neutron scattering to study the lattice dynamics of LuVO_3 , a REV distinguished by possessing the rare-earth element with the smallest ionic radius. Consequently, it exhibits unique properties that have attracted significant scientific attention. In agreement with the behavior of other REVs, at room temperature, LuVO_3 adopts an orthorhombic $Pbnm$ crystal structure [1, 2] due to a size mismatch between the vanadium and lutetium ions, as indicated by a Goldschmidt tolerance factor of $\alpha = 0.83$ [3]. The two unpaired electrons of the vanadium ion facilitate a cooperative Jahn-Teller effect, distorting the surrounding oxygen octahedra concurrent with the presence of long-range orbital order (OO).

When the temperature is lowered below T_{OO1} , the REV undergo a structural phase transition to the monoclinic $P2_1/b$ structure, accompanied by the emergence of G-type OO. The individual values of T_{OO1} fall within the range of $160 \text{ K} < T_{\text{OO1}}(\text{REV}) < 210 \text{ K}$, with $T_{\text{OO1}}(\text{LuVO}_3) = 177 \text{ K}$. Adhering to the Goodenough-Kanamori rules [4], C-type spin order (SO) emerges with further cooling below T_{SO1} . LuVO_3 and similar REV containing rare-earth elements with small ionic sizes experience a second structural phase transition at the lowest ordering temperature $T_{\text{SO2}} = 82.5 \text{ K}$. At that temperature, they revert to the room-temperature orthorhombic $Pbnm$ structure, concomitant with a change to G-type SO and C-type OO. LuVO_3 's magnetic structure and spin dynamics have been the subject of significant scientific interest. A preceding disagreement regarding the explanation of an unconventional magnetic scattering phenomenon, initially explained by an orbital-Peierls dimerization model [5], has been resolved in favor of a Jahn-Teller-mediated alteration of the in-plane magnetic exchange parameters [2].

In the subsequent investigation within this work, we will explore the lattice dynamics in a single crystal of LuVO_3 focusing on the longitudinal and transversal acoustic phonon modes, which are intimately connected to the elastic constants of the compound. Utilizing triple-axis spectroscopy, we observe the softening of a specific transversal phonon branch. Upon cooling below T_{SO2} , the energy of the transversal acoustic TA1 phonon mode discontinuously decreases by 0.3 meV at the zone boundary, concomitant with the structural phase transition. Albeit only constituting 3% of the total phonon energy, 10 meV , the softening was reproducibly observed across various instruments and beamtimes. Within the resolution limits, this softening is not accompanied by a change in linewidth. We interpret these findings in the context of elastic anomalies during structural phase transitions [6] and find good qualitative agreement with the behavior predicted by an improper ferroelastic transition.

The second part of the thesis is dedicated to assessing the current state of neutron optics and proposing **NMOs** as an advancement beyond the presently used long, non-linearly tapered guides.

Despite being a powerful and versatile technique, neutron scattering faces various challenges, including small samples, weak (magnetic) scattering signals, comparatively weak sources, and extensive sample environments that increase the background of the measurements. Consequently, experiments often involve prolonged measurement times, if feasible at all. Neutron optics have been developed to enhance the flux at the sample position while minimizing the number of interactions of neutrons with the sample environment, aiming to improve the signal-to-noise ratio [7, 8]. However, when combined with compact sources, these solutions are limited by the under-illumination of large neutron guides, drastically reducing the instrument's efficiency [9]. Special attention is required to prevent under-illumination at modern high-brilliance sources like the butterfly moderator at the European Spallation Source [10] and the planned accelerator-driven Jülich High Brilliance Source [11, 12]. A reliable solution to under-illumination effects during neutron extraction would enable the free optimization of the moderator design to achieve the highest possible brilliance usually obtained for more compact sources matching the extent of the sample. Intending to ultimately expand the present toolkit of contemporary neutron optics, we will present in the second part of this thesis **NMOs** as a potential solution to address the under-illumination problem.

In essence, **NMOs** are based on an assembly of laterally nested reflective surfaces with common focal points, drawing inspiration from similar configurations employed in X-ray spectroscopy [13] and from previous applications for enhancing neutron beam characteristics [14, 15, 16, 17, 18]. Specifically, our double planar **NMOs**, encompassing both parabolic and elliptic mirror geometries, preserve the neutron phase space density and thereby facilitate the extraction of a compact neutron source and the subsequent transport with high efficiency [19].

Throughout this work, we combined analytic calculations, Monte Carlo simulations, and neutron measurements to validate the excellent transport properties of **NMOs**. We utilized a position-sensitive detector and neutron imaging to confirm the simulated and calculated characteristics, demonstrating a high efficiency of transport $Q \geq 70\%$ and the preservation of the emitted beam shape; however, not without unexpected challenges. An unforeseen deformation of the mirrors was observed during the investigation of the non-polarizing prototypes. This deformation was attributed to a tensile surface stress induced by applying the supermirror coatings on a single side of the substrates and was carefully examined using a 3D scanner.

Supported by Monte Carlo simulations, we explore various applications of **NMOs**, focusing on their potential in beam extraction, long-distance transport, and, ultimately, focusing neutrons onto a compact sample. The discussions and findings underscore the promising potential of **NMOs** as a transformative technology for shaping the future landscape of neutron optics and beamline design.

Outline

The thesis is structured as follows: We begin with a concise review of neutron scattering, covering the theory and instrumentation for triple-axis and imaging applications.

Chapter 4 details the investigation of the lattice dynamics in LuVO_3 . We begin by reviewing rare-earth vanadates, emphasizing their structural properties and the consequential cooperative Jahn-Teller effect. Presented neutron scattering data from triple-axis spectroscopy reveal unexpected changes in LuVO_3 's lattice dynamics, discussed in the context of anomalous changes of the elastic constants during structural phase transitions.

The second part commences with a review of neutron sources and the role of neutron guides. As a solution to the prevalent issue of under-illumination, we then propose nested mirror optics as an alternative to long guides. We explore the theory of nested mirror optics, addressing geometric aberrations in elliptic guides and showcasing **NMOs** as a natural solution. Additionally, we present the preliminary investigation of an **NMO** prototype at MIRA-2, confirming its transport efficiency. Subsequently, the evaluation of the imaging properties of further prototypes at BOA is discussed, followed by a thorough examination of the observed mirror deformations. In the concluding chapters, we highlight potential applications of **NMOs** in beam extraction, transport, and focusing, suggesting a promising avenue for advancing neutron optics. The thesis concludes with a summary of the main results and an outlook proposing further investigations.

2. Neutron Scattering - Quantifying the Interaction between Neutrons and Matter

The history of neutron scattering dates back to the 1930s before the scientific community was aware of the existence of neutrons. One could argue that it started with Chadwick and Feather, who explored the interaction between an unknown form of radiation, now known to consist of neutrons, and various materials [20]. The two monitored the characteristics of the scattering to determine the mass of the unknown particles, estimating it to roughly equal that of a proton.

Today, with the properties of the neutron being well established, we continue to use various scattering techniques. However, our focus has shifted from elucidating the properties of the neutron itself to gaining insights into the characteristics of the scattering partner. Neutron scattering now is an important tool for probing condensed matter on various temporal and spatial scales. Neutrons, being uncharged particles, offer complementary insights compared to probes that strongly couple to the electromagnetic field, such as electrons or photons. Specifically, neutrons interact with the nuclei and weakly with any magnetic moments, enabling the investigation of the corresponding properties of the sample.

To harness the potential of neutrons for the investigation of lattice dynamics and magnetic excitations, one must obtain a solid understanding of the theory describing the interaction between neutrons and matter, comprehensively summarized here.

2.1 Properties of the Neutron

We will begin our introduction with an overview of the fundamental properties of the neutron. A more detailed account can be found in the summary by Abele [21].

The neutron is an uncharged particle, meaning it carries zero measurable electric charge⁽¹⁾. It possesses a mass of $m_n = 1.674\,927\,498\,04(95) \times 10^{-27}$ kg, slightly greater than that of the proton with a ratio of $m_p/m_n = 0.998\,623\,478\,12(49)$ [23]. A free neutron, not bound within a nucleus, undergoes β -decay, resulting in a proton, an electron, and an electron neutrino with a mean lifetime of $\tau = 878.4(5)$ s [24]. Neutrons are classified as spin- $\frac{1}{2}$ particles possessing a magnetic moment of $\mu_n = -9.662\,365\,1(23) \times 10^{-27}$ JT⁻¹ [23]. There is an ongoing debate regarding the existence and the magnitude of the neutron's electric dipole moment. As of 2023, it has not been observed, with the current best estimate being $d_n = (0.0 \pm 1.1_{\text{stat}} \pm 0.2_{\text{sys}}) \times 10^{-26}$ e cm [25].

In addition to these fundamental characteristics, neutrons possess a kinetic energy, E_{kin} , which is often expressed in terms of other, related magnitudes,

$$k_B T_{\text{mod}} = E_{\text{kin}} = \frac{v^2 m_n}{2} = \frac{p^2}{2m_n} = \frac{\hbar^2 k^2}{2m_n} = \frac{h^2}{\lambda^2} \frac{1}{2m_n}. \quad (2.1)$$

Here, v represents the velocity of the neutron, p is its momentum, and k denotes the wavevec-

⁽¹⁾Baumann et al. determined the neutron's charge to be $q_n = -0.4(11) \times 10^{-21}$ e [22], which is in good agreement with the expected lack of charge.

tor, which is related to the de Broglie wavelength by $k = 2\pi/\lambda$ ⁽²⁾. $h = 6.626\,070\,15 \times 10^{-34}$ J s and $\hbar = \frac{h}{2\pi}$ denote the Planck constant and the reduced Planck constant.

Neutrons are often classified based on the temperature of the moderating material, T_{mod} , resulting in the loosely defined terms of *cold*, *thermal*, and *hot* neutrons. Table 2.1 gives an overview of these categories in terms of the other magnitudes presented in Eq. (2.1). It should be noted that Eq. (2.1) only holds for non-relativistic neutrons, which is well justified for typical moderator temperatures. In summary, we observe that the energies and wavelengths

category	T_{mod} (K)	E (meV)	k (\AA^{-1})	λ (\AA)	v (m/s)
cold	25	2.2	1.02	6.16	642
thermal	300	26	3.53	1.78	2224
hot	2300	200	9.78	0.64	6158

Table 2.1: Characterization of neutrons in terms of commonly used physical quantities. The values for the cold, thermal, and hot regimes are approximate and can vary depending on the field of study or personal preferences. The here quoted temperature values correspond to the specific sources installed at the FRM-II [26].

of thermal and cold neutrons align well with the energies of collective excitations, such as phonons and magnons, and the interatomic distances of common crystals, respectively. This observation qualifies neutrons as ideal probes for investigating typical condensed matter systems.

Following this overview of the fundamental properties of the neutron, our focus shifts towards describing the characteristics of a neutron beam, which is, in essence, a large number of neutrons traveling in a similar direction.

2.2 Properties of a Neutron Beam

In the context of neutron optics, neutron beams are commonly characterized in terms of their flux, brightness, and brilliance. These magnitudes will briefly be defined here to prevent any misinterpretations.

- Neutron flux, Φ , quantifies the number of neutrons passing through a specific area, A , in unit time, t , normalized by that time and area:

$$\Phi = \frac{\# \text{ neutrons passing through area } A \text{ during time } t}{A t} \left[\frac{1}{\text{cm}^2 \text{ s}} \right]. \quad (2.2)$$

Here, A is oriented such that its surface normal is parallel to the average direction of the neutron beam. Integrating the flux over a given time yields the *fluence* [$1/\text{cm}^2$].

- Neutron brightness, b , is a differential measure that incorporates information about the angular distribution of neutrons. It is defined as the neutron flux in a specific

⁽²⁾The de Broglie relationship, $|\vec{p}| = h/\lambda = \hbar|\vec{k}|$, is utilized to express the neutron momentum, \vec{p} , in terms of its wavevector, \vec{k} .

direction enclosed by a solid angle, $d\Omega$, normalized by this solid angle:

$$b = \frac{\Phi \text{ in a given direction enclosed by } d\Omega}{d\Omega} \left[\frac{1}{\text{cm}^2 \text{ s sr}} \right]. \quad (2.3)$$

- Neutron brilliance, B , refers to a double differential magnitude that considers both the angular and energy distribution of the neutrons. In comparison to the brightness, b , only neutrons with an energy between E and $E + dE$ are considered [27]:

$$B = \frac{b \text{ with neutron energies between } E \text{ and } E + dE}{dE} \left[\frac{1}{\text{cm}^2 \text{ s sr meV}} \right]. \quad (2.4)$$

Whereas neutron flux serves as the fundamental indicator for beam intensity, neutron brightness offers a more nuanced perspective by accounting for the angular distribution of neutrons. Brilliance provides the most profound description of a neutron beam by additionally considering its energy distribution. Collectively, these magnitudes serve as metrics quantifying the vague term of *beam quality*.

2.3 Scattering Theory

This section closely follows the introduction given in the book of Squires [28], wherein the theory of thermal neutron scattering is explored in greater detail than we can cover within this thesis.

As a starting point, we consider a constant current of neutrons impinging onto the target with a flux Φ , which gives rise to a specific rate of interaction events $J \left[\frac{1}{\text{s}} \right]$ of any nature. Consequently, we define the total cross-section,

$$\sigma = \frac{J}{\Phi} [\text{cm}^2], \quad (2.5)$$

which is typically expressed in terms of barns, $1 \text{ b} = 1 \times 10^{-24} \text{ cm}^2$. This total cross-section encompasses all potential outcomes of the interaction between the neutron and the target. This includes elastic or inelastic scattering with a cross-section σ_s , or the absorption of the neutron into the nucleus with a cross-section σ_a , yielding

$$\sigma = \sigma_a + \sigma_s. \quad (2.6)$$

After an absorption event, the nucleus either i) decays into its ground state by emitting a γ -quantum, ii) emits charged particles, or iii) decays into smaller fragments by fission. Apart from resonances occurring at nucleus-specific energies, typically exceeding 100 keV, the absorption cross section for thermal and cold neutrons smoothly varies as [29]

$$\sigma_a \propto \frac{1}{v}, \quad (2.7)$$

where v denotes the velocity of the neutron.

Besides absorption into the nucleus, a neutron can be deflected from its trajectory by the strong nuclear force or magnetic interaction. Any scattering process can be classified as either *elastic* or *inelastic*, depending on its effect on the energy of the neutron.

In an elastic scattering process, the total kinetic energy of the system remains constant, which is equivalent to constant neutron energy due to the large mass of the sample, $m_{\text{sample}} \gg m_n$. Conversely, an inelastic scattering process gives rise to a change in the energy of the neutron. The kinetic energy of a typical thermal or cold neutron, $E_n \ll 1$ eV is insufficient to excite individual nuclei or electrons⁽³⁾. Instead, these interactions primarily involve collective atomic or magnetic motions, such as phonons or magnons. We will now discuss how different interactions play into the above scattering cross sections.

We begin by observing that the quantum mechanical state of a neutron is fully determined by its momentum (or wavevector) and spin, denoted as:

$$|\hbar\vec{k}, \sigma\rangle. \quad (2.8)$$

From this state, the energy can be derived as $E = (\hbar^2|\vec{k}|^2)/(2m_n)$. A comparison of the initially prepared state and the measured state after scattering at the sample yields information about the scattering process regarding the transferred momentum, energy, and spin.

In an experimental setup, however, one cannot directly determine the state of a neutron after scattering; instead, one measures rates of scattered neutrons. By discriminating neutrons based on their direction and energy after scattering, we obtain the [double differential cross section \(DDCS\)](#),

$$\left(\frac{d^2\sigma}{d\Omega dE}\right) = \frac{\text{rate of neutrons scattered into solid angle } d\Omega \text{ around direction } \theta, \phi, \text{ with final energy between } E_f \text{ and } E_f + dE}{\Phi d\Omega dE}. \quad (2.9)$$

Here, Φ denotes the incident flux onto the sample. The other terms in Eq. (2.9) are illustrated in Fig. 2.1. If the experiment does not account for the energy of the scattered neutrons, we instead obtain the *differential cross section*,

$$\left(\frac{d\sigma}{d\Omega}\right) = \frac{\text{rate of neutrons scattered into solid angle } d\Omega \text{ around direction } \theta, \phi, \text{ regardless of } E_f}{\Phi d\Omega} = \int_0^\infty \left(\frac{d^2\sigma}{d\Omega dE'}\right) dE'. \quad (2.10)$$

Finally, if the experiment does not account for the energy or the direction of the scattered neutrons, we obtain the *total scattering cross section*,

$$\sigma_s = \int_{4\pi} \left(\frac{d\sigma}{d\Omega}\right) d\Omega, \quad (2.11)$$

which accounts for any scattering events, regardless of their nature. These cross-sections are obtained in a neutron scattering experiment by carefully monitoring the rates of neutrons in the incident beam and after interacting with the sample. A comparison of the thereby obtained rates with theoretical predictions elucidates the physical processes occurring within the sample.

⁽³⁾Compare, for example, the Rydberg energy $hcR_\infty = 13.605\,693\,122\,994(26)$ eV, which represents the ionization energy of a ground-state electron in hydrogen [23].

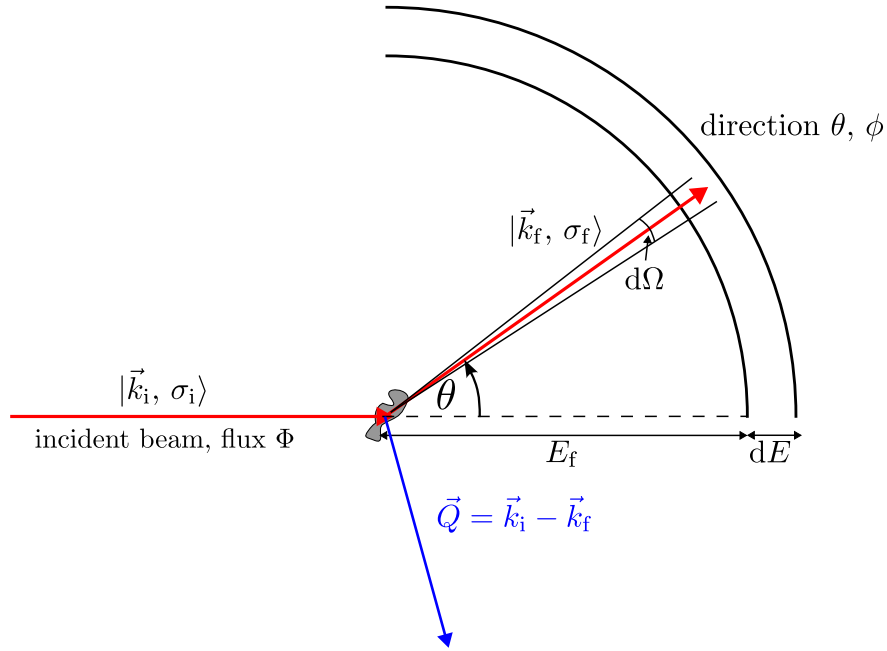


Figure 2.1: Sketch of a scattering geometry, illustrating the magnitudes defining the **DDCS** according to Eq. (2.9). An incident beam with flux, Φ , consisting of neutrons with states $|\vec{k}_i, \sigma_i\rangle$ illuminates the sample. Neutrons are scattered in the direction θ, ϕ , into a solid angle $d\Omega$, with a final energy between E_f and $E_f + dE_f$. The final state is denoted by $|\vec{k}_f, \sigma_f\rangle$, resulting in a momentum transfer, $\vec{Q} = \vec{k}_i - \vec{k}_f$, highlighted in blue. Figure is reproduced from the work of Beddrich [30].

Following the typical convention in neutron scattering, we describe the scattering process in terms of the transferred momentum and energy,

$$\begin{aligned}\vec{Q} &= \vec{k}_i - \vec{k}_f \\ \Delta E &= \frac{\hbar^2}{2m_n} \left(|\vec{k}_i|^2 - |\vec{k}_f|^2 \right).\end{aligned}\quad (2.12)$$

At low neutron energies (cold and thermal neutrons), far away from resonances, and in small samples, where multiple scattering does not occur, the transition probability for a combined neutron and sample state can be expressed using *Fermi's golden rule* [31, 32], giving rise to the following **DDCS** [28],

$$\left(\frac{d^2\sigma}{d\Omega dE} \right)_{\lambda_i \rightarrow \lambda_f} = \frac{|\vec{k}_f|}{|\vec{k}_i|} \left(\frac{m_n}{2\pi\hbar^2} \right)^2 \left| \langle \vec{k}_f, \lambda_f | V | \vec{k}_i, \lambda_i \rangle \right|^2 \delta(E_{\lambda_i} + E_i - (E_{\lambda_f} + E_f)). \quad (2.13)$$

Here, the combined initial state of the neutron and the sample, $|\vec{k}_i, \lambda_i\rangle$ ⁽⁴⁾ transitions into the final state $|\vec{k}_f, \lambda_f\rangle$ as a result of the interaction between the neutron and the sample, characterized by its potential, V . The matrix element encompassed by $|\dots|$ describes the transition

⁽⁴⁾Here and in the following, the spin state of the neutron is conveniently omitted, as no polarized or magnetic scattering experiments were performed within the scope of this work.

probability between the two combined states. δ denotes the Dirac delta distribution, the main property of which,

$$\int \delta(x - x_0) f(x) dx = f(x_0), \quad (2.14)$$

ensures the preservation of energy during the scattering process.

The interaction potential V is at the heart of the neutron scattering experiment, encapsulating the strong nuclear and magnetic interaction between the neutron and the sample. First, we will quantify the potential, V , and subsequently derive the **DDCS** for nuclear elastic scattering processes.

2.3.1 Nuclear Elastic Scattering

In this simple case, neutrons are deflected by a periodic arrangement of atoms, such as a crystal lattice, without changing their initial energy. Facilitating the analytic calculation, we assume the incoming and scattered neutrons to be represented by plane waves,

$$\begin{aligned} |\vec{k}_i\rangle &= \exp(-i\vec{k}_i\vec{r}), \\ |\vec{k}_f\rangle &= \exp(-i\vec{k}_f\vec{r}). \end{aligned} \quad (2.15)$$

Additionally, the potential of the scattering system is assumed to be a superposition of the potentials from individual nuclei, V_j , which depends solely on the distance between the neutron and the respective nucleus, $\vec{r} - \vec{R}_j$. We can then derive the total interaction potential:

$$V(\vec{r}) = \sum_j V_j(\vec{r} - \vec{R}_j). \quad (2.16)$$

Evaluating the integral over the incident and final neutron states, one obtains the following expression,

$$\langle \vec{k}_f, \lambda_f | V | \vec{k}_i, \lambda_i \rangle = \sum_j V_j(\vec{Q}) \langle \lambda_f | \exp(i\vec{Q}\vec{R}_j) | \lambda_i \rangle, \quad (2.17)$$

where $V_j(\vec{Q})$ is given by⁽⁵⁾,

$$V_j(\vec{Q}) = \int V_j(\vec{x}_j) \exp(i\vec{Q}\vec{x}_j) d\vec{x}_j. \quad (2.18)$$

If the neutron wavelength is large compared to the range of the potential, which is satisfied for any interaction via the strong nuclear force and thermal neutron wavelengths, the *Fermi pseudo potential* [33] provides a reasonable approximation for the interaction potential,

$$\begin{aligned} V_j(\vec{r}) &= \frac{2\pi\hbar^2}{m_n} b_j \delta(\vec{r} - \vec{R}_j), \\ V_j(\vec{x}_j) &= \frac{2\pi\hbar^2}{m_n} b_j \delta(\vec{x}_j). \end{aligned} \quad (2.19)$$

⁽⁵⁾During the derivation, we substituted $\vec{x}_j = \vec{r} - \vec{R}_j$.

Here, the strength of the interaction potential is conveniently absorbed into nucleon-specific scattering length, b_j . Using this approximation, we can calculate the matrix element,

$$\langle \vec{k}_f, \lambda_f | V | \vec{k}_i, \lambda_i \rangle = \sum_j \frac{2\pi\hbar^2}{m_n} b_j \langle \lambda_f | \exp(i\vec{Q}\vec{R}_j) | \lambda_i \rangle, \quad (2.20)$$

which is subsequently inserted into the **DDCS**,

$$\left(\frac{d^2\sigma}{d\Omega dE} \right)_{\lambda_i \rightarrow \lambda_f} = \frac{|\vec{k}_f|}{|\vec{k}_i|} \left| \sum_j b_j \langle \lambda_f | \exp(i\vec{Q}\vec{R}_j) | \lambda_i \rangle \right|^2 \delta(E_{\lambda_i} + E_i - (E_{\lambda_f} + E_f)). \quad (2.21)$$

So far, we have only considered the transition probability between two specific states. However, the experimentally obtained **DDCS** will contain various transitions between different states, which must be accounted for in our derivation. We achieve this by calculating a weighted average over all initial states and summing over the possible final states, considering the relevant conservation laws, such as energy, momentum, and spin. Transforming the δ -function in terms of its integral representation, we obtain,

$$\delta(E_{\lambda_i} - E_{\lambda_f} + E_i - E_f) = \frac{1}{2\pi\hbar} \int_{-\infty}^{\infty} \exp\left[i\frac{(E_{\lambda_f} - E_{\lambda_i})t}{\hbar}\right] \exp(-i\omega t) dt, \quad (2.22)$$

where the energy transfer is given by, $\omega = \frac{E_i - E_f}{\hbar}$. Substituting this into Eq. (2.21), and accounting for all possible transitions we get,

$$\left(\frac{d^2\sigma}{d\Omega dE} \right) = \frac{|\vec{k}_f|}{|\vec{k}_i|} \frac{1}{2\pi\hbar} \sum_{i,i'} b_i b_{i'} \int_{-\infty}^{\infty} \left\langle \exp[-i\vec{Q}\vec{R}_{i'}(0)] \exp[i\vec{Q}\vec{R}_i(t)] \right\rangle \exp(-i\omega t) dt. \quad (2.23)$$

Here, $\vec{R}_i(t) = \exp(iHt/\hbar)\vec{R}_i \exp(-iHt/\hbar)$ denotes the time evolution of the position operator of atom i , which consequently implies

$$\exp[-i\vec{Q}\vec{R}_i(t)] = \exp(iHt/\hbar) \exp(-i\vec{Q}\vec{R}_i) \exp(-iHt/\hbar). \quad (2.24)$$

Finally, the expression encompassed by $\langle \dots \rangle$ denotes the thermal average over the initial states, $\langle A \rangle = \sum_i p_i \langle \lambda_i | A | \lambda_i \rangle$ with the weights p_i distributed according to the Boltzmann distribution,

$$p_i = \frac{\exp\left(\frac{-E_i}{k_B T}\right)}{\sum_i \exp\left(\frac{-E_i}{k_B T}\right)}. \quad (2.25)$$

In Eq. (2.23), two cases can be separated as follows: firstly, scattering arises due from correlations between different nuclei, $i \neq i'$, and secondly, it arises due to self-correlations from the same atom at different times, $i = i'$. By separating and averaging those contributions, we obtain the following **DDCS** [28],

$$\begin{aligned} \left(\frac{d^2\sigma}{d\Omega dE} \right)_{\text{coh}} &= \frac{\sigma_{\text{coh}}}{4\pi} \frac{|\vec{k}_f|}{|\vec{k}_i|} \frac{1}{2\pi\hbar} \sum_{i,i'} \int_{-\infty}^{\infty} \left\langle \exp[-\vec{Q}\vec{R}_{i'}(0)] \exp[i\vec{Q}\vec{R}_i(t)] \right\rangle \exp(-i\omega t) dt \\ & \quad , \quad (2.26) \\ \left(\frac{d^2\sigma}{d\Omega dE} \right)_{\text{inc}} &= \frac{\sigma_{\text{inc}}}{4\pi} \frac{|\vec{k}_f|}{|\vec{k}_i|} \frac{1}{2\pi\hbar} \sum_i \int_{-\infty}^{\infty} \left\langle \exp[-\vec{Q}\vec{R}_i(0)] \exp[i\vec{Q}\vec{R}_i(t)] \right\rangle \exp(-i\omega t) dt \end{aligned}$$

where $\sigma_{\text{coh}} = 4\pi (\sum_n f_n b_n)^2 = 4\pi (\bar{b})^2$ and $\sigma_{\text{inc}} = 4\pi [(\sum_i f_n b_n^2) - (\sum_n f_n b_n)^2]$. Here, b_n denotes the scattering length of atom n occurring with frequency f_n in the scattering system. The individual scattering lengths vary due to isotopic composition and the spin state of a nucleus, even in a perfect Bravais crystal.

From Eq. (2.26), we observe that coherent scattering arises from correlations between different nuclei at different times, $i \neq i'$, and self-correlations of a single nucleus at different times $i = i'$. The coherent scattering from any system equals the scattering from a system where every nucleus possesses the mean scattering length of the first system, $\sum_i f_i b_i$. Conversely, incoherent scattering arises only from self-correlations of the same nucleus at different times. Mathematically it acts as a correction to coherent scattering and arises as a consequence of the deviations of individual scattering lengths from the mean scattering length, $(\sum_i f_i b_i^2) - (\sum_i f_i b_i)^2$.

An overview of values for σ_{coh} and σ_{inc} for various elements can be found in the work of Dawidowski et al. [34]. We note that this derivation utilized the Fermi pseudopotential, considering only nuclear scattering, which is sufficient for the scope of this thesis.

In the following subsections, we will explore Eq. (2.26) in the context of coherent elastic Bragg scattering and scattering involving one-phonon processes.

2.3.2 Nuclear Coherent Elastic Scattering

Assuming coherent elastic scattering without energy transfer between a neutron and a crystal structure (Bragg-scattering), we obtain the following coherent [DDCS](#)⁽⁶⁾,

$$\left(\frac{d^2\sigma}{d\Omega dE} \right)_{\text{coh}} = \frac{\sigma_{\text{coh}}}{4\pi} N \frac{(2\pi)^3}{V_0} \overbrace{\exp(-2W)}^{\text{Debye-Waller factor}} \sum_{\vec{G}} \overbrace{\delta(\vec{Q} - \vec{G})\delta(\omega)}^{\text{laws of conservation}}. \quad (2.27)$$

After trivially integrating over all final energies ensuring $w = 0$, this simplifies to,

$$\left(\frac{d\sigma}{d\Omega} \right)_{\text{coh}} = \frac{\sigma_{\text{coh}}}{4\pi} N \frac{(2\pi)^3}{V_0} \exp(-2W) \sum_{\vec{G}} \delta(\vec{Q} - \vec{G}), \quad (2.28)$$

where N is the total number of scattering nuclei in the crystal, V_0 denotes the volume of the crystal's unit cell, and the sum is over all reciprocal lattice vectors, \vec{G} , which are conveniently defined by the relation,

$$\exp(i\vec{G}_m \vec{R}_n) = 1. \quad (2.29)$$

Here, \vec{R}_n denotes any lattice vector $\vec{R}_n = n_1 \vec{a} + n_2 \vec{b} + n_3 \vec{c}$ with $n_1, n_2, n_3 \in \mathbb{Z}$ and \vec{a}, \vec{b} , and \vec{c} being the primitive lattice vectors of the real-space lattice⁽⁷⁾. The *Debye-Waller factor*, $\exp(-2W)$, accounts for the thermal motion of individual scattering centers, causing a reduction in scattering intensity with increasing temperature without affecting the momentum transfers at which scattering occurs or broadening the peaks in \vec{Q} .

⁽⁶⁾Compare chapter 3 of the textbook of Squires [28] for the derivation of this result.

⁽⁷⁾A more comprehensive introduction to reciprocal lattice vectors including their derivation from the real-space lattice can be found in the textbook of Hunklinger [35].

When generalizing to a non-Bravais crystal with more than one scattering center per unit cell, we adjust the DDCS slightly,

$$\begin{aligned} \left(\frac{d\sigma}{d\Omega}\right)_{\text{coh}} &= N \frac{(2\pi)^3}{V_0} \sum_{\vec{G}} \delta(\vec{Q} - \vec{G}) \left| F_N(\vec{G}) \right|^2 \\ F_N(\vec{Q}) &= \sum_{\vec{d}} \bar{b}_d \exp(i\vec{Q}\vec{d}) \exp(-W_d). \end{aligned} \quad (2.30)$$

Here, the sum in the *nuclear unit-cell structure factor*, $F_N(\vec{Q})$, encompasses the positions of all scattering centers inside the unit cell, \vec{d} . Essentially, the first part of Eq. (2.30) corresponds to the Bragg condition⁽⁸⁾ for the Bravais lattice. $F_N(\vec{Q})$ modifies the scattering intensity of the Bragg peaks depending on the positions and the average scattering length, \bar{b}_d , of the atoms within one unit cell.

2.3.3 Nuclear Coherent Inelastic Scattering and One-Phonon Processes

For inelastic scattering processes, which give rise to the creation or annihilation of one phonon, the single-phonon contribution to the DDCS in a non-Bravais lattice is described by [28, 36],

$$\begin{aligned} \left(\frac{d^2\sigma_{\text{pho}}}{d\Omega dE}\right)_{\text{coh}} &= \frac{(2\pi)^3}{V_0} \frac{|\vec{k}_f|}{|\vec{k}_i|} \sum_s \left[\underbrace{\sum_{\mu} \overbrace{\exp(-W_{\mu})}^{\text{Debye-Waller}} \frac{\overbrace{\bar{b}_{\mu}}^{\text{scattering length}}}{\sqrt{2M_{\mu}\omega_s(\vec{q})}} \overbrace{(\vec{Q}\vec{e}_{\mu,s})}^{\text{polarization}} \exp(-i\vec{Q}\vec{r}_{\mu})}_{\text{dynamical structure factor}}} \right]^2 \times \\ &\sum_{\vec{G}} \left[\underbrace{\overbrace{(n(\omega_s(\vec{q}) + 1) \delta(\omega - \omega_s(\vec{q})) \delta(\vec{Q} - \vec{G} - \vec{q}))}_{\text{one-phonon creation}}}}_{\text{Bose occupation}} \overbrace{\delta(\omega - \omega_s(\vec{q})) \delta(\vec{Q} - \vec{G} - \vec{q})}^{\text{laws of conservation}}} + \underbrace{\overbrace{n(\omega_s(\vec{q})) \delta(\omega + \omega_s(\vec{q})) \delta(\vec{Q} + \vec{q} - \vec{G})}_{\text{one-phonon annihilation}}} \right]. \end{aligned} \quad (2.31)$$

The phonon, a collective lattice excitation, is characterized by its momentum, \vec{q} , its energy, $\hbar\omega_s(\vec{q})$, and its polarization s , determined by the direction in which atoms are displaced from their equilibrium positions, \vec{e}_s ⁽⁹⁾. The subscript μ distinguishes specific atoms in the unit cell. The DDCS accounts for contributions from all reciprocal lattice vectors, \vec{G} . The Bose occupation factor, $n(\omega_s) = \left[\exp\left(\frac{\omega_s(\vec{q})}{k_b T}\right) - 1 \right]^{-1}$ considers the temperature-dependent population of phonon states with various frequencies, $\omega_s(\vec{q})$.

The inner product between the total momentum transfer and the polarization vector of the phonon, $\vec{Q}\vec{e}_s$, determines which phonon branches are experimentally accessible within a specific geometry. Only phonons whose polarization is approximately parallel to the momentum

⁽⁸⁾A discussion of the equivalency between Bragg's law and the expression taking advantage of the reciprocal lattice vectors can be found in the textbook of Hunklinger [35].

⁽⁹⁾A more comprehensive treatment of phonons can be found in section 4.5 of this thesis and in various textbooks, see for example the book of Hunklinger [35].

transfer, $\vec{Q} \parallel \vec{e}_s$, can be probed effectively. Consequently, we investigate longitudinal phonon branches, where $\vec{q} \parallel \vec{e}_s$, by choosing a momentum transfer such that $\vec{Q} \parallel \vec{q}$. A transversal phonon along a high-symmetry direction, $\vec{q} \perp \vec{e}_s$, is usually investigated in a setting where \vec{Q} and \vec{q} are only approximately perpendicular. Both the investigation of a longitudinal and a transversal phonon branch are illustrated in Fig. 2.2 (a) and (b), respectively.

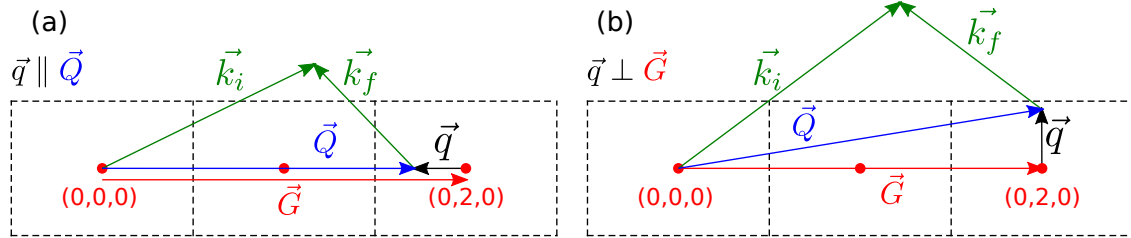


Figure 2.2: Investigation of the DDCS associated with a one-phonon process using inelastic neutron scattering. The figure illustrates the relationship between the momentum transfer, \vec{Q} , the reciprocal lattice vector, \vec{G} , and the phonon momentum, \vec{q} . Panels (a) and (b) illustrate the investigation of a longitudinal phonon, $\vec{q} \parallel \vec{G}$, and a transversal phonon $\vec{q} \perp \vec{G}$, respectively. In both cases, the energy of the excited phonon amounts to $\hbar\omega = \hbar^2(|\vec{k}_i|^2 - |\vec{k}_f|^2)/(2m_n)$.

Additionally, to maximize the factor $\vec{Q}\vec{e}_s$, phonon branches are usually investigated in Brillouin zones as distant to the origin as allowed by the experimental setup. For a comprehensive overview of the scattering from one-phonon processes, including the derivation of Eq. (2.31), the reader is referred to the book of Squires [28].

In the upcoming chapter, we will explore the operating principles of neutron scattering experiments and the utilization of specialized instruments to investigate the DDCS at specific momentum and energy transfers. We will primarily focus on the working principle of *triple-axis spectroscopy* (TAS) and the fundamentals of neutron imaging techniques.

3. Instrumentation - Expanding the Possibilities of Research

Within this thesis, the experimental work encompassed two distinct domains. Firstly, we used [triple-axis spectroscopy \(TAS\)](#) to investigate the softening of a transversal phonon of LuVO_3 , a representative compound of the rare-earth vanadates. Secondly, the focusing characteristics of the [NMO](#) prototypes were investigated using a position-sensitive detector and neutron imaging techniques.

Expanding the preceding discussion of the interaction between neutrons and matter, our focus in the present chapter shifts toward acquiring and interpreting data from specific neutron experiments. Gaining insight into the data acquisition process facilitates the comparison of experimental findings with theoretical predictions, thereby allowing for a better understanding of the underlying physical processes.

3.1 Triple-Axis Spectroscopy

Brockhouse and Shull initiated the field of [triple-axis spectroscopy](#) back in 1951 at the NRX reactor located at the Chalk River Laboratory. Their work led to the establishment of the first triple-axis spectrometer prototype in 1952 [37]. In recognition of their contribution, Brockhouse and Shull were awarded the Nobel prize in 1994 for their “*pioneering contributions to the development of neutron scattering in condensed matter research*” [38].

To this day, [TAS](#) remains a cornerstone of modern neutron scattering, facilitating the exploration of the [DDCS](#) of a sample at arbitrary momentum and energy transfers with remarkable resolution. This is achieved by precisely determining the initial and final states of the neutrons in the beam through the three eponymous scattering axes. The energies of the incident and scattered neutrons are selected by Bragg scattering at the first and last axes, known as the monochromator and the analyzer, respectively. The position of these devices relative to the sample, which represents the second scattering axis, governs the directions of the momenta of the incident and scattered neutrons. As a result, the configuration of the instrument geometrically defines the initial and final states of the neutrons, $|\vec{k}_i\rangle$ and $|\vec{k}_f\rangle$ ⁽¹⁾.

Within the upcoming section, we provide a concise introduction to [TAS](#), focusing on the methods for energy selection and neutron manipulation at the specific axes. Additionally, we present various scan types utilized for systematically exploring the reciprocal space. Finally, we will present additional instrumentation for improving the beam quality and the signal-to-noise ratio. A detailed account of the topic is available in the book of Shirane [39].

3.1.1 Monochromator and Analyzer

Concerning [TAS](#), the monochromator and analyzer play pivotal roles by selecting neutrons of specific energy from the beam through elastic Bragg scattering off of a crystal with known lattice spacing. By adjusting the angle between the incident beam and the surface of the monochromator/analyzer, $\theta_{m/a}$, the wavelength of the scattered neutrons can be freely de-

⁽¹⁾Again, the spin of the neutron is conveniently neglected.

terminated according to Bragg's law [40],

$$2d_{m/a} \sin(\theta_{m/a}) = n\lambda_{i/f} = n \frac{2\pi}{|\vec{k}_{i/f}|}. \quad (3.1)$$

Here, $d_{m/a}$ denotes the lattice spacing between the scattering planes, and $\theta_{m/a}$ is the angle between those crystal planes and the incident neutrons. Neutrons with a wavelength $\lambda_{i/f}$ satisfy Bragg's law and are ultimately deflected by an angle $2\theta_{m/a}$ from their initial trajectory. The parameter $n \in \mathbb{N}$ denotes the order of reflection, implying that neutrons with an integer fraction of $\lambda_{i/f}$ also satisfy Bragg's law. These *higher order contaminations* typically have to be eliminated by filters to diminish the measurement background.

An overview of a commonly used **TAS** geometry is given in Fig. 3.1 (a). Following the neutron beam through the instrument, the monochromator initially scatters neutrons with a specific wavelength from the incident white beam, thereby defining the direction and magnitude of \vec{k}_i . After the interaction between the beam and the sample, the direction and magnitude of \vec{k}_f are determined by the positioning and the angle of the analyzer, respectively. Consequently, the momentum and energy transfers governing the **DDCS** are given by,

$$\begin{aligned} \vec{Q} &= \vec{k}_i - \vec{k}_f \\ \Delta E &= \frac{\hbar^2(|\vec{k}_i|^2 - |\vec{k}_f|^2)}{2m_n} \end{aligned} \quad (3.2)$$

Fig. 3.1 (b) illustrates the momenta of the neutron beam visualized in (a) in reciprocal space. The total momentum transfer, \vec{Q} can be separated into a reciprocal lattice vector \vec{G} and the *reduced momentum transfer* \vec{q} .

We will now briefly touch upon the properties of the crystals employed as the monochromator and the analyzer. A perfect crystal would only satisfy Eq. (3.1) for an infinitesimally narrow range of wavelengths. While this would offer impeccable energy resolution, the count of neutrons with that exact wavelength dwindles to zero. Generally, the number of neutrons suitable for being reflected at the monochromator decreases with increasing energy resolution.

In practice, one resorts to *perfectly imperfect* crystals featuring a certain degree of *mosaic spread* to strike a balance between the required energy resolution of an experiment and the flux required to perform the experiment in a timely fashion [41]. Mosaicity refers to the extent of the deviation in the orientation of the crystallites within a single crystal, which is typically modeled by a Gaussian distribution [42]. Due to these deviations, neutrons that closely approximate the Bragg equation can still be reflected by a correspondingly oriented crystallite instead of being transmitted. A more comprehensive treatment of the scattering off of a mosaic crystal is left to the work of Sears [43].

A common material for constructing monochromators for cold neutrons is **pyrolytic graphite (PG)** with a mosaicity of about 1° [44, 45]. Although theory predicts that monochromators based on diamond should outperform all existing designs [46], the practical limitation of fabricating diamond crystals with a sufficiently homogeneous mosaic spread is restricting their current usage [47].

It is worth noting that the monochromator rarely is a single continuous crystal, but rather an arrangement of similarly oriented smaller pieces of crystal, typically possessing an area

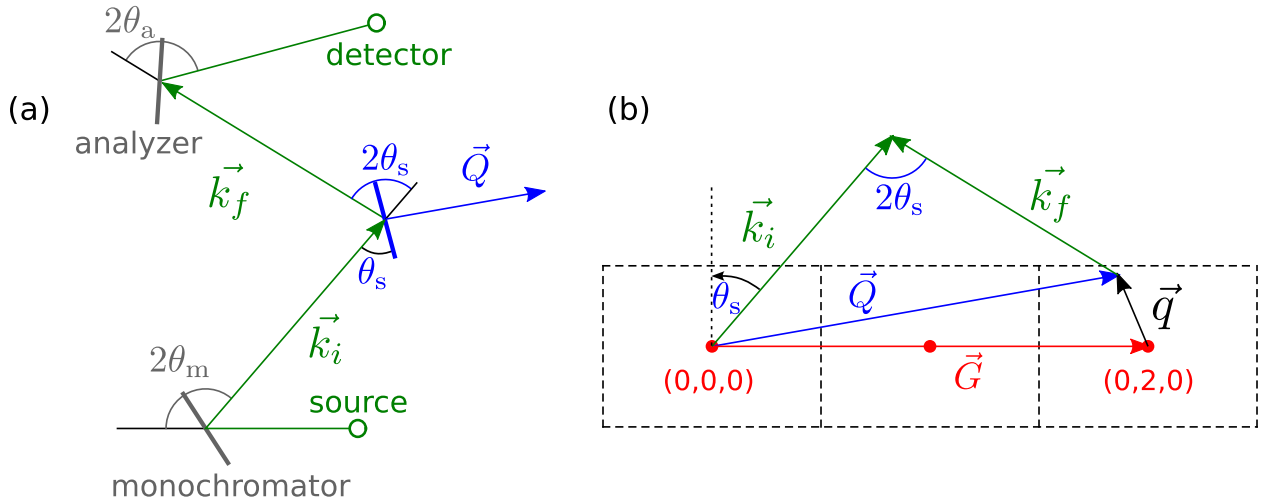


Figure 3.1: (a) Geometry of a triple-axis spectrometer, and (b) a representation of the wave vectors in the reciprocal lattice of the investigated sample. (a) The relative position of the three scattering axes, the monochromator, the sample and the analyzer, determine the directions of \vec{k}_i and \vec{k}_f , whereas the monochromator and the analyzer angles, θ_m and θ_a , determine the magnitudes of those vectors, respectively. (b) In terms of the reciprocal space of the crystal, the momentum transfer, $\vec{Q} = \vec{k}_i - \vec{k}_f$, can be separated into a reciprocal lattice vector, \vec{G} , and the corresponding reduced momentum transfer \vec{q} . The angle θ_s determines the orientation of the sample with respect to \vec{k}_i .

of about $1 \times 1 \text{ cm}^2$. This configuration allows for individual crystal adjustments, enabling horizontal or vertical focusing. While this may increase the flux at the sample position, it comes at the expense of increasing the divergence [48, 49].

3.1.2 Scan Modes

TAS is an extremely versatile method for investigating the DDCS at specific points in the four-dimensional Q, E -space. Several scanning techniques have been established to systematically investigate collective excitations such as phonons and magnons. Here, we provide a concise overview of the most common ones.

- Elastic scattering:

In the case of elastic scattering, $\Delta E = 0$, the magnitudes of the incident and the outgoing wavevectors are equal. Assuming a Bragg reflection, $\vec{Q} = \vec{G}$, as a starting point, one usually performs a longitudinal scan $\vec{q} \parallel \vec{Q}$ or a transversal scan $\vec{q} \perp \vec{Q}$. Considering Fig. 3.1, we observe that the longitudinal scan involves a change of $2\theta_s$ by a certain angle together with a rotation of the sample by half that angle, θ_s , to maintain the orientation between \vec{Q} and \vec{G} . This type of elastic scan is often also referred to as a θ - 2θ -scan. Conversely, by rotating only the sample and keeping $2\theta_s$ constant, \vec{G} is rotated with respect to \vec{Q} , which results in a transversal scan, $\vec{q} \perp \vec{Q}$, for small angles of rotation. This type of scan is usually called θ -or rocking-scan.

- Constant Q -scan: In this more common inelastic scan mode, the momentum transfer

$|\vec{Q}|$ is kept constant, while the energy transfer ΔE is varied.

- **Constant E -scan:** In cases where a constant Q -scan is unfeasible, such as for the investigation of very steep dispersions where the energy of the excitation changes quickly with varying momentum transfer, the energy transfer is kept at a constant value, while the momentum transfer is varied.

Typically, both inelastic scans require complex adjustments of several axes. Modern instrumentation allows researchers to input the orientation of the crystal and the desired positions in Q, E -space, with the software handling the calculations for the required adjustments automatically. For a detailed insight into these calculations, the reader is referred to the following references [39, 50, 51].

3.1.3 Enhancing Beam Quality with Filters and Collimators

In addition to the primary three axes, various devices are routinely employed to improve the beam quality and remove unwanted neutron contamination, thereby improving the signal-to-noise ratio. Here, we introduce those devices in the order in which the neutron beam will encounter them in a typical TAS setup.

As mentioned previously, Bragg scattering generates higher-order contamination, i.e., neutrons with integer fractions of the desired wavelength, complicating the evaluation of the obtained data. A filter is usually positioned directly behind the monochromator to remove those unwanted neutrons. It consists of small, randomly oriented crystallites with a specific lattice spacing, d_{filter} . The lack of orientation entails that the value of the sine-term in Bragg's equation (Eq. (3.1)) varies freely between 0 and 1. Consequently, all neutrons with $\lambda \leq 2d_{\text{filter}} = \lambda_{\text{cut}}$ undergo elastic scattering, deviating away from the original trajectory, thus removing the higher order contamination for a well-chosen value of d_{filter} . Common materials for this purpose include pyrolytic graphite ($\lambda_{\text{cut}} = 6.7 \text{ \AA}$) [52], polycrystalline beryllium ($\lambda_{\text{cut}} = 4.0 \text{ \AA}$), or bismuth ($\lambda_{\text{cut}} = 6.6 \text{ \AA}$), sometimes used interchangeably or in combination with each other [53].

Besides filtering unwanted neutrons with respect to their wavelength, further options are available for removing neutrons whose direction deviates too strongly from the intended path. *Soller collimators* are based on thin, straight, parallel channels coated with a strongly neutron-absorbing material originally designed for X-ray scattering [54, 55]. If the divergence, α , i.e., the angle between a neutron and the optical axis, exceeds a threshold determined by the geometry of the collimator, $\alpha_{\text{coll}} = \tan^{-1}(d/l)$, the neutron is always absorbed [56]. Here, d and l denote the spacing between two absorbing plates and the length of the individual plates, respectively. It can readily be shown that the transmission through such a collimator gives rise to a triangular intensity distribution with respect to the divergence of the neutrons [56],

$$T = \begin{cases} 1 - \frac{|\alpha|}{\alpha_{\text{coll}}} & \text{for } |\alpha| \leq \alpha_{\text{coll}} \\ 0 & \text{else} \end{cases} \quad (3.3)$$

At this point, it should be noted that the divergence of a neutron beam typically refers to the **full width at half maximum (FWHM)** of the divergence distribution of the individual neutrons, which matches α_{coll} for the triangular shape of the recovered distribution. While

collimators can be placed anywhere along the neutron path, they are most commonly positioned directly before or after the sample.

3.1.4 Monitors

To determine the **DDCS**, we must measure neutron rates before the sample and after the energy selection by the analyzer. However, different considerations apply to these two measurements. Before encountering the sample, the beam should pass the monitor mostly unobstructed. In this scenario, a low detection efficiency is preferred. Consequently, monitors typically utilize fission chambers equipped with thin foils coated with small amounts of ^{235}U [57]. Conversely, the detector behind the analyzer should be designed to count neutrons with the highest achievable efficiency. For **TAS**, state-of-the-art detectors are currently based on ^3He -filled fingers [58], tailored towards maximizing neutron capture and detection.

We now offer a brief overview of the three triple-axis-spectrometers utilized within the context of this thesis.

3.1.5 Cold Triple-Axis Spectrometer MIRA-2, FRM-II, DE

MIRA-2, located at the FRM-II facility in Garching near Munich, is a multi-purpose instrument with a primary focus on cold **TAS** [59]. This instrument played a pivotal role in the preliminary investigation of the **NMO** prototypes and the study of the lattice dynamics in LuVO_3 at small \vec{Q} .

Tailored towards the cold spectrum in which MIRA-2 typically operates, the monochromator and analyzer are assembled from **PG** (PG002) with a lattice spacing of $d_{\text{PG002}} = 3.355 \text{ \AA}$. To mitigate higher-order contamination, a liquid nitrogen-cooled beryllium filter is positioned behind the monochromator. MIRA-2 operates within a wavelength range of $3.97 \text{ \AA} \leq \lambda \leq 5.2 \text{ \AA}$. Due to instruments downstream of MIRA-2, inelastic measurements are primarily performed using a constant k_i mode, where the modulus of the incoming neutron momentum is kept at a constant value while the energy transfer is selected at the analyzer. Although this approach is equivalent to the constant k_f mode in terms of probing the **DDCS**, one has to account for the energy-dependent reflectivity of the analyzer. This is achieved by normalizing the intensity measured by the detector by a factor [39],

$$|\vec{k}_f|^3 \tan(\theta_f). \quad (3.4)$$

In the constant k_f mode, the energy-dependent efficiency of the monochromator can easily be accounted for during the data evaluation by comparing the detector data to flux measurements obtained from a monitor positioned between the monochromator and the sample.

Throughout the study of the **NMOs**, a position-sensitive **CASCADE** [60] detector was mounted onto a linear stage, the details of which will be discussed at a later point dedicated to the measurement geometry at MIRA-2, section 6.1.1.

3.1.6 Thermal Triple-Axis Spectrometer EIGER, PSI, CH

Initial phonon measurements were conducted at the thermal triple-axis spectrometer **EIGER** at **PSI** [61]. It operates in constant \vec{k}_f mode, with $k_f = 2.662 \text{ \AA}^{-1}$. Similar to MIRA-2, both the monochromator and the analyzer rely on the (002) reflection of pyrolytic graphite. The monochromator allows for horizontal and vertical focusing. To mitigate higher-order reflections, **EIGER** employs a **PG**-filter with $\lambda_{\text{cut}} = 6.7 \text{ \AA}$.

3.1.7 Thermal Triple-Axis Spectrometer PUMA, FRM-II, DE

Operating at a smaller wavelength than MIRA-2, the longitudinal phonon modes of LuVO_3 closer to the zone boundary were investigated at PUMA at FRM-II [62]. PUMA was operated in constant \vec{k}_f mode with $\vec{k}_f = 2.662 \text{ \AA}^{-1}$. The monochromator and the analyzer employ the (002) reflection of PG and have focusing options.

3.2 Neutron Imaging

This section draws inspiration from the comprehensive summary of the history of neutron scattering by Brenzier [63] and the overview of different types of spatially resolving detectors found in the work of Lehmann et al. [64].

Less than ten years after the identification of the neutron by James Chadwick in 1932 [20], Kallmann and Kuhn produced radiographic neutron images akin to those previously obtained with X-rays. They achieved this by utilizing a Ra-Be neutron source and a photographic neutron detection system based on lithium foils, which functioned similarly to X-ray films [65, 66]. Owing to substantial differences in the total cross-sections compared to X-rays and the isotopic sensitivity of the neutron, neutron imaging ever since provides unique insights for non-destructive testing, complementing X-ray scattering techniques.

Besides improvements in neutron beam quality and data reduction, significant progress has been made in neutron detection techniques, particularly in improving spatial and temporal resolution. The uncharged nature of the neutron necessitates its conversion into secondary particles for detection, i.e., α , β , and γ . This conversion is typically achieved through neutron capture in materials such as lithium, boron, or gadolinium [67]. Subsequently, the intensity distribution of these secondary particles is digitized using techniques established in X-ray radiography.

Photostimulable phosphor plates or systems based on scintillators have replaced previously used X-ray films in visualizing the secondary particles [68, 64]. These technologies offer several practical advantages, including reusability with no need for post-processing of the films and no waste disposal. Furthermore, they offer a linear response to the neutron intensity over a large range of exposures and provide a large field of view. The optical light emitted by these devices is detected and digitized by [charge-coupled device \(CCD\)](#) cameras.

In the following section, we provide a brief overview of the processes involved in converting the spatial intensity distribution of a neutron beam into a digital image, emphasizing the quantitative evaluation of the data.

3.2.1 Spatially Resolving Neutron Detection Systems

An effective neutron radiography detector requires a specific spatial resolution, a minimum signal-to-noise ratio, linearity between the detected signal and the incident neutron flux over an extensive dynamic range for quantitative evaluation, and, in some cases, sufficient time resolution [64]⁽²⁾. The extent to which specific requirements must be satisfied depends on the nature of the conducted experiment. Today, CCD camera-based detection systems, which convert light emitted by neutron-sensitive scintillators into digital data, meet these requirements for most neutron imaging experiments, making them the primary choice. The

⁽²⁾For the work conducted within this thesis, time resolution was not necessary.

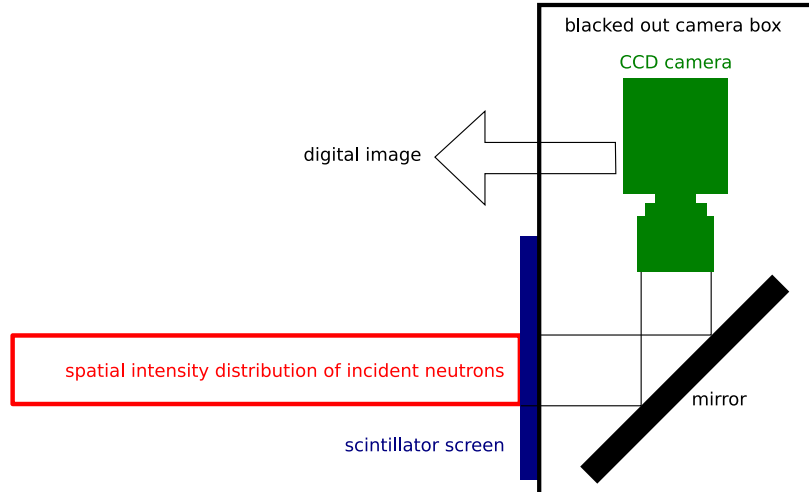


Figure 3.2: Schematics of a neutron imaging setup based on a scintillator and a [CCD](#) camera. The figure is reproduced from the work of Lehmann [64].

typical configuration of such a system is illustrated in Fig. 3.2.

The conversion of a neutron beam into a digital image can be separated into distinct steps. First, the spatial intensity distribution of neutrons incident onto the scintillator screen is converted into a spatial distribution of secondary particles through neutron capture reactions. Typically used isotopes include ${}^6\text{Li}$, ${}^{10}\text{B}$, and ${}^{158}\text{Gd}$ giving rise to the following reactions,



In the case of neutron capture in Gd, the excited nucleus emits electrons and betas, which can then be detected [69, 70].

Already upstream of the scintillator, the spatial resolution can be compromised if either the divergence of the incoming neutron beam or the distance between the sample and the scintillator is too large. Proper collimation of the beam helps achieve the optimum resolution, typically limited by the conversion of neutrons into charged particles and subsequently visible light.

Within the scintillator screen, the energetic secondary particles interact with the photoactive components of the scintillator, typically ZnS:Cu, emitting visible light as a result. The spatial resolution of this process is influenced by the range of the charged particles and the thickness of the scintillator [69], which is itself dictated by the required light yield. Increasing the scintillator thickness increases the light yield but decreases the resolution. For ${}^6\text{Li}$ -based ZnS:Cu scintillators, the spatial resolution is typically $50\ \mu\text{m}$, while for Gd-based scintillators the resolution can be improved to about $20\ \mu\text{m}$ [69, 71].

After the scintillator, the light yield is directed to and digitized into a grayscale image by a low-background [CCD](#) camera positioned outside the direct beam to reduce radiation damage from activation. While the high resolution of the camera does not impede the overall spatial resolution of the measurement, thermal noise can affect the signal-to-noise ratio. The camera is usually cooled with liquid nitrogen to mitigate this noise [64]. Additionally, to prevent

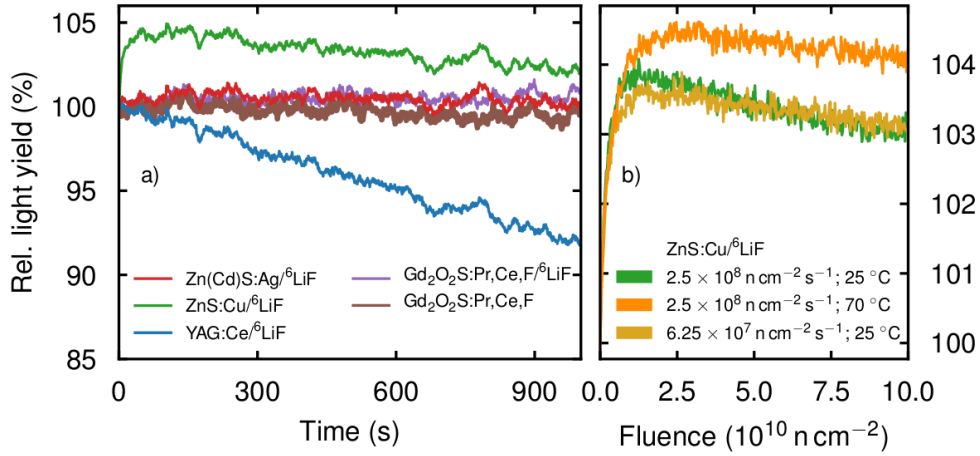


Figure 3.3: a) Time-dependent light yield for various scintillation screens normalized to their initial light yield at $t = 0$. b) Relative light yield as a function of the time-integrated flux for different incident flux values and scintillator temperatures. The figure is taken from the work of Neuwirth et al. [67].

negative entries in the data, a constant positive offset is applied to the entire image, which must be accounted for during the data evaluation process. The entire system is enclosed in a light-tight camera box to suppress noise from ambient sources of light [72].

Finally, we explore the impact of the incident neutron flux on the resulting light yield, and the timescale over which this light is emitted. A comprehensive discussion covering various types of scintillators can be found in the work of Neuwirth et al. [67]. Here, we summarize the results, focusing on the ⁶LiF-based scintillator employed at BOA, which utilizes ZnS:Cu for the secondary conversion to visible light.

Compared to other scintillator compositions, ⁶LiF/ZnS:Cu-based detectors provide the highest light yield, which allows for an extensive dynamic range and improves the signal-to-noise ratio. Regarding the linearity of the light yield, it should be noted that the relative light yield increases to about 104% during the first 60s of illumination. In other words, during the first 60s of exposure, the light yield increases by 4% compared to the first image taken. This minor effect is attributed to the delayed emission of trapped electrons, as discussed by Neuwirth et al. [67]. In terms of fluence, being the time-integrated flux, the peak in light yield is reached after a fluence of $f_{\text{peak}} = 10 \times 10^{10} \text{ cm}^{-2}$, independent of the incident flux. To put this into perspective, the maximum light yield is achieved after roughly 160s of illumination at a flux of $6.25 \times 10^7 \text{ cm}^{-2} \text{ s}^{-1}$. Subsequently, the relative light yield slowly decreases at a rate of $\frac{10\%}{200 \times 10^{10} \text{ cm}^{-2}}$. The decline in light yield is mainly attributed to radiation damage to the crystal structure, leading to defects that capture electrons, thereby reducing the light yield. The resulting changes in light yield are illustrated in Fig. 3.3. Being emitted as a result of neutron capture and subsequent conversion processes, not all photons are immediately emitted upon neutron irradiation, entailing an afterglow effect following neutron exposure. After 2s, the afterglow amounts to approximately 1.98% of the initial light yield after, which decreases to 0.1% at 40s post-exposure. Although this afterglow can give rise to ghost images, the slow-paced nature of our experiment reduces the effects

significantly. Care was taken to schedule a delay between subsequent images to mitigate the issue further. In conclusion, the ${}^6\text{LiF}/\text{ZnS}:\text{Cu}$ -based scintillation plates demonstrate reasonable linearity regarding their light yield as a function of exposure time and neutron flux. This linearity facilitates a quantitative analysis of experiments using these detectors.

3.2.2 Data Evaluation

As a figure of merit for an **NMO**, we are typically interested in the ratio of correctly redirected neutrons, i.e., neutrons arriving within a designated focal spot, compared to the total number of neutrons incident on the **NMO**. To quantify this ratio, we capture three images, which include one with the **NMO** redirecting the beam, a *flat-field image* without the device, and a *dark-field image* obtained with a closed shutter⁽³⁾. The latter accounts for the background originating from thermal noise in the camera and the constant positive offset discussed earlier. These images are represented in Fig. 3.4 (b), (c), and (d), respectively. In terms of these acquired images, the transport efficiency is given by the grayscale value integrated within the focal spot of Fig. 3.4 (b) (outlined in orange), I_{foc} , divided by the integrated grayscale of the flat-field Fig. 3.4 (c), I_{ff} . However, care has to be taken to correctly account for the constant background of the dark field, I_{df} , represented in Fig. 3.4 (d). The resulting formula for the transport efficiency is given by,

$$Q = \frac{\left(\frac{I_{\text{foc}} - I_{\text{df}}}{M_{\text{foc}}}\right)}{\left(\frac{I_{\text{ff}} - I_{\text{df}}}{M_{\text{ff}}}\right)} = \frac{\left(\frac{I_{\text{foc}} - I_{\text{df}}}{M_{\text{foc}}}\right)}{S_{\text{ff}}}. \quad (3.6)$$

Here, M_{foc} and M_{ff} are the upstream monitor readings for the images with and without the optical device, respectively. The normalization of the data to those monitors accounts for both the dependence of the light yield on the exposure time and any fluctuations in the neutron flux, which are common at spallation sources such as the PSI.

We will now discuss the panels in Fig. 3.4 in more detail, focusing on their role in data evaluation. It should be noted that all images, originally 2048×2048 pixels large, have been filtered with a 4×4 median filter to correct for gamma spots and other irregularities in the data. As an additional benefit, this operation reduces the file size significantly.

Panel (b) displays the color plot of the grayscale values acquired from the focused beam. We observe a sharp central line corresponding to the one-dimensionally focused neutrons. Panel (c) represents the flat-field image obtained by removing the **NMO** from the beam path. A small modulation of intensity is attributed to the employed Soller collimator. Additionally, we observe the mask used to confine the beam to the entrance area of the **NMO**, resulting in a quadratic illumination area on the detector. The color plot in panel (d) depicts the grayscale values of the dark-field image obtained with a closed neutron shutter shortly after the illumination performed for panel (c). This image expresses a constant background with a value of approximately 300 grayscale units. This constant offset is in place to prevent negative entries in the data and remains independent of the exposure time. Conversely, the afterglow effect, which contributes about 10 grayscale units, scales non-linearly with the exposure time and is thus more difficult to account for.

⁽³⁾We can assume that no neutron traverses a closed shutter, effectively reducing the incident neutron flux to zero.

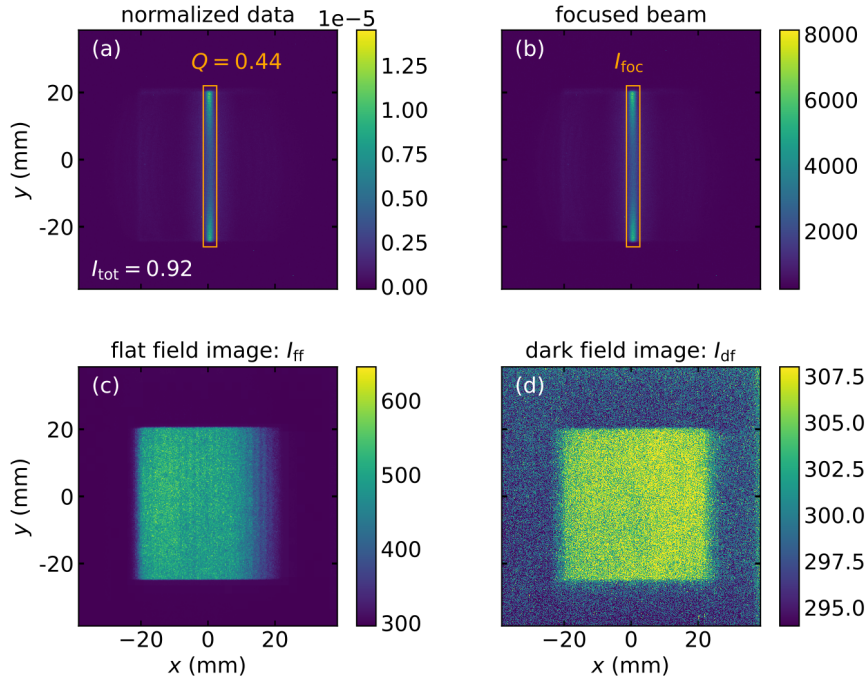


Figure 3.4: Illustration of the data normalization process utilized for the imaging data. All panels show color plots of spatial intensity distributions. Panel (a) shows the focused neutron beam, with the grayscale values normalized according to Eq. (3.6). Panel (b) shows the raw grayscale values obtained with the NMO in the beam. Panel (c) shows grayscale values of the flat-field image, with the NMO removed from the beam. Subtracting the dark field, integrating the resulting grayscale values, and normalizing to the monitor yields S_{ff} . Panel (d) shows the grayscale values of the dark field obtained with a closed shutter shortly after the previous illumination. The square-shaped afterglow of the detector system amounting to ≤ 10 grayscale units is observed in the central part of the data.

Regarding the efficiency of transport given by Eq. (3.6), we first performed a pixel-wise⁽⁴⁾ subtraction of the dark field (d) from the flat-field image (c). Next, the resulting data is normalized to the respective monitor value, M_{ff} . In cases of constant incident flux, M_{ff} is proportional to the exposure time. The normalized flat-field image was then integrated, yielding the denominator of Eq. (3.6), which we denoted as S_{ff} . This value represents the monitor-normalized number of neutrons potentially interacting with the NMO.

Similarly, we subtracted the dark field from the raw data obtained with the NMO in the beam (b) on a pixel-wise basis. Subsequently, the data is normalized to the monitor reading, M_{foc} . To further normalize this image to the situation without the NMO present, we divided it by S_{ff} , generating the data shown in Fig. 3.4 (a). The integrated intensity amounts to $I_{\text{tot}} = 0.92$. A value of one would indicate the ideal case where no neutrons are absorbed or scattered away from the detector during focusing. By selecting a specific area of integration,

⁽⁴⁾Pixel-wise refers to an operation that is performed independently on each pair of corresponding pixels between two or more images.

such as the orange rectangle in (a), we determine the transport efficiency for that particular area, yielding $Q = 44\%$.

3.2.3 Imaging Beamline BOA, PSI, CH

We provide a brief overview of the imaging beamline BOA (**B**eamline for neutron **O**ptics and other **A**pplications) at PSI (Switzerland), where the high-resolution investigations of the **N**M**O**s were conducted. For a more detailed review of the instrument, the reader is referred to the work of Morgano et al.[73] from which this subsection draws inspiration.

BOA replaced the former FUNSPIN instrument at PSI and is dedicated to testing advanced neutron scattering and optics techniques. It offers excellent flexibility and a high spatial resolution. The neutron guide leading to BOA is aligned with the cold source from which, after passing a polarizing bender and a horizontally focusing guide, polarized neutrons with a divergence of $\approx 40'$ are provided in a square area measuring $40 \times 40 \text{ mm}^2$.

Under standard operating conditions with a proton current of 1.48 mA hitting the target, the total flux at the entrance of the instrument amounts to $1.7 \times 10^8 \text{ cm}^{-2}\text{s}^{-1}$ peaking in intensity at around $\lambda = 3 \text{ \AA}$ [73], as depicted in Fig. 3.5. The dependence of the flux

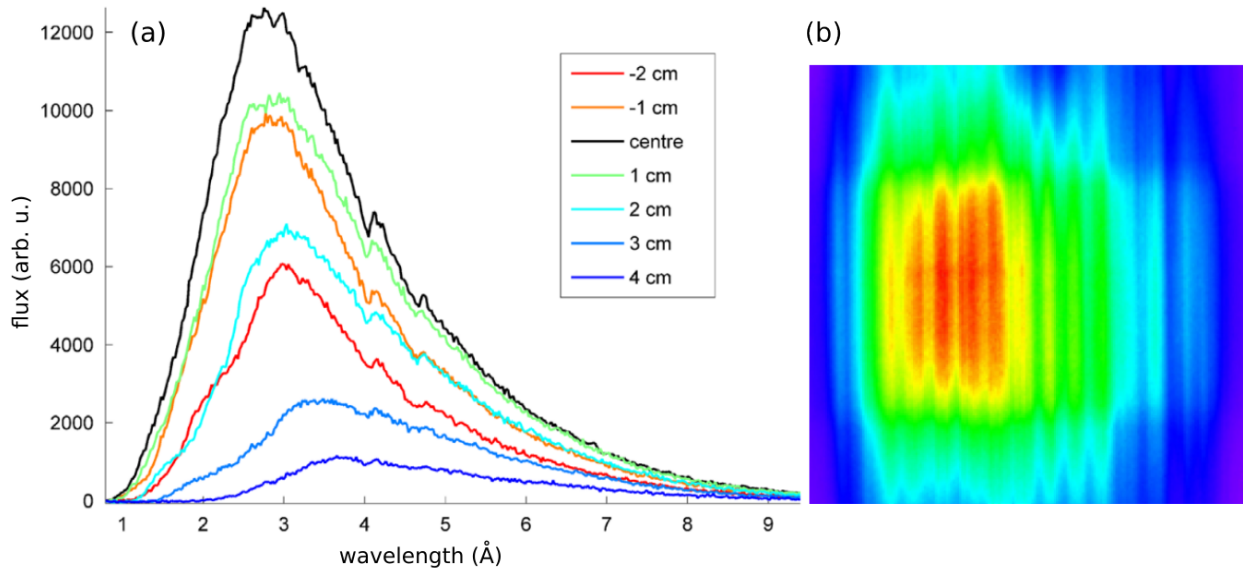


Figure 3.5: Beam characteristics at BOA. (a) Wavelength spectra were recorded at seven different positions in the horizontal plane of the beam. Reflection at larger angles (positive positions) reduces intensity and shifts the maximum towards longer wavelengths. (b) Spatial intensity modulation at the beam hole as seen through a pin-hole configuration. The intensity fluctuations are attributed to reflections at individual mirror planes of the bender. Figures are taken with permission from Morgano et al.[73].

distribution on the horizontal position is attributed to the dependence of the supermirror reflectivity on the wavelength (compare Fig. 5.4 (a)). Reflection at larger angles leads to a reduction in intensity and a shift of the maximum intensity toward larger wavelengths. To optimize for long wavelengths and to minimize the measurement background, the direct line of sight between the beam hole and the cold moderator is blocked.

As illustrated in Fig. 3.5 (b), the beam experiences a notable spatial intensity modulation in a pin-hole configuration. This is attributed to reflections from individual channels of the bender. In our experiments, we utilized the entire 40 mm of horizontal extent, effectively averaging this intensity modulation, as validated by the flat-field images. Before interacting with the focusing device, the beam underwent collimation by Soller type collimators $\alpha \in \{10', 20', 40'\}$ and monochromatization by a [double crystal monochromator \(DCM\)](#) with a wavelength range of $2.5 \text{ \AA} \leq \lambda \leq 6.1 \text{ \AA}$. Finally, the spatial intensity distribution of the neutron beam arriving at the detector is converted to a digital image by a standard ${}^6\text{LiF}/\text{ZnS}:\text{Cu}$ scintillator coupled to a [CCD](#) camera. This setup provides a resolution of approximately $100 \mu\text{m}$, sufficient for discerning subtle features in the spatial intensity distribution of the manipulated neutron beams.

4. Anomalous Lattice Dynamics in LuVO_3 - A Triple-Axis Scattering Investigation

This chapter is divided into three parts. First, we introduce **rare-earth vanadates (REV)** with a focus on LuVO_3 ⁽¹⁾. Secondly, we discuss the experimental techniques used to study the lattice dynamics and present the resulting phonon dispersions along several high-symmetry directions. Finally, we analyze the obtained results in the context of anomalous changes in elastic constants due to phase transitions and compare them to similar studies on related compounds.

4.1 Properties of Rare-Earth Vanadates

This opening section describes the crystal and electronic structure of **rare-earth vanadates (REV)**, focusing on LuVO_3 . We will also highlight the diverse phase diagrams of **REV** and the relationship between the lattice distortions and the electronic and magnetic structures. **REV** belong to the larger family of perovskites and have the chemical formula $R\text{VO}_3$, where R denotes a rare-earth element (a lanthanide, Sc, Y, and Lu). The subsequent sections draw inspiration from several studies by Radhakrishnan [74], Benckiser [75], Goodenough et al. [76] and Mizokawa et al. [77], to which the reader is referred for a more comprehensive analysis of some aspects of this group of compounds.

4.1.1 Crystal Structure of $R\text{VO}_3$

At room temperature, $R\text{VO}_3$ compounds commonly crystallize in the orthorhombic $Pbnm$ space group (No. 62(2))⁽²⁾. In comparison to an ideal cubic perovskite (chemical formula ABO_3), which crystallizes in the $Pm\bar{3}m$ space group (No. 221), the size mismatch between the R and the V atoms entails a distortion of the formerly cubic structure with several implications [79], which are also visualized in Fig. 4.1:

- Compared to the cubic case, the V-O-V angles are smaller than 180° , indicating that the oxygen octahedra are tilted with respect to each other.
- Due to the size mismatch between the R and V atoms, the lengths of the individual V-O bonds deviate from their former common value. This distortion leads to a distortion of the shape of the oxygen octahedron, thereby lowering the symmetry of the crystal field surrounding the V atom, which splits the $3d$ orbitals of the V atoms.
- In sum, the breaking of symmetry changes the space group from a cubic perovskite structure to the orthorhombic structure; $Pm\bar{3}m \rightarrow Pbnm$ [80, 81].

The rotation of the oxygen octahedra is referred to as the GdFeO_3 -type rotation [77, 82]. One can construct a pseudo-cubic unit cell within the room-temperature orthorhombic structure

⁽¹⁾Being the last member of the lanthanide series possessing the smallest ionic radius, lutetium belongs to the rare earths sharing many of their properties.

⁽²⁾The interested reader is referred to the work of Souvignier et al. [78] for an overview of the here used Hermann–Mauguin symbols.

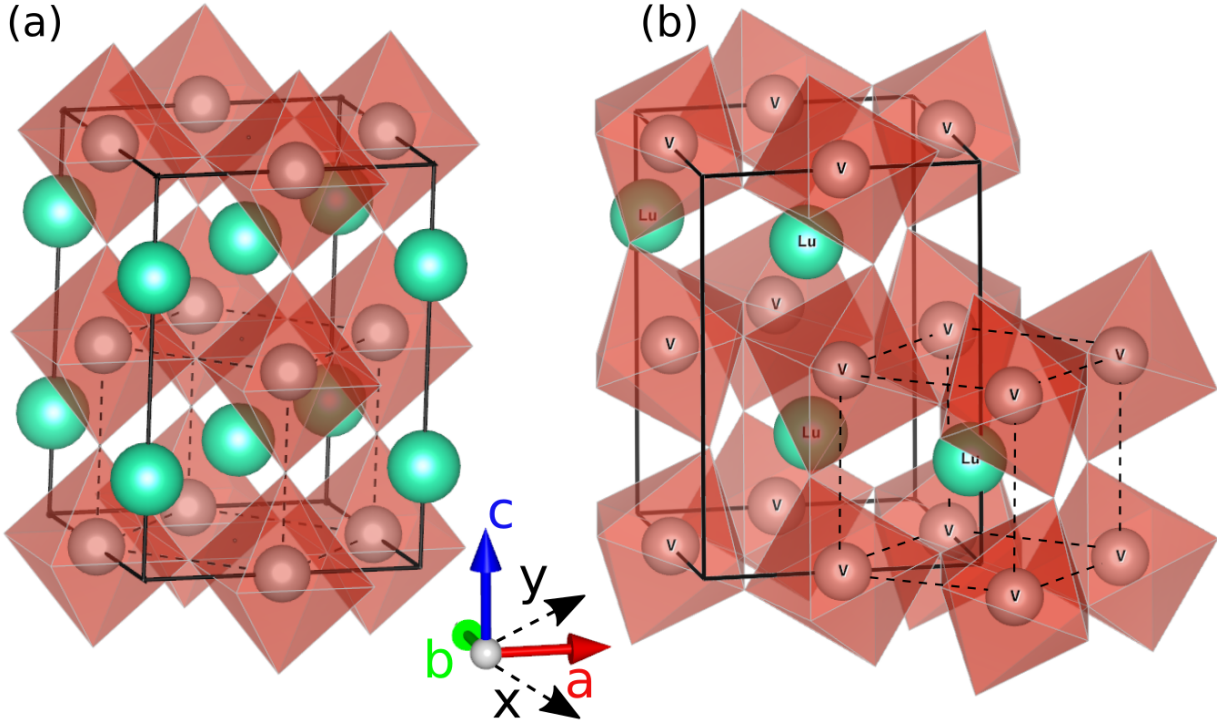


Figure 4.1: (a) Ideal cubic perovskite structure with point group $Pm\bar{3}m$ and (b) room-temperature crystal structure of $R\text{VO}_3$, $Pbnm$, at the example of LuVO_3 . The orthorhombic unit cell is indicated by solid, black lines, while the ideal cubic (a) and pseudo-cubic (b) unit cells are indicated by dashed, black lines. The oxygen octahedra (red) in the orthorhombic $Pbnm$ structure are tilted with respect to the ideal perovskite structure as a result of the size mismatch between R and V (GdFeO_3 -type rotation). Figure is reproduced from Goodenough et al. [76].

to visualize the distortion of the cubic perovskite precursor. The axes of this pseudo-cubic cell (x, y, z) have the following relationship with the axes of the orthorhombic unit cell $x = y \approx \sqrt{a^2 + b^2}/2$, $z \approx c/2$ [83]. Taking LuVO_3 as an example, Fig. 4.1 shows both the ideal perovskite structure (a) and the room-temperature $Pbnm$ unit cell of $R\text{VO}_3$ (b), which are rotated by 45° with respect to their parallel c - and z -axes.

The emergence of deviations from a perfect cubic structure in the context of the reduced ionic radius of R can be comprehended through the empirical tolerance factor, initially introduced by Goldschmidt [3]. It is defined by

$$\alpha := \frac{1}{\sqrt{2}} \frac{r_A + r_O}{r_B + r_O}, \quad (4.1)$$

where r_A, r_B and r_O denote the effective ionic radii of the elements A, B and O for the perovskite ABO_3 , respectively [84, 85]. Despite recent discussions, whether the tolerance factor can on its own reliably predict the structure, stability, and lattice parameters of perovskite compounds [86], it still serves as a first estimate of potential lattice distortions.

For example, $SrTiO_3$ crystallizes in an ideal, cubic perovskite structure, which is reflected by its tolerance factor close to unity, $\alpha = 1.009$, where $r_A = r_{Sr} = 1.44 \text{ \AA}$, $r_B = r_{Ti} = 0.605 \text{ \AA}$ and $r_O = 1.35 \text{ \AA}$ are obtained from the work of Shannon et al. [85] for coordination numbers corresponding to the cubic perovskite, 12, 6 and 2, respectively⁽³⁾.

In the case of RVO_3 , $r_V = 0.64 \text{ \AA}$, $r_O = 1.35 \text{ \AA}$, the rotation of the oxygen octahedra entails a reduction of the coordination number of R and V to 8 and 6, respectively. It should be noted that the tabulation of the ionic radii by Shannon [85] does not extend to all R for the required coordination numbers, and we, in some instances, relied on the approximated values calculated by Jia [88]. The resulting tolerance factors for RVO_3 range from $\alpha = 0.89$ for $r_{La} = 1.16 \text{ \AA}$ to $\alpha = 0.84$ for $r_Y = 1.02 \text{ \AA}$ and $\alpha = 0.83$ for $r_{Lu} = 0.98 \text{ \AA}$, respectively. All **REV** fall in the range $0.8 \leq \alpha \leq 0.89$, for which the distorted perovskite structure is expected [89].

In summary, a trend towards smaller r_R suggests a more pronounced distortion of the cubic perovskite structure. A gradual variation of the ionic radii belonging to different R and the associated distortion towards a more orthorhombic structure are expected to result in significant changes in the magnetic and orbital ordering, which has attracted significant scientific interest [1, 2, 77, 79, 82, 90, 91, 92, 93, 94, 95]. Possessing the smallest ionic radius among all **REV**, $LuVO_3$ stands out by potentially exhibiting more pronounced effects.

4.1.2 Electronic Structure of RVO_3

The electronic structure of the RVO_3 Mott insulators is governed by two electrons occupying the $3d$ shell of the V^{3+} ions. The cubic crystal fields associated with the undisturbed oxygen octahedra ($Pm\bar{3}m$) cause a splitting of the originally five-fold degenerate $3d$ levels [96], which is shown in Fig. 4.2 (a). This results in one triply degenerate t_{2g} orbital and one doubly degenerate e_g orbital. The repulsion between the electron clouds of the $3d$ orbitals and the negatively charged oxygen ligand ions in octahedral surroundings favors minimizing overlap. Consequently, the triply degenerate t_{2g} set (xy , yz , and zx orbitals), is energetically favored compared to the e_g set being composed of $x^2 - y^2$ and $2z^2 - x^2 - y^2$ orbitals [97, 96]. The corresponding electron densities are sketched in Fig. 4.2 (b), where the negatively charged oxygen ions comprising the octahedron are located on the axes of the coordinate system. The large energy gap between the e_g and t_{2g} orbitals ($10 Dq$) makes a mixture of states unlikely [75, 97].

The degeneracy of the t_{2g} orbital is further lifted by a mixture of two effects. Firstly, the $GdFeO_3$ -type rotation results in non-uniform V-O bond lengths, causing the t_{2g} orbitals to split by a small amount at all temperatures [77]. Secondly, an additional distortion of the oxygen octahedron reduces the cubic symmetry of the crystal field to a tetragonal or trigonal one. As shown in Fig. 4.2 (a), this reduction in symmetry splits the t_{2g} and e_g orbitals such that energy is gained by partially occupying the resulting lower energy orbitals. If this energy gain from this more favorable occupation exceeds the loss associated with the deformation of the crystal structure, the distortion is realized, and the compound is called Jahn-Teller-active [98].

⁽³⁾A readily available overview of the ionic radii published by Shannon can be found in an online database [87].

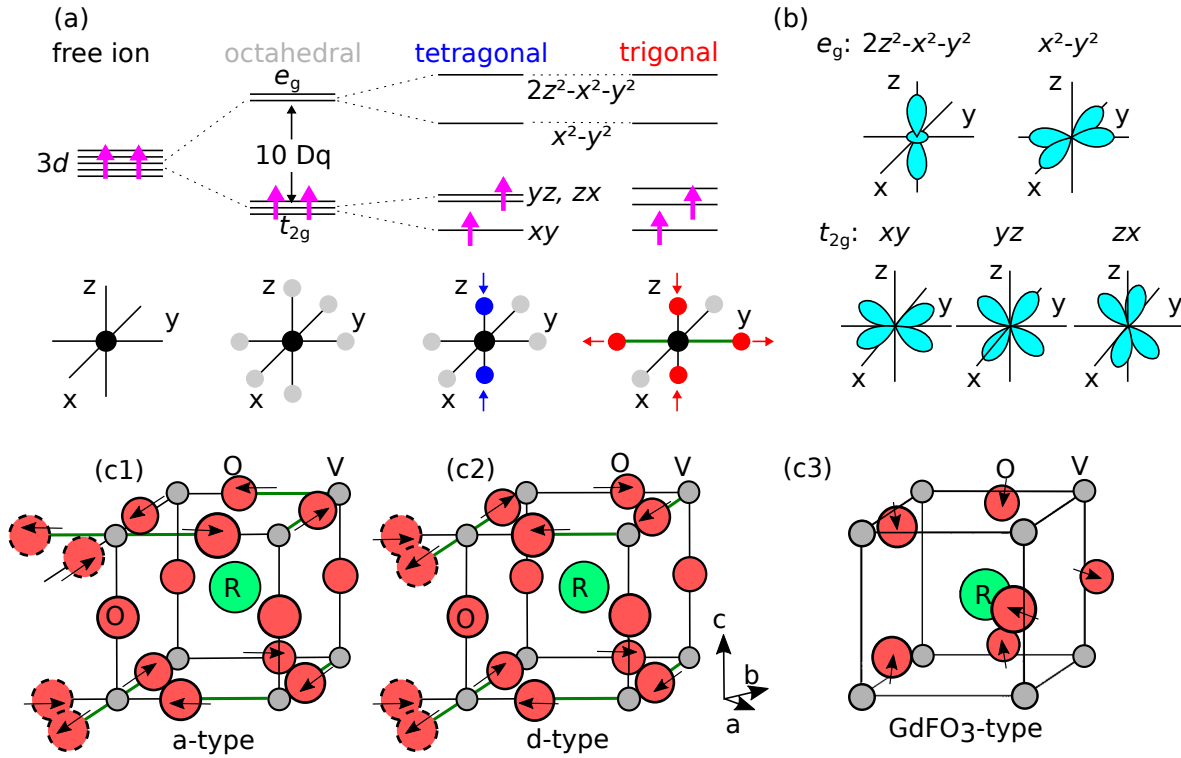


Figure 4.2: (a) Splitting of the five-fold degenerate $3d$ orbitals in a crystal field with different symmetries. When subjected to a crystal field with cubic symmetry, the $3d$ orbitals are split into a triply degenerate t_{2g} and a doubly degenerate e_g orbital. Due to the orientation of the negatively charged O-ligands, t_{2g} is energetically favored to e_{2g} . When the symmetry of the crystal field is further reduced by compression of the oxygen octahedra, the degeneracy of the orbitals is further lifted. The occupation of the orbitals by two valence electrons in V^{3+} according to Hund's rules is indicated by pink arrows. (b) shows the distribution of electron densities for various $3d$ orbitals. While the density of the e_g orbitals is maximized along the coordinate axes, the density of the t_{2g} is localized between two axes, respectively. Figures (a) and (b) are reproduced from Kugel et al. [96]. (c) The systematic distortion of the corner-sharing oxygen octahedra gives rise to the collective Jahn-Teller effect. (c1) and (c2) For a- and d-type Jahn-Teller effects, the elongated bonds (highlighted in green) within the ab -plane are oriented perpendicular and parallel when traversing the c -axis, respectively. (c3) Tilting of oxygen octahedra in the GdFeO_3 -type rotation. Figures (c1-3) are reproduced from Mizokawa et al. [77].

In the case of V^{3+} ions, only two electrons are available to fill the three t_{2g} orbitals, one electron always occupying xy and the other either yz or zx . Due to the sharing of corners between octahedra, individual Jahn-Teller distortions become coupled and give rise to the collective Jahn-Teller effect. For a more comprehensive treatment of this topic, the reader is referred to the work of Kugel and Khomskii [96].

Fig. 4.2 (c1 and c2) illustrate two expressions of the collective Jahn-Teller effect differing only with respect to the stacking of the distorted octahedra along the c -axis [77]. For the a -type distortion (c1), the elongated bonds of two adjacent octahedra, indicated in dark green, are rotated by 90° around the c -axis with respect to each other when moving through the crystal along the c -direction. However, in the d -type distortion (c2), the elongated bonds are parallel when traversing the crystal along c . When moving through the crystal along either the x - or y -direction, the elongated bonds are consistently rotated by 90° around the c -axis with respect to each other. The additional tilting of the octahedra associated with the GdFeO_3 rotation (c3) subtly influences the choice between a - and d -type Jahn-Teller distortions. It has been demonstrated through the minimization of the free energy that the d -type Jahn-Teller distortion is energetically favored over the a -type distortion when a large GdFeO_3 -type distortion is present, specifically for a small ionic size of R [77].

Importantly, the different types of Jahn-Teller distortions are intertwined with a corresponding orbital order (OO). In agreement with the symmetry of neighboring oxygen octahedra, for the a -type distortion, an alternating occupation of yz and zx orbitals is expected along all directions, i.e., anti-ferro G-type OO. Similarly, if the Jahn-Teller distortion is of d -type, one encounters the same occupation of orbitals when moving along z , with alternating orbitals along x and y , i.e., C-type OO [96]. According to the *Goodenough-Kanamori rules*, in perovskites, the magnetic spin order (SO) correlates strongly with the OO, where G-type (C-type) OO favors C-type (G-type) SO, respectively [76].

The importance of the cation size for orbital and magnetic transitions in $R\text{VO}_3$ can be understood by comparing the temperature dependence of the SO and the OO for different occupants of the R -site, which is summarized in Fig. 4.3. In panel (a), the specific heat of $R\text{VO}_3$ as a function of temperature is plotted for various elements R , revealing small peaks indicative of phase transitions in the respective curves. Upon cooling the compounds below T_{OO1} , the orthorhombic $Pbnm$ space group transitions to the monoclinic $P2_1/b$ space group (No. 3). The onset of G-type orbital ordering accompanies this transition. At T_{SO1} , C-type spin ordering emerges in addition to the existing G-type OO. Lastly, for compounds with relatively small ionic sizes of R , starting with Dy, a final phase emerges at temperatures below T_{SO2} . The OO transitions from G-type to C-type, and the SO changes from C-type to G-type. This observation is consistent with an increasing tilt angle for smaller cations, favoring a collective d -type Jahn-Teller distortion, giving rise to C-type orbital ordering. These changes of the SO and the OO at T_{SO2} were reported to be accompanied by a structural transition from $P2_1/b$ back to the room temperature structure $Pbnm$ [2, 99].

4.2 Properties of LuVO_3

LuVO_3 , the member among the $R\text{VO}_3$ compounds with the smallest ionic radius, experiences the most pronounced GdFeO_3 distortion. This has attracted considerable research interest, which will be briefly discussed here.

An overview of the various structural, orbital, and magnetic phases in LuVO_3 is given in table 4.1. We follow the naming convention for the individual phases by Skoulatos et al. [2]. At room temperature, LuVO_3 crystallizes in the $Pbnm$ space group without exhibiting either OO or SO (phase 0). Upon cooling below $T_{\text{OO1}} = 177$ K, G-type OO emerges alongside with a structural transition to $P2_1/b$ (phase I). Further cooling below $T_{\text{SO1}} = 105$ K is associated

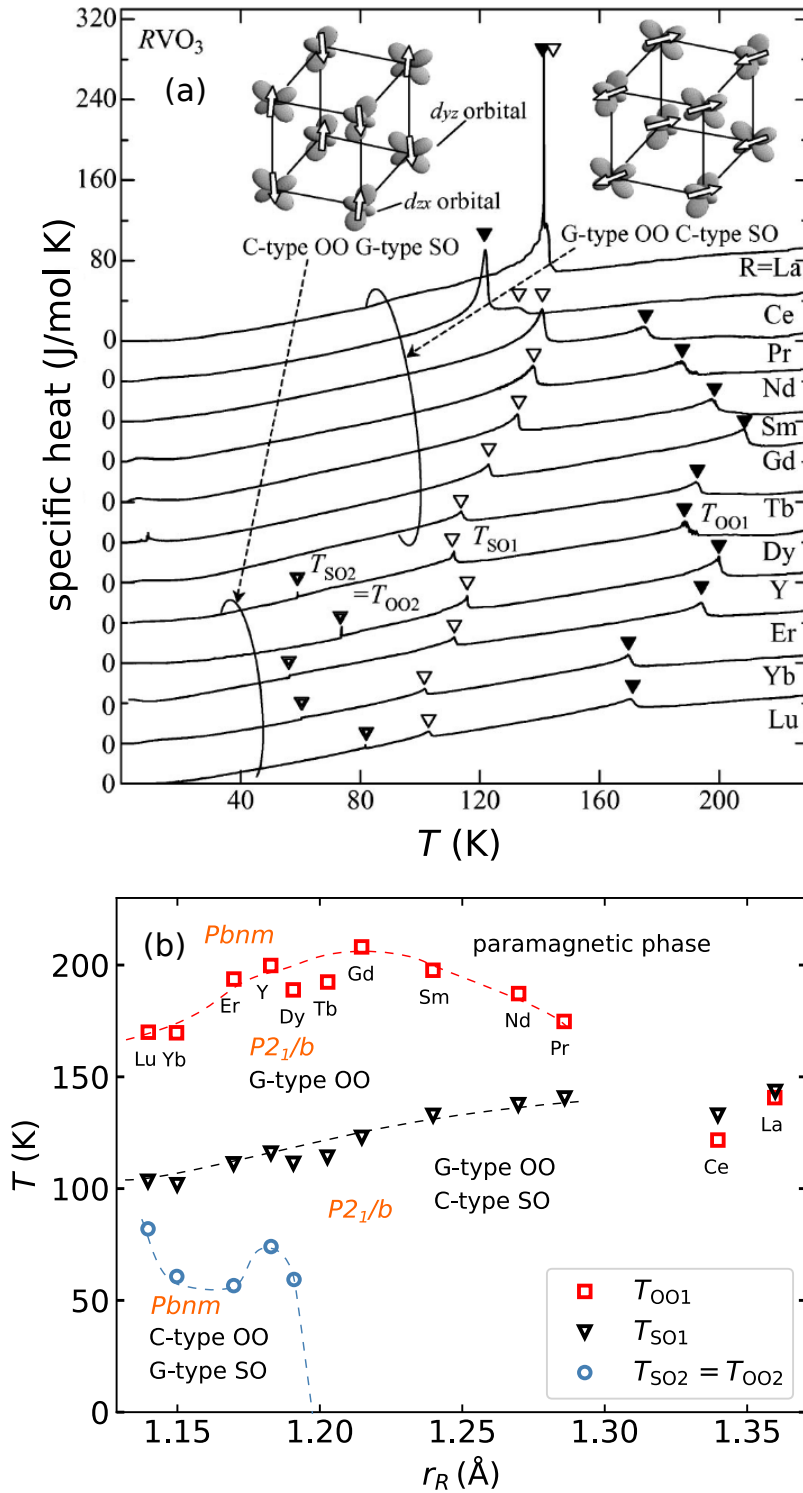


Figure 4.3: (a) Temperature dependence of the specific-heat for $R\text{VO}_3$, where R denotes a rare earth element. Transition temperatures associated with G-type orbital ordering (T_{OO1}), C-type spin ordering (T_{SO1}), and the combined G-type spin and C-type orbital ordering ($T_{\text{SO2}} = T_{\text{OO2}}$) are indicated by closed, open, and double triangles, respectively. The left inset shows C-type OO and G-type SO. The right inset shows G-type OO and C-type SO for comparison. Open arrows and shaded lobes indicate spin direction and d_{yx} and d_{xz} orbitals of the vanadium atoms, respectively. (b) Overview of different types of SO and OO in $R\text{VO}_3$ plotted against the ionic radius of R , r_R . Figure is reproduced from the work of Miyasaka et al. [1]

with the appearance of a slightly canted C-type SO and a transformation of the OO to C-type (phase II). Finally, as the temperature drops below $T_{\text{SO2}/\text{OO2}} = 82.5$ K, the OO changes to C-type and the SO transitions to G-type (phase III). Additionally, the crystal structure reverts back to $Pbnm$ at $T_{\text{SO2}/\text{OO2}}$. This behavior is consistent with that observed in other

	temperature	space group	OO	SO
phase 0	$T \geq 177 \text{ K}$	$Pbnm$; No. 62(2)	-	-
phase I	$177 \text{ K} \geq T \geq 105 \text{ K}$	$P2_1/b$; No. 3	G-type	-
phase II	$105 \text{ K} \geq T \geq 82.5 \text{ K}$	$P2_1/b$; No. 3	G-type	C-type
phase III	$82.5 \text{ K} \geq T$	$Pbnm$; No. 62(2)	C-type	G-type

Table 4.1: Crystal structure and orbital and magnetic ordering in LuVO_3 at various temperature ranges.

RVO_3 compounds with small ionic radius, e.g., Yb, Er, Y, Dy (see Fig. 4.3 and [99]). Fig. 4.4 visualizes the OO and the SO for the phases II and III. The monoclinic structure in phase II lifts the equivalency between V-atoms along the c -axis, which is visualized by darker shades of the orbitals. Importantly, the magnetic spins in the G-type SO in phase III are aligned parallel to the c -axis, while in phase II, they are canted in the bc -plane. Fig. 4.5

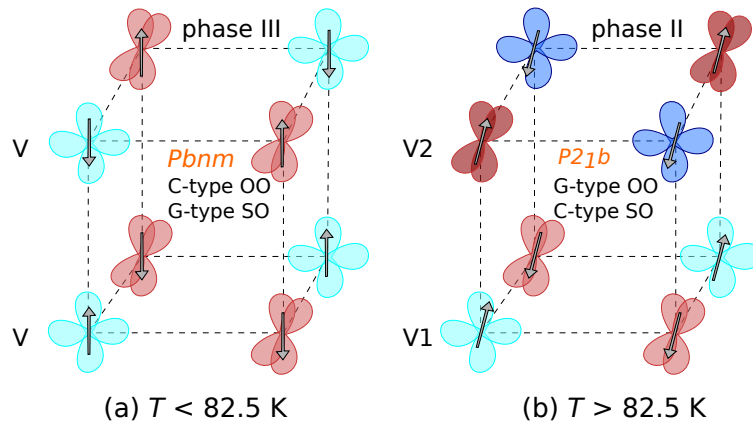


Figure 4.4: OO and SO of LuVO_3 visualized for V atoms of a single pseudo-cubic unit cell. Red and blue hues indicate occupied yz and zx orbitals, and light and dark shades indicate orbitals belonging to crystallographically different V atoms in the $P2_1/b$ structure (only for $T > 82.5 \text{ K}$). Gray arrows indicate the SO, which is consistent with the Goodenough-Kanamori rules. See text for more details. The Figure is reproduced from Skoulatos et al. [2].

shows an overview of the temperature dependence of the lattice parameters and the V-O bond lengths. Investigating the parameters of the pseudo-cubic cell at room temperature yields $x = y = \sqrt{a^2 + b^2}/2 = 3.81 \text{ \AA}$, which is significantly larger than $z = c/2 = 3.75 \text{ \AA}$, in agreement with the xy orbital being energetically favored by the Jahn-Teller distortion.

One observes a minute change in bond lengths and a change in the slope of the lattice parameters upon cooling below $T_{\text{OO1}} = 177 \text{ K}$ which is concomitant with the change from $Pbnm$ to $P2_1/b$. The onset of C-type SO is accompanied by a significant change in bond length but does not impact the lattice parameters. However, the transition to G-type SO

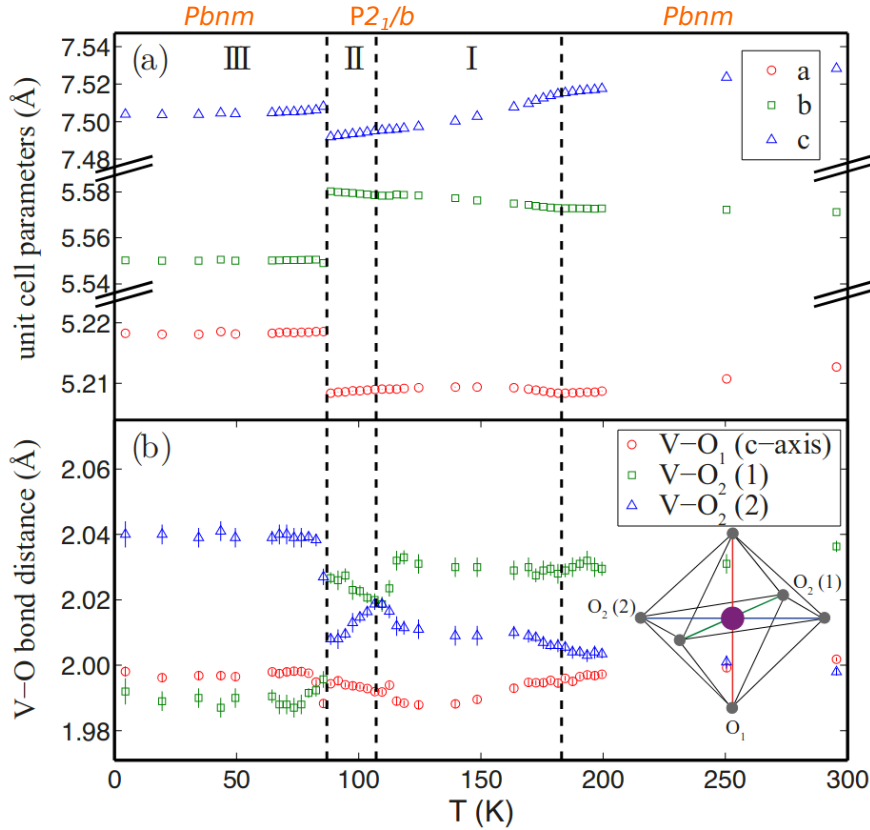


Figure 4.5: Lattice parameters (a) and V-O bond lengths (b) in LuVO_3 as a function of temperature. The values are refined from high-resolution X-ray synchrotron data. Figure is reproduced with permission from taken from Skoulatos et al. [2].

and C-type OO at $T_{\text{SO}2}$ is accompanied by discontinuities in both the bond lengths and the lattice parameters.

Across all observed T , the $V-O_1$ bond distance along the c -axis remains relatively constant and compressed, indicating that the permanent occupancy of the xy orbital is unchanged. In contrast, the lengths of the two distinct V-O2 bonds exhibit a significant change during the III-to-II phase transition. The difference between them changes sign, possibly indicating a corresponding swap in the occupancies of the zx and yz orbitals.

In conclusion, we expect substantial modifications of the effective Hamiltonian across the transition and the occurrence of orbital fluctuations in phase II, as predicted by theoretical models [100]. Furthermore, the abrupt albeit small change in lattice parameters, $< 0.5\%$, suggests that the elastic constants coupled to the electronic structure via the Jahn-Teller effect might change, which would result in a noticeable alteration of the lattice dynamics of the compound.

Magnetic Properties

In the closely related REV compound YVO_3 , Ulrich et al. [101] report neutron scattering data hinting at unusual magnetic properties. They find an anomalously small magnetic

moment, $1.05(2) \mu_B$, in YVO_3 's equivalent of phase II. The authors attribute the attenuation from the free ion value of $2 \mu_B$ to strong quantum fluctuations in the orbital phase. Further, they report unusual features in the magnon dispersions obtained in phase II, e.g., $|J_c| > |J_{ab}|$ and a splitting of the acoustic spin wave into an acoustic and an optical branch with a gap of 5 meV. The gap was explained by employing a model where J_c significantly varies between the inequivalent V atoms along the c -axis, which produces alternating bonds along c . This proposed model, a “orbital Peierls” dimerization state, requires degenerate yz and zx orbitals sharing a single electron (with the other occupying xy). However, cluster calculations yield a splitting of the orbital energy of yz and zx , contradicting this model [75].

An alternate hypothesis brought forth by Fang and Nagoasa [92] explains the reported magnetic properties of YVO_3 by a model based on the Jahn-Teller effect, in which J_{ab} alternates along c instead of varying J_c . The LDA + U calculations⁽⁴⁾ are in qualitative agreement with experimental data regarding the spin-wave gap. The deviations between the calculated magnetic moment ($1.72 \mu_B$) and the experimentally obtained value ($1.05 \mu_B$), which have been brought forth as an argument supporting the orbital Peierls state, can be attributed to the elevated measurement temperature of 77 K at which the moment is not saturated.

Similarly, in $LuVO_3$, Skoulatos et al. have resolved the debate between a quantum “orbital Peierls” model and a semi-classical Jahn-Teller model in favor of the latter [2]. To this end, they showed that the magnon dispersions in previously investigated directions agreed with both models. However, the observed dispersion of the optical band between $(0, 1, 2)$ and $(0, 2, 2)$ could not be explained using the orbital Peierls model and is instead predicted by a Jahn-Teller induced alteration of J_{ab} along c . The authors also state that the spin alignment in phase II and the crystal structure of $LuVO_3$ differs from what is observed for YVO_3 with respect to the canting direction of the spins (compare Fig. 4.4). Additionally, their polarized neutron scattering data confirms the space group of the low-temperature phase III to be $Pbnm$, while the intermediate phase II crystallizes in a $P2_1/b$ space group. This result is in disagreement with previous work, where Muñoz et al. [94] describe $LuVO_3$ to undergo a structural phase transition from orthorhombic $Pbnm$ to monoclinic $P2_1/n$ space group at $T \leq 94$ K.

Within this work, we investigated the lattice dynamics of $LuVO_3$ using triple-axis neutron scattering within various structural, orbital, and magnetic phases. More specifically, the temperature dependence of acoustic and low-energy optical phonon dispersions was obtained along several high-symmetry directions. An unusual change in energy transfer, i.e., a softening of a transversal acoustic phonon branch, was observed and described in the context of elastic anomalies at structural phase transitions.

4.3 Experimental Details

Elastic and inelastic neutron scattering techniques were employed to study the lattice dynamics in $LuVO_3$ across its different structural, orbital, and magnetic phases. Within this section, we first report on the investigated crystal and then summarize the measurements

⁽⁴⁾LDA+U, also known as Hubbard U or DFT+U describes a computational approach for characterizing systems with strongly correlated electrons using the name-giving local density approximation. A detailed review of the technique can be found in the work of Anisimov et al. [102].

performed before discussing the treatment of the obtained data to extract the phonon dispersions.

4.3.1 Single Crystal of LuVO_3

A large single crystal of LuVO_3 with a mass of $m = 4$ g was grown by Tung Le in a high-temperature Xenon arc furnace. The crystal growth process consisted of a number of steps as outlined in [103]. Initially, LuVO_4 powder was produced by annealing stoichiometric quantities of Lu_2O_3 and V_2O_5 (99.9% purity) at 1100°C for 48 h. Subsequently, LuVO_3 powder was created by reducing LuVO_4 powder in a H_2 atmosphere at a temperature of 1000°C for a duration of 10 h. Finally, the LuVO_3 powder was grown into single crystals using the floating zone technique [104]. The seeds for the growth process were created by subjecting a small quantity of the powder to hydrostatic pressure and annealing the resulting rods in an argon atmosphere for 6 h at 1500°C [105]. Fig. 4.6 illustrates the crystal growth process and shows an image of the crystal mounted on its sample holder.

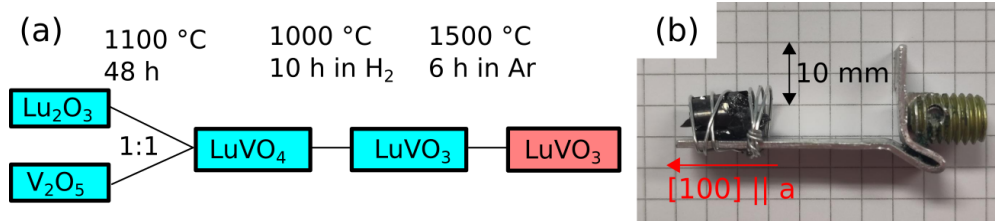


Figure 4.6: Schematics of the crystal growth of LuVO_3 and the resulting single crystal attached to a sample holder. (a) The growth process including the different stages is outlined, with blue rectangles representing powders and a red rectangle denoting the resulting single crystal. (b) During all experiments, the crystal was carefully aligned such that its a -axis (and the $[100]$ direction) was vertically oriented.

4.3.2 Measurement Strategy

The complex nature of the Jahn-Teller active compound, LuVO_3 , gives rise to a diverse phase diagram characterized by structural transitions involving the emergence of OO and SO . To unravel this intricate relationship, inelastic neutron scattering was employed as a powerful tool to probe the lattice dynamics in the material. This technique enables the precise determination of the phonon dispersion relations along different momentum transfer directions \vec{Q} . The measurements presented in this study were conducted by Tobias Weber (Planning and Conduction of the experiments) and Markos Skoulatos (Conduction of the experiments) at various TAS instruments, including EIGER at PSI in 2016, and 2017, MIRA-2 at FRM II in 2017, and PUMA at FRM II in 2018. The obtained data is analyzed and presented for the first time in this work.

To track the evolution of acoustic phonon dispersions (both longitudinal and transversal) across different phases characterized by distinct OO and SO , a systematic investigation at various temperatures was performed. An overview of all the scan paths is provided in Fig. 4.7. All investigations presented here were performed with the LuVO_3 single crystal being oriented in the $[001]$, $[010]$ scattering plane, such that its a -axis was oriented vertically

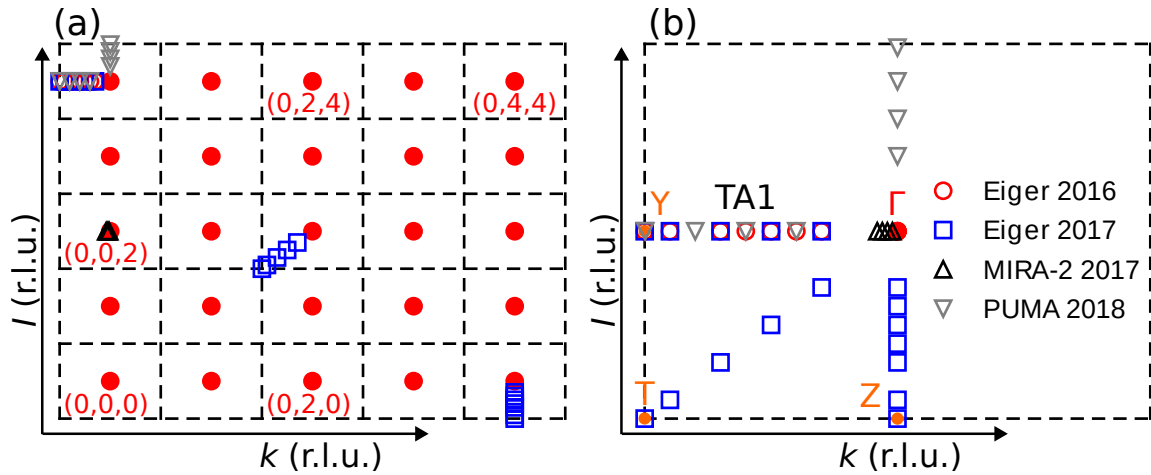


Figure 4.7: Overview of the conducted scans in reciprocal space (a), and their projection into the first Brillouin zone (b). Full red circles depict the reciprocal lattice points, while the zone boundaries are indicated by dashed, black lines. Orange circles indicate selected high symmetry points within the first Brillouin zone [106] to which the scans extend. Scans performed at large negative values of k or l are shifted into the first quadrant of the reciprocal space for visualization.

in the TAS experiment (compare Fig. 4.6 (b)). Due to the increase in signal strength from phonon modes with increasing momentum transfer, $S(\vec{Q}, \omega) \propto |\vec{Q}|^2$, one usually investigates the phonons in Brillouin zones as distant from the origin as the instrumental setup allows. A projection of all scans into a common BZ is visualized in (b). Several scans along very high symmetry directions, such as [010], [001], and [011], were obtained from the different measurements. Most of them extend towards the zone boundaries (dashed, black lines), where the change in phonon energy, i.e., the softening, is expected to be most pronounced. Each marker in Fig. 4.7 represents a series of constant- Q scans performed over an energy range enabling the determination of the phonon dispersion (typically ranging between 1 meV and 15 meV depending on the energy of the lattice excitation). Each constant- Q scan was repeated at a multitude of temperatures ranging from 9 K to 250 K to track subtle changes through the various magnetic and structural phases.

In contrast, the exceptional resolution in Q and ΔE of MIRA-2, FRM II was employed to determine the slope of the phonon dispersion close to the zone center, where its steep nature requires constant- E scans instead of constant- Q scans. Fig. 4.8 (a) and (b) show exemplary constant- Q and constant- E scans, respectively.

In order to extract the energy and momentum transfers from the data, theoretical models were fitted, which are indicated by solid lines in (a) and (b). Assuming a Gaussian profile for the resolution function of the TAS [107, 108]⁽⁵⁾ and a Lorentzian line shape for the phonon

⁽⁵⁾For the calculation of the resolution function, a Gaussian mosaic of the monochromator and the analyzer crystals is assumed together with a Gaussian intensity profile after collimation, which is typically well justified.

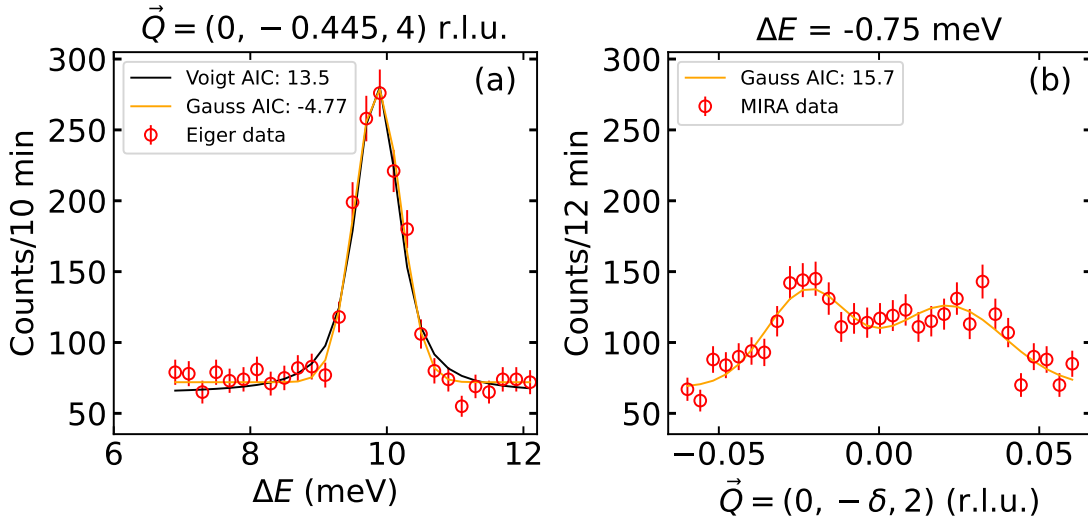


Figure 4.8: Exemplary constant- Q (a) and constant- E (b) scans investigating the phonon dispersions obtained at EIGER and MIRA-2, respectively. Various models fitted to the data are shown together with their AIC, which measures the chosen model’s *goodness* with a lower value indicating a better fit.

itself, one would expect the measured data, i.e., the convolution of the two, to be of Voigtian shape (indicated by a solid, black line)⁽⁶⁾. However, as presented in Fig. 4.8 (a) the data is better approximated by a simple Gaussian line shape with a constant background C , area A , center E_0 and width σ , e.g.,

$$\text{Counts} = A \frac{\exp\left(\frac{-(\Delta E - E_0)^2}{2\sigma^2}\right)}{\sqrt{2\pi}\sigma} + C, \quad (4.2)$$

reflected by a smaller Akaike information criterion (AIC) [109, 110]. This indicates that the line width of the phonon, Γ , is small compared to the instrument resolution, which complicates the determination of the former. A further determination of Γ utilizing resolution de-convolution does not promise significant improvements over the simple fitting procedure. Considering the small relative change in the energy transfer, the resolution ellipsoid is not expected to change significantly.

The data obtained by constant- E scans (b) was approximated by the sum of two Gaussian line shapes with different widths corresponding to the same transversal phonon branch obtained at $\pm(0, \delta, 2)$. One observes the influence of the instrumental resolution resulting in one focusing and one de-focusing branch at positive and negative values of δ ⁽⁷⁾. By combining the resulting energy and momentum transfers from individual scans, we obtain dispersion relations for different directions and temperatures.

⁽⁶⁾A Voigt line shape is defined as the convolution of a Gaussian lineshape with a Lorentzian lineshape. Often, a pseudo-Voigt profile is used as a model instead, which is the sum of the former two.

⁽⁷⁾Compare the work of Cooper and Nathans [107] for a detailed discussion of focusing effects in TAS measurements.

4.4 Phonon Dispersions

An extensive investigation regarding different phonon branches in LuVO_3 was conducted with an emphasis on temperature-dependent changes in phonon energy and linewidth hinting at the influence of changing structure, OO and SO. Dispersions along various directions were established during the experiments. Only the main results are presented here, with an overview of the raw scans found in the appendix A.

We first discuss an acoustic transversal phonon, propagating in the [010]-direction, polarized along [001], which was investigated around the (004) Bragg reflection. We will refer to this branch as TA1, compare Fig. 4.7 (b). An initial investigation at EIGER in 2016 hinted at a subtle softening of this phonon branch at the zone boundary as visualized in Fig. 4.9. We investigated TA1 at four different temperatures, $T \in \{50 \text{ K}, 70 \text{ K}, 90 \text{ K}, 110 \text{ K}\}$. Fig. 4.9 (a) shows the obtained dispersions, in excellent agreement with a sine-dispersion law [35],

$$\Delta E = \left| A \sin \left(\frac{xq}{2} \right) \right|. \quad (4.3)$$

The phonon possesses an amplitude of about $A = 10 \text{ meV}$ and extends from the zone center $q = 0$ to its boundary $xq = \pi$. However, in proximity to the zone boundary at $\vec{Q} = (0, -0.5, 4)$, one observes a decrease in the determined phonon energy of about 0.3 meV upon lowering the temperature from 90 K to 70 K , see inset. Fig. 4.9 (b) highlights the four constant- Q scans obtained for different temperatures at $\vec{Q} = (0, -0.5, 4)$. When comparing temperatures below and above $T_{\text{OO}_2} = 82.5 \text{ K}$, one observes a shift in phonon energy, characterized by the change of the peak position of the constant- Q scans, together with a minor increase in the total number of scattered neutrons. In addition to the main peak associated with TA1, centered around $\Delta E = 10 \text{ meV}$, one observes a weak signal attributed to a transverse optical phonon around 12.5 meV , which did not express any anomalous behavior.

A second investigation of TA1 at temperatures closer to $T_{\text{SO}_2} = 82.5 \text{ K}$ was conducted at EIGER, PSI, in 2017 with the obtained dispersions and scans being presented in Fig. 4.9 (c) and (d) following the same fashion as above. During this measurement, we confirmed the softening of the transversal phonon in addition to refining the temperature at which it occurs to a range between 80 K and 85 K . Due to a smaller range in investigated energy transfers, $8 \text{ meV} \leq \Delta E \leq 12 \text{ meV}$, the optical phonon was not observed here. Curiously, the difference in scattering rates above and below T_{SO_2} is smaller than in the previous experiment, which might be attributed to a slight difference in crystal alignment.

Besides the reproducible softening occurring close to the zone boundary, $\delta \in [-0.5, -0.4] \text{ r.l.u.}$, no significant change in energy is observed closer to the zone center, $\delta \leq 0.4 \text{ r.l.u.}$ Expanding on this observation, Fig. 4.10 shows the temperature dependence of the phonon energy at various fixed Q -positions. The figure combines the data from the dispersions and a designated temperature scan at $Q = (0, -0.5, 4)$. The findings are summarized as follows:

- TA1 undergoes a significant shift in phonon energy of about 0.3 meV at the zone boundary, $\vec{Q} = (0, -0.5, 4)$, at the second orbital ordering temperature $T_{\text{SO}_2} = 82.5 \text{ K}$. This change is concomitant with the structural transition, where the intermittent $P2_1/b$ structure reverts back to the room-temperature $Pbnm$ structure upon cooling, Fig. 4.10 (a) and (b).

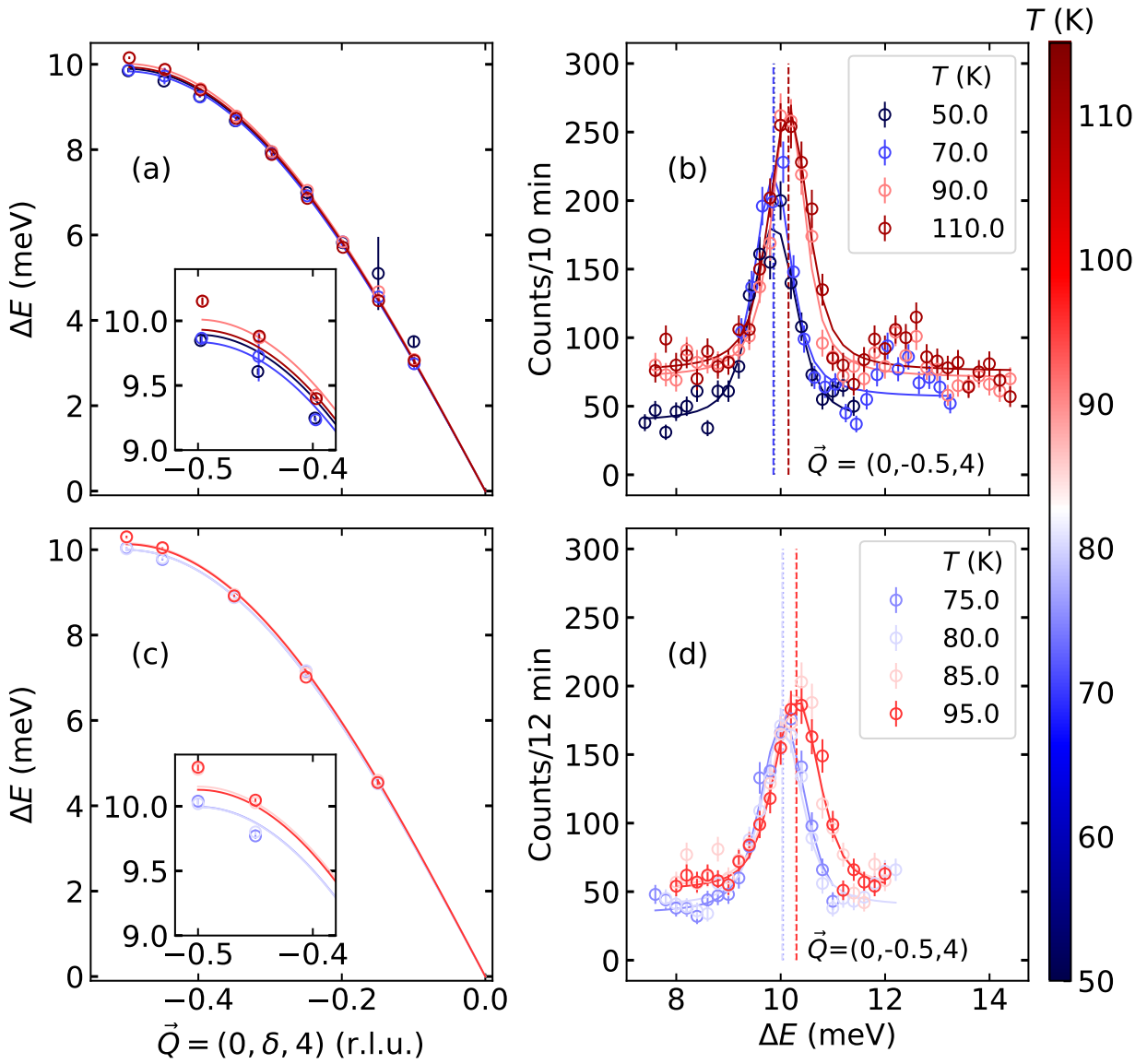


Figure 4.9: Dispersion relations of the transverse, acoustic phonon branch TA1 obtained at EIGER in 2017 (a) together with selected underlying constant- Q scans at $Q = (0, -0.5, 4)$ (b). The data from a later repetition of a similar experiment at EIGER in 2017 is shown in (c) and (d) for comparison. Solid lines of corresponding color depict fits to the data, i.e., a simple sine-dispersion law (Eq. (4.3)) for (a) and (c) and Gaussian models, Eq. (4.2), for (b) and (d).

- Upon increasing the temperature above 82.5 K, the energy of TA1 decreases linearly with a suggestion of a slight drop at the first ordering temperature $T_{\text{OO}1}$, Fig. 4.10 (a) and (b).
- The optical phonon TO1, observed at $\vec{Q} = (0, -0.5, 4)$ around $\Delta E = 12.5$ meV, is less

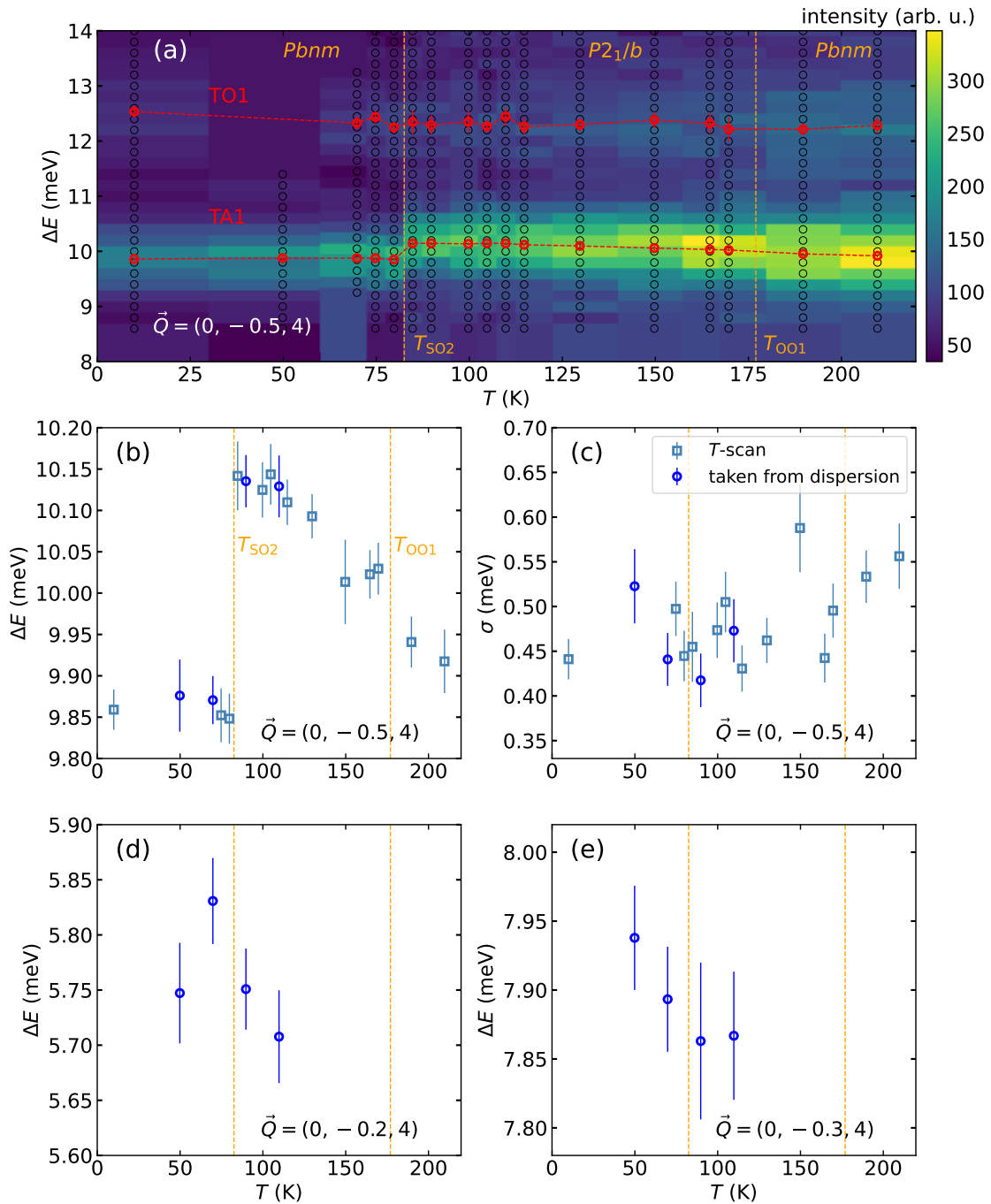


Figure 4.10: Temperature dependence of phonon energy and linewidths obtained at different Q -points for the TA1 mode of LuVO₃ as obtained around $\vec{Q} = (0, -0.5, 4)$ r.l.u. The color plot in panel (a) depicts the obtained neutron intensity per 10 min normalized to a common monitor as a function of both the applied temperature and the energy transfer at the sample. Additionally, energy transfers of the modeled acoustic and the optical phonon branches are indicated by broken red lines (error bars correspond to the uncertainties of the fits). Panel (b) provides a more detailed illustration of the temperature dependence of the energy transfer of TA1, revealing a significant change in ΔE at $T_{SO2} = 82.5$ K. However, as depicted in (c), no significant change of the width, σ , of the Gaussian fits was observed. Panels (d) and (e) show no significant temperature-dependent change of the phonon energy distant from the zone center. All error bars represent the uncertainty of ΔE obtained from the performed Gaussian fits to the data.

intense and does not exhibit a significant change in energy at T_{SO_2} or T_{OO_1} , Fig. 4.10 (a).

- Within the measured data, no significant change in linewidth is observed at T_{SO_2} , Fig. 4.10 (c).
- The phonon softening cannot be resolved distant to the zone boundary at either $\vec{Q} = (0, -0.2, 4)$ or $\vec{Q} = (0, -0.3, 4)$ possibly due to the instrument resolution, Fig. 4.10 (d), (e) and Fig. 4.11.

As a main result, the observed transversal acoustic phonon TA1 exhibits a significant softening in energy when cooled below T_{SO_2} , concomitant with a structural phase transition from $P2_1/b$ to $Pbnm$ together with the change of G-type (C-type) OO (SO) to C-type (G-type) OO (SO). Additional investigations of phonons along the longitudinal [001] and [011] high-

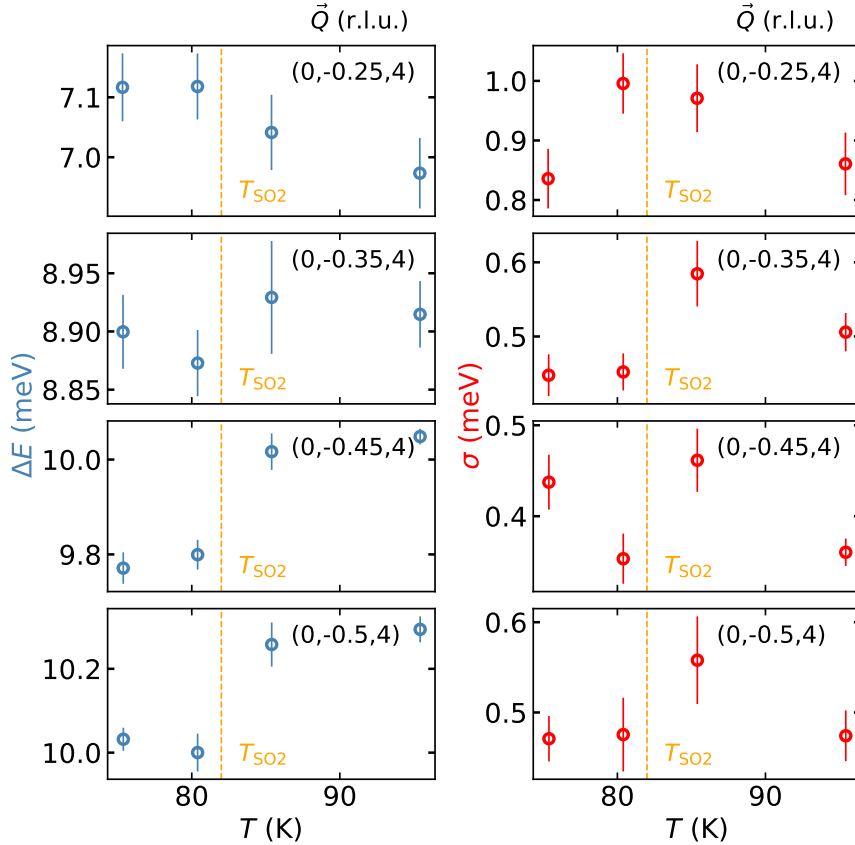


Figure 4.11: LuVO_3 TA1 phonon energies and widths of the Gaussian fits for several temperatures and Q positions.

symmetry directions did not yield any anomalies. Fig. 4.12 and Fig. 4.13 present data and fits of the phonon dispersions obtained along the [011] and the longitudinal [001]-direction, respectively. These directions extend to the T, and the Z-point highlighted in Fig. 4.7. Sinusoidal fits generally agree with the data but seem to be of decreased quality compared

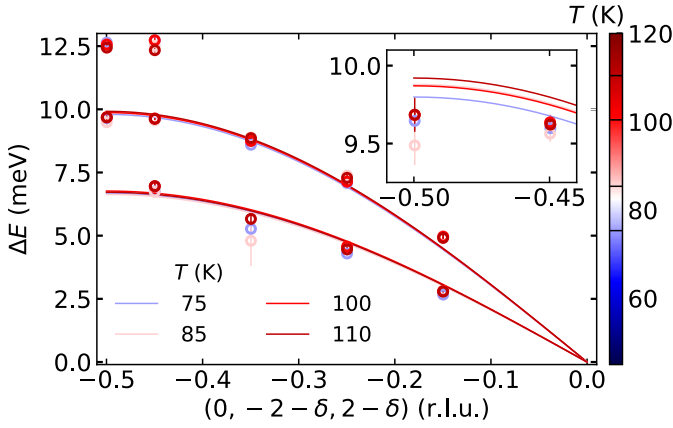


Figure 4.12: Phonon dispersions in the $[011]$ -direction around $\vec{Q} = (0, -2, 2)$ measured at EIGER. Three phonon branches can be identified: At the highest energies, remnants of a longitudinal optical phonon branch are observed close to the zone boundary at $\Delta E = 12.5$ meV. At medium energy, $\Delta E = 10$ meV, a longitudinal acoustic phonon is observed. At the lowest energies, we suspect a transversal acoustic phonon. No unusual softening in energy is observed at $T_{\text{SO}_2} = 82.5$ K in any of the branches. The dispersions were investigated for $T \in \{75 \text{ K}, 85 \text{ K}, 100 \text{ K}, 110 \text{ K}\}$ as indicated by black lines on the colorbar.

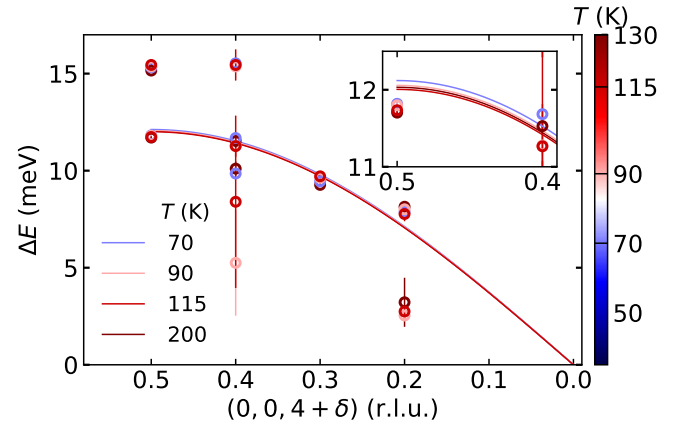


Figure 4.13: Phonon dispersions in longitudinal $[001]$ -direction around the $(0, 0, 4)$ Bragg-reflection were obtained at PUMA. The highest-energy feature is a longitudinal optical phonon observed only at the zone boundary $\Delta E \geq 15$ meV. At $\Delta E = 12.5$ meV, and $\vec{Q} = (0, 4.5, 0)$ the longitudinal acoustic mode is observed. No unusual softening is observed upon cooling below $T_{\text{SO}_2} = 82.5$ K. The dispersions were investigated for $T \in \{70 \text{ K}, 90 \text{ K}, 115 \text{ K}, 200 \text{ K}\}$ as indicated by black lines on the colorbar.

to the fits to TA1, compare Fig. 4.9. Nevertheless, the fit parameters should still reflect a significant change in the energy of the phonon branch. In summary, none of the other modes observed show any significant softening during the structural phase transition as observed for the TA1 phonon branch around $\vec{Q} = (0, -0.5, 4)$ r.l.u. The data only expresses a small and regular softening of the phonon modes with increasing temperature, attributed to the crystal lattice's thermal expansion [35].

4.5 Discussion

During the investigation of phonon dispersions along several high-symmetry directions in LuVO_3 using inelastic neutron scattering in a TAS-geometry, we have demonstrated an anomalous change in the phonon energy of the transversal acoustic TA1 branch concomitant with the structural, orbital and magnetic phase transition at $T_{\text{SO}_2} = 82.5$ K. The softening is most pronounced close to the zone boundary at $\vec{Q} = (0, -0.5, 4)$ r.l.u. This softening occurred reproducibly irrespective of the instrument (EIGER, PSI or PUMA, FRM II) and expresses no hysteresis irrespective of heating or cooling the crystal through the transition.

There exists a large body of literature on various phonon anomalies in perovskites and similar compounds, ranging from soft optical modes in PbTiO_3 investigated with TAS by Shirane et al. [111] to more recent investigations of spin-phonon coupling in transition-

metal perovskites investigated by DFT+ U computer simulations [112]. However, the lattice dynamics of REV have been less thoroughly investigated, with their magnetic properties being at the focus of scientific interest instead [2, 92, 101]. We believe the present case can be explained in simple terms with the Jahn-Teller-induced structural phase transition occurring together with the softening. Some alternative theories will also briefly be mentioned.

Our discussion will closely follow the extensive work of Carpenter et al., which discusses the topic of “*elastic anomalies in minerals due to structural phase transitions*” in [6]. Additional insights are taken from [113].

4.5.1 Lattice Dynamics and Elastic Constants

To compare the obtained phonon dispersions to changes in elastic modulus, the calculation of which will be discussed in section 4.5.3, we briefly discuss the influence of changing elastic constants on the lattice dynamics of the system. To keep the introduction short, we discuss only the case of waves in a continuous medium⁽⁸⁾, which yields a linear dispersion between energy and momentum, with a short finishing remark concerning the present case, in which the wavelength is comparable to the lattice parameters of the periodic crystal.

The general equation of motion for elastic waves in a continuous medium is given by:

$$\rho \frac{\partial^2 u_i(x_j)}{\partial t^2} = \sum_j \frac{\sigma_{ij}(x_j)}{\partial x_j}, \quad (4.4)$$

where ρ denotes the homogeneous mass density and u_i denotes the displacement along i at distance x_j from the origin in the direction j . The components of the stress tensor σ_{ij} are visualized in Fig. 4.14. All here used indices $ijkl$ indicate one of three orthogonal directions

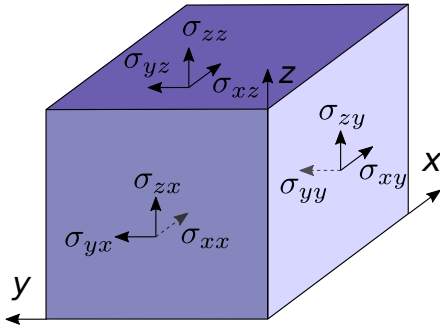


Figure 4.14: Schematics of the components of strain. The first index in σ_{ik} denotes the direction in which the force is pointing, and the second index indicates the surface normal on which the point of attack is located.

among xyz . Substituting the stress by inserting Hooke’s law and the definition of strain,

$$\begin{aligned} \sigma_{ij}(x_j) &= C_{ijkl} e_{kl}(x_j), \\ e_{kl}(x_j) &= \frac{1}{2} \left(\frac{\partial u_k(x_j)}{\partial x_l} + \frac{\partial u_l(x_j)}{\partial x_k} \right), \end{aligned} \quad (4.5)$$

into Eq. (4.4), we obtain the well-known wave equation for elastic waves in a continuous

⁽⁸⁾This approximation is valid also for phonons in a crystal, if the wavelength of the phonons is much larger than the interatomic distances, i.e., small q and ω close to the zone center.

medium,

$$\rho \frac{\partial^2 u_i(x_j)}{\partial t^2} = \sum_{jkl} C_{ijkl} \frac{\partial^2 u_l(x_j)}{\partial x_j \partial x_k} \quad (9). \quad (4.6)$$

One solution to the above wave equation is the plane wave ansatz,

$$u_i(x_j) = u_{0i} \exp[i(q_j x_j - wt)], \quad (4.7)$$

with w denoting the frequency and u_{0i} representing the amplitude of the wave in direction i . q_j denotes the component of the wavevector in the direction parallel to the direction of x_j . Plugging this expression back into Eq. (4.6), yields the dispersion relation,

$$\rho \omega^2 u_i(x_j) = \sum_{jkl} C_{ijkl} q_j q_k u_l(x_j). \quad (4.8)$$

In favor of studying this general equation, we discuss only situations where the wave travels along the high-symmetry directions investigated during the experiments. When a softening was observed in LuVO₃, a transverse wave travels along the b -direction of the LuVO₃ crystal, [010] with its polarization in c -direction, along [001]. In that case, Eq. (4.8) becomes,

$$\rho \omega^2 u_c(x_b) = C_{cbbc} q_b^2 u_c(x_b) \quad (4.9)$$

with the linear dispersion relation following immediately after canceling $u_c(x_b)$,

$$\omega = q_b \left(\frac{C_{cbbc}}{\rho} \right)^{\frac{1}{2}}. \quad (4.10)$$

We now leave the discussed case of an elastic continuum and discuss the present case, where the wavelength of the waves is on the same order of magnitude as the interatomic distances. Eq. (4.10) suggests that at the zone center, i.e., small q , we expect a linear dispersion with a slope

$$\frac{\Delta E}{q} = \hbar \left(\frac{C_{cbbc}}{\rho} \right)^{\frac{1}{2}} \quad (4.11)$$

proportional to the root of the corresponding elastic constant.

To understand the situation closer to the zone boundary, we discuss the simplest case of a one-dimensional chain with only nearest-neighbor interaction. Here, the general dispersion relation can be expressed as [35]

$$\omega^2 = \frac{4}{M} C_n \sin^2 \left(\frac{qa}{2} \right), \quad (4.12)$$

where M is the mass of an individual atom in the chain, C_n denotes the spring constant between neighboring atoms, a is the equilibrium distance between the atoms, and q denotes the wavevector. In the limit of small q , this reduces to Eq. (4.10), with ρ denoting the

⁽⁹⁾In comparison to the work of Carpenter et al. [6], the ordering of the indices k and l is inverted in favor of the more modern notation found for example in the book of S. Hunklinger [35].

line density $\rho = a^2/M^{(10)}$. Taking the root of Eq. (4.12) yields the sine-dispersion given in Eq. (4.3) with $A = 2(C_n/M)^{\frac{1}{2}}$. When extended to the three-dimensional case, see for example [35], we again obtain proportionality between the phonon energy and the root of the elastic constant corresponding to the specific branch, $\Delta E \propto \sqrt{C_{ijkl}}$. The behavior of those elastic constants in the context of various types of phase transitions is summarized in the work of Carpenter et al. [6].

4.5.2 Variations of Elastic Constants

Elastic constants are known to vary with temperature in different ways. On the one hand, anharmonic terms in the Hamiltonian of the lattice dynamics lead to an expansion of the crystal concomitant with a linear decrease in the elastic constants with increasing temperature. On the other hand, the behavior of elastic constants at phase transitions is more involved including strong variations and even discontinuities. Fig. 4.15 and Fig. 4.16 show both behaviors for Mg_2SiO_4 at high temperatures above the Debye temperature and the α - β structural transition in quartz, respectively. We believe both effects to be reflected

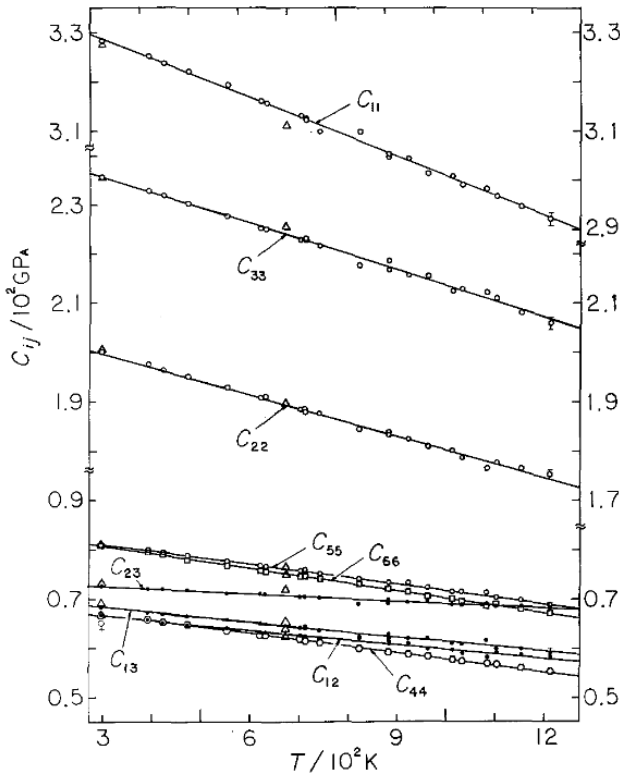


Figure 4.15: All elastic constants (Voigt notation) of Mg_2SiO_4 at $T \gg T_{\text{Debye}}$ decrease linearly with temperature. The slopes differ between the various constants. Figure taken from Suzuki et al. [114].

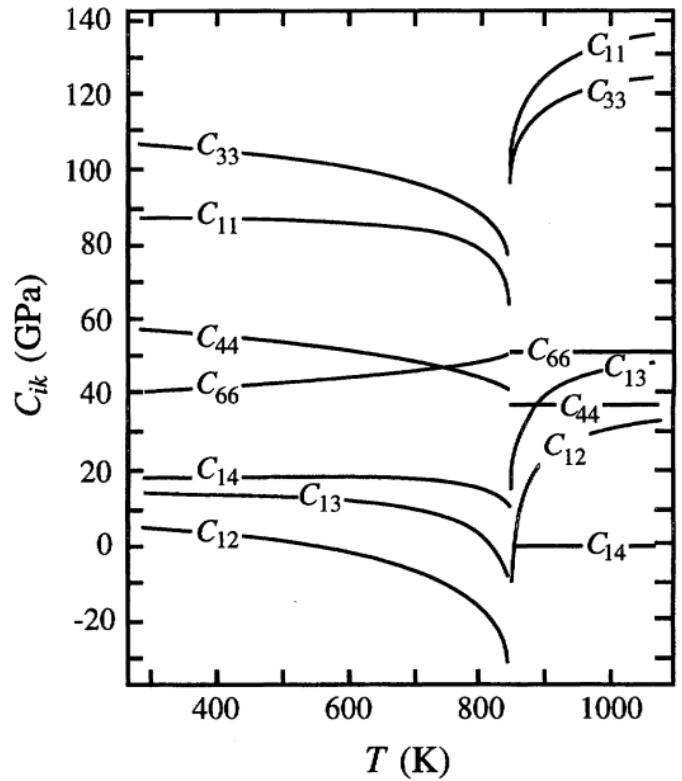


Figure 4.16: Various elastic constants in quartz around the α to β structural transition, $T_c = 846$ K, express strongly anomalous behavior. Elastic constants increase or decrease discontinuously at the phase transition. Figure taken from [6].

⁽¹⁰⁾Note that C_{ijkl} and C_n have different units.

in the phonon dispersion of TA1, where a discontinuity in the phonon energy is observed at $T_{\text{SO}_2} = 82.5 \text{ K}$ together with a linear decrease upon increasing the temperature above T_{SO_2} , compare Fig. 4.10. We will first investigate the anomaly at the phase transition before discussing the linear decrease and comparing it to the observed changes in the lattice parameters.

4.5.3 Elastic Anomalies due to Structural Phase Transitions

In the limit of small strains (no anharmonic effects), the relationship between the stress, σ , and the resulting strain, e , is given by a generalized Hooke's law,

$$\sigma_i = C_{ik}e_k, \quad (4.13)$$

where C_{ik} denotes an element of the elastic tensor in Voigt notation⁽¹¹⁾ [115, 35]. Similarly, the elastic energy stored in a crystal subjected to a small deformation is given by [116]

$$G_{\text{elastic}} = \frac{1}{2} \sum_{i,k} C_{ik}e_i e_k, \quad (4.14)$$

where the sum runs over all six components of the strain in Voigt notation, i.e., three compressive or tensile and three shear stresses. Ensuring the stability of the crystal, even for vanishing components of C_{ik} (which might occur at structural phase transitions as we will see later on), Hooke's law and consequently the elastic energy is expanded by higher order terms in e leading to

$$G_{\text{elastic}} = \frac{1}{2!} \sum_{i,k} C_{ik}e_i e_k + \frac{1}{3!} \sum_{i,k,l} C_{ikl}e_i e_k e_l + \frac{1}{4!} \sum_{i,k,l,m} C_{iklm}e_i e_k e_l e_m + \dots, \quad (4.15)$$

where the sums again run over all six entries in the strain vector in Voigt notation, and C denotes generally temperature-dependent elastic constants of up to fourth order in Voigt notation. The prefactors account for counting equivalent terms multiple times, such as $C_{ik} = C_{ki}$.

The authors highlight the similarity between Eq. (4.15) and a Landau expression of the free energy [117, 118], where the strains represent the order parameters driving the transition ⁽¹²⁾.

⁽¹¹⁾In general stresses and strains are expressed using 3×3 matrices, which are consequently connected by a rank four tensor with 81 entries. Considering symmetries in stress and strain, e.g., $\sigma_{ik} = \sigma_{ki}$ due to $\sum \vec{M} = 0$, we obtain a maximum of 6 unique entries for σ and e . Rearranging the entries yields the relationship in Voigt notation, as shown below. The change in the notation for the strains is analogous.

$$\begin{pmatrix} \sigma_1 := \sigma_{xx} & \sigma_6 := \sigma_{xy} & \sigma_5 := \sigma_{xz} \\ \sigma_6 := \sigma_{yx} & \sigma_2 := \sigma_{yy} & \sigma_4 := \sigma_{yz} \\ \sigma_5 := \sigma_{zx} & \sigma_4 := \sigma_{zy} & \sigma_3 := \sigma_{zz} \end{pmatrix} \rightarrow \begin{pmatrix} \sigma_1 \\ \sigma_2 \\ \sigma_3 \\ \sigma_4 \\ \sigma_5 \\ \sigma_6 \end{pmatrix}$$

⁽¹²⁾A single symmetry-breaking strain is sufficient but multiple strains can combine for various types of structural phase transitions [6].

Following the work of Carpenter et al. [6], we investigate the above formalism by the example of an orthorhombic-to-monoclinic phase transition, reflecting the structural phase transition occurring in LuVO_3 at T_{SO_2} . In the most simple case, where the symmetry-breaking shear strain e_4 ⁽¹³⁾ represents the order parameter, and the excess energy equals the elastic energy; we get the following Landau expansion

$$G = G_{\text{excess}} = G_{\text{elastic}} = \frac{1}{2}a(T - T_c)e_4^2 + \frac{1}{4}be_4^4. \quad (4.16)$$

Solving for a minimum in G with respect to e_4 ,

$$\frac{\partial}{\partial e_4}G = 0 = a(T - T_c)e_4 + be_4^3, \quad (4.17)$$

yields the following two expressions for e_4 ,

$$e_4^2 = \begin{cases} 0 & \text{for } T > T_c \\ \frac{a}{b}(T_c - T) & \text{for } T < T_c \end{cases}. \quad (4.18)$$

The associated elastic constant, C_{44} , is obtained by double differentiation of G with respect to e_4 ,

$$C_{44} = \left. \frac{\partial^2}{\partial e_4^2}G \right|_{e_4} = a(T - T_c) + 3e_4^2 = \begin{cases} a(T - T_c) & \text{for } T > T_c \\ -2a(T - T_c) & \text{for } T < T_c \end{cases}. \quad (4.19)$$

C_{44} is expected to soften to 0 for T approaching T_c from either side with slopes in a 1 : 2 ratio. Identifying the prefactors of Eq. (4.16) with the ones in Eq. (4.15) yields an agreement for $T > T_c$.

While this basic example of a second-order phase transition suffices in demonstrating the anomalous change of the elastic constants close to phase transitions, the observed behavior of C_{44} does not agree with the discontinuity in the phonon energy observed for TA1⁽¹⁴⁾. Therefore, an investigation more tailored to the present problem is needed.

As discussed, in the case of LuVO_3 , the strains are closely intertwined with the electronic structure by nature of the collective Jahn-Teller effect, indicating that a purely elastic model does not suffice to accurately describe this phase transition. We now consider the case in which the phase transition is driven by an order parameter, Q , different from the strains. Under the assumption that this order parameter couples to the symmetry-breaking strains to various extents, the excess energy is expressed as

$$G_{\text{excess}} = \frac{1}{2}a(T - T_c)Q^2 + \frac{1}{4}bQ^4 + \dots + \sum_{i,m,n} \lambda_{i,m,n} e_i^m Q^n + \frac{1}{2} \sum_{i,k} C_{ik}^0 e_i e_k, \quad (4.20)$$

where the coupling is described by the terms $\lambda e^m Q^n$. Different coupling mechanisms correspond to different exponents m and n , typically integers among 1, 2, 3. The variety of possible

⁽¹³⁾ e_4 denotes the movement of a plane with surface normal parallel to x in the z -direction.

⁽¹⁴⁾A discontinuity in an elastic constant entails a discontinuity in the energy of the corresponding phonon branch, $\Delta E \propto \sqrt{C_{ij}}$.

couplings results in a multitude of behaviors, which the elastic constants can express during and while approaching the structural phase transitions. In general, the temperature dependence of the elastic constants can be calculated by taking the second derivatives of G_{excess} with respect to the respective strains while considering the structural changes induced by a changing Q ,

$$C_{ij} = \frac{\partial^2 G_{\text{excess}}}{\partial e_i \partial e_j}. \quad (4.21)$$

An overview of the behavior of C_{44} for various types of phase transitions from orthorhombic to monoclinic point-group symmetries is given in Fig. 4.17. (a1-3) show the resulting

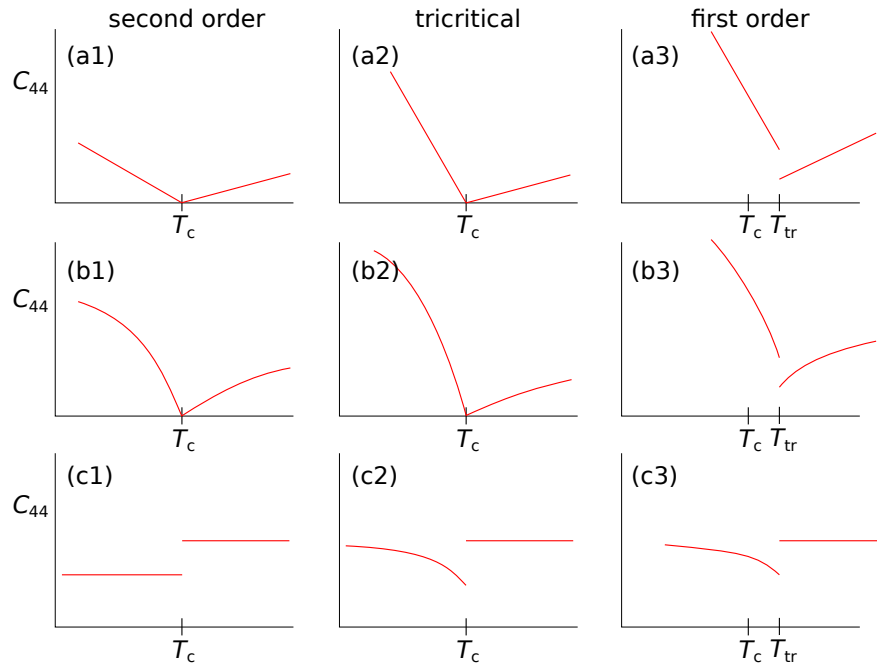


Figure 4.17: Variations of C_{44} around phase transitions of point group mmm to $2/m$ with e_4 as the symmetry-breaking strain. The three columns depict the behavior at second-order, tricritical, and first-order transitions. (a1-3) Proper ferroelastic phase transition with the symmetry-breaking e_4 being the order parameter. (b1-3) Pseudo-proper ferroelastic transition. (c1-3) Improper ferroelastic transition $Pmma$ to $P2/c$. The figure is reproduced from the work of Carpenter et al. [6].

temperature dependence of C_{44} in the above discussed case of e_4 representing the sole order parameter with no external coupling. The slopes express the determined 2 : 1 ratio. (a1) shows the behavior at a second-order phase transition for which we assume $C_{4444} > 0$. (a2) and (a3) show the variation of C_{44} at a tricritical point and a first-order transition, respectively. Analogous to the previous calculation, we assumed the strain e_4 to be the symmetry-breaking order parameter driving the transition. For the calculation of the tricritical transition, we assumed a positive sixth-order term, $C_{444444} > 0$, together with a zero fourth-order term, $C_{4444} = 0$. As a result, C_{44} softens linearly when approaching T_c . However, this time, the ratio between the slopes is 4 : 1. For the first order transition, we assumed

a negative value of $C_{4444} < 0$ and a positive $C_{444444} > 0$, which results in a discontinuity of C_{44} at a transition temperature T_{tr} slightly larger than the original T_c . However, none of the three ‘‘proper ferroelastic’’ transitions qualitatively describe the behavior expressed by the neutron scattering experiment, where we observe a discontinuous decrease of phonon energy when cooling below T_{SO_2} . In contrast, we observe a discontinuous increase during the proper ferroelastic first-order transition in (a3).

We can describe the situation in LuVO_3 more accurately by introducing a coupling term between the orbital order parameter, $Q^{(15)}$, and e_4 . (b1-3) show the behavior of C_{44} in the case of a ‘‘pseudo-proper ferroelastic transition’’ where we assume a linear coupling between the order parameter, Q , and the strain, $\lambda_4 e_4 Q$ in Eq. (4.20). As before, i) C_{44} varies smoothly to zero, and ii) the ratio of the slopes is 2 : 1 and 4 : 1 for the second-order or tricritical phase transitions, respectively. Similar to the behavior observed for the first-order proper ferroelastic transition, the discontinuity in C_{44} at the first-order pseudo-proper ferroelastic transition does not agree with the observed phonon dispersion.

We now assume a quadratic coupling term between the order parameter and the symmetry-breaking strain, $\lambda_4 e_4 Q^2$. Fig. 4.17 (c1-3) visualizes the behavior of C_{44} around the resulting ‘‘improper ferroelastic’’ transition. The calculation starts with the excess energy and its minimization with respect to Q ,

$$\begin{aligned} G_{\text{excess}} &= \frac{1}{2}a(T - T_c)Q^2 + \frac{1}{4}bQ^4 + \lambda_4 e_4 Q^2 + \frac{1}{2}C_{44}^0 e_4^2, \\ \frac{\partial G_{\text{excess}}}{\partial Q} &= a(T - T_c)Q + bQ^3 + 2\lambda_4 e_4 Q = 0, \end{aligned} \quad (4.22)$$

and yields the following solutions:

$$Q^2 = \begin{cases} 0 & \text{for } T > T_c \\ \frac{-a(T - T_c) - 2\lambda_4 e_4}{b} & \text{for } T < T_c \end{cases}. \quad (4.23)$$

Inserting the result back into G_{excess} and double differentiating with respect to e_4 results in the following expression for the elastic constant [6]

$$C_{44} = \begin{cases} C_{44}^0 & \text{for } T > T_c \\ C_{44}^0 - \frac{2\lambda_4^2}{b} & \text{for } T < T_c \end{cases}. \quad (4.24)$$

The behavior of C_{44} across this improper ferroelastic transition is sketched in Fig. 4.17 (c1). We observe a discontinuity with no softening as T_c is approached from either side.

Fig. 4.17 (c2) and (c3) demonstrate the behavior of C_{44} under the assumption of a quadratic coupling between the order parameter and the strain for a tricritical or a first-order phase transition, respectively. For the tricritical and the first order transition, one assumes $C_{4444} = 0$, $C_{444444} > 0$ and $C_{4444} < 0$, $C_{444444} > 0$, respectively.

The comparison of the discontinuity in the energy of the phonon mode and the calculated elastic constant C_{44} yields an excellent qualitative agreement suggesting an improper ferroelastic transition at T_{SO_2} . Regarding the order of the transition, the picture is less clear.

⁽¹⁵⁾See the work of Kressdorf et al. for a possible definition of an orbital order parameter [119], which can couple to the corresponding strain.

However, the determination of the order of the transition remains less conclusive. The interplay of the discussed effects, coupled with the typical temperature dependence of elastic constants, necessitates further investigation into any anomalous behavior and a thorough comparison to the above calculations.

4.5.4 Elastic Properties Distant from Phase Transitions

In addition to the behavior at the phase transition, we briefly discuss the general temperature dependence of phonon modes. Commonly, the elastic constants decrease linearly with temperature according to [114],

$$C_{ik}(T) = C_{ik}^0 - \chi E(\tau, T), \quad (4.25)$$

where C_{ik}^0 denotes the elastic constant at some normalizing temperature, and E is the thermal energy according to the Debye model (at high temperatures, the energy is proportional to the temperature T , [35]) using an empirical value for the characteristic temperature τ , which replaces the Debye temperature. $\chi := \gamma\delta_S/V_0$ denotes a constant value > 0 comprising the Grüneisen parameter, γ , and the isobaric anharmonic parameter (the Anderson-Grüneisen constant), δ_S . In general, we observe a linear dependence between C_{ik} and T , with distinct slopes for specific combinations of ik that vary depending on the material, as illustrated in Fig. 4.15.

Instead of expressing this behavior in terms of T , one can directly link the relative change in the volume of the unit cell $(V(T) - V_0)/V_0$ to the relative change in the energy of acoustic phonons $(\Delta E(T) - \Delta E_0)/\Delta E_0$. This dependence is given by [35],

$$-\frac{\Delta E(T) - \Delta E_0}{\Delta E_0} = \gamma \frac{V(T) - V_0}{V}, \quad (4.26)$$

where γ denotes the Grüneisen parameter, typically a positive value between 1 and 3 [35]. While the thermal expansion cannot account for the abrupt change in phonon energy, the change in unit cell volume at the structural phase transition can be compared to the change in phonon energy. Fig. 4.18 shows the relative change in volume of the unit cell together with the relative change in phonon energy. Distant to the phase transition at $T_{\text{SO}_2} = 82.5$ K, the relative change in energy is in perfect qualitative agreement with the relative change in the volume of the unit cell. While both are constant in T below T_{SO_2} , they increase linearly with T above T_{SO_2} . The ratio of the slopes (red and blue lines indicate linear fits to the data) yields a Grüneisen parameter of $\gamma = 9.4$, which is anomalously large. At the phase transition, however, we see opposite directions in the jumps, indicating that this simple model based on thermal expansion breaks down at T_{SO_2} .

We thereby propose that both the vanishing slope below T_{SO_2} and the decreasing slope above T_{SO_2} can be explained by a model based on the expansion of the crystal, with the only unexpected behavior occurring at the phase transition. This suggests that the corresponding elastic constant does not undergo any unexpected behavior during the approach to T_{SO_2} . A comparison of this finding to the calculated behavior of C_{44} in Fig. 4.17 (c1-3) suggests a second order improper ferroelastic phase transition at T_{SO_2} .

Notably, a relative increase in the elastic modulus leads to an elevation in the observed phonon energy at the zone boundary. However, one expects the same relative increase for all

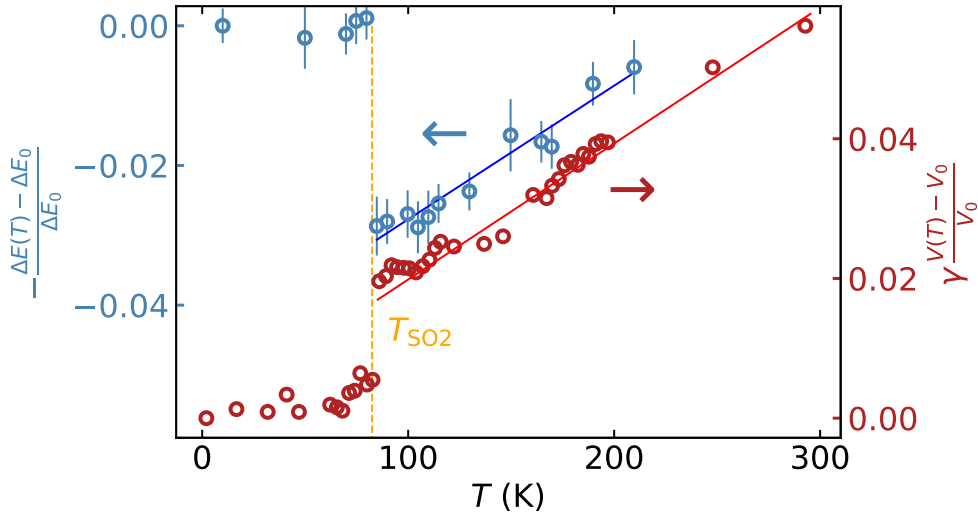


Figure 4.18: Relative change in unit cell volume, $\frac{V(T)-V_0}{V_0}$, and phonon energy $\frac{\Delta E(T)-\Delta E_0}{\Delta E_0}$ plotted against T . The volume of the unit cell is calculated from the data presented in Skoulatos et al. [2], compare Fig. 4.5. Besides the opposite direction of the discontinuity at the phase transition, the relative change in phonon energy is in excellent qualitative agreement with the relative change in the volume of the unit cell. Red and blue lines represent linear fits to the data, the comparison of which yields a Grüneisen parameter of $\gamma = 9.4$, which is anomalously large.

investigated momentum transfers (compare Eq. (4.3)). Interestingly, during the experiment, no change was observed further from the zone boundary, as seen in Fig. 4.11. This observation can be explained by considering that while the relative change in phonon energy remains constant, the absolute value of the difference decreases as one moves further from the zone boundary. Eventually, this decrease reaches a point where it becomes indiscernible due to the uncertainties inherent in the experiment.

The apparent lack of change in phonon linewidth also strengthens the theory of changing elastic modules. Typically, a coupling of the phonon to some excitation would also change its lifetime and, therefore, the linewidth observed in the neutron experiment [120]. However, the limited resolution of the TAS experiments might have limited the investigation of any change in linewidths here.

No unusual softening was observed during the investigation of phonon dispersions along other high-symmetry directions, which agrees with the monoclinic to orthorhombic phase transition. When cooling below T_{SO_2} , a structural phase transition occurs concomitant with a change from G-type OO to C-type OO . This impacts only the stacking of orbitals along c from alternating between zx and yz to keeping one orientation but does not affect the stacking along other directions, compare Fig. 4.4. From the calculation, one consequently expects only a single elastic constant to express a discontinuity at T_{SO_2} , which agrees with the obtained phonon dispersions.

4.6 Conclusion and Outlook

In this study, we investigated a softening of the transversal acoustic TA1 phonon branch, concomitant with the structural phase transition occurring at $T_{\text{SO}_2} = 82.5$ K. At the zone boundary, $\vec{Q} = (0, 0.5, 4)$ r.l.u., the phonon energy undergoes a minor relative energy change of 3%, which corresponds to an absolute value of 0.3 meV. This small but significant softening was repeatedly observed at several instruments across multiple beamtimes. It is much less pronounced near the Γ -point, potentially due to instrumental resolution limitations. Assuming a basic sinusoidal relationship between the energy and the momentum described in Eq. (4.3), we note that the relative softening of the phonon mode should remain constant, indicating that the absolute change in phonon energy is reduced closer to the Γ -point. Consequently, the softening cannot be resolved distant to the zone boundary where it is most pronounced. Alternatively, this behavior might be explained by a "zone boundary soft acoustic mode" as described in the textbook of Dove [121]. No significant change in the phonon linewidth was discernible within the resolution of our triple-axis neutron measurements.

The observed softening of TA1 was discussed within the framework of elastic anomalies due to structural phase transitions, suggesting an improper ferroelastic transition. Notably, no softening could be observed in any other direction in reciprocal space, which is attributed to the special symmetry of the coupling strain.

Moving forward, we intend to perform supersonic measurements to gain immediate knowledge about the elastic constants while acknowledging the limitations of those in direct comparison with neutron data due to the vastly different frequencies observed. Furthermore, the phase transition's order could be elucidated using high-precision heat capacity measurements. To examine the softening phenomenon near the zone center, where the absolute difference in energies is smaller, we propose utilizing neutron resonant spin-echo methods, employing their superior energy resolution. This approach might also provide additional insights into the behavior of the phonon linewidth around the phase transition [50].

Expanding on the current investigation, we propose subjecting the crystal to external uniaxial stress using a bellow-driven pressure in-situ cell [122, 123], which could offer valuable insights into the response of the phonon dispersion to stress applied along various directions. Additionally, subjecting the crystal to hydrostatic pressure and monitoring the response of both the phonon dispersion and lattice constants promises information about the elastic response of the system.

Finally, we propose simulation-assisted theoretical investigations, considering various couplings between the TA1 phonon mode and other excitations, focusing on understanding the connection between the anomalous lattice dynamics and the alterations in the symmetry of the OO.

5. Theory of Nested Mirror Optics

In the upcoming three chapters, we comprehensively explore parabolic and elliptic nested mirror optics (NMOs), the central theme of this thesis. The three chapters cover the theory, the performance investigation, and the applications of NMOs in neutron scattering.

This first chapter is structured as follows: We briefly introduce neutron guides, discussing their various geometries and their advantages and drawbacks. Subsequently, we explore elliptic and parabolic NMOs, detailing how they overcome the limitations associated with conventional neutron guides. Finally, we present the analytic framework associated with the neutron beam transport through a NMO and the Monte Carlo simulations utilized to evaluate their performance.

5.1 The History of Neutron Guides

As demonstrated during the investigation of the lattice dynamics in LuVO_3 in chapter 4, neutrons are a remarkably versatile tool in condensed matter physics, offering unique insights that complement those obtained with charged probes.

However, the finite lifetime of free neutrons, after which they undergo beta-decay, $\tau = 878.4(5)\text{s}$ [24], presents a challenge in experimental contexts. To address the limited lifetime, we require sources capable of generating neutrons in proximity to any experimental setups. Here, we will provide a concise overview of various neutron-generating sources and the subsequent transport of these neutrons to the instruments with neutron guides.

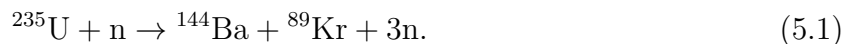
Neutron Sources

Modern methods of neutron generation rely on the extraction of neutrons from heavy nuclei. This process relies on the interplay between the range-limited strong nuclear force and the much weaker electromagnetic force, which dictates the optimum ratio of neutrons to protons, N/Z_{opt} . By optimizing the binding energy of a nucleus according to the Bethe-Weizsäcker mass formula [124, 125], we obtain the ideal ratio of neutrons to protons for a given number of nucleons,

$$N/Z_{\text{opt}} \approx 1 + \frac{a_c}{2a_A} A^{2/3}.$$

Here, A denotes the mass number of the nucleus, while a_c and a_A represent empirically determined, positive constants that account for the Coulomb term and the Pauli exclusion term of the mass formula, respectively. Notably, N/Z_{opt} increases with the mass number A , indicating that the fragmentation of a heavy nucleon into smaller fragments is typically accompanied by the release of excess neutrons [126].

Each fission event of ${}^{235}_{92}\text{U}$, a common fuel source for power plants and research reactors, releases an average of 160 MeV of kinetic energy, and is accompanied by the release of an average of 2.43 neutrons [126]. The exact number depends on the specific fission process, such as



The highly excited fission fragments evaporate the excess neutrons with an average kinetic energy of about 2 MeV.

For a typical reactor design, an average of 0.5 neutrons are absorbed in the control rods, and parasitic neutron captures, e.g., in cooling water or by ^{238}U and one neutron is required to initiate one subsequent fission event. The surplus neutron can be transported from the reactor core to be utilized in an experiment [126].

In contrast to fission events, the generation of free neutrons in *spallation* sources relies on the bombardment of dense elements with large mass numbers, e.g., uranium, tungsten, tantalum, mercury, or lead, using high-energy charged particles, typically protons of $E_{\text{kin}} \approx 1$ GeV [127, 128, 129]. The term *spallation* encompasses several nuclear evaporation processes theoretically described by Victor Weisskopf in 1937 [130]. During spallation, high-energy particles collide with heavy nuclei, leaving the latter highly excited. These excited nuclei subsequently emit additional particles with sufficient energy to excite different nuclei in a cascading reaction. Neutrons are evaporated from these excited nuclei where energetically allowed, skewing the ratio of neutrons and protons, ultimately resulting in β^+ -decays and the emission of additional γ -radiation. On average, a single 1 GeV-proton causes the evaporation of 10 neutrons with kinetic energies of 2 MeV. Roughly 40% of the incoming proton's energy is deposited in the nuclei available for neutron evaporation, with the remainder being cooled from the target. The available cooling power ultimately limits the achievable flux [131]. Ongoing research aims to bypass the limitations of fission and spallation sources by minimizing the excess energy, which is not available for neutron evaporation.

Fundamentally differing in their principles of neutron generation, these sources are based on i) the electron bremsstrahlung to evaporate neutrons from the nuclei [132], ii) laser-driven fusion of deuterium and tritium, which results in the emission of one neutron [133], iii) high energy laser pulses to release proton pulses from aluminum foils, which are then transformed to neutron pulses at a heavy target [134, 135], or iv) halo nuclei, which are isomers excited by the inverse Compton effect resulting in the binding energy of the outermost neutron approaching zero. This neutron can then be released by a low-energy photon beam, producing a neutron beam with similar energy and polarization qualities [136, 137]. While these source designs offer the potential for significant gains in either peak neutron flux or beam quality, they currently face technological challenges that must be overcome before they can be considered viable alternatives to conventional neutron sources.

Fig. 5.1 summarizes the development of neutron sources differentiating by the principle of neutron generation and the achieved peak neutron flux. Neutron science was initiated with continuous cyclotron-based spallation sources; the subsequent generation of neutron sources was based on the fission of ^{235}U , with the flux quickly approaching the limit determined by the achievable cooling power. At the time of writing, the highest continuous flux amounting to $1.5 \times 10^{15} \text{ cm}^{-2}\text{s}^{-1}$ is available at the [Institut Laue-Langevin \(ILL\)](#) in Grenoble, France, which was commissioned in the 1970s and today operates at a thermal power of 58.3 MW. Operating in pulsed mode, contemporary particle-driven spallation sources, e.g., SNS, ISIS, MLF at J-PARC, and the upcoming ESS, achieve significantly higher peak neutron flux with comparable time-averaged flux.

Except for specific applications, such as high energy neutron radiography [139] or palliative cancer treatments [140, 141], the desired neutron energies are typically much smaller than that of fission or spallation neutrons. Additionally, the probability for neutron capture in ^{235}U drops with increasing neutron energy [142]. This indicates that reducing the initial

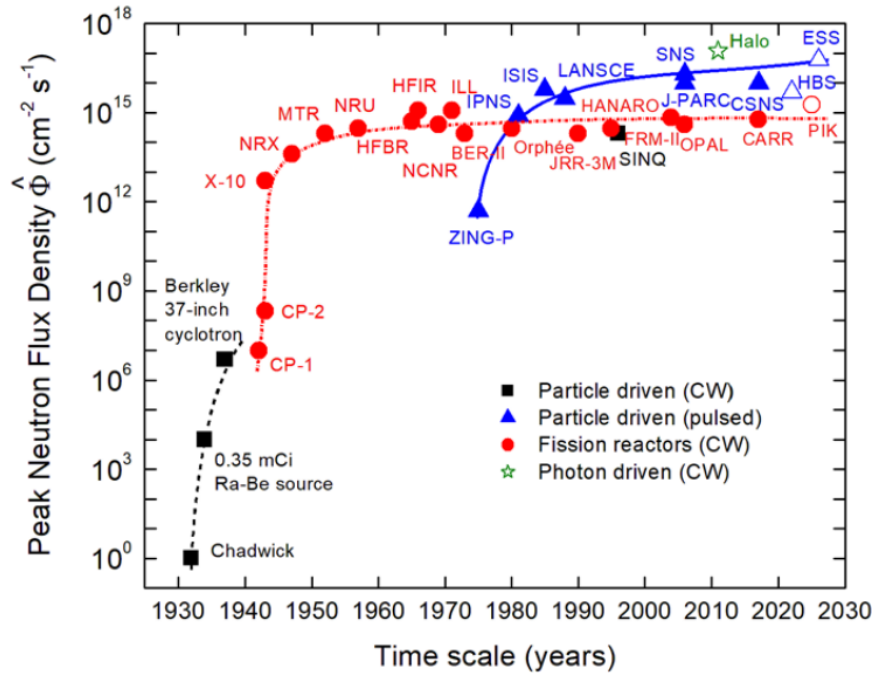


Figure 5.1: Development of peak neutron flux of neutron sources operating in pulsed and continuous (CW) modes. The figure is reproduced from the book of Bolton et al. [138].

neutron energy is favorable for maintaining the criticality in fission-based reactors. During this *moderation* process, the excess energy of the neutrons is released into the moderating medium, e.g., water, heavy water, or graphite, by elastic collisions until a thermal equilibrium is reached or the neutron leaves the moderating material [143]. The kinetic energies of thermalized neutrons follow a Maxwell-Boltzmann distribution governed by the temperature of the moderator. Besides moderation to ambient temperatures, hot or cold sources can provide neutrons of higher or lower energies, respectively [144, 145]. Compare table 2.1 for an overview of the properties of such generated neutrons.

Neutrons are typically extracted from the moderator via beam tubes, which are evacuated aluminum tubes inserted into holes in the shielding material surrounding the core. They are strategically directed at the point of highest neutron flux in the moderator [146]. As the neutrons undergo random motion through the moderating material, the total available flux is distributed evenly over a solid angle of 4π . In the limit of large distances to the source, this uniform distribution in solid angles decreases the available flux with the squared distance to the source. Due to the small solid angle under which samples are seen by the source, there is a significant reduction of neutron flux compared to the flux within the moderator.

Neutron guides can mitigate this reduction in flux. They are designed to efficiently transport neutrons over considerable distances without suffering significant losses in flux, thereby drastically increasing the flux, brightness, and brilliance at the instrument's position.

Neutron Guides

When taking a guided tour at the FRM II, one might encounter an anecdote of uncertain accuracy about the supposed origins of neutron guides. It recalls a time when radiation safety was handled less stringently, and scientists, eager to save time, would take shortcuts through experimental areas, even crossing the paths of neutron beams. While time-efficient, this practice also disturbed the experiments of others, leading to some researchers enclosing their neutron beams within evacuated metal tubing to prevent such interruptions.

Interestingly, besides preventing any disturbances to the neutron beams, it was soon discovered that installing the evacuated metal tubes increased the neutron flux at the sample position, surpassing what was expected from the evacuation alone. This discovery is said to have heralded what we now recognize as neutron guides.

While a fortunate alignment of circumstances has played a role in many scientific breakthroughs, or as Louis Pasteur aptly put it, “*chance only favors the mind which is prepared*”, the success story of the neutron guide likely began in 1945 with the discovery of Fermi and Zinn that neutrons exhibit total reflection when striking metallic surfaces at very shallow angles [147].

It was Maier-Leibnitz and Springer who proposed the use of metal-coated neutron tubes with a rectangular cross-section [7] to address the decrease of neutron flux with the square of the distance from the source. This innovation marked a fundamental shift in the design of beamlines and instruments. Previously, instruments were placed as close to the reactor core as shielding allowed, resulting in significant measurement background and crowded experimental halls. The introduction of neutron guides revolutionized this by enabling the efficient transport of long-wavelength neutrons, which allowed for increased distances between the point of neutron generation and the instrument. This entailed significantly improving the achievable signal-to-background ratio and a more efficient use of the available neutrons, as more than one instrument can be positioned along the guide.

Understanding the characteristics of neutron total reflection at metallic surfaces is crucial for designing neutron optical devices for i) extracting neutrons from sources, ii) efficiently transporting neutrons from sources to experiments, and iii) tailoring the extent and divergence of neutron beams towards specific experiments. We here provide a concise overview of the behavior of neutrons at plane interfaces between two materials with different neutron optical properties.

Total Reflection and Refraction of Neutrons

The total reflection of neutrons at the interface between air and a metallic surface was experimentally observed in 1944 by Fermi and Zinn [147] and thoroughly discussed in a quantum mechanical picture by Goldberger in 1947 [148]. This behavior can also be understood by considering a change in the indices of refraction, $n_1 \rightarrow n_2$, analogous to the concept used to describe the interaction between optical light and matter. Similarly, the kinematics of neutron reflection and refraction are captured by Snell’s law,

$$n_1 \sin \theta_1 = n_2 \sin \theta_2. \quad (5.2)$$

Here, $\theta_{1,2}$ denote the angle between the surface normal, \vec{n} , and the momentum of the incident and the refracted neutrons, as illustrated in Fig. 5.2. The indices of refraction, n_1 , n_2 , encapsulate the interaction between neutrons and the matter surrounding them. This interaction

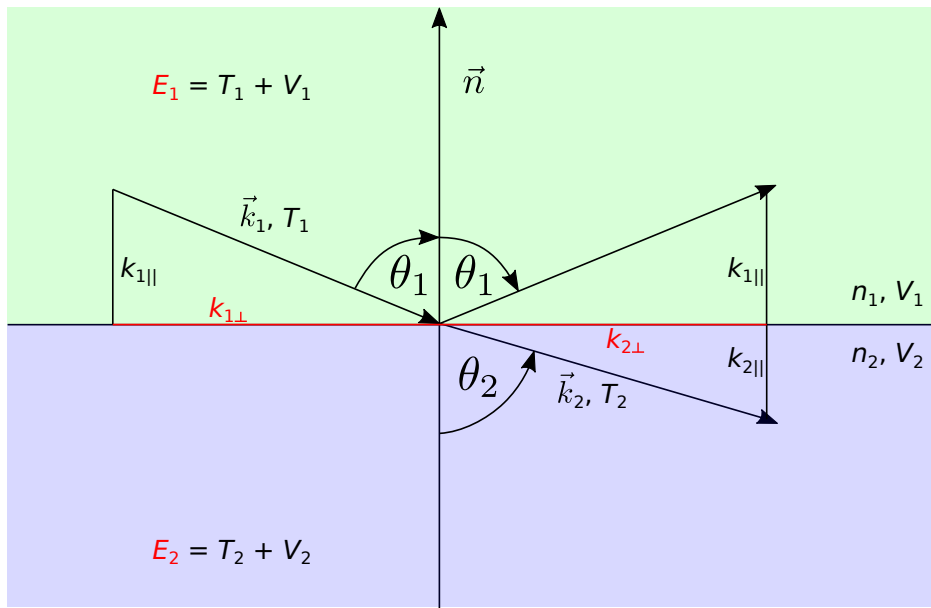


Figure 5.2: Behavior of a neutron at material interfaces with different neutron potentials V_i . The total energy of the neutron, comprising kinetic and potential energy, $E = T + V$, as well as the component of momentum perpendicular to the surface normal, k_{\perp} , are preserved at the interface. Both constants are highlighted in red.

depends on the number density of the nuclei, ρ_n , and their bound coherent scattering length, b_{coh} . Using the Fermi pseudopotential to approximate the interaction potential mediated by the strong nuclear force [33], the squared refractive index of a material comprising different nuclei, j , can be calculated as [149]

$$n^2 = 1 - \frac{\lambda^2 \sum_j b_{\text{coh},j} \rho_{n,j}}{\pi}. \quad (5.3)$$

Here, λ denotes the wavelength of the neutron. A detailed derivation of this result is provided in the appendix B.

The qualitative behavior of neutrons at the interface depends on the relationship between the two indices of refraction. For $n_2 > n_1$ or $n_2 < n_1$, neutrons are refracted towards or away from the surface normal, respectively. In the latter case, if a neutron approaches the interface at a sufficiently large angle relative to \vec{n} , such that the refracted neutron would move parallel to the surface, the neutron is instead totally reflected, maintaining its angle relative to the surface normal. The corresponding angle between the momentum of the incident neutron and the surface is defined as the critical angle of that interface, θ_c ⁽¹⁾. For a neutron at the interface between vacuum, $b_{\text{coh},j} = 0$, $n_1 = 1$ and a medium with a refractive index n_2 , the critical angle, denoted as θ_c , can be calculated as $\theta_c = \frac{\pi}{2} - \arcsin(n_2)$. When n_2 is approximately equal to 1, which is typically the case for neutrons, this expression can

⁽¹⁾It should be emphasized that the angle θ_c denotes the angle between the surface and the trajectory of the incoming neutron, in contrast to θ_1 denoting the angle to the surface normal.

be approximated by

$$\theta_c \approx \lambda \sqrt{\frac{\rho_n b_{\text{coh}}}{\pi}}. \quad (5.4)$$

The linear relationship between the critical angle and the wavelength of the incident neutron suggests that cold and thermal neutrons can be transported more efficiently than unmoderated or hot neutrons. This enables separating neutrons useful for the experiment from high energy neutrons, which primarily contribute to the background noise [7].

In addition to the wavelength dependence, θ_c also increases with the number density, ρ_n , and the bound coherent scattering length, b_{coh} . This indicates that densely packed, strongly scattering nuclei have a greater influence on the trajectory of a neutron. Fig. 5.3 illustrates the values of b_{coh} for various naturally occurring isotopic compositions with respect to their atomic number. Except for Dysprosium, which has an exceptionally large neutron absorption

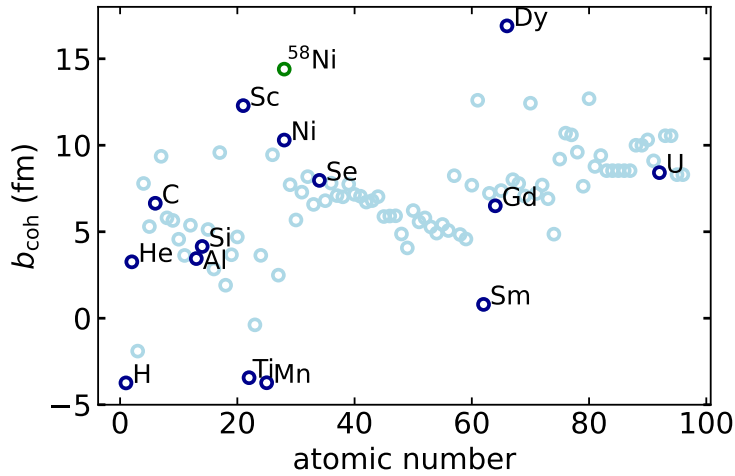


Figure 5.3: Overview of the bound coherent scattering lengths of various elements plotted against their atomic number. Unless specified otherwise, the values correspond to naturally occurring isotopic compositions. Elements with comparatively large/small scattering lengths or relevance in neutron scattering are highlighted and denoted. The large value of $b_{\text{coh}} = 14.4$ fm makes ^{58}Ni a prime candidate for the coating of neutron guides. The data illustrated here is taken from the work of Dawidowski et al. [34].

cross-section limiting its use as a neutron reflector, ^{58}Ni offers one of the highest critical angles $\theta_{c, ^{58}\text{Ni}} = \lambda \cdot 0.119^\circ/\text{\AA}$. The naturally occurring isotopic composition of Ni also provides a reasonable critical angle, $\theta_{c, \text{Ni}} = \lambda \cdot 0.099^\circ/\text{\AA} = \lambda \cdot \kappa$, coupled with manageable absorption. Its metallic properties allow the creation of coatings with very low roughness, making the natural isotopic composition of Ni the baseline for critical angles in neutron reflection. The development of supermirror coatings marked a breakthrough in neutron optics, for the first time enabling the reflection of an extensive range of neutron wavelengths at larger momentum transfers than previously achievable with simple metallic coatings.

Reflection of Neutrons at Supermirror Coatings

During a neutron scattering study of nerve fibers in 1970 [150], Kirschner and Caspar noted that repeating two alternating layers with positive and negative neutron potential could produce neutron monochromators with surprisingly high reflectivity. This discovery laid the foundation for what we now know as *supermirror coatings*. In essence, their fabrication and working principle can be traced back to the simple recipe discovered back then: Layered structures (*synthetic crystals*) consist of alternating materials with significantly different neutron potential. These structures can serve multiple purposes, including i) the reflection of hot neutrons under large angles, ii) the polarization of a neutron beam, and iii) providing a monochromatic neutron beam. Their working principle is based on Bragg's law,

$$2d \sin \theta = n\lambda, \quad (5.5)$$

where d , θ , and λ denote the distance between two layers of the same material, i.e., the lattice spacing of the synthetic crystal, the angle between the incident neutrons and the surface of the crystal, and the wavelength of the neutron, respectively.

By slowly varying the lattice spacing of successive layers within the supermirror, neutrons can be reflected for a wide range of wavelengths and incident angles, each combination satisfying the Bragg condition for a specific value of d . This idea predates the experiments mentioned above and is likely to be first published by Turchin in 1966, who introduced them as "*stratified systems*" [151]. Due to the predominance of natural nickel during the early days of neutron guides, the critical angle of supermirrors is still expressed as a multiple, m , of the critical angle of Ni, $\theta_{c, m} = m\theta_{\text{Ni}}$. Starting with the first experimental realizations of supermirrors [8, 152], the quality of produced supermirrors quickly improved. Using a recipe for determining optimum layer thicknesses [153], the guide system at SINQ (Switzerland) was fully equipped with $m = 2$ supermirrors [154, 155]. Since then, the achievable m -value has continuously increased up to $m = 8$ in recent years [154].

However, the quality of a supermirror coating is not only characterized by the critical angle but also by the reflectivity at that angle, the *edge reflectivity* R_e . Under the assumption of ideal layers, with optimum thickness, perfectly sharp interfaces with zero roughness, no diffusing atoms, and no absorption in the coatings, the reflectivity should equal $R = 1$ for all angles up to $\theta_{c, m}$. However, these effects are impossible to eliminate in real systems, which entails a decrease in reflectivity for increasing momentum transfer. Computation has shown that the absorption alone limits the achievable critical angle to approximately $m = 10$ [154].

Fig. 5.4 shows data from a measured reflectivity curve for an $m = 4$ supermirror and theoretical approximations for supermirrors with $m = 2, 4, 6$. All reflectivities are plotted against the neutron momentum transfer parallel to the surface normal normalized by the critical momentum transfer of Ni, $2k_{\parallel}/k_{c, \text{Ni}}$, where $k_{c, \text{Ni}} = 0.0217 \text{ \AA}^{-1}$. Furthermore, the critical trajectories (reflection under the critical angle) of neutrons with $\lambda = 4 \text{ \AA}$ are illustrated atop the figure, making tangible the complications associated with creating optical devices for such limited angles of reflection. The reflectivity curves consist of three distinct parts. Firstly, a thin Ni-layer atop the mirror reflects all neutrons with $k_{\parallel} \leq k_{c, \text{Ni}}$ with near perfect efficiency, i.e., $R_0 \simeq 99\%$. When exceeding $k_{c, \text{Ni}}$, neutrons penetrate deeper into the supermirror coating until they arrive at a layer spacing d satisfying the Bragg equation, where they will be reflected with high probability. As d typically decreases with the distance

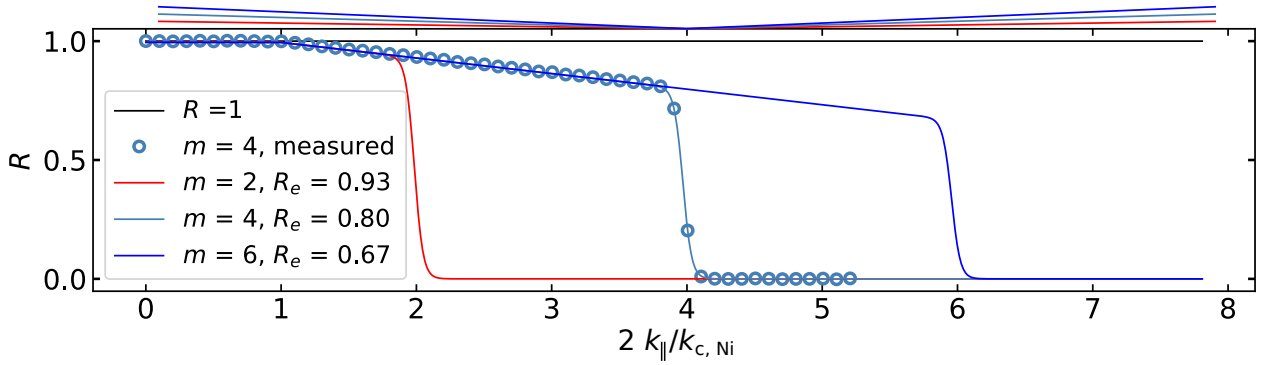


Figure 5.4: Calculated and measured supermirror reflectivities for various m -values as a function of the neutron momentum transfer parallel to the normal vector, $2k_{\parallel}$, normalized by the critical momentum transfer of Ni, $k_{c, \text{Ni}} = 0.0217 \text{ \AA}^{-1}$. Above the main panel, lines with colors corresponding to the m -values of the main figure illustrate the critical trajectories for $\lambda = 4 \text{ \AA}$ neutrons.

from the surface, neutrons with higher k_{\parallel} penetrate deeper into the coating before being reflected, with the associated absorption decreasing the observed reflectivity. Lastly, the reflectivity quickly drops to zero when the critical angle is exceeded. For a more detailed discussion of supermirrors, the theory governing their reflectivity, and their fabrication, the reader is referred to the literature [156, 157, 158].

Building upon this discussion of neutron reflection at flat surfaces, we will now focus on the intricacies of fabricating neutron guides from reflective surfaces, designed to operate at small angles of incidence.

5.2 Long Guides with Rectangular Cross Section

5.2.1 Straight guides

In their seminal paper from 1963 titled “*The use of neutron optical devices on beam-hole experiments*”, Springer and Maier-Leibnitz propose several applications for the recently discovered neutron guides, which include i) separating high-energy neutron and gamma background by capitalizing on the wavelength-dependent critical angle of reflection (compare section 5.1), ii) the separation of cold from thermal beams through the same principle, and iii) significantly enhancing the neutron intensity at the sample beyond the geometrical constraints imposed by the source-to-sample distance [7].

During that era, neutron guides were typically fabricated with rectangular cross-sections made of glass, subsequently coated with naturally occurring nickel. Nevertheless, the authors envisioned advanced geometries that would be realized decades later. One such concept involved the combination of two elliptic guides for phase space preserving neutron transport from one focal point to another, now known today as a Selene-type optic [159, 160].

For the extraction of neutrons from the moderator at a reactor or spallation source, the entrance of the guide is preferably aligned with the region of maximum neutron flux while avoiding a direct line of sight onto the reactor core to minimize background contamination. Along the trajectory of a neutron, the cross-section of the guide remains constant up to the

instrument. Historically, due to the ease of fabrication, parallel-sided neutron guides with rectangular and constant cross-sections were the predominant choice for neutron extraction and transport.

The advent of more compact, high-brilliance neutron sources [27, 12, 161] introduces complexities to the above-described neutron extraction process, which relies on large moderators and their spatially extended clouds of neutrons. As a result, innovative and novel designs are required to effectively capitalize on the high-brilliance neutron beams offered by these new sources.

5.2.2 Large Guides and Compact Sources – Under-illumination

When utilizing compact neutron sources and conventional guides, a significant challenge known as *under-illumination* arises due to the dilution of neutron phase space. It occurs when extracting neutrons into a guide from a source that lacks sufficient size to fully utilize that guide’s capabilities [9].

We consider a simplified one-dimensional geometry, where neutrons with a given wavelength, λ , are extracted by a guide with a critical angle, θ_c , corresponding to this wavelength. To ensure that the guide is fully illuminated at the given wavelength, every neutron that can be transported by the available θ_c must also be able to geometrically access the guide, i.e., the guide must be filled with neutrons up to its *acceptance* [9]. Fig. 5.5 illustrates why

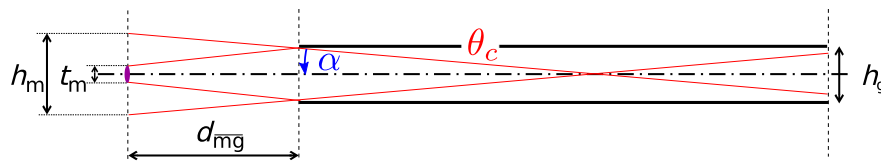


Figure 5.5: Illustration of under-illumination. The distance between the guide entrance and the moderator, d_{mg} , the height of the guide, h_g , and the critical angle of the guide θ_c , determine the extended footprint of the guide necessary for full illumination, h_m . If this footprint exceeds the size of the moderator, t_m , the transported neutrons will be diluted over the height of the guide, which entails under-illumination. The figure is adapted from the work of Herb et al. [19].

a complete illumination of the guide requires that the moderator surface must exceed

$$h_m \geq h_g + 2d_{mg} \tan \theta_c \quad (5.6)$$

in the considered dimension. If this condition is not met, neutrons emitted by the source will be diluted over the guide’s acceptance, resulting in a reduced available flux compared to that present at the source. According to Liouville’s Theorem, which states that the neutron phase space can only decrease, and considering that the absolute value of neutron divergence is not affected by a parallel-sided neutron guide, it becomes evident that the original neutron brilliance as emitted by the source cannot be recovered.

Additionally, since the critical angle scales linearly with λ , we can conclude that for every $h_m \geq h_g$, there exists a critical wavelength above which the guide remains under-illuminated and more neutrons could be transported if the source were of infinite size.

In scenarios where $h_m \leq h_g$, the guide remains under-illuminated regardless of the wavelength. Here, the guide lacks neutrons passing parallel to the reflective surfaces of the guide close to the top and bottom of the guide. To assess the overall efficiency of the extraction process within this dimension, we define the wavelength-dependent extraction efficiency,

$$E_{\text{eff}} = \begin{cases} t_m/h_m & \text{for } t_m < h_m \\ 1 & \text{for } t_m > h_m \end{cases}. \quad (5.7)$$

For reactor sources, the neutron cloud within the moderator is typically large compared to the cross-section of the guides used to extract the neutrons [162]. Consequently, under-illumination rarely reduces E_{eff} significantly. However, as we transition towards smaller sources with higher brilliance, such as the para hydrogen moderator planned for the ESS, where the vertical extent of the source is as small as $h_m = 0.03$ m, under-illumination becomes a critical issue, as the guides can be located no closer than $d_g = 2$ m to the source [163].

In contrast to parallel-sided guides, guides with elliptically shaped side walls naturally facilitate point-to-point transport of neutrons between spatially constrained focal areas due to the geometric properties of the ellipse. However, the phase space present at the first focal point is disturbed significantly during the transport, as discussed in the following. Additionally, elliptic neutron guides similarly suffer from under-illumination as conventional guides with rectangular cross-sections.

5.3 Long Elliptic Guides

While guides with a constant rectangular cross-section are suitable for extracting neutrons from an extensive source, where under-illumination is less problematic, the increasing number of reflections necessary to transport neutrons over large distances reduces the efficiency for increasing m -values and distances. To mitigate the losses associated with multiple reflections, ballistic guides have been successfully implemented [164, 165]. The concept features a cross-section diverging in the first half of the guide and reconverging in the second half, which reduces the number of reflections during transport. Today, most beamlines at the ESS use such a concept with the guide cross-section following an elliptic profile [166].

Apart from large-scale applications, the point-to-point transport capabilities of elliptic guides can also be leveraged on smaller scales. Brandl et al. successfully employed two elliptic neutron guides located between the sample and the monochromator, and the sample and the analyzer to increase the signal-to-noise ratio of an inelastic TAS experiment [167]. During the investigation of an acoustic phonon in lead, the signal-to-noise ratio could be increased by a factor of ≈ 20 .

While elliptic guides provide numerous advantages over transport systems based on constant cross sections [164], such as improved transport efficiency due to the reduced number of reflections, and better performance for small sources, in practice, they also suffer from several problems. Ideally, an elliptic guide should transport all neutrons emerging from its first focal point, F_1 , directly toward the second focal point, F_2 in a single reflection. However, gravity and finite mirror waviness⁽²⁾ can result in multiple reflections along the guide

⁽²⁾Waviness refers to local deviations of the surface normals from their intended values. To quantify the magnitude of the waviness, we quote the width of the normal distribution in angles, η [168].

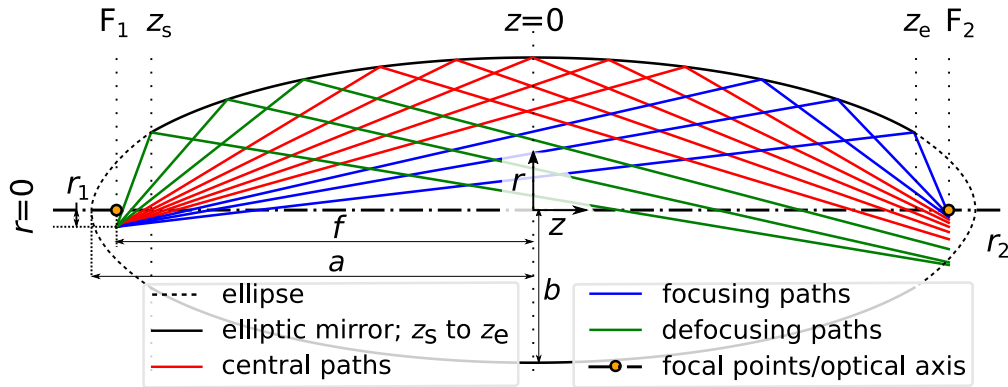


Figure 5.6: Trajectories of neutrons emitted below the first focal point F_1 with an offset r_1 from the optical axis (depicted as a black broken line). The semi-major and semi-minor axes of the ellipse, a and b , respectively, define the focal points, located at $z = \pm f$, where $f = \sqrt{a^2 - b^2}$. Neutrons reflected at points with $z < 0$ arrive at F_2 with an increased offset from the optical axis, i.e., *defocused* ($|r_2| > |r_1|$, green trajectories), whereas those reflected at $z > 0$ are focused toward F_2 ($|r_2| < |r_1|$, blue lines). Neutrons reflected at $z \approx 0$ arrive at F_2 with $r_2 \approx r_1$ (red lines). The length of the elliptic guide is given by $l = z_e - z_s$. Figure is reproduced from the work of Herb et al. [19].

[169]. Furthermore, the typically extended source size gives rise to geometric aberrations that distort the neutron phase space [170].

Depending on the point of reflection along the neutron guide, z , neutrons emitted with a vertical offset to the optical axis, r_1 , may either be focused or defocused at F_2 , as illustrated in Fig. 5.6. The relation between the local magnification r_2/r_1 and the point of reflection, z , is commonly described by

$$\frac{r_2}{r_1} = \frac{f - z}{f + z}, \quad (5.8)$$

where f denotes the focal length of the ellipse.

However, we have improved on the precision of this result by first analytically calculating r_2 as a function of r_1 and z and subsequently performing a Taylor expansion rather than relying solely on geometric arguments as previously done. A detailed explanation of this calculation is presented in the appendix C, and the summarized results are illustrated in Fig. 5.7. Here, the dependence of the magnification r_2/r_1 on z is shown for a long elliptic mirror with a focal length, $f = 0.675$ m, semi-minor axis, $b = 0.02$ m, and total length, $l = 0.8$ m⁽³⁾. The presented data corresponds to $r_1 = 2$ mm, but it should be noted that the result shows little dependence on r_1 . The high-precision python simulation and the analytic calculation (compare Eq. (C.6) in appendix C) exhibit perfect agreement, validating both.

However, the commonly used approximation given in Eq. (5.8) deviates slightly for $|z| \gg 0$, as illustrated in the insets in Fig. 5.7. We propose an improved approximation given by,

$$\frac{r_2}{r_1} \approx 1 + \left(\frac{f - z}{f + z} - 1 \right) \frac{(f^2 - b^2 + b r_1)}{b^2 + f^2}. \quad (5.9)$$

⁽³⁾If not specified otherwise, elliptic guides are oriented symmetrically with respect to their semi-minor axis, i.e., $z_s = -l/2$, $z_e = l/2$.

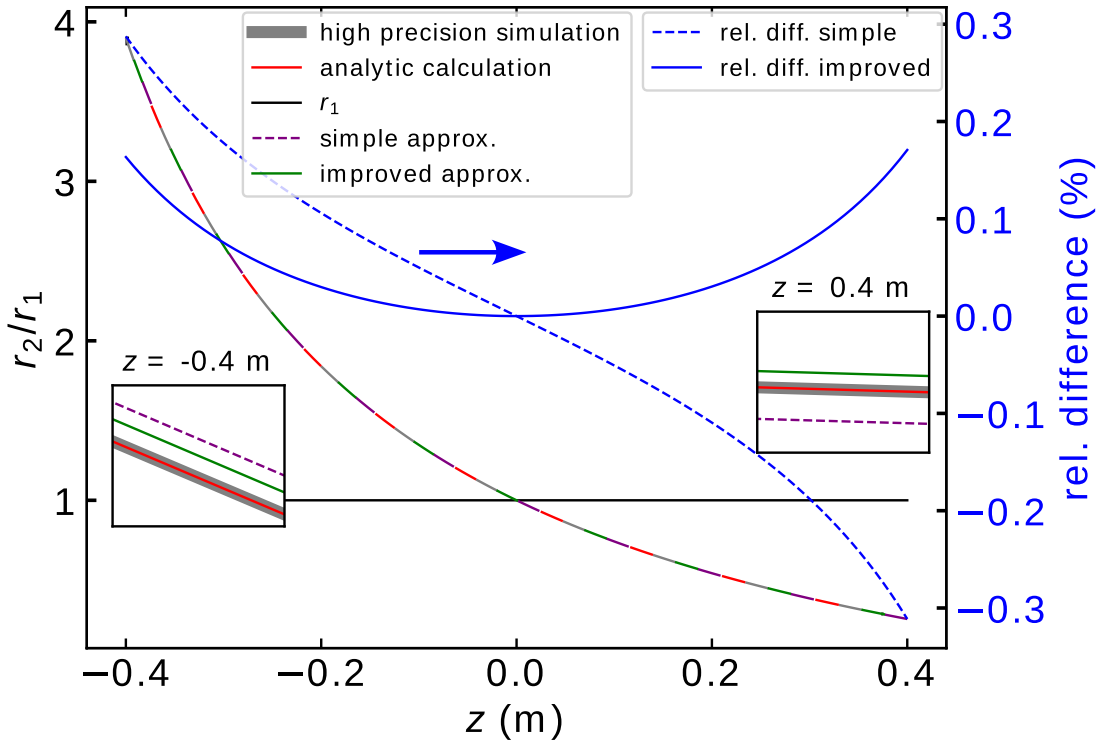


Figure 5.7: Dependence of the local magnification in an elliptic guide on the point of reflection, $r_2/r_1(z)$. The high precision simulation (gray band) and the analytic calculation (red, compare Eq. (C.6)) are in perfect agreement. Both the simple approximation given in Eq. (5.8) (broken, purple line) and the improved approximation (light blue), Eq. (5.9), are in reasonable agreement with the calculation for the chosen geometry. The horizontal black line represents the desired imaging with unit magnification, $r_2/r_1 = 1$. The two insets illustrate that the improved approximation significantly reduces the relative difference between the exact solution and the approximation, $(approx. - calc.)/calc.$, when neutrons are reflected at the mirror's entrance and exit, $|z| = 0.4$ m. While the relative difference (y-axis labeling on the right) remains below 0.2% for the improved approximation (solid blue line), it exceeds 0.3% for the simple approximation (dashed blue line).

It takes into account the semi-minor axis, b , and demonstrates significantly better agreement with the analytic simulation than Eq. (5.8) (error of order $\mathcal{O}(z^2)$ instead of $\mathcal{O}(z)$). It reduces the relative error by a factor greater than 2 for most z . For $f \gg b \geq r_1$, Eq. (5.9) approaches Eq. (5.8) as expected. Given the small discrepancy between the analytic solution and Eq. (5.9), the latter might be used as a pre-estimation tool to assess the quality of beam transport in long elliptic guides before investing computational resources into a Monte-Carlo approach. However, it should be noted that the here disregarded influence of gravity is likely to be more important already for small transport distances.

In addition to quantifying the focusing and defocusing effects as a function of z , we have also calculated the spatial intensity distribution at the second focal point directly from the initial distribution of neutrons. Performing the analytic calculation requires the simplifying

assumption that the points of reflection are uniformly distributed in z between the start and the end of the elliptical mirrors. We will later see that this assumption is only justified in the case of short mirrors and improve on this approximation. The resulting [probability density function \(PDF\)](#) describes the uniform probability that a neutron is reflected between z and $z + dz$ normalized by dz ,

$$p_z(z) = 1/l, z \in [-l/2, l/2]. \quad (5.10)$$

Here, l denotes the length of the elliptical mirror along z , $l = z_e - z_s$. Furthermore, we assume the vertical offsets to the optical axis under which neutrons are emitted at F_1 to be uniformly distributed with [PDF](#),

$$p_{R_1}(r_1) = 1/h, r_1 \in [-h/2, h/2], \quad (5.11)$$

where h denotes the height of the source in the considered dimension.

Assuming that these two distributions are independent, we can calculate the joint probability that a neutron is emitted at r_1 and subsequently reflected at z as the product of Eq. (5.10) and Eq. (5.11). Employing the simplified relation between r_2, r_1 , and z given in Eq. (5.8), we can analytically calculate the [PDF](#) of r_2 , which corresponds to the spatial intensity distribution of neutrons arriving at F_2 normalized to 1,

$$p_{R_2}(r_2) = \begin{cases} \frac{2f}{hl} \left[\ln \left(\frac{f+l/2}{f-l/2} \right) - \frac{l}{2f} \right] & \text{for } |r_2| \leq \frac{h}{2} \frac{f-l/2}{f+l/2} \\ \frac{2f}{hl} \left[-\frac{1}{4} (2 + l/f) + \frac{2|r_2|}{2|r_2|+h} + \ln \left(\frac{(|r_2|+h/2)(2f+l)}{4f|r_2|} \right) \right] & \text{for } \frac{h}{2} \frac{f-l/2}{f+l/2} \leq |r_2| \leq \frac{h}{2} \frac{f+l/2}{f-l/2} \\ 0 & \text{for } \frac{h}{2} \frac{f+l/2}{f-l/2} \leq |r_2|. \end{cases} \quad (5.12)$$

The derivation is presented in appendix D⁽⁴⁾. The resulting [PDF](#) can be shown to integrate to 1 and exhibits continuous behavior at $r_2 = \frac{h}{2} \frac{f-l/2}{f+l/2}$ as expected for an intensity distribution. It has to be noted that Eq. (5.12) does not account for double reflections possible within the guide and does not include the effects of gravity.

We observe three distinct regions into which $|r_2|$ might fall. If the magnitude of r_2 exceeds the limits imposed by the ranges of r_1 and z , $|r_{2,\max}| = \frac{h}{2} \frac{f+l/2}{f-l/2}$ ⁽⁵⁾, no neutrons can be found, i.e., $p_{R_2}(r_2) = 0$. For a small region centered around the optical axis $|r_2| \leq \frac{h}{2} \frac{f-l/2}{f+l/2}$, the density of neutrons remains constant at a value $p_{R_2}(r_2) = \frac{2f}{hl} \left[\ln \left(\frac{f+l/2}{f-l/2} \right) - \frac{l}{2f} \right]$. Between these two values, i.e., $\frac{h}{2} \frac{f-l/2}{f+l/2} \leq |r_2| \leq \frac{h}{2} \frac{f+l/2}{f-l/2}$, the intensity drops monotonously from the value observed in the inner region to zero. In the case of a very short mirror, where $l = \epsilon$, the expression approaches $\frac{2f}{hl} \left[\frac{2l-l}{2f} \right] = 1/h$ for $|r_2| \leq h/2$, which correctly equals the distribution of neutrons at the first focal point, as given by Eq. (5.11).

The influence of the mirror length l becomes evident if we compare $p_{R_2}(r_2)$ for various values of l while keeping $f = 1.35$ m, and $h = 0.005$ m, constant. These are typical values for a small elliptic guide setup. As illustrated in Fig. 5.8, the results from Eq. (5.12) (continuous lines) are in excellent agreement with a Python simulation (open circles).

⁽⁴⁾Within this work, we assume for simplicity that $|z| \neq f$, which is always true if the mirror does not extend to the focal points, $l < 2f$.

⁽⁵⁾This limiting value of r_2 is achieved for a neutron that is emitted at the maximum distance from the optical axis, $r_1 = h/2$ and subsequently reflected at the entrance of the neutron guide $z = -l/2$.

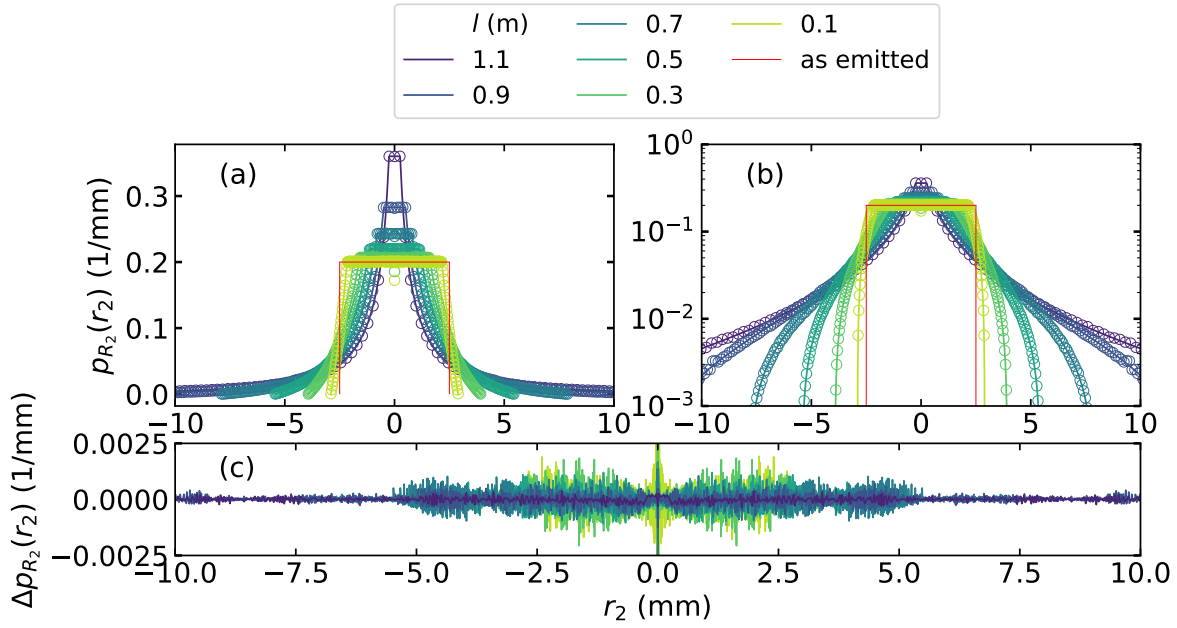


Figure 5.8: Spatial intensity distributions at F_2 as a function of r_2 for various mirror lengths, l , on a linear (a) and a logarithmic (b) scale. Solid lines illustrate the analytically obtained intensity distributions, see Eq. (5.12). Data from Python simulations under analogous assumptions, i.e., uniform distributions in r_1 and z , are shown as empty circles of matching color. The rectangular intensity distribution as emitted at F_1 is outlined in red, compare Eq. (5.11). Panel (c) shows the difference between the simulation and the calculation, yielding a good agreement exhibiting no systematic discrepancies. All data is obtained with $f = 0.675$ m, $h = 5$ mm and perfectly reflecting mirrors.

The intensity distributions are symmetric around $r_2 = 0$ and comprise the three regions described above. This includes a central region of constant value, which becomes narrower and more intense as l increases, along with tails of intensity whose width expands with increasing l . This progressing distortion of the initial, rectangular intensity distribution, outlined in red, is attributed to a growing portion of neutrons being reflected distant to the semi-minor axis, $z = 0$, at either the entrance or the end of the elliptic guide, resulting in focusing or de-focusing effects. Finally, for $|r_2| \geq \frac{h}{2} \frac{f+l/2}{f-l/2}$ the probability to find a neutron is zero. This simple approximation already reveals that increasing the length of the elliptical mirrors entails a more pronounced distortion of the initial intensity distribution found at F_1 during the transport.

However, a real source emits neutrons uniformly concerning their angle to the optical axis and r_1 , leading to a non-uniform distribution of points of reflection along the mirror. When considering a flat reflecting surface parallel to the optical axis, it is evident that the number of neutrons per unit length decreases with increasing distance from the source, d_s , for two reasons. Firstly, in a two-dimensional context, the intensity of the neutron beam decreases proportionally with $1/d_s$ ⁽⁶⁾. Secondly, the angle of incidence also decreases with increasing

⁽⁶⁾This is analogous to the $1/d_s^2$ -law for three dimensions.

d_s . Both effects conspire to decrease the neutron density with increasing z .

Conversely, in the case of a long, elliptic mirror, the angle of incidence increases at large values of z , qualitatively opposing the first effect concerning the neutron density. A detailed analysis of this observation is presented in appendix E, with Fig. 5.9 summarizing the results.

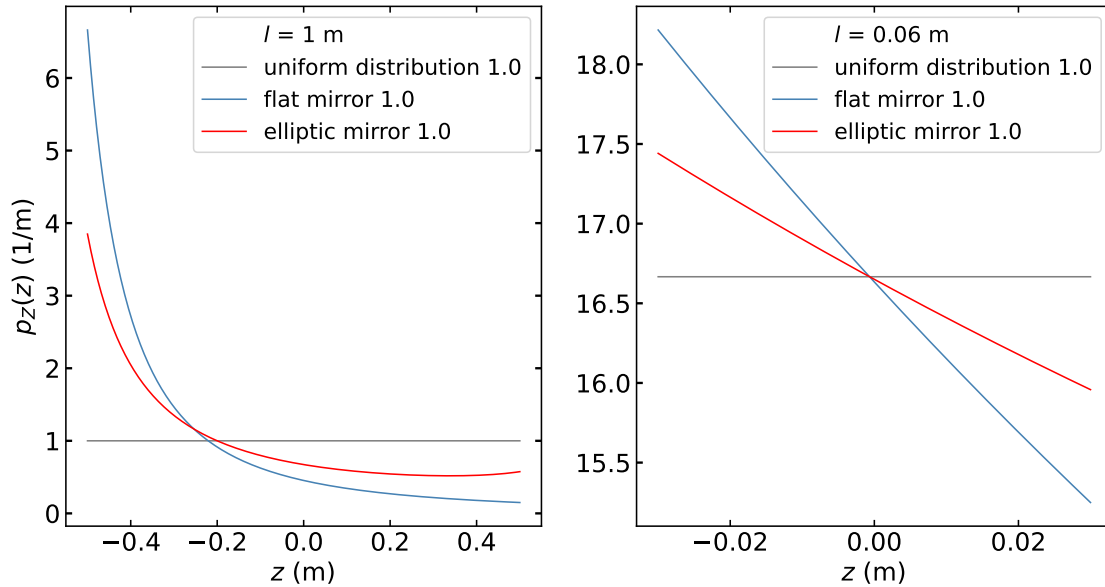


Figure 5.9: Neutron densities at the reflecting surface as a function of the point of reflection z for differently shaped mirrors. The black line refers to the assumption of uniform density employed for the derivation of Eq. (5.12). Blue and red lines correspond to flat and elliptic mirror geometries with their maximum distance to the optical axis, $b = 0.02$ m, respectively. Panels (a) and (b) show the respective distributions for two different total lengths of the mirror $l = 1$ m and $l = 0.06$ m. All distributions correctly integrate to 1 as highlighted in the legend.

For the calculation, we assumed all neutrons to be emitted from one focal point, with the maximum distance between the optical axis and the elliptic and the flat mirror being, $b = 0.02$ m. The focal length of the elliptic mirror amounts to $f = 0.675$ m. Panels (a) and (b) show results for $l = 1$ m and 0.06 m, respectively. For $l = 1$ m, the intensity distributions for the flat mirror (blue) and the elliptic one (red) show qualitative differences, with both differing significantly from the uniform intensity distribution (black). When going to large $z > 0.25$ m, the density of neutrons impinging on the reflective surface per length element in z monotonically decreases for the flat mirror. Considering the elliptic mirror, the increase in incident angle overcomes the reduction in density with increasing distance from the source, such that the overall density increases when z approaches 0.5 m. In the case of very short mirrors $z = 0.06$ m, the observed behavior is dominated by a linear term in z , which is easily obtained from a series expansion (compare appendix E). Due to the discussed effects with an opposing sign, $p_z(z)$ obtained for the elliptic mirror changes at half the rate with z compared to the case of the flat mirror.

In conclusion, the initial assumption of a uniform distribution of the points of reflection over the length of the guide is only satisfied in the case of short guides, e.g., $l/f \approx 1/10$, where the relative difference does not exceed 10%. For long guides, however, the relative difference to the uniform distribution becomes prohibitively large, which necessitates using the true $p_Z(z)$ when calculating $p_{R_2}(r_2)$.

The analytic transformation of the PDFs, even with the help of computer algebra systems (Mathematica [171]), becomes impossible at this point. Additionally, for an extended source of neutrons, we anticipate a slight deviation in $p_Z(z)$ compared to the one calculated under the assumption that all neutrons are emitted from F_1 . Lastly, the relationship between r_2 and r_1 determined by Eq. (C.6) cannot be integrated analytically.

To obtain the intensity distribution at the second focal point, we employ numerical integration as discussed in appendix F. The resulting intensity distributions are visualized in Fig. 5.10 similarly to those in Fig. 5.8. Two key differences can be observed compared to

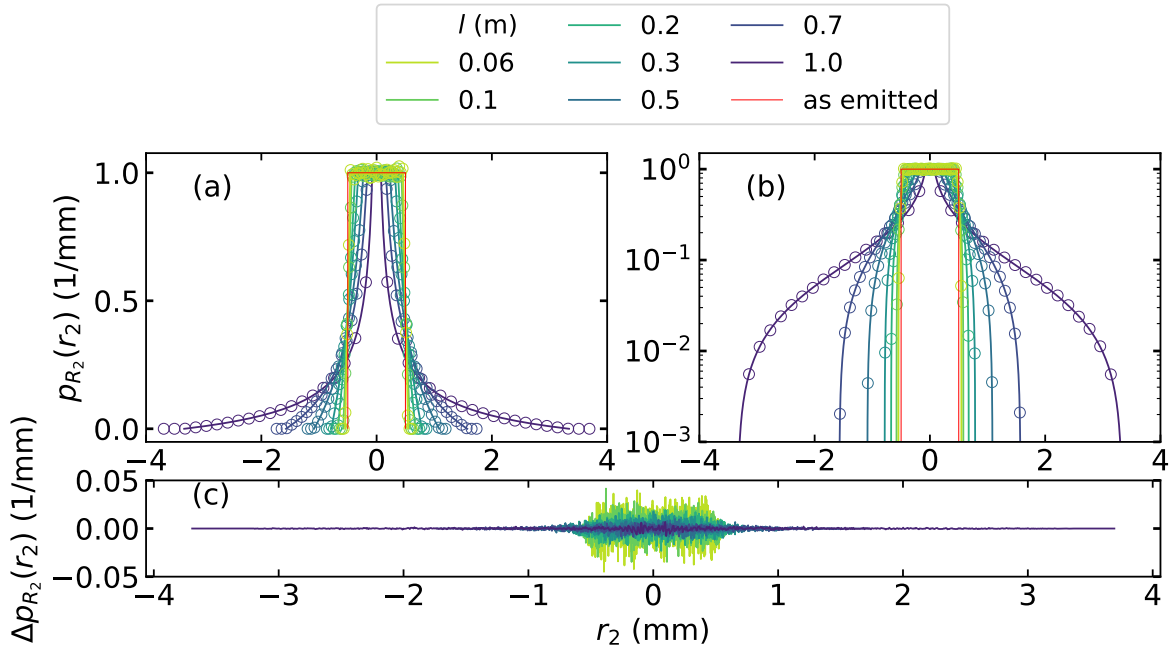


Figure 5.10: Spatial intensity distributions for various mirror lengths, l , on a linear (a) and logarithmic (b) scale. Solid lines represent the intensity distributions at F_2 derived from a transformation of the intensity distribution of neutrons at F_1 . To account for the exact elliptic shape of the reflective surface and the uniform distribution of neutrons in r_1 and their angle to the optical axis, α , numerical integration had to be utilized as outlined in appendix F. Data obtained from McStas simulations under analogous assumptions is shown as empty circles of matching color. The difference between the two datasets is illustrated in (c), exhibiting no systematic discrepancies. Outlined in red is the rectangular distribution of intensity as found at F_1 , $p_{r_1}(R_1)$.

the data obtained under the assumption of a constant $p_Z(z)$ (compare Fig. 5.8). Firstly, the values of $p_{R_2}(r_2)$ obtained for various values of l all plateau at the same value instead of increasing with decreasing l . Secondly, the flanks of intensity are more pronounced. Both

effects are attributed to the difference in $p_z(z)$, where the uniform distribution overestimates the number of neutrons reflected in the second half, which are focused. The McStas simulation is in excellent agreement with the numerical integration, validating both.

Irrespective of the calculation mode, the comparison of intensity distributions for guides of various lengths reveals that shorter guides preserve the emitted, rectangular intensity distribution to a higher degree, whereas the neutron distribution transported through a long elliptic guide experiences significant spatial distortion.

Elucidating this distortion of the neutron phase space in more detail, we simulated the neutron transport through a long elliptic guide using the McStas software package [172]. Fig. 5.11 illustrates the intensity distribution at F_2 as a function of both the distance to the optical axis r_2 and the vertical divergence α_v . Fig. 5.11 (a) compares the spatial intensity

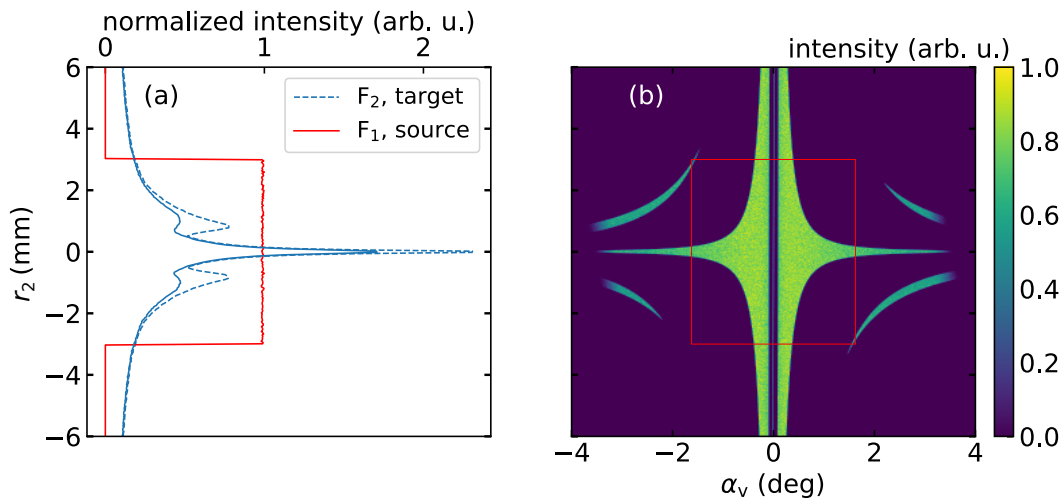


Figure 5.11: Beam quality after transport by a long elliptic guide. Solid and broken lines represent results from simulations with ($m = 4.1$, $R_e = 82\%$), and with ideal reflectivity, respectively. (a) Horizontally integrated intensity distribution at F_2 plotted against the vertical distance from the optical axis, r_2 . The emitted rectangular spatial intensity distribution is outlined in red. After the transport through the long elliptic guide, the rectangular shape at the second focal point is heavily distorted. A reflection close to the exit of the guide results in a central peak of focused neutrons close to the optical axis, $z = 0$. Conversely, neutrons reflected close to the entrance of the guide contribute to the tails of intensity, which extend much further than the original rectangular intensity distribution. (b) The color plot shows the neutron intensity at F_2 as a function of the vertical divergence, α_v , and r_2 , normalized to the uniform intensity of the emitted volume of phase space. The red rectangle indicates the outline of the volume of phase space as emitted by the source at F_1 .

The simulated long guide is characterized by the following dimensions: $f = 20$ m, $b_0 = 0.132$ m, and $l = 39.5$ m. The neutron beam used in the simulation was monochromatic with a wavelength of $\lambda = 4$ Å. The figure is adapted from the work of Herb et al. [19].

distributions at F_1 and F_2 , respectively. The emitted rectangular peak of uniform intensity (red) becomes severely distorted during the transport through the long elliptic guide, resulting in a sharp peak of focused neutrons close to the optical axis and tails of weak

intensity far away from the optical axis. To further disentangle the contributions to the resulting neutron distribution, Fig. 5.11 (b) shows the intensity at the second focal point as a function of both the vertical deviation from the optical axis, r_2 , and the vertical divergence, α_v . This reveals contributions of focused (small $|r_2|$, large $|\alpha_v|$) and defocused (large $|r_2|$, small $|\alpha_v|$) neutrons, which correspond to reflections close to the exit and entrance of the guide, respectively (compare Fig. 5.6). Additionally, isolated islands of intensity arise due to doubly-reflected neutrons. Multiple interactions with the same mirror (*garland reflections*) or subsequent interactions with two opposing mirrors (*zig-zag reflections*) result in intensity arising in the upper left (and lower right) and upper right (and lower left) quadrant, respectively. Apart from the geometric aberrations, multiple reflections occurring over the course of a long guide as a consequence of gravity or finite mirror waviness may furthermore complicate the divergence and intensity profile at F_2 , compared to the situation at F_1 .

To visually summarize the geometric aberrations introduced into the neutron phase space by a long elliptic guide, Fig. 5.12 illustrates the results of a Python simulation. We simulated the transport of a grid-like intensity pattern from one focal point of a long elliptic guide to the other, emphasizing the distortions and complexities encountered during the neutron transport through such a guide. Instead of returning to their initial position relative to F_1 , neutrons arrive at F_2 with significant variations in offsets. Those focused toward the optical axis manifest as a sharp central peak, while the defocused neutrons are dispersed further from their emission point. The intensity emitted from the individual slits becomes thoroughly blended due to the discussed geometric aberrations.

While Fig. 5.12 vividly illustrates why geometric aberrations in long elliptic guides render them unsuitable for imaging experiments, the complications associated with the distortion of the emitted volume of neutron phase space are more profound in real experiments. In the context of neutron scattering, precise knowledge of the initial state of neutrons, including their distribution in energy and momentum, is crucial. Researchers then aim to determine the state of the scattered neutrons and infer the difference between the two to understand the interaction between neutrons and the sample. Complex initial intensity distributions make this comparison between theory and experimental results more challenging, potentially requiring advanced corrections and data analysis techniques⁽⁷⁾.

In the next section, we will explore a solution to reduce geometric aberrations based on an assembly of shortened mirrors replacing a single long mirror.

5.4 Elliptic Nested Mirror Optics

By constraining the guide length, l , to values much smaller than the focal length, f , we ensure that neutrons are reflected close to the semi-minor axis, which reduces geometric aberrations, ensuring the preservation of the volume of phase space as emitted at F_1 . However, a shortening of the mirrors entails a significant reduction of the angular acceptance of the guide, consequently reducing the amount of transported neutrons significantly. The impact of these two effects on the transported intensity distribution is illustrated in Fig. 5.13. Ideally, one would recover the entire angular range transported by a long elliptic guide while maintaining the improved quality of imaging enabled by the shortened mirrors.

⁽⁷⁾Usually, it is assumed that the phase space of the incident neutrons can be approximated by Gaussian resolution ellipsoids in momentum and energy space [108, 107, 173].

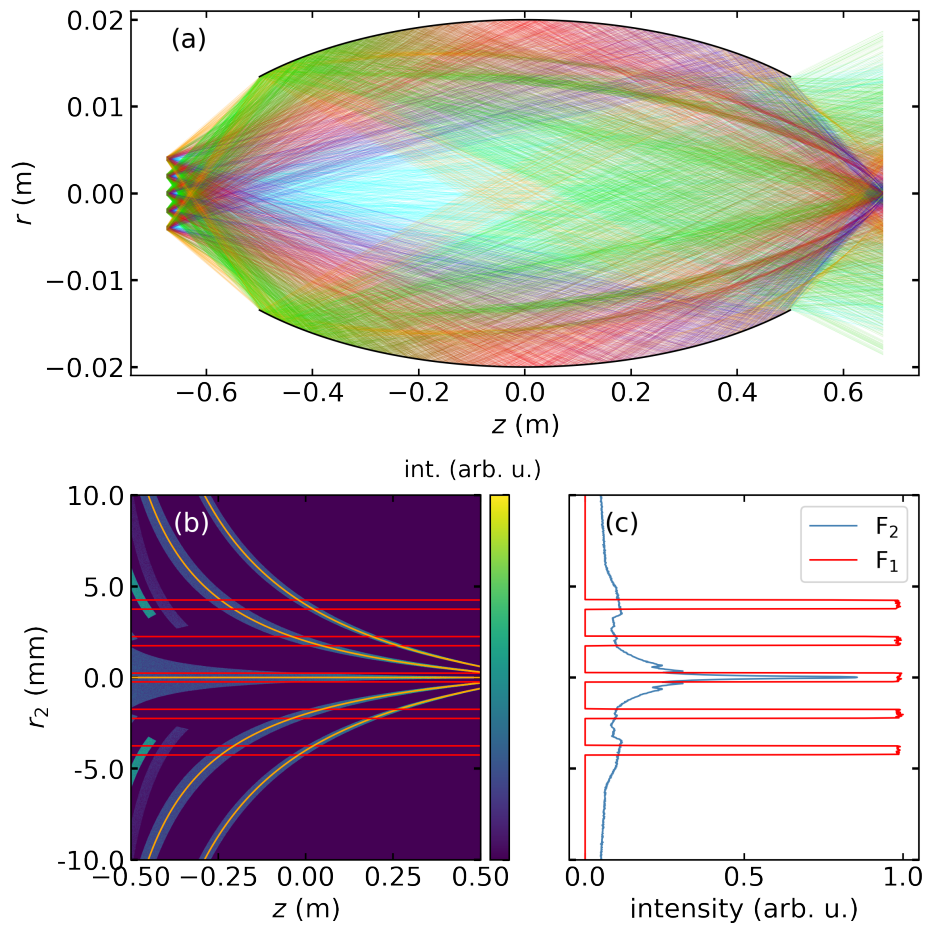


Figure 5.12: Simulated transport of a grid-like intensity distribution through a long elliptic guide. Neutrons are emitted at F_1 in five equidistant stripes, each with a width of 0.5 mm and spaced 2 mm apart. They are subsequently transported to F_2 by a long elliptic guide characterized by the following parameters: $f = 0.675$ m, $l = 1$ m, $b = 0.02$ m and perfectly reflecting mirrors. Panel (a) illustrates the neutron trajectories, color-coded according to their first point of reflection. Green and dark blue trajectories correspond to neutrons reflected close to the entrance and the exit of the guide, respectively. Red and light blue trajectories correspond to neutrons reflected close to $z = 0$ and neutrons that pass through the guide without reflection. The present geometry also allows for doubly reflected neutrons indicated by orange lines. It should be noted that the figure is not to scale.

Panel (b) displays the intensity distribution at F_2 as a function of the distance to the optical axis, r_2 , and the initial point of reflection, z . Red lines indicate the positions at which neutrons are emitted at F_1 , i.e., the grid. Orange lines depict the approximate relationship between r_1 and r_2 given by Eq. (5.8) for each of the slits showing a good agreement with the color plot. The intensity around $z = -0.45$ m corresponds to doubly reflected neutrons. Panel (c) presents the data from (b) after integration over z , which is equivalent to the spatial intensity distribution after the transport at F_2 (blue). This distribution contains focused neutrons near $r_2 = 0$ and defocused tails of neutron intensity far from the optical axis, $|r_2| \gg 0$. In summary, the originally grid-like intensity distribution emitted at F_1 (depicted in red) undergoes a significant transformation during transport, making it unrecognizable at F_2 .

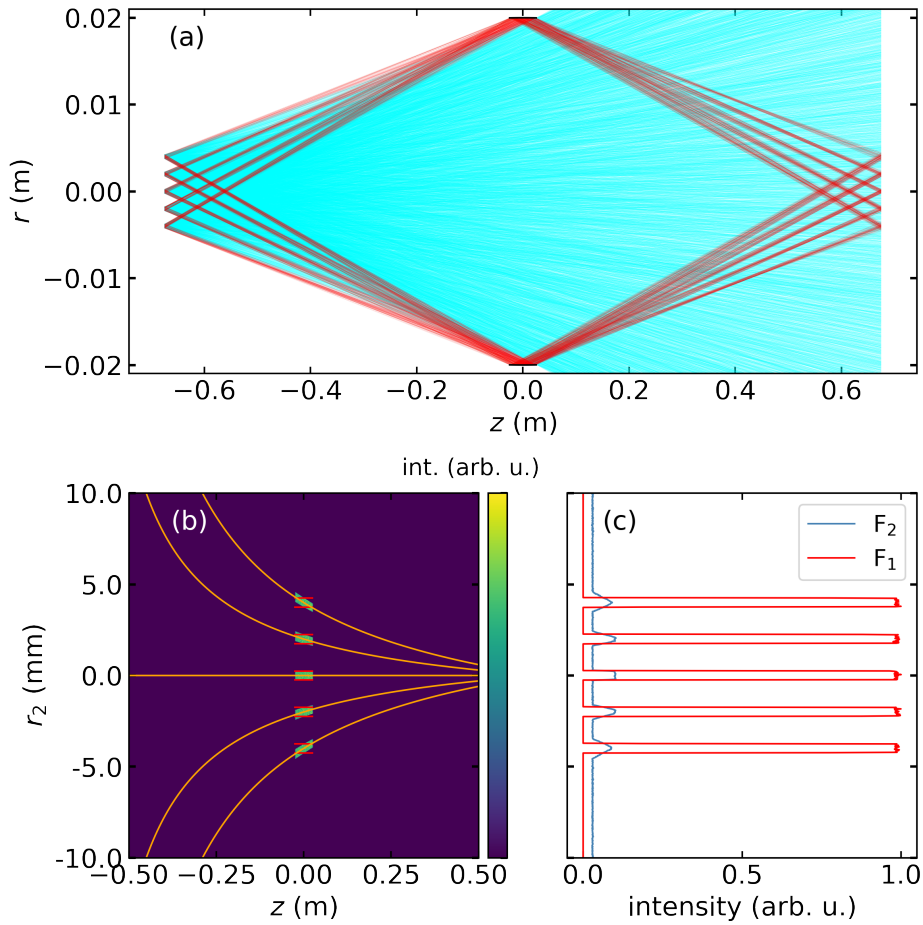


Figure 5.13: Simulated intensity distributions at F_2 similar to those presented in Fig. 5.12. By reducing the guide length from $l = 1$ m to $l = 0.05$ m, geometric aberrations are reduced significantly, even enabling the recovery of the emitted grid-like structure at F_2 . However, the significant reduction of l limits the efficiency of neutron transport. Both effects can be observed in the horizontally averaged intensity distributions (c), where small peaks in intensity appear at the correct distances from the optical axis, with the intensity dropping to a constant background in between. The peak shapes can be understood directly from the shape of the integrated data (b). The constant background is attributed to neutrons passing the very short mirrors without reflection, illustrated in light blue in (a).

As discussed by Zimmer [174] and detailed in appendix G for non-symmetric geometries, this can be achieved by nesting several elliptic mirrors with coinciding focal points but different semi-minor axis b_n . One obtains the full angular acceptance while reducing the distortions to the neutron phase space. Fig. 5.14 illustrates the construction process, including the neutron trajectories that determine the geometry. The m -value of the outermost mirror and the requirements for the reflected beam, such as the desired divergence and the position of the two focal points, jointly determine the semi-minor axis of this outermost mirror b_0 . After selecting a common length for the individual mirrors, l , one can calculate the semi-minor axis of the next inner mirror by requiring that a line from F_1 to the end of one mirror

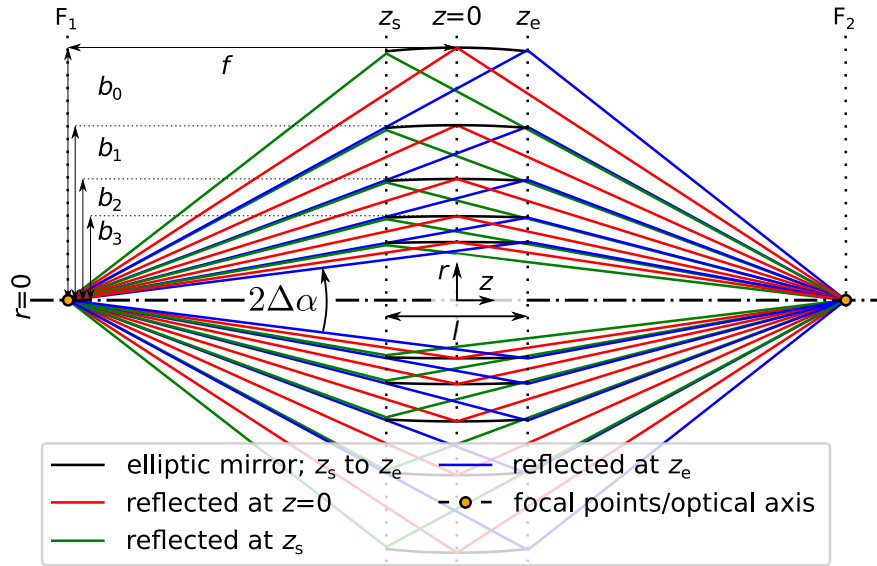


Figure 5.14: Schematics of a symmetric elliptic NMO including shape-determining neutron paths being reflected either at the entrance, z_s , or the exit, z_e of the NMO. The common focal points of all elliptic surfaces are highlighted in orange. The figure is reproduced from the work of Herb et al. [19].

coincides with the entrance of the next inner mirror. Following this recipe ensures that every neutron emitted at F_1 interacts with precisely one mirror, enabling the device to transport a geometrically defined range of angles [19].

The total number of mirrors required on each side to transport the desired angular range $\alpha \in |\alpha_{\min}, \alpha_{\max}|$ can be approximated by

$$N \approx \ln \left(\frac{\alpha_{\max}}{\alpha_{\min}} \right) \frac{f}{l}. \quad (5.13)$$

The derivation of this result can be found in the appendix G and [174]. Accordingly, the number of required mirrors increases logarithmically with the angular range and linearly with the ratio of the focal length, f , to the mirror length, l . Curiously, the total neutron reflecting area remains constant under variations of l . This is because the area of an individual mirror scales proportionally to l while the number of mirrors scales reciprocally. This observation supports utilizing shorter mirrors, as they offer reduced geometric aberrations.

In practical terms, the finite thickness of the mirror substrates restricts the minimum distance between two adjacent reflecting surfaces. Consequently, neutrons emitted at minimal angles $\leq \Delta\alpha$ do not partake in the reflection process and instead traverse the *divergence hole* unobstructed. These neutrons can either be absorbed by a beam stop or be partially reflected by equidistantly spaced mirrors, which is discussed at a later stage.

Furthermore, neutrons emitted at a given distance from the optical axis, r_1 , can pass between any two mirrors without interaction or undergo a double reflection, depending on their initial emission angle. Fig. 5.15 (a) and (b) illustrate these two cases, respectively. In the first case, the origin of the neutron, characterized by the sign of r_1 , and the point of reflection occur on the same side relative to the optical axis, as shown in panel (a). We can

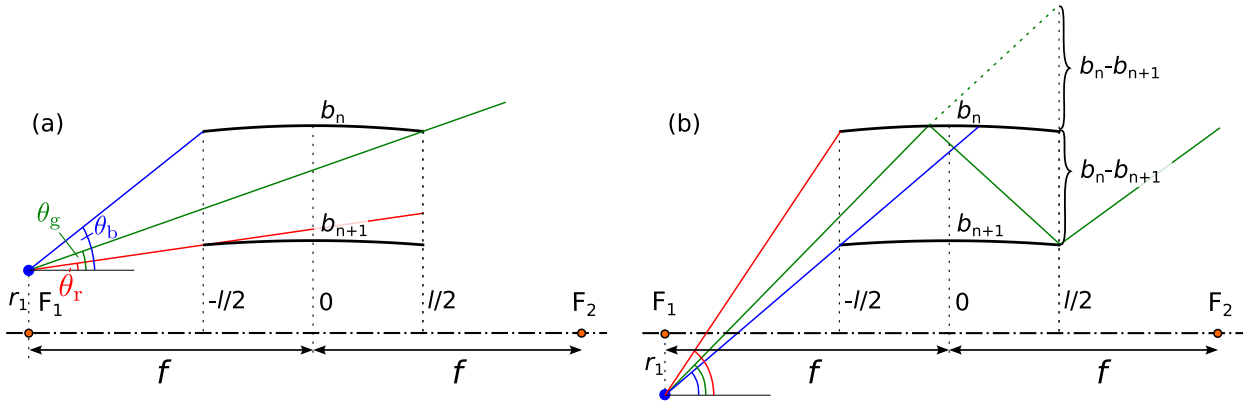


Figure 5.15: Schematics illustrating how neutrons pass between two mirrors of the elliptic NMO either unobstructed (a) or doubly-reflected (b). Neutrons emitted on trajectories encompassed by the red and the green lines are either non- or doubly reflected. In contrast, neutrons traveling between the green and the blue lines are correctly reflected once.

then approximate the ratio of neutrons passing between two mirrors without interaction to the total number of neutrons incident between the two mirrors by

$$R_{\text{loss, passing}} = \frac{\theta_g - \theta_r}{\theta_b - \theta_r} \approx \frac{\arctan\left(\frac{b_n - r_1}{f - l/2}\right) - \arctan\left(\frac{b_{n+1} - r_1}{f - l/2}\right)}{\arctan\left(\frac{b_n - r_1}{f - l/2}\right) - \arctan\left(\frac{b_{n+1} - r_1}{f - l/2}\right)} \approx \frac{r_1}{b_n}. \quad (5.14)$$

Here, b_n and b_{n+1} are the semi-minor axes of the two adjacent mirrors and θ_g , θ_r and θ_b denote the angles between the optical axis and the green, red, and blue trajectories in Fig. 5.15 (a), respectively. The fate of a neutron is determined by its emission angle compared to those angles. Neutrons emitted within a range of angles between the green and the red line, $\theta_g - \theta_r$, do not interact with any mirror, while those emitted between the blue and the green line, $\theta_b - \theta_g$, are correctly reflected. Under the assumption of approximately flat mirrors (constant distance to the optical axis b_n), utilizing the small angle approximation⁽⁸⁾, and considering the relation between the semi-minor axes of two adjacent mirrors, $b_{n+1} \approx b_n \frac{f - l/2}{f + l/2}$ (compare appendix G), we finally derive the approximate loss ratio: $R_{\text{loss, passing}} \approx \frac{r_1}{b_n}$. The implicit assumption that the angular distribution of neutrons is uniform is well supported for the small angular range necessary to illuminate the space between two adjacent mirrors.

For neutrons that interact with a mirror on the opposite side relative to their point of origin, the ratio of doubly-reflected neutrons to all neutrons incident between the mirrors is given by a similar factor

$$R_{\text{loss, double reflection}} = \frac{\theta_r - \theta_g}{\theta_r - \theta_b} \approx \frac{\arctan\left(\frac{b_n + r_1}{f - l/2}\right) - \arctan\left(\frac{2b_n - b_{n+1} + r_1}{f + l/2}\right)}{\arctan\left(\frac{b_n + r_1}{f - l/2}\right) - \arctan\left(\frac{b_{n+1} + r_1}{f - l/2}\right)} \approx \frac{r_1}{b_n}, \quad (5.15)$$

where the same assumptions as above were utilized. Here, the angles θ_r , θ_g , θ_b correspond to

⁽⁸⁾Specifically, all arctan functions in Eq. (5.14) are approximated by their argument.

the angles between the optical axis and the red, green, and blue trajectories depicted in Fig. 5.15 (b), respectively.

For either case and to first order independent of l and f , the geometric loss ratio for neutrons passing between the n^{th} and $(n + 1)^{\text{th}}$ mirror can be approximated by

$$R_{\text{loss}} \approx r_1/b_n, \quad (5.16)$$

indicating that the innermost mirrors suffer the greatest geometric losses and larger NMOs offer better transport efficiency when keeping constant the extent of the source. The average loss for an extended source with width w is readily obtained:

$$\overline{R_{\text{loss}w}} = \frac{\int_{-\frac{w}{2}}^{\frac{w}{2}} \frac{|r_1|}{b_n} dr_1}{w} = \frac{w}{4b_n}. \quad (5.17)$$

Typically, neutron optical systems are limited by the critical angle of the supermirror coating, which in turn determines the maximum transportable divergence leaving the source. For a given source geometry (height h , divergence θ_s), the losses can be reduced by utilizing a NMO with a larger focal length, and consequently larger semi-minor axes $b_0 \approx \theta_s f$, thereby reducing the loss ratio. However, a larger focal length imposes stricter requirements on the mirror waviness and necessitates additional mirrors towards the center of the NMO. Additionally, for large wavelengths, gravitational distortions of the neutron trajectories can pose disadvantages when exceeding a certain travel time of the neutrons, $t_f \propto f$, requiring careful simulation-supported consideration when choosing the size of the NMO.

Highlighting the optical imaging quality, Fig. 5.16 presents McStas Monte-Carlo simulations of a one-dimensional, elliptic NMO comparing the intensity distribution at F_2 with the emitted distribution at F_1 . The geometry for this simulation, considering only the vertical dimension, is similar to the one for the long elliptic guide shown in Fig. 5.11⁽⁹⁾. In the present setup, a source with height, $h_s = 6$ mm, illuminates a symmetric, one-dimensional, elliptic NMO equipped with mirrors with length, $l = 1.6$ m. Fig. 5.16 (a) illustrates that the emitted spatial intensity distribution (red) remains well preserved during the transport through the NMO, with only a minor deviation at the upper edge, $r_2 = 3$ mm, attributed to gravitational effects. In both simulations, one with ideal reflectivity (dashed blue line) and another considering a realistic supermirror reflectivity profile with $m = 4.1$ and $R_e = 82\%$ (solid blue line), a small and constant reduction in intensity compared to the source is observed. While the discussed geometric losses account for the reduction to $\leq 90\%$, the finite mirror reflectivity accounts for another 10% loss.

When investigating the intensity as a function of the vertical position, r_2 , and the vertical divergence, α_v , as shown in Fig. 5.16 (b), the emitted uniform intensity distribution (red outline) is well-preserved during the transport, except for a slight smearing at the upper edge, $r_2 = 3$ mm, due to gravity. The fine texture of the intensity is attributed to contributions reflected by individual mirrors. A substantial decrease of the intensity around $\alpha_v = 0$ marks the divergence hole, and the slight decrease in intensity towards higher angles of incidence corresponds to the decreasing supermirror reflectivity for larger angles of reflection, compare Fig. 5.4.

⁽⁹⁾The simulated NMO consists of 40 individual mirrors on both sides of the optical axis, each with a thickness, $d_{\text{sub}} = 0.5$ mm, $f = 20$ m, $b_0 = 0.8$ m, $l = 1.6$ m, and $m = 4.1$, $R_e = 82\%$.

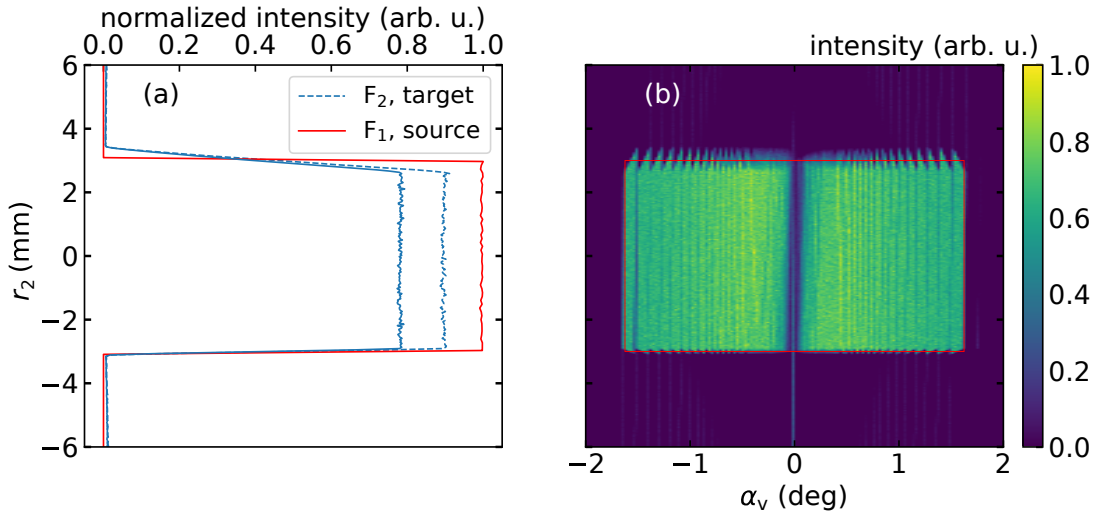


Figure 5.16: Beam quality after transport through an elliptic NMO. (a) Horizontally integrated intensity distributions at F_1 (red) and F_2 (blue) plotted against the vertical distance from the optical axis, r_2 . Solid and broken lines represent results from simulations with ($m = 4.1$, $R_e = 82\%$), and with ideal reflectivity, respectively. (b) Intensity at F_2 as a function of α_v and r_2 normalized to the uniform density of the emitted volume of phase space. The red rectangle indicates the outline of the volume of phase space emitted at F_1 . Overall, the intensity distribution recovered at F_2 closely resembles the distribution emitted at F_1 , suggesting that the original phase space volume is successfully preserved during the transport. The figure is adapted from the work of Herb et al. [19].

5.5 Parabolic Nested Mirror Optics

In addition to using nested elliptic mirrors for neutron transport between two focal points, a similar system can be realized based on parabolic mirrors. This is equivalent to relocating one of the focal points shown in Fig. 5.14 to an infinite distance from the former semi-minor axis. The resulting parabolic mirrors are arranged in a nested fashion, such that each neutron belonging to the incident parallel beam is focused onto the focal point, as illustrated in Fig. 5.17. Designed for a parallel beam, the distance from the optical axis at the exit of the n^{th} mirror, $r_n(z_e)$, must equal the distance from the optical axis at the entrance of the adjacent inner $(n + 1)^{\text{th}}$ mirror, $r_{n+1}(z_s)$. As visualized by the blue and green neutron trajectories, this procedure ensures that every neutron of a parallel beam is focused on the common focal point. Similarly, the device can transform all neutrons emerging from the focal point into a zero divergence beam. Determining the parabolic shapes with coinciding focal points follows a methodology similar to the one discussed for the elliptic NMO in the appendix G. Neutrons belonging to the innermost part of the parallel beam do not participate in the reflection process, which leads to a divergence hole $2\Delta\alpha$ at the focal point analogous to the one discussed for the elliptic NMO.

Whereas elliptic NMOs excel at conserving the beam phase space during transport from one focal point to another, **parabolic focusing nested mirror optics** (pfNMO) perform a different task in that they transform a low-divergence, spread out beam into a high-divergence focused

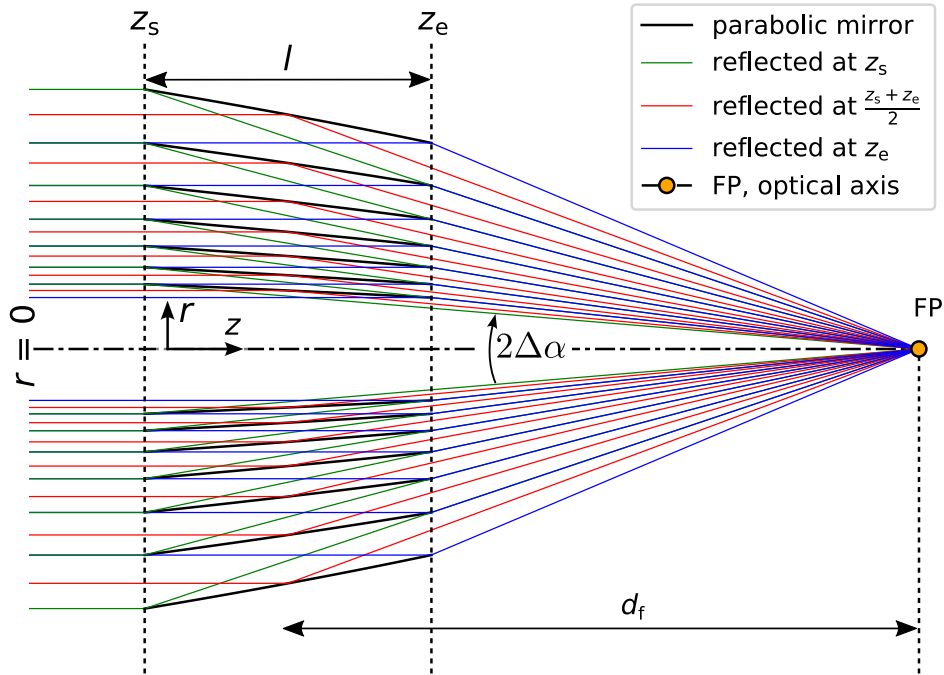


Figure 5.17: Schematics of a parabolic NMO including shape-determining neutron trajectories being reflected at z_s (green) or z_e (blue). The common focal point of all parabolic mirrors is shown in orange.

beam while preserving the phase space density. A second set of [parabolic de-focusing nested mirror optics](#) (pdNMO) can then reverse this transformation, recovering the original phase space of the beam with minor losses.

Supported by McStas simulations, we will now discuss the key differences between a [pfNMO](#) and a long parabolic *trumpet* [175], which is commonly utilized for focusing a beam onto a sample position. The presented arguments are equally valid for the inverse case, in which either device transforms a compact source into a low-divergence beam.

The short length of the parabolic mirrors $l \ll f$ ensures that all neutrons interact with the [pfNMO](#) at a similar distance far away from the focal point. This distance, d_f , geometrically determines the relationship between the incident divergence before the [pfNMO](#), α_i , and the distance from the optical axis the neutron possesses at the focal point, r_f . The relationship is given by

$$r_f \approx d_f \alpha_i. \quad (5.18)$$

Following Eq. (5.18), a [pfNMO](#) provides the capability to adjust the beam width at its focal point by manipulating the divergence of the incident neutron beam. Matching this width to the extent of the sample potentially improves the signal-to-noise ratio. Conversely, the points of reflection in a parabolic trumpet occur within a broader range of distances to the focal point, leading to a less straightforward relationship between the incoming divergence and the size of the focused beam.

Fig. 5.18 provides additional insights into the focusing properties of both devices for beams with different incoming divergences, α_i , as indicated above each column. The color plots in the first row illustrate the simulated intensity distributions at the focal point of a long

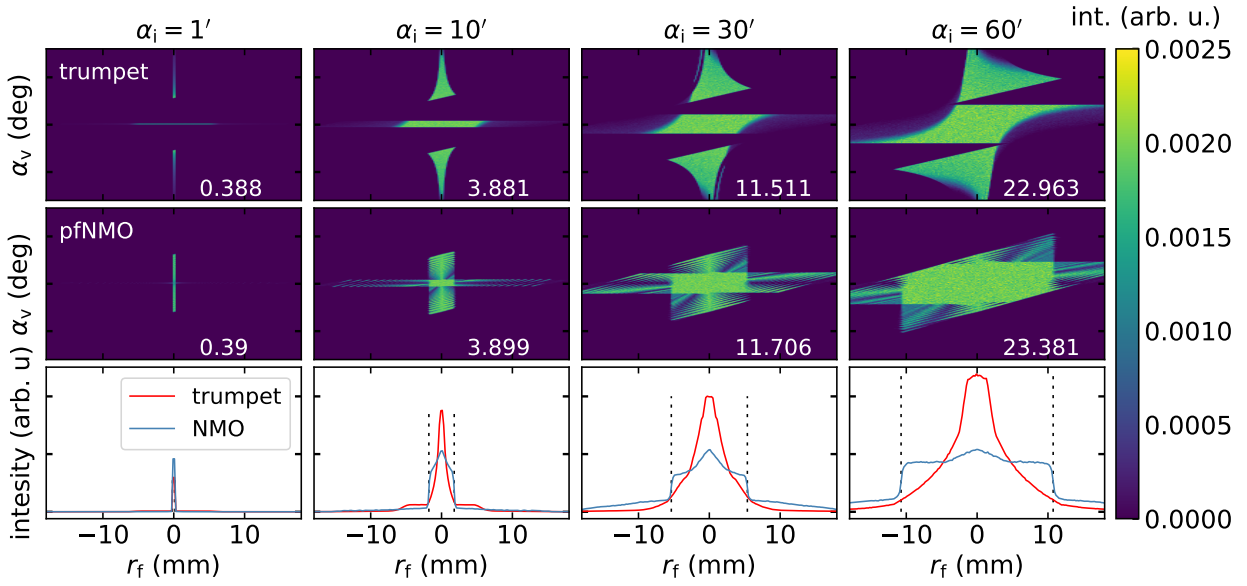


Figure 5.18: Beam characteristics at the focal point of a vertically focusing parabolic trumpet (first row) and of a parabolic **NMO** (second row) illuminated with various incident divergences, α_i , indicated above each column. Accounting for the simulated geometries, only the vertical dimension is considered. The color plots display the intensity of the neutron beam at the focal point of the devices as a function of the vertical divergence, α_v , and the vertical offset from the optical axis, r_f . The data illustrated in the color plots was integrated over all values of α_v , resulting in spatial intensity distributions shown in the third row. Here, the broken black lines indicate the width of the beam according to Eq. (5.18), which is in excellent agreement with the peak shape provided by the **pfNMO**.

For all simulations, the focusing devices were illuminated by a neutron beam with uniform and constant brilliance. Consequently, the total number of neutrons arriving at the focal point indicated in white is proportional to the incident divergence, α_i . The incident beam featured a wavelength of $\lambda = 4.9(5) \text{ \AA}$ and a constant height of $h = 32 \text{ mm}$. While the horizontal divergence was kept at zero (neutrons are only focused vertically), the incident vertical divergence was systematically adjusted to various values, α_i . The simulated **pfNMO** consisted of 40 mirrors characterized by the following parameters $f = 0.675 \text{ m}$, $b_0 = 0.016 \text{ m}$, $m = 4$, $R_e = 82\%$, $l = 0.12 \text{ m}$. f , l and b_0 are measured from the entrance of the **NMO** at $z = 0$, respectively. The simulated parabolic trumpet shared similar characteristics, namely $f = 0.675 \text{ m}$, $b_0 = 0.016 \text{ m}$, $m = 4$, $R_e = 82\%$, and $l = 0.65 \text{ m}$. The influence of gravity was disregarded during all simulations, given the relatively short distances considered.

parabolic trumpet as a function of the vertical distance from the optical axis, r_f , and the vertical divergence, α_v . Three distinct components can be observed, spanning an increasingly large area with increasing α_i . Neutrons being reflected at the upper (lower) reflective surface of the trumpet appear at the lower (upper) island of intensity in the color plot. Neutrons passing the central part of the nozzle without reflection contribute to the central parallelogram. At the end of the trumpet, neutrons are reflected close to the optical axis under angles exceeding θ_c . The reflectivity curve of the $m = 4$ coating results in a reduc-

tion of intensity under large angles, which appears instead as a horizontal extension of the parallelogram around $\alpha_v = 0^\circ$.

In comparison, for all investigated α_i , the parabolic NMO gives rise to a connected, well-defined, and uniform phase space volume, as observed in the second row. The spatial extent of this phase space volume smoothly increases proportionally with α_i . This is highlighted in the third row, highlighting the data of both devices integrated over all values of α_v , corresponding to the spatial intensity distribution at the focal point. The two black, broken vertical lines indicate the calculated width of the beam according to Eq. (5.18), which is in perfect agreement with the simulated peak shape obtained for the pfNMO. As both devices were illuminated by a beam with constant and uniform brilliance, the integrated intensity indicated in white for each panel increases proportionally with α_i .

Apart from offering a more uniform volume of phase space, the distance between the reflective surfaces of the NMO and its focal point enables utilizing an extensive sample environment, which would interfere with a parabolic trumpet.

5.6 Two-Dimensional Nested Mirror Optics

Two approaches are available for two-dimensional imaging or focusing of neutrons using NMOs. Firstly, the geometries shown in Fig. 5.14 or Fig. 5.17 can be rotated around the optical axis to create a toroidal geometry. In this case, the radial coordinate is denoted by r . Secondly, the geometry can be translated into the paper plane, where r represents the Cartesian coordinate oriented perpendicularly to the optical axis and the mirrors. This geometry redirects neutrons in only one dimension, necessitating a second perpendicularly oriented device for two-dimensional redirection. The two devices can be positioned behind each other along the optical axis, with one device occupying the space from $-l/2$ to 0 and the other from 0 to $l/2$, which we call a double-planar geometry. Albeit technically highly challenging, it would be possible to intersect the orthogonal mirrors, creating one common device. Fig. 5.19 illustrates both the toroidal and the double-planar geometries.

A toroidal NMO requires only a single reflection for two-dimensional imaging, thereby reducing transport losses associated with finite supermirror reflectivity. However, the fabrication process of such devices is complex, which limits their range of practical applications. Based on an electrochemical replication technique commonly employed in X-ray grating incidence optics, toroidal Ni-mirrors have been fabricated and investigated successfully [176]. Nevertheless, the application of supermirror coatings to non-planar surfaces is still challenging. Despite some advances in the field [177], as of the current writing, truly toroidal NMOs are still in their infancy. Recent progress has been reported by Wu et al., who investigated a toroidal device consisting of two approximately elliptic mirror shells coated with $m = 2$ supermirror. Each mirror shell was divided axially into four parts and azimuthally into six segments, resulting in a total of 48 segments [178, 179]. In the limit of very short mirrors, $l \ll f$, the coating of flat substrates subsequently bent into a cylindrical shape or a tessellation of small pieces of flat mirrors might allow for a combination of the advantages from toroidal NMOs and supermirror coatings.

The double-planar geometry offers an attractive alternative, which allows the utilization of supermirror coatings with $m \geq 4$. During fabrication, flat silicon substrates are first coated with a supermirror before being pushed into yokes with the corresponding shape-determining

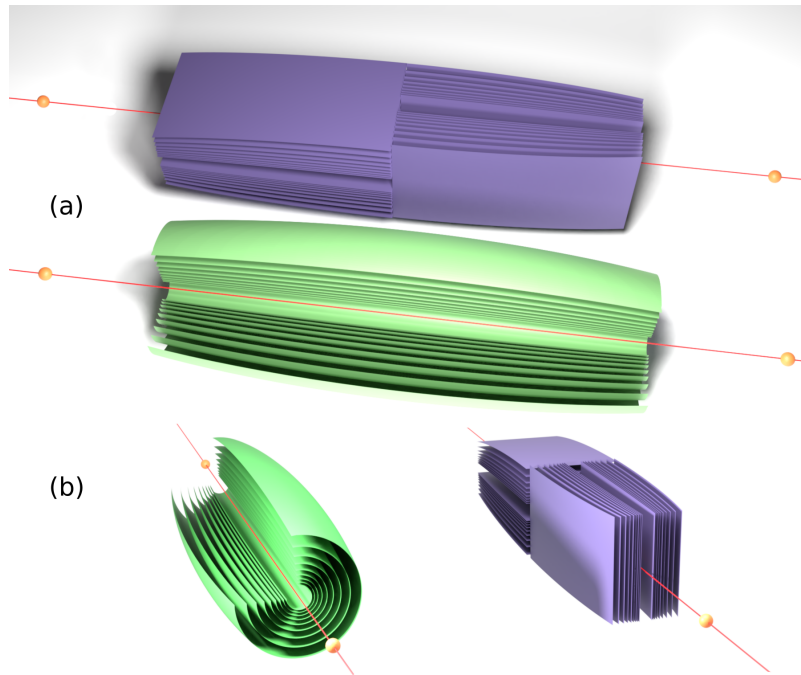


Figure 5.19: Schematics of double-planar (violet) and toroidal (green) elliptic NMOs enabling two-dimensional focusing of neutrons. (a) and (b) show views along different angles to the optical axis. For illustration, the eccentricity of the elliptic shapes is greatly exaggerated, and a quarter of the toroidal NMO was made transparent. Figures are reproduced from Herb et al. [19].

grooves. Besides their simpler realization, double planar systems geometrically fit today's rectangular guide shapes and allow for simple beam polarization. Furthermore, separating the beam transport into two reflections in orthogonal dimensions helps mitigate the influence of gravity, as will be discussed in more detail later on. Additionally, the separation of dimensions allows for the independent control of the phase space of the transported neutrons in both dimensions orthogonal to the optical axis.

The overall ease of fabrication finally supported the decision to realize a prototype of a double-planar system to investigate its properties and compare them to simulation and theory.

5.7 McStas Simulations of Nested Mirror Optics

In contrast to the simplified calculations presented earlier, the real-world performance of elliptic or parabolic NMOs is influenced by many subtle effects that are not easily accounted for analytically. To assess the overall performance of NMOs and compare it to currently employed neutron optical solutions, we conducted Monte Carlo simulations using McStas [172]. To obtain results that closely align with realistic conditions, the simulations should take into account various effects, including the *true* elliptic or parabolic geometry of the substrates, mirrors coated on one or both sides with supermirror including channeling effects within these mirrors, realistic supermirror reflectivity profiles, double reflections and neutron

leakage between adjacent mirrors, and absorption, refraction, and total reflection governed by the silicon substrates onto which the coatings are applied.

A new simulation component was developed for parabolic and elliptic NMOs, based on code designed initially by Giacomo Resta in the context of [176]. This novel component enables the modeling of double-planar devices and accounts for all the effects mentioned above. Furthermore, the influence of gravity can be closely approximated. Starting from McStas version 3.4, this *FlatEllipse_finite_mirror* component is now accessible to all users as a contributed component [180].

We present a brief overview of the developed simulation component, emphasizing the adjustable parameters for the interested reader. Addressing a broad spectrum of potential users, the simulation component enables the determination of the geometry of each mirror constituting the assembly from a single point on the outermost mirror surface, the position of the two focal points, and the intended length of the individual mirrors, following the recipe provided in the appendix G. Suppose more intricate control over the characteristics of each mirror is required. In that case, one can also provide a file containing shape-determining points of the individual mirrors (a combination of z and r for each mirror).

Fig. 5.20 depicts the simulation geometry in its local coordinate system. The z - and

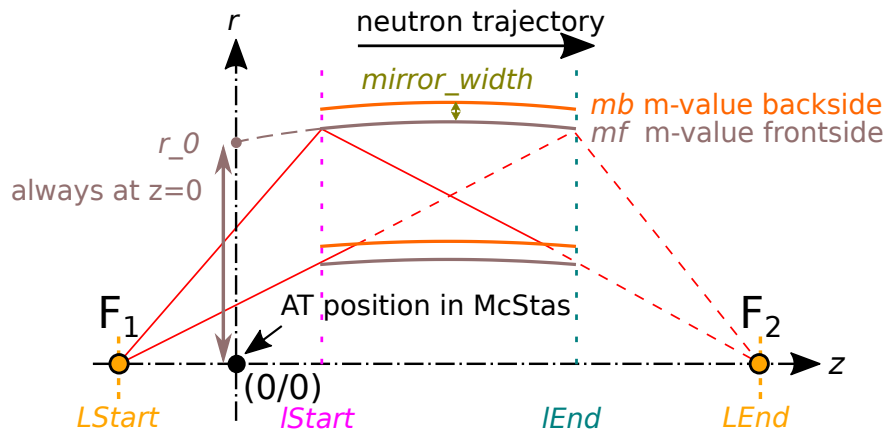


Figure 5.20: Schematics of the simulation geometry of a planar NMO including extreme neutron trajectories (red). The geometry-defining parameters of the simulation are denoted in italics, with the remaining ones being discussed in the text.

r -coordinates denote the directions parallel and perpendicular to the optical axis, with r indicating the horizontal direction, denoted by x in McStas. The outermost mirror surface is defined by the z -coordinates of the two focal points, $LStart$ and $LEnd$, and the r -coordinate at $z = 0$, r_0 . Subsequent mirror shapes can be automatically computed by considering the z -coordinates of the entrance and the exit of the NMO, $lStart$ and $lEnd$, and the number of mirrors, $nummirror$. Reflective surfaces are always generated in pairs on both sides of the optical axis (not depicted in Fig. 5.20).

A finite substrate thickness is accounted for if one chooses $mirror_width > 0$. In this case, the m -values of the coatings applied to the inner and outer sides of the mirrors can be chosen individually, mf , mb . A value of 0 corresponds to all neutrons passing the surface (unless the silicon substrate totally reflects them), and an unrealistically high value of $m > 10$

results in ideal reflectivity. For other m -values, a realistic supermirror profile is computed, see Fig. 5.4. Additionally, one can allow or disallow reflections from the convex outer side of a mirror by setting the *doubleReflections* parameter to either 1 or 0 respectively. The width of the mirror blades along a lateral direction perpendicular to both the optical axis and the normal vector of the mirror surface is determined by *mirror_sidelength*. All of the parameters mentioned above are specified in units of meters where applicable. If it is necessary to configure a geometry that reflects neutrons vertically, it is advisable to rotate the entire component within McStas using the ROTATED keyword.

To approximate parabolic geometries, one of the focal points can be relocated to a great distance from the reflective surfaces. When selecting the position of this focal point, using an excessively distant location can introduce numerical uncertainties, while positioning it too closely may lead to geometric errors. Based on prior tests, a z -value of $LStart = \pm 5000$ m has been deemed reasonable. It should be noted that the insertion point (AT) in the McStas .instr file must be located between those of the two adjacent geometries.

6. Characterization of Nested Mirror Optics Prototypes

The upcoming chapter will provide a detailed account of the investigations performed on all elliptic and parabolic **NMO** prototypes. On the one hand, we will focus on determining the efficiency of transport through an elliptic **NMO**, with the measurements conducted at MIRA-2 utilizing a spatially resolving CASCADE detector. On the other hand, we report on examining the peak shape of beams transported by the elliptic and parabolic **NMOs**, utilizing neutron imaging techniques at BOA.

6.1 Investigation of the Polarizing Elliptic NMO at MIRA-2

Here, we report on the investigation of the first prototype of a polarizing planar elliptic **NMO** at MIRA-2 using a CASCADE detector. Due to the fast count rate of the detector coupled with a rather coarse resolution, emphasis was put on determining the efficiency of transport of the elliptic **NMO**. Some of the here presented results have already been published in the work of Herb et al. [19], serving as a template for the present section.

The investigated **NMO** is a planar, elliptic system designed for horizontal focusing. It consists of mono-crystalline silicon substrates coated with polarizing FeSi supermirror, $m = 4.1$, $R_e = 82\%$. The mirrors were inserted into shape-determining elliptic grooves in iron yokes, as shown in Fig. 6.1. As the mirrors were salvaged from a previous bender assembly, the

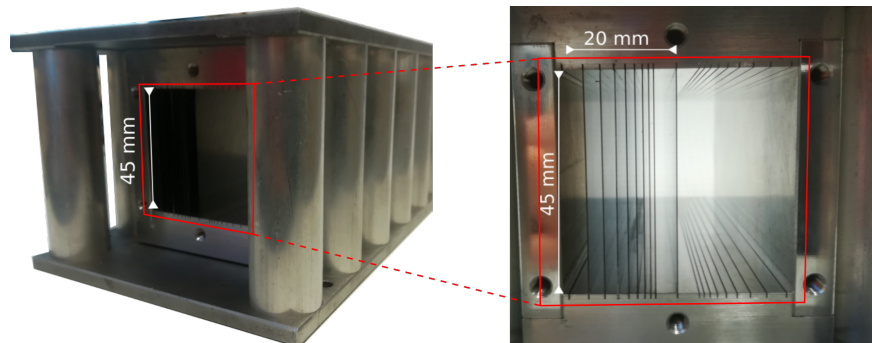


Figure 6.1: Pictures of the polarizing elliptic **NMO** prototype. The device contains eight elliptic mirror blades, with a ninth central mirror aiding the alignment process. Columns on either side of the mirrors house the permanent magnets supplying the field to saturate the polarizing FeSi supermirror coatings. Figure is reproduced from the work of Herb et al. [19].

supermirror coating was applied on both sides of the substrates, entailing effects discussed in more detail in section 6.1.5. All mirror substrates share the same geometry featuring a length, $l = 120$ mm, a thickness, $d_{\text{sub}} = 0.15$ mm, and a height of 45 mm. No absorbing sublayers were applied during the coating process, such that neutrons exceeding the polarization-dependent critical angle θ_c^\pm are transmitted through the mirror with high probability.

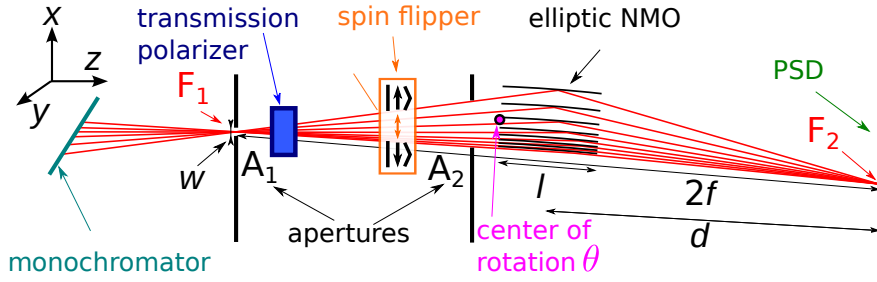


Figure 6.2: Experimental setup at the instrument MIRA-2 at FRM II (top-down view). The geometry of the unpolarized beam was defined by using the apertures A_1 and A_2 . The NMO images A_1 onto the position-sensitive detector. A transmission polarizer and a spin flipper were installed to account for a polarized beam, along with suitable magnetic fields to guide the neutron polarization between the polarizer and the NMO. Figure is reproduced from Herb et al. [19].

The shape of the elliptic grooves was calculated according to the method discussed in appendix G, with the elliptic mirrors being positioned symmetrically around the semi-minor axes of the ellipses, which possess a common focal length of $f = 0.6$ m. Corresponding to the critical angle of a $\lambda = 5$ Å neutron, the outermost ellipse possesses a semi-minor axis of $b_0 = 20.76$ mm. Due to the limited beam divergence provided by the monochromator of MIRA-2, where the initial experiments were conducted, mirrors were inserted into the device only on one side of the optical axis. The shape-determining ellipses had semi-minor axes ranging between $4 \text{ mm} \leq b_n \leq 17 \text{ mm}$ (compare Fig. 6.1). The casing was placed between two iron plates that are connected and magnetized by columns of NdFeB magnets, forming a yoke with a field of ≈ 50 mT, sufficient to saturate the FeSi supermirrors.

6.1.1 Measurement Geometry at MIRA-2

The prototype of the polarizing elliptic system with unit magnification was investigated using the multi-purpose three-axis spectrometer MIRA-2 at the Maier-Leibnitz-Zentrum (MLZ, FRM II) [59]. The primary goal of this investigation was to assess the quality of the neutron optical image and the efficiency of neutron transport. Fig. 6.2 illustrates the experimental setup for investigating the polarizing elliptic NMO. The monochromator of MIRA-2 selects and provides neutrons with a wavelength of $\lambda = 4.9$ Å, with $\delta\lambda/\lambda \approx 1\%$. The neutron beam was then geometrically defined by two remotely adjustable apertures: A_1 , with width w , defined a virtual neutron source at the first focal point of the NMO, F_1 , which was then imaged onto its second focal point, at F_2 . A second aperture, A_2 , restricts the extent of the beam at the entrance of the NMO to its geometric acceptance. The careful beam preparation allows the definition of the neutron transport efficiency of the NMO as the ratio of two integrated neutron rates: that encompassing the focused beam image and that encompassing all neutrons arriving at the detector with the NMO removed from the setup.

To facilitate the alignment, the NMO was mounted on a rotation table, such that its vertical axis of rotation coincided with the entrance area of the NMO. This configuration ensured that the exposed area of the NMO remained consistent during rotation within the narrow range of angles θ required to scan through the optimum beam focusing. The imaged

intensity distribution at F_2 was determined by utilizing a [position-sensitive detector \(PSD\)](#), positioned at a distance d from the center of the [NMO](#). With a large area of $200 \times 200 \text{ mm}^2$ and a spatial resolution of $2.5(1) \text{ mm}$ ([FWHM](#)) [181], the detector enabled the discrimination of distinct reflected and transmitted beam components and facilitated the alignment process. Additionally, the [PSD](#) was mounted on a motorized linear stage, enabling the variation of the distance d and thereby facilitating the investigation of the imaged intensity distribution at varying distances from the focal point F_2 . To account for the polarizing supermirror coating, the beam could be polarized by a transmission polarizer positioned between A_1 and the [NMO](#). This device consisted of a stack of silicon plates coated with a polarizing FeSi supermirror and a collimator to remove the reflected beam with the unwanted polarization state. Notably, the installation of this transmission polarizer did not alter the trajectory of the transmitted and polarized beam from that previously defined in the setup without polarization. The polarization of the beam incident on the [NMO](#) could be inverted with a flat-coil spin flipper. Several magnetic coils were installed between the polarizer and the [NMO](#), tuned to meet the requirements of the spin flipper and the guide fields. All adjustments aimed for an optimum *flipping ratio*, defined as the ratio of count rates in the focused beam image with the spin flipper switched on and off, respectively. In its final configuration, with a guide field exceeding 2 mT throughout the space between the polarizer and the [NMO](#), we achieved a flipping ratio of 16. This was sufficient for studying the polarization dependence of the various reflected and transmitted beam components after passing through the [NMO](#).

6.1.2 Alignment of the Elliptic NMO

In an initial step towards assessing the general transport properties of the [NMO](#), we determined transport efficiency. To obtain accurate results, proper orientation of the [NMO](#) with respect to the virtual source and the [PSD](#) is crucial. We will briefly discuss the comparatively simple alignment process, which simultaneously represents an advantage of an [NMO](#) compared to contemporary guide systems.

An unpolarized beam was utilized throughout this initial alignment process. The [NMO](#) was positioned in the extension of the virtual source at a distance matching its focal length, $f = 600 \text{ mm}$. To achieve optimum focusing conditions, two parameters were independently varied: the angle of incidence, θ , at which neutrons from the virtual source hit the entrance of the [NMO](#) and the distance between the [PSD](#) and the [NMO](#), d . The widths of the apertures A_1 and A_2 were kept constant throughout these adjustments, with A_1 representing a compact virtual source, $w = 0.5 \text{ mm}$, and A_2 configured to illuminate the entrance of the [NMO](#) ensuring that all neutrons interact with at least one mirror.

To assess the quality of focusing and adjust the alignment of the [NMO](#) accordingly, we monitored the peak amplitude of the vertically integrated detector data. Exemplary data are presented in Fig. 6.3. Fitting a Gaussian-type function to the vertically integrated detector data allows determining its horizontal position, x_0 , amplitude, A , width, σ , and the constant background, C . The fitted function is given by:

$$I(x) = A \exp\left(-\frac{(x - x_0)^2}{2\sigma}\right) + C. \quad (6.1)$$

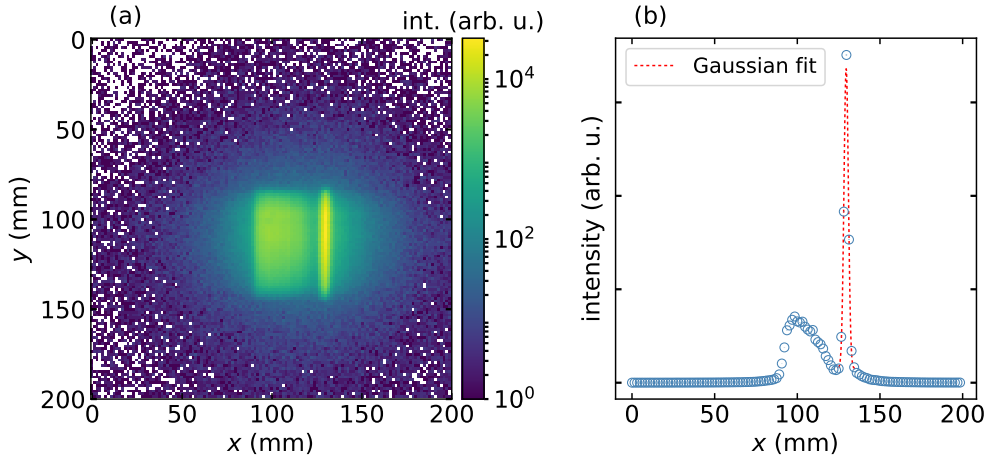


Figure 6.3: Intensity distribution at F₂ when imaging a virtual source with width, $w = 0.5$ mm, utilizing the polarizing elliptic NMO. Panel (a) illustrates the detector data on a logarithmic scale (a), whereas the vertically integrated data on a linear scale is depicted in panel (b). The NMO and the detector were optimally oriented for an unpolarized beam with $\theta = 0$ and $d = 600$ mm. Both images show a sharp peak of correctly reflected *spin-up* neutrons to the right of an extended region of neutrons leaking through the optic due to their *spin-down*-state or for geometric reasons. The statistical uncertainties of the raw data are confined within the markers. The Gaussian fit (red) is in good agreement with the data. The Figure is reproduced from the work of Herb et al. [19].

The contour map in Fig. 6.4 (a) provides an overview of the obtained normalized values of A , with red dots indicating the specific combinations of d and θ at which the data was obtained. Cuts through this map at constant values of d and θ are depicted in Fig. 6.4 (b) and (c), respectively. The offset of θ was adjusted such that the global maximum of A occurs at $\theta = 0^\circ$. Using this convention, the intensity peaks in a small region around $\theta = 0^\circ$ and drops significantly already at deviations of $|\theta| = 0.25^\circ$. In comparison, the influence of d seems less important. At $\theta = 0$ mm, the amplitude plateaus within a range of d -values, $570 \text{ mm} \leq d \leq 630 \text{ mm}$, which is consistent with performed Monte-Carlo simulations (not shown).

Following this initial alignment of the elliptic NMO, the components for beam polarization were introduced into the setup as described in section 6.1.1. The results from a subsequent repetition of the alignment procedure are shown in Fig. 6.5. Under consideration of the respective investigated ranges of d -values, the data found in Fig. 6.4 and Fig. 6.5 are qualitatively similar. Besides introducing the equipment required for neutron polarization, we slightly reduced the vertical extent of A₂ to maximize the flipping ratio, which could have changed the characteristics of the reflected neutron beam slightly. The rather coarse resolution of the detector prevented the tracking of those more subtle alterations.

Following the alignment, we investigated the imaging properties of the polarizing elliptic NMO. This investigation focused on quantifying the ratio of neutrons successfully transported from F₁ to F₂. Additionally, we determined the extent to which the peak shape at F₁ is preserved as the beam is transported through the NMO.

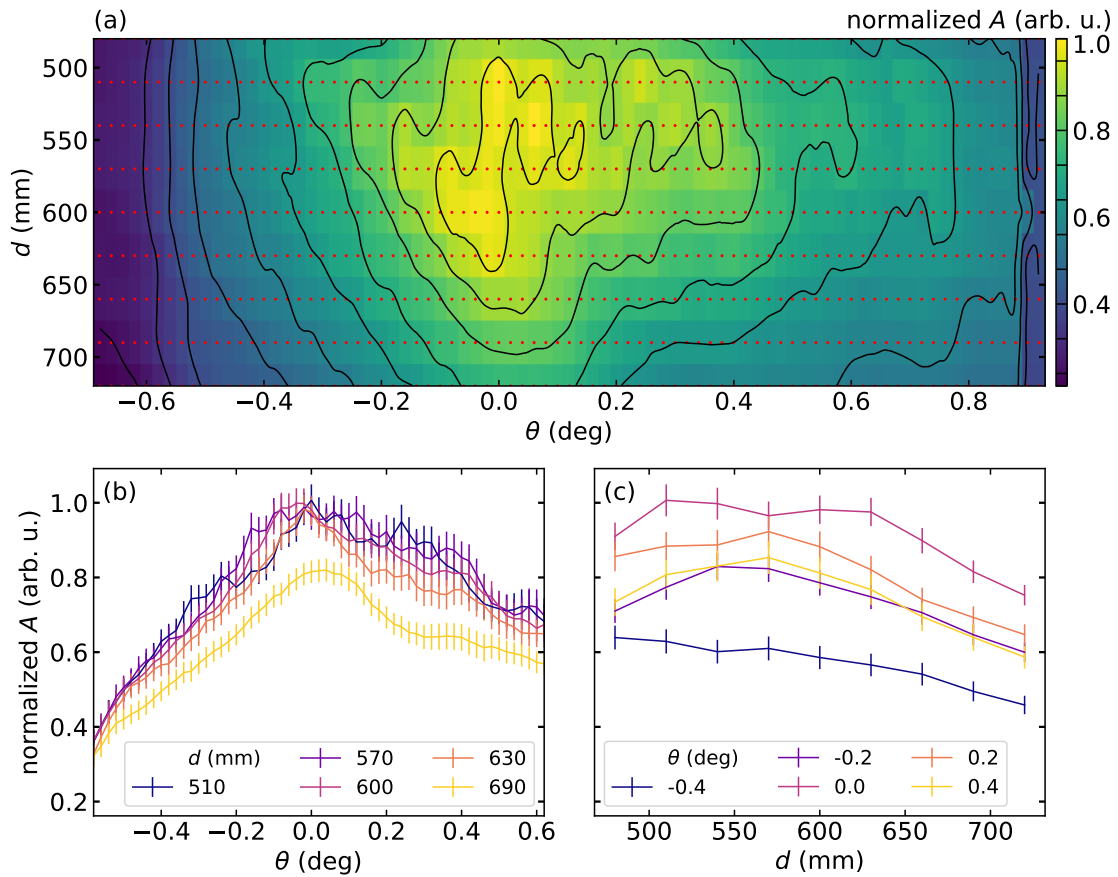


Figure 6.4: (a) Contour plot of the imaged amplitudes, A , for the unpolarized beam setup. Data were acquired only for the combinations of θ and d indicated by red dots. The observed maximum around $\theta = 0^\circ$ is broadened significantly due to the limited resolution of the detector. Panels (b) and (c) depict cuts through the contour map at specific values of d and θ , respectively. The error bars include, apart from statistical fluctuations, a fitting error of the non-Gaussian peak shape of both, the intensity of the focused neutrons and the point spread function of the employed PSD [181]. Figure is reproduced from Herb et al. [19].

6.1.3 Efficiency of Transport

After setting the values of θ and d to those determined for optimum focusing, as presented in Fig. 6.5, we proceeded to investigate the performance of the NMO at various widths of the virtual source, w . To this end, we systematically varied the width of A_1 within a range of $0.25 \text{ mm} \leq w \leq 6 \text{ mm}$. Conversely, the width of the beam-defining aperture A_2 was kept constant at 8 mm, which limited the illumination of the NMO to five out of the available eight mirrors. The obtained normalized detector images are displayed in Fig. 6.6, with w indicated on the top left of each panel. All images exhibit a similar structure, characterized by a sharp peak representing focused neutrons on the right, adjacent to a diffuse region of intensity. This region is attributed to neutrons passing the optic either due to geometric losses (leakage and double reflections) or incorrect spin orientation. As w increases, both the width of the reflected beam and the number of leaking neutrons increase, in agreement

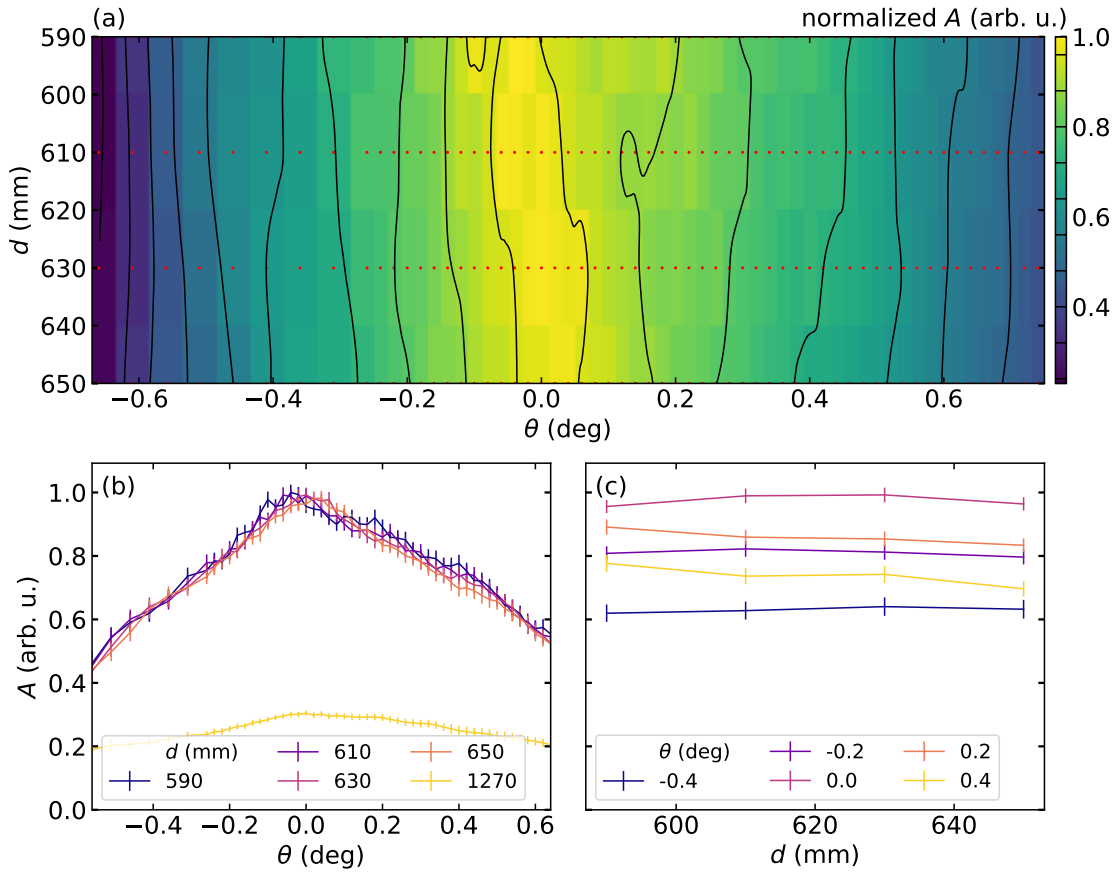


Figure 6.5: (a) Contour plot of the amplitudes A for the polarized beam setup. The distribution with a distinct maximum at $\theta = 0^\circ$ is qualitatively equivalent to the results obtained for the unpolarized setup (compare Fig. 6.4). Note the narrower range of d -values that is presented here. Within uncertainties, the amplitudes for detector distances between $590 \text{ mm} \leq d \leq 650 \text{ mm}$ are indistinguishable. (b) and (c) show cuts through the contour map at fixed values of d and θ , respectively. Figure is reproduced from Herb et al. [19].

with Eq. (5.16). For each w , the total rate of neutrons arriving within a defined window, characterized by a width, $w_{\text{int}} = 9 \text{ mm}$, and a height, $h_{\text{int}} = 62.5 \text{ mm}$, delineated in red in Fig. 6.6, is represented by I_{F_2} . A second rate, I_{A_2} , was determined by counting all neutrons hitting the detector when the elliptic NMO was entirely removed from the setup, with all other parameters kept constant. This rate corresponds to all neutrons passing A_2 and illuminating the mirrors. The ratio of these two quantities defines the efficiency of transport, expressed as:

$$Q(w, w_{\text{int}}) \equiv \frac{I_{F_2}(w, w_{\text{int}})}{I_{A_2}(w)}. \quad (6.2)$$

The obtained values of Q , as presented in Fig. 6.6, saturate around $Q \approx 73\%$ for small w , and exhibit a slight decrease at the largest width investigated, with $Q(6 \text{ mm}, 9 \text{ mm}) = 68\%$. While the overall trend aligns with the expectation that an increasing w results in more neutrons either remaining unreflected or undergoing double reflection between adjacent mirrors

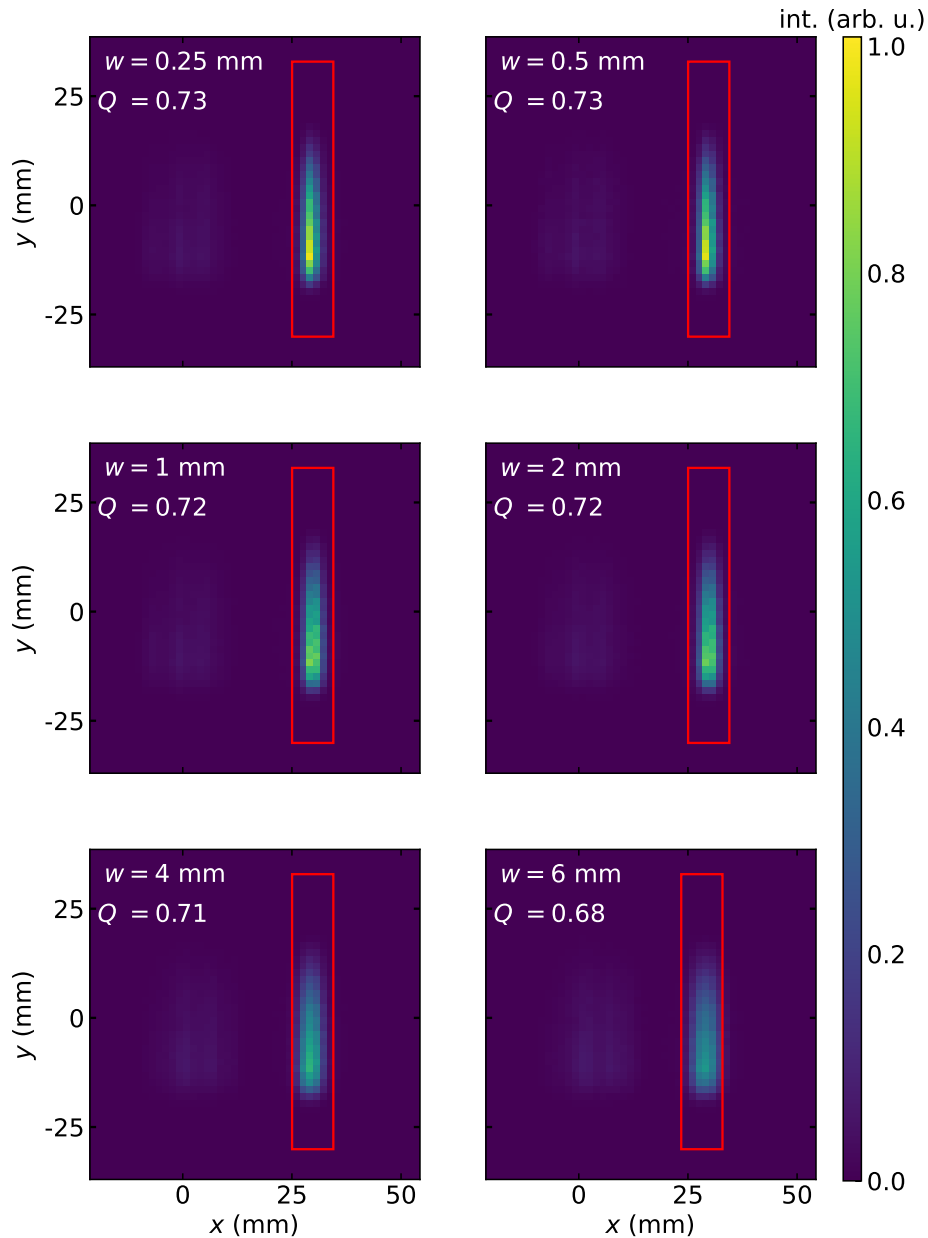


Figure 6.6: Measured neutron intensity distributions at F_2 after transport through the elliptic NMO for various widths, w , of the virtual source at F_1 . The data was utilized for the determination of the experimental figure of merit $Q(w, w_{\text{int}})$, as defined in Eq. (6.2). The area of integration, characterized by a width, $w_{\text{int}} = 9$ mm, and height, $h = 62.5$ mm, which encompasses I_{F_2} is outlined by a red rectangle. Neutrons that bypass the NMO can be faintly discerned in a diffuse region to the left of the prominent peak of focused neutrons. The transport efficiencies are approximately $Q \approx 72\%$ for most values of w , with a slight decline observed at the largest width, as anticipated due to the increased geometric losses described by Eq. (5.17). All images are normalized to their total intensity. Figure is reproduced from Herb et al. [19].

(compare Eq. (5.17)), the current scenario is nuanced due to the double-side coated substrates. Further details and the effects on transport efficiency are discussed in section 6.1.5.

It should be noted that a critical quantity for the characterization of neutron optic systems is the *brilliance transfer*, which quantifies the efficiency of neutron transport by comparing the brilliance of a neutron beam before and after an optical device, respectively. In practical applications, the brilliance is typically averaged over a finite volume of phase space that is the same for both the source and the target, with the ratio between these averages defining the brilliance transfer. One may then define the integrated brilliance transfer for a NMO by choosing equal areas at the first and second focal point and comparing the neutron flux at both positions within the angular and wavelength acceptance of the NMO.

For the current configuration of an elliptic NMO focusing in only one dimension, we define the partly-integrated brilliance transfer similarly to the efficiency of transfer, Q , with an integration width equal to the width of the virtual source,

$$B(w) \equiv Q(w, w). \quad (6.3)$$

The rationale behind considering $w_{\text{int}} \geq w$ for the determination of the transport efficiency was to mitigate the influence of the limited detector resolution $\text{FWHM} = 2.5(1) \text{ mm}$, which hinders the precise determination of the brilliance transfer for small w . For the largest width studied $w = 6 \text{ mm}$, one finds $B(6 \text{ mm}) = 0.62$, in good agreement with the efficiency of transport $Q(6 \text{ mm}, 9 \text{ mm}) = 0.68$. These experimental figures already encompass *real-world*-factors such as neutron losses due to imperfect machining precision, absorption in the Si-wafers and coatings, imperfect polarization, and finite supermirror reflectivities, ranked in order of significance. Monte-Carlo simulations conducted to disentangle the individual contributions are discussed in greater detail in section 6.1.5.

6.1.4 Preservation of Beam Shape

In addition to maximizing the neutron transport efficiency, maintaining the spatial distribution of the neutron beam during transport is a distinctive characteristic of an elliptic NMO. To explore the relationship between the width of the focused beam and the primary beam at F_1 , w , we evaluated the detector data displayed in Fig. 6.6. The data was initially vertically integrated and then interpolated using a cubic spline. The **FWHM** of the peak was subsequently determined based on that interpolation. The determined **FWHM** values were in good agreement with their respective w for large values of $w \geq 4 \text{ mm}$ (red circles). However, the physical resolution of the PSD limited the investigation of smaller virtual sources. To overcome this limitation, we conducted a subsequent, similar experiment at the BOA imaging beamline (see section 6.2 for more details). In this experiment, neutrons were detected using a standard scintillator plate with a resolution of $\text{FWHM} = 100 \mu\text{m}$. The obtained **FWHM** values are indicated by blue circles in Fig. 6.7 and plotted together with McStas simulations of extremely high resolution (black squares). For very small values of w , the imaging capabilities of the elliptic NMO investigated are potentially limited by the waviness of the supermirror coating, estimated to be $\eta = 2 \times 10^{-4} \text{ rad}$. The resulting **FWHM** can be approximated by $\text{FWHM}_{\text{wav}} = 2 \times 2.355 \times 0.6 \text{ m} \times 2 \times 10^{-4} \text{ rad} = 0.57 \text{ mm}^{(1)}$, which

⁽¹⁾The factor $2\sqrt{2\ln(2)} = 2.355$ describes the relationship between the width of the Gaussian distribution used to describe the waviness and the **FWHM** of the same distribution. 0.6 m denotes the distance between

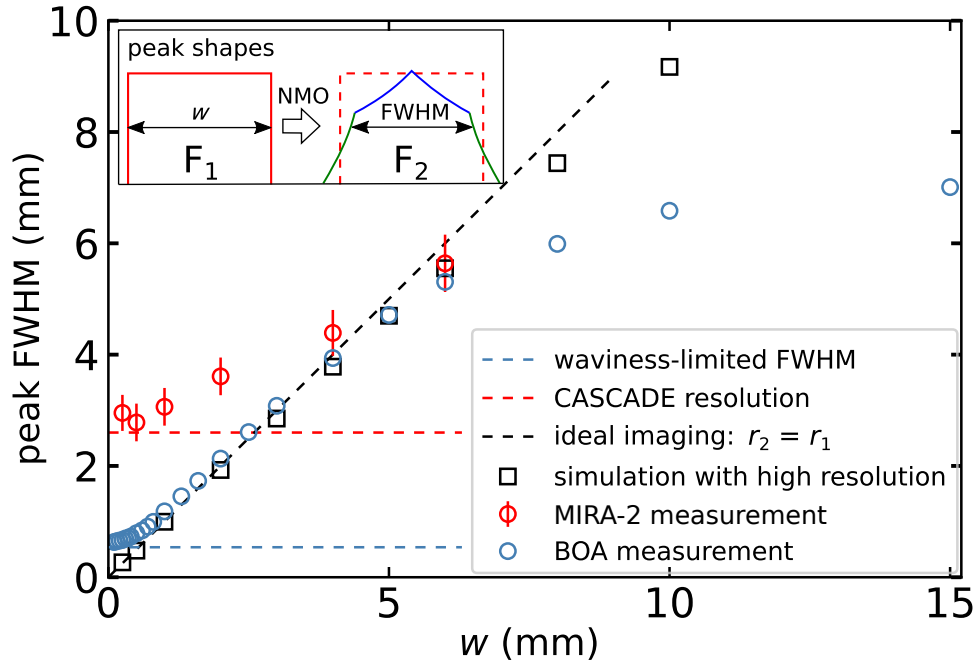


Figure 6.7: Dependence of the horizontal **FWHM** at F_2 on the width, w , of the primary rectangular beam at F_1 . The black squares represent the results of McStas simulation, which are in good agreement with ideal one-to-one imaging ($r_2 = r_1$, represented by the black broken line). Conversely, the **FWHM** values measured at MIRA-2 (red circles) were limited by the finite resolution of the detector of 2.5(1) mm, as indicated by the horizontal, red broken line. In contrast, the data obtained at BOA (blue circles) agree with unit magnification from very small values of $w \geq 0.5$ mm up to $w = 6$ mm, beyond which they start to deviate from the simulated values. The inset illustrates the effect of geometric aberrations on the **FWHM** of the focused beam as described in the text.

is in good agreement with the asymptotic behavior of the **FWHMs** obtained at BOA for $w \leq 0.5$ mm.

For widths exceeding the waviness limit, the data for $w \leq 6$ mm aligns well with the anticipated unit magnification. A minor deviation, consistent with the high-resolution simulation, is observed for $w \geq 6$ mm. This slight discrepancy between the simulated **FWHM** and w is a result of geometric aberrations in (short) elliptic guides, as discussed earlier (Eq. (5.8) and Fig. 5.6). Neutrons reflected in the second half of the ellipse produce a triangular feature on top of the initial rectangular peak shape (shown in blue in the inset in Fig. 6.7), while neutrons reflected in the first half of the ellipse smear out the flanks of the peak shape (green). These two effects work together to reduce the **FWHM** compared to the width at F_1 .

In comparison to the simulation, where this effect becomes significant only for $w \geq 10$ mm, the agreement between the **FWHM** and w breaks down much earlier in the measured data. This deviation is mainly attributed to the illumination of the virtual source using a parabolic **NMO**, which provides a beam of limited size depending on the distance from the focal point, as discussed in section 6.2.3.3.

the reflective surfaces and F_2 .

6.1.5 Comparison to Simulations

Supporting the interpretation of the experimental findings, we conducted Monte-Carlo simulations using the McStas software package [172], as detailed in section 5.7. The simulated setup replicates the experimental geometry, incorporating mirrors with their geometry and reflectivity matching their real double-side coated counterparts. We obtain a reasonable agreement between the simulated and experimentally obtained transport efficiencies, as listed in table 6.1. The plateau of Q observed for $w \leq 2$ mm is effectively replicated in

w (mm)	0.25	0.5	1	2	4	6
Q_{exp}	0.73	0.73	0.72	0.72	0.71	0.68
Q_{sim}	0.82	0.81	0.81	0.80	0.77	0.73

Table 6.1: Measured and simulated efficiencies of transport, Q . The simulation accurately replicates the experimentally observed plateau for widths $w \leq 2$ mm. The generally higher values of Q_{sim} are mainly attributed to the assumption of ideal polarizing components in the simulation.

the simulation. The minor drop in intensity for increasing w appears less pronounced in the measured data, which can be attributed to the finite resolution of the CASCADE detector. A significant portion of the remaining quantitative disparity can be attributed to neglecting polarization-associated effects in the simulation. These effects were not accounted for due to the limited knowledge of the individual efficiencies of the polarizer, the spin flipper, and the NMO. Assuming that the polarizer provides a beam with a polarization of 98 % [59], the measured flipping ratio of 16 corresponds to a polarization of 90 % after the NMO. This would be sufficient to account for the observed difference between the measured and simulated values of Q in table 6.1. We expect the finite mirror waviness to have a negligible effect on the obtained values for Q_{exp} . Even if we generously assuming a waviness of $\eta = 4 \times 10^{-4}$ rad, the displacement of a reflected neutron at F_2 would amount to $2.355 \times 2\eta \cdot 0.6 \text{ m} = 1.1 \text{ mm}$, which is small compared to the FWHM of the point-spread-function of the detector of 2.56 mm.

A comparison of both the experimentally obtained and the simulated data to the anticipated geometric losses of an NMO, as calculated in Eq. (5.17), is presented in Fig. 6.8. Employing the approximation of the geometric losses in an NMO derived in Eq. (5.17), $R_{\text{loss}} \approx \frac{w}{4b}$, we can express the experimentally obtained Q -values by

$$Q = Q_0 \left(1 - \frac{w}{4b}\right). \quad (6.4)$$

Here, the factor Q_0 accommodates loss mechanisms primarily independent of the neutron trajectory, instead encompassing aspects like finite supermirror reflectivity and polarization-related losses. In an ideal scenario, where mirrors exhibit perfect reflectivity, the beam is fully polarized, and there is no waviness; this value is expected to be $Q_0 = 1$. Fitting Eq. (6.4) to both the simulated and measured transport efficiencies displayed in Fig. 6.8 enables the extraction of the corresponding values for b , which govern the reduction of the Q -values as w increases. The b -value returned from each fit represents an average of all semi-minor axes

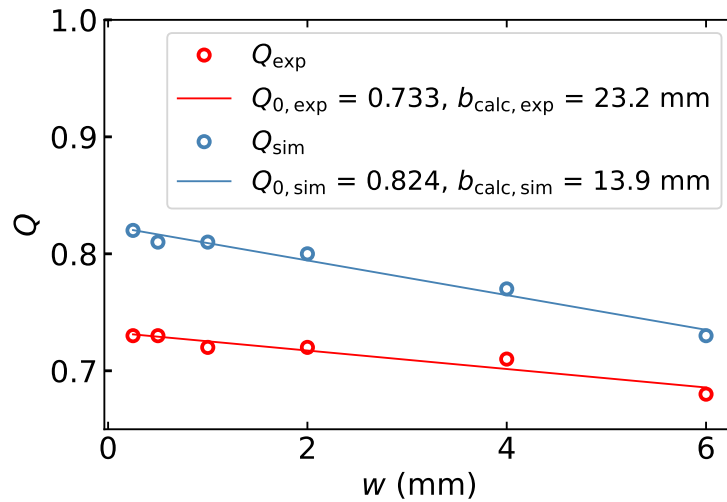


Figure 6.8: Efficiencies of transport, Q , for various widths of the virtual source, w , as obtained experimentally at MIRA-2 and from Monte Carlo simulations. A linear fit to the data reasonably agrees with the loss ratio derived in Eq. (5.17).

of the **NMO**, which can then be compared to the nominal geometry. For the measured and the simulated data, the obtained values are $b_{\text{calc, exp}} = 23(3)$ mm and $b_{\text{calc, sim}} = 14(1)$ mm, respectively. While the value obtained from the simulation is in good agreement with the geometry of the elliptic **NMO**, with semi-minor axes ranging between $9 \text{ mm} \leq b_n \leq 17 \text{ mm}$, the large value of $b_{\text{calc, exp}}$ suggests that additional effects are influencing the slope of the measured data. Potentially, a minor lateral misalignment of the **NMO** during the experiment induced geometric losses even at $w = 0$, thereby lessening the impact of increasing w on the efficiency of transport.

In addition to simulating the actual experimental geometry, we conducted additional simulations to explore the impact of the substrate thickness, d_{sub} , and the supermirror reflectivity on the transport efficiency, Q . These simulations maintained the experimental geometry, modeling a double-side coated **NMO** illuminated by a neutron beam with a wavelength of $\lambda = 4.9 \text{ \AA}$ and a wavelength spread of $\delta\lambda/\lambda = 0.1$.

Table 6.2 summarizes the impact of d_{sub} and w on the transport efficiency. Two sets of efficiencies were obtained: Q_{ideal} (left column), utilizing an ideal reflectivity curve, and Q_{real} (right column), which used the measured reflectivity curve of an $m = 4.1$, $R_e = 82\%$ supermirror. The relative drop in intensity $(Q_{\text{real}} - Q_{\text{ideal}})/Q_{\text{ideal}} \approx 5\%$ remains below the 20% reduction associated with the edge reflectivity of the $m = 4.1$ supermirrors, which is expected given the small angles of reflection and the long wavelength of the beam with $\lambda = 4.9 \text{ \AA}$. The gradual decrease in Q with increasing d_{sub} is attributed to channeling and double reflections, as illustrated in Fig. 6.9. Additionally, the decrease in Q with increasing w is due to increased geometric losses.

Additionally, we compared the transport efficiency of elliptic **NMOs**, examining cases of both single-side and double-side coatings, ($m = 4.1$, $R_e = 82\%$). One might assume that single-side coated mirrors would be more suitable for **NMOs**, since the neutron transport relies on single reflections at well-defined distances from the optical axis. However, for mirrors

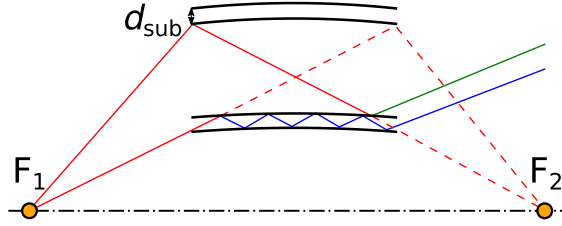


Figure 6.9: Illustration of channeling (blue trajectory) and double reflections (green trajectory) for selected initial neutron trajectories (red) in an NMO equipped with double-side coated mirrors (black). As the affected neutrons miss the second focal point, the efficiency of transport, Q , is reduced. Dashed red lines depict the ideal, unperturbed neutron trajectories for very thin mirrors. Figure is reproduced from Herb et al. [19]

w (mm)	$d_{\text{sub}} = 0$ mm	$d_{\text{sub}} = 0.15$ mm	$d_{\text{sub}} = 0.30$ mm
0.25	0.99 0.93	0.85 0.82	0.70 0.69
0.5	0.99 0.92	0.85 0.81	0.70 0.69
1	0.97 0.91	0.85 0.81	0.70 0.69
2	0.94 0.88	0.84 0.80	0.69 0.67
4	0.89 0.83	0.81 0.77	0.69 0.67
6	0.84 0.79	0.77 0.73	0.67 0.66

Table 6.2: Dependence of the efficiencies of transport, Q ($w = 6$ mm, $w_{\text{int}} = 9$ mm), on the Si-substrate thickness, d_{sub} , and the width of the virtual source, w . The first and the second entries in each cell correspond to results obtained for ideally reflecting mirrors and for a realistic $m = 4.1$ reflectivity profile, ($Q_{\text{ideal}}|Q_{\text{real}}$). The simulations replicated the experimental setup, including aperture A_2 , and the double-side coated mirrors. The bold column corresponds to the data presented in table 6.1. Table is reproduced from Herb et al. [19].

with finite reflectivity, double-side coated wafers can potentially enhance NMO efficiency if the mirrors are sufficiently thin. Neutrons that penetrate through the first coating and into the substrate can be reflected by the second coating on the opposite side. To arrive at F_2 , these neutrons must traverse the first coating once again. Despite the low probability of this occurring, there could still be a net gain in the overall transport efficiency depending on the reflectivity of the coatings.

As d_{sub} increases, the front faces of the wafers represent a larger portion of the entrance of the NMO, as indicated by an increasing filling fraction, ζ . The discussed benefit from the increased reflectivity of double-side coated mirrors is quickly offset by the channeling and double reflection effects illustrated in Fig. 6.9. For the investigation of the elliptic NMO, the filling fraction amounted to approximately $\zeta = 5 \times 0.15/8 = 9.4\%$ for our prototype, where five mirrors with $d_{\text{sub}} = 0.15$ mm were illuminated through the aperture A_2 , set to a width of 8 mm.

Fig. 6.10 illustrates the transport efficiencies obtained from McStas simulations for the NMO equipped with mirrors on both sides of the optical axis. The aperture A_2 is removed in this configuration, but the remainder of the geometry resembles the experimental setup. Therefore, this simulation includes the divergence hole as an additional source of neutron loss. The data qualitatively agrees with the expectations from the previous discussion. For

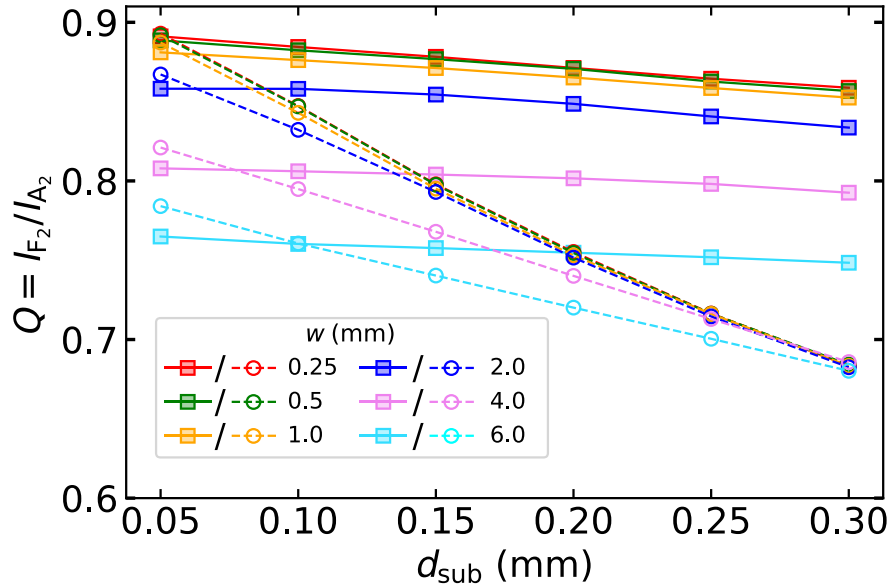


Figure 6.10: Dependence of the simulated efficiency of transport, Q , on d_{sub} and w , for single-sided (filled squares, solid lines) and double-sided (empty circles, broken lines) $m = 4.1$, $R_e = 82\%$ supermirror coatings. Figure is reproduced from Herb et al. [19].

all investigated values of w , the dependence of Q on d_{sub} is weak for single-side coated mirrors, as the influence of refraction and absorption effects caused by the silicon substrates is minute. Notably, double-side coatings might offer a marginal advantage for very thin mirrors and large w . However, as d_{sub} increases, the transport efficiency provided by the double-side coated NMOs linearly decreases due to the growing filling fraction ζ and the associated effects shown in Fig. 6.9.

In conclusion, the decision to use double-side coatings over single-side coatings must be determined on a case-by-case basis supported by Monte Carlo simulations. Double-side coatings are better suited for larger NMOs, where ζ is smaller. Additionally, they might be used for the outer mirrors of an NMO, where large m -values are required that entail reduced edge reflectivity.

Overall, the investigation of the elliptic NMO at MIRA-2 revealed a high efficiency of neutron transport, consistent with the calculations and the conducted simulations. However, due to the limitations of the CASCADE detector's resolution, a follow-up experiment was carried out at BOA to investigate the shape of the transported beam further.

6.2 Investigation of NMOs at BOA

The upcoming chapter details the investigation of the second generation of our **NMO** prototypes at the imaging beamline BOA. These prototypes include two non-polarizing elliptic **NMOs** and one polarizing as well as one non-polarizing parabolic **NMO**, all of which were specifically designed for use at MIRA-2. Additionally, we conducted further experiments on the polarizing elliptic **NMO** that had previously been studied. To complement our earlier research on the transport efficiency conducted at MIRA-2 (compare section 6.1), we utilized a high-resolution **PSD** to explore the spatial details of the imaged neutron beam that were previously inaccessible due to the limited resolution of the CASCADE detector. Additionally, we utilized the novel elliptic **NMO** prototypes to image more complex intensity distributions in one and two dimensions.

6.2.1 Double-Planar Parabolic NMO

We begin the exploration of parabolic **NMOs** by providing an overview of the investigated devices. This is followed by a detailed description of the experimental setup, concluding with a discussion of the obtained results. Fig. 6.11 displays an overview of the double-planar parabolic **NMO**. Fig. 6.11 (a) displays the geometry of the double-planar device including exemplary neutron trajectories. The neutrons first encounter the **polarizing horizontally focusing parabolic NMO (phpNMO)**. Measured from the midpoint between the two devices at $z = 0$, indicated by a vertical, black broken line, the mirrors of the **phpNMO** extend from $z = -(l + g) = -61$ mm to $z = -g = -1$ mm. Each mirror is $l = 60$ mm long, possesses a height of 40 mm, and is coated only on the side facing the optical axis with polarizing FeSi $m = 4$ supermirror with an edge reflectivity of $R_e = 82\%$. On either side of the optical axis, there are 18 symmetrically arranged mirrors with a thickness of 0.3 mm, spaced according to a recipe similar to the one discussed in appendix G. The maximum distance between the reflective surface of the outermost mirror and the optical axis occurs at $z = -61$ mm and amounts to 20 mm. Furthermore, 22 mirrors, each with a thickness of 0.2 mm, are positioned closer to the optical axis. To alleviate the impact of the divergence hole, these mirrors have been equidistantly arranged such that the distance between two reflective surfaces always exceeds 0.4 mm. This distance was considered the smallest achievable during the fabrication process. The red lines in Fig. 6.11 (a) illustrate trajectories of neutrons reflected at this device (not to scale). Whereas the actual device is equipped with mirrors on both sides of the optical axis (represented by black and gray parabolic lines), the trajectories are displayed only on one side of the optical axis for clearer visualization. Fig. 6.11 (c) presents an image of the entrance of a horizontally focusing **NMO**, featuring a large number of vertical mirrors.

Subsequently, the beam encounters the **non-polarizing vertically focusing parabolic NMO (npvpNMO)**. Its mirrors, all with length, $l = 60$ mm, and height, 40 mm, extend from $z = g = 1$ mm to $z = l + g = 61$ mm. The gap of $2g = 2$ mm between both devices was necessary for the construction process. This section contains 18 mirrors with a thickness of 0.3 mm on each side of the optical axis, which are spaced similarly to the schema given in appendix G. An additional 21 mirrors, placed equidistantly and separated by a minimum distance of 0.4 mm, have a thickness of 0.2 mm to fill the divergence hole. Each mirror is coated with non-polarizing $m = 4$ NiTi supermirror with an edge reflectivity of $R_e = 82\%$, applied only on the side closer to the optical axis. Blue lines in Fig. 6.11 (a) show the

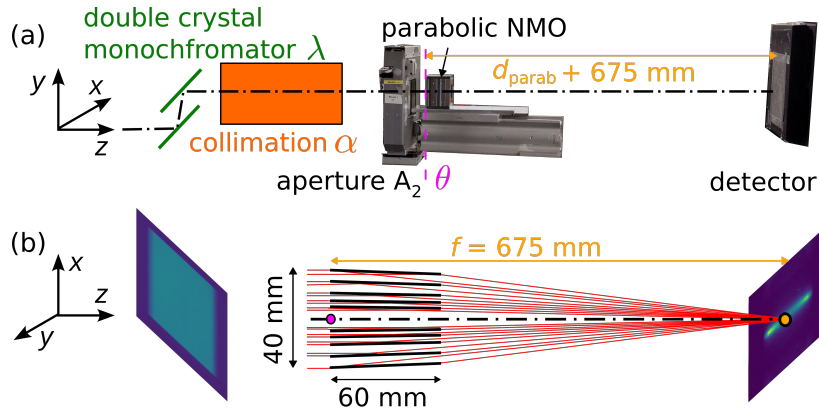


Figure 6.12: Sketched measurement geometry at BOA enabling the investigation of the **non-polarizing vertically focusing parabolic NMO** using a scintillator. (a) The neutron beam is monochromatized by a double crystal monochromator (green) and collimated by Soller collimators (orange) before being focused by the rotated parabolic **NMO**. The aperture A_2 allows illuminating selected areas of the **NMO**. Panel (b) depicts a top-down view of exemplary neutron trajectories and detector images before and after focusing, respectively.

that all neutrons arriving at the **NMO** are effectively reflected by its $m = 4$ mirrors, the beam was then monochromatized by a double crystal monochromator set to a wavelength of $\lambda = 4.5 \text{ \AA}$. Importantly, to facilitate the alignment process utilizing the available rotational stages, the **non-polarizing vertically focusing parabolic NMO** was rotated by 90° around the optical axis such that it instead focused neutrons in the horizontal direction⁽²⁾. This rotated **NMO** was positioned on a rotational table such that its axis of rotation coincides with the entrance window of the **NMO**. Upstream of the **NMO**, a remote-controlled aperture, A_2 , enabled the illumination of selected parts of the **NMO**. The difference between the nominal focal length of the parabolic **NMO**, $f_{\text{parab}} = 675 \text{ mm}$, and the actual distance to the detector, d_{exp} , is given by $d_{\text{parab}} = d_{\text{exp}} - f_{\text{parab}}$, which could be adjusted by moving the detector along the optical axis. Fig. 6.12 (b) displays a schematic representation of the system, showcasing neutron trajectories and detector images before and after focusing. To describe the acquired data, we use the coordinate system employed in McStas, where z represents the direction parallel to the optical axis, y points upwards in the vertical direction, and x completes the right-handed system.

6.2.1.2 Properties of Focusing

Fig. 6.13 presents a preliminary assessment of the focusing characteristics of the **non-polarizing vertically focusing parabolic NMO** illuminated by a neutron beam with $\lambda = 4.5 \text{ \AA}$, and $\alpha_h \approx 20'$. During the data acquisition, the aperture A_2 was adjusted to selectively illuminate the top part of the rotated, now vertical mirrors⁽³⁾. The cascading plot depicts

⁽²⁾Unless otherwise specified, the **non-polarizing vertically focusing parabolic NMO** was rotated by 90° around the optical axis, such that it focused neutrons horizontally. However, due to its intended use and to maintain consistency, we will keep referring to it as the “**non-polarizing vertically focusing parabolic NMO**”.

⁽³⁾To facilitate the alignment, the **non-polarizing vertically focusing parabolic NMO** was rotated by 90° around the optical axis resulting in horizontal focusing along x .

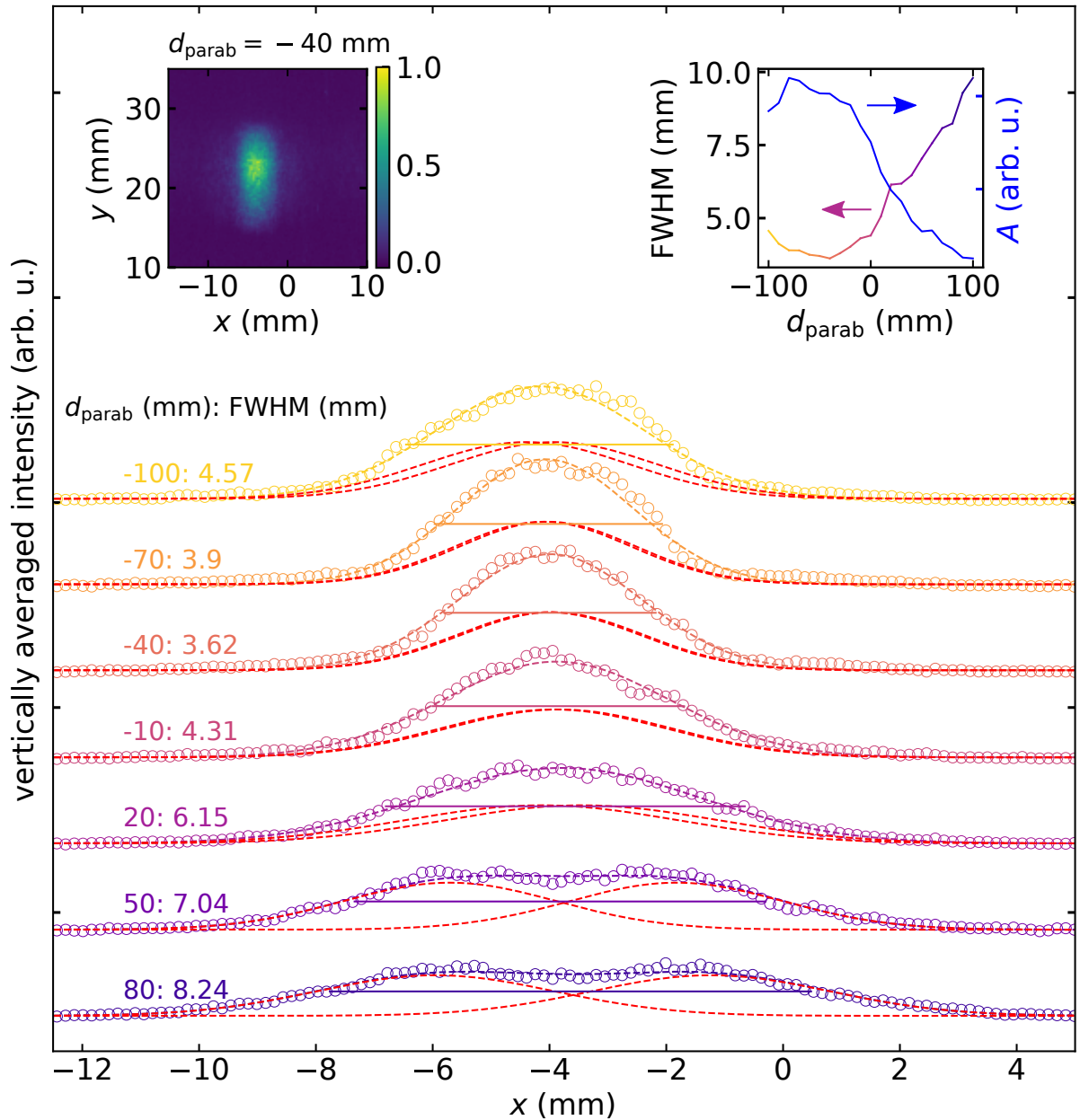


Figure 6.13: Relationship between the peak shape provided by the rotated **non-polarizing vertically focusing parabolic NMO** and the difference between the actual distance to the detector and the nominal focal length, d_{parab} . Values of $d_{\text{parab}} < 0$ indicate that the detector is too close to the **NMO**. The incoming beam was uncollimated, which corresponds to a divergence of $\alpha_h \approx 20'$. The cascading plot displays vertically integrated, normalized detector data for various values of d_{parab} as open circles. An exemplary detector image (acquired for $d_{\text{parab}} = -40$ mm) is presented in the top left inset, with the axes labeled according to the coordinate system shown in Fig. 6.12. The red dashed lines in the main plot represent two Gaussian peaks, the sum of which approximates the measured data, as indicated by the dashed line of the corresponding color. The horizontal solid lines within the plot indicate the **FWHM** of the peaks, with specific **FWHM** values provided on the left side of the figure. The inset at the top right illustrates the relationship between the **FWHM** and d_{parab} . Additionally, the amplitude A of the peaks is presented in this inset.

vertically averaged detector data for various deviations from the nominal focal length of the NMO, d_{parab} . The normalized data, shown as open circles, is well approximated by the sum of two Gaussian peaks, corresponding to contributions from mirrors on opposing sides of the optical axis; compare for example the neutron trajectories in Fig. 5.17. Two broken red lines indicate the individual peaks, with the sum of these contributions represented by a broken line, color-coded to match the measured data. Whereas the two peaks overlap well for small values of d_{parab} , separating the overall peak into two individual contributions becomes distinctly apparent for larger deviations from the nominal focal length.

In the cascading plot, the corresponding FWHM values of the peaks are indicated by solid horizontal lines, with the specific values provided on the left side. The inset at the top right illustrates the relationship between the FWHM and d_{parab} . The minimum FWHM value is achieved at $d_{\text{parab}} = -40$ mm, which is in good agreement with the obtained maximum of the amplitude, A , both indicating the optimum focusing configuration. However, this implies that the focal length of the NMO is smaller than intended. We attribute this observation to an excess curvature of the mirrors, likely caused by the single-side coating, a topic to be discussed in greater detail in section 6.3. The inset in the top left provides exemplary horizontally focused normalized detector data at the focal point for reference.

In addition to the observed relationship between the shape of the focused peak and d_{parab} , we also noticed a significant and unexpected variation in the FWHM of the focused peak depending on the point of illumination along the vertical y -direction. This effect was visible in the raw detector data and became more apparent when the data was vertically integrated within specific regions, as depicted in Fig. 6.14. We obtain similar data by averaging the data

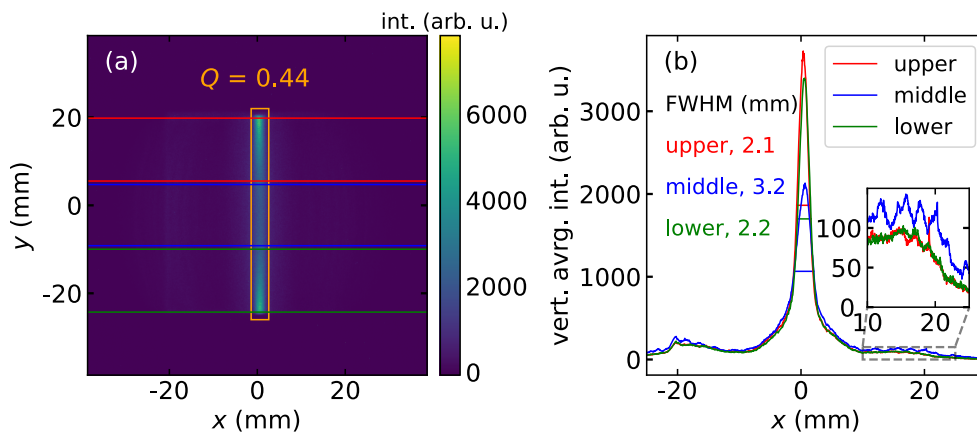


Figure 6.14: Horizontal focusing of a white neutron beam with divergence $\alpha_h = 10'$ by the rotated non-polarizing vertically focusing parabolic NMO. Panel (a) shows exemplary detector data obtained at the focal point, $d_{\text{parab}} = 0$ mm, with the axes labeled according to Fig. 6.12. A ratio of $Q = 0.44$ of all neutrons incident on the NMO is recovered inside the exemplary sample volume outlined in orange. Panel (b) depicts data vertically averaged between two horizontal lines of matching color in (a). The trend of the FWHM values for the three segments indicates that the quality of focusing is worse in the central part of the NMO, where the FWHM is significantly higher. As illustrated in the zoom region inset, the intensity that is missing from the central peaks reappears in the flanks of the distribution.

between the two red and green lines in panel (a), which corresponds to neutrons reflected near the top and the bottom of the NMO. The data exhibits a central peak of well-focused neutrons, $\text{FWHM} \approx 2.2$ mm, sitting atop a triangular shape of intensity, compare Fig. 6.14 (b). Besides the main peak, neutrons leaking through the NMO appear as small side peaks at $x = \pm 17$ mm, which exhibit a small amount of intensity texture due to the contributions from individual mirrors. Overall, these findings agree with our expectations.

However, the main peak is significantly less pronounced when considering only the central region delineated by the blue lines, $\text{FWHM} = 3.2$ mm. This observation contradicts the assumption that the mirrors remain translationally invariant along the vertical axis. Moreover, we note a redistribution of the intensity, where neutrons missing from the central peak reappear at the flanks of the distribution, as depicted in the inset.

To elucidate this phenomenon, we defined five horizontal stripes in the detector data of the neutron beam focused by the non-polarizing vertically focusing parabolic NMO. Subsequently, we determined the FWHM of the vertically averaged data for each of those segments for various values of d_{parab} , with the results illustrated in Fig. 6.15.

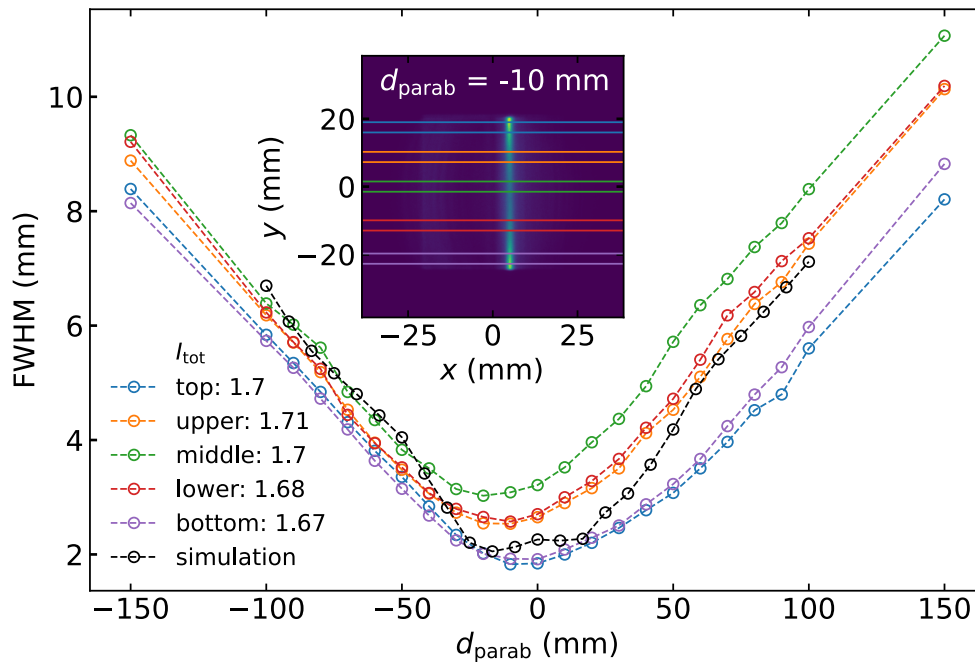


Figure 6.15: FWHM of a white neutron beam, $\alpha_h = 10'$, after horizontal focusing by the rotated non-polarizing vertically focusing parabolic NMO as a function of the segment of the focused peak and d_{parab} . The five stripes of the obtained detector data, for which the FWHM values were obtained individually, are delineated by the two lines of corresponding color as depicted in the inset. While the minimum achievable FWHM increases when moving from the outer part of the focused beam towards the center, the distance at which this FWHM is achieved decreases, indicating that optimal focusing occurs at distances smaller than the nominal focal length. The total integrated intensities for each of the investigated areas are in excellent agreement, as indicated in the legend. Additionally, results from a McStas simulation are depicted, which reasonably align with the results obtained for the outer areas.

For each area encompassed by two lines of matching color in the inset, we observe the expected linear increase of the **FWHM** with the deviation between d_{parab} and the distance at which minimum focusing is observed. However, comparing the **FWHM** values for different segments along the focused peak reveals two unexpected effects. Firstly, the minimum achievable **FWHM** notably worsens towards the center of the focused peak, whereas the top and bottom regions closely agree with respect to their **FWHM**. Secondly, the minimum **FWHM** is achieved for increasingly negative values of d_{parab} towards the vertical center of the focused peak.

Examining the underlying cause for the decrease in focusing quality towards the center of the **NMO**, we note that the quality of focusing is best when the neutrons interact with the reflective surfaces close to the shape-determining grooves, specifically at the top and the bottom of the focused peak. In contrast, the central part of the mirror deforms freely and deviates from its nominal shape if subjected to external forces, attributed to the single-side supermirror coating, a topic discussed in greater detail in section 6.3. As the mirrors are coated only on the one side facing the optical axis, the resulting tensile stress would favor an increased curvature. This curvature becomes more pronounced closer to the center of the mirrors and entails the observed reduction of the overall focusing quality and the decrease in the distance of optimum focusing compared to the nominal focal length.

To elucidate how individual parts of the **NMO** contribute to the overall focused beam and how each part transports neutrons to the focal point, we segmented the entrance window of the **non-polarizing vertically focusing parabolic NMO**, measuring $40 \times 40 \text{ mm}^2$, into 25 square segments of equal area, each spanning $8 \times 8 \text{ mm}^2$. Utilizing the aperture A_2 upstream of the **NMO**, we illuminated each segment one at a time. The resulting detector data acquired for focusing a neutron beam with $\lambda = 4.5 \text{ \AA}$, $\alpha_h = 10'$, and $d_{\text{parab}} = 0 \text{ mm}$ is presented in Fig. 6.16. The position of each individual panel corresponds to the specific segment of the **NMO** illuminated by the incident beam. For instance, the data in the top left panel was obtained when the neutron beam illuminated the top left segment of the **NMO**. Apart from this manipulation of A_2 , the geometry was maintained during all measurements.

Each image exhibits a central peak of focused neutrons that appears at a constant horizontal coordinate, $x \approx 1 \text{ mm}$. This indicates that regardless of its distance to the optical axis, every part of the initial beam is focused correctly with a common focal length. Additionally, a diffuse intensity region appears due to unreflected and doubly reflected neutrons keeping their original direction. Consequently, the position of this region within the detector data aligns with the position of the corresponding panel within the grid. Since the **NMO** only focuses in the horizontal dimension, the vertical position of both the focused peak and the diffuse region is the same in each row.

Within each panel, the **FWHM** of the vertically integrated data is denoted in white. Generally, the **FWHM** increases when the incoming beam illuminates a more central part of the **NMO**. The smallest **FWHM** is achieved when the lower left segment is illuminated, with a value of **FWHM** = 2.11 mm, in good agreement with Eq. (5.18), $r_f = \frac{10^\circ}{60} \frac{\pi}{180^\circ} 0.65 \text{ m} = 1.9 \text{ mm}$. In contrast, illuminating the central portion of the **NMO** results in the worst focusing, with **FWHM** = 6.8 mm. The increase in **FWHM** for neutrons arriving at the more central mirrors presented in the middle column is expected due to the overlap of the non-reflected and the focused components of the beam. However, the change in **FWHM** with

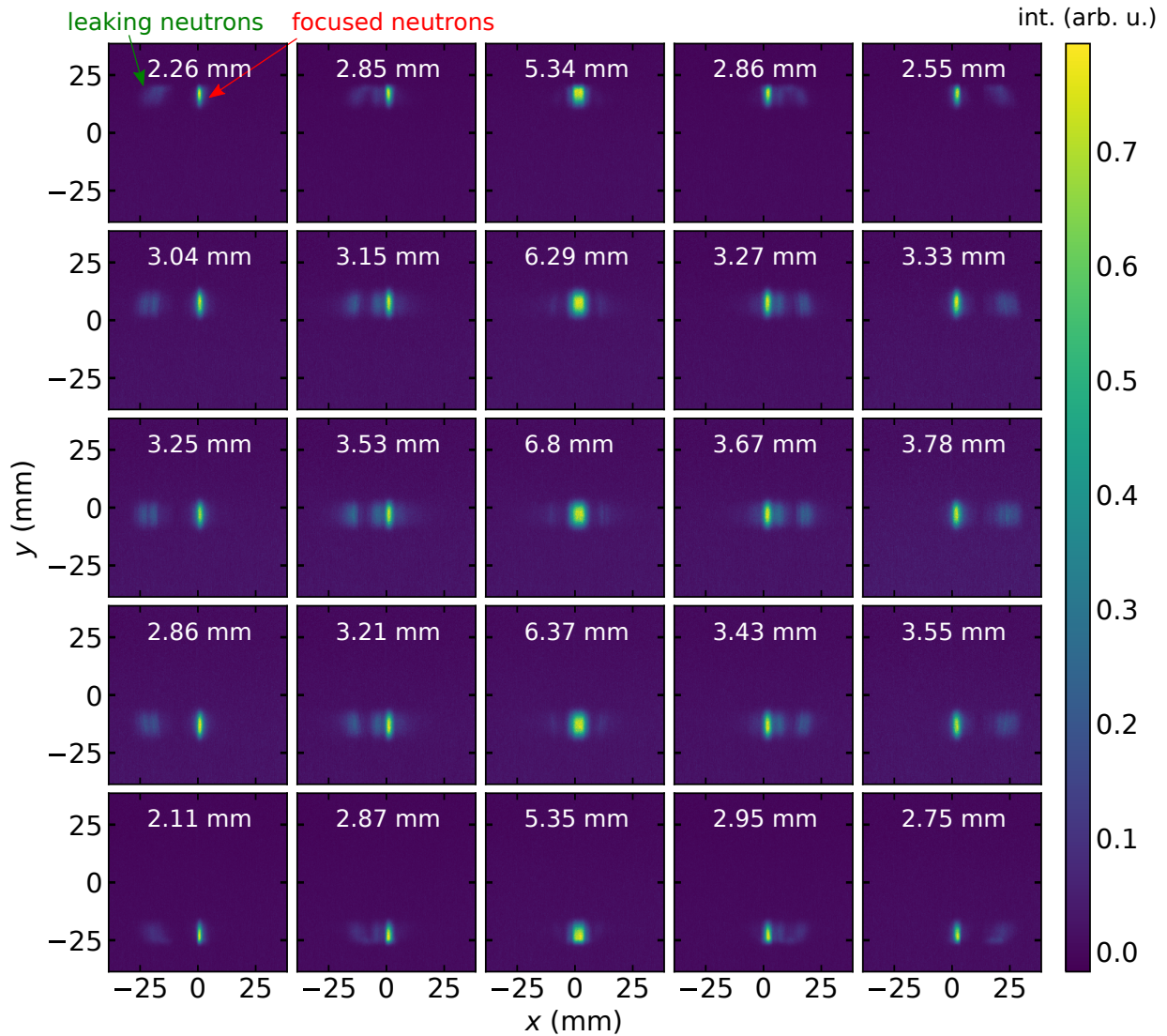


Figure 6.16: Horizontally focused intensity distributions obtained in optimum focusing conditions, i.e., $d_{\text{parab}} = 0$. The position of each respective panel in the grid corresponds to the illuminated segment of the rotated **non-polarizing vertically focusing parabolic NMO**. For instance, the top-left panel displays data obtained when the top-left segment of the **NMO** was exposed (more details in the text). Each panel exhibits a central peak of *focused neutrons*, and a diffuse region attributed to *leaking neutrons* that are either not reflected by the mirrors or double reflected during their transport through the **NMO**. The **FWHM** of the vertically averaged data corresponding to the peak of focused neutrons is indicated in white within the corresponding panels. The observed increase of the **FWHM** values towards the center of the **NMO** indicates a reduction of the focusing quality.

the vertical position of the point of illumination along the mirrors indicates a deformation of the mirrors, particularly distant from the shape-determining grooves. This effect is consistently observed for each column, suggesting that it is independent of the initial curvature

or the thickness of the mirrors. All vertically integrated data displaying the **FWHM** and the center positions of the peaks, x_0 , are shown in Fig. 6.17, with the panel placements matching Fig. 6.16. The minute dependence of x_0 on the point of illumination indicates that the position of the **NMO** is in good agreement with its nominal focal length.

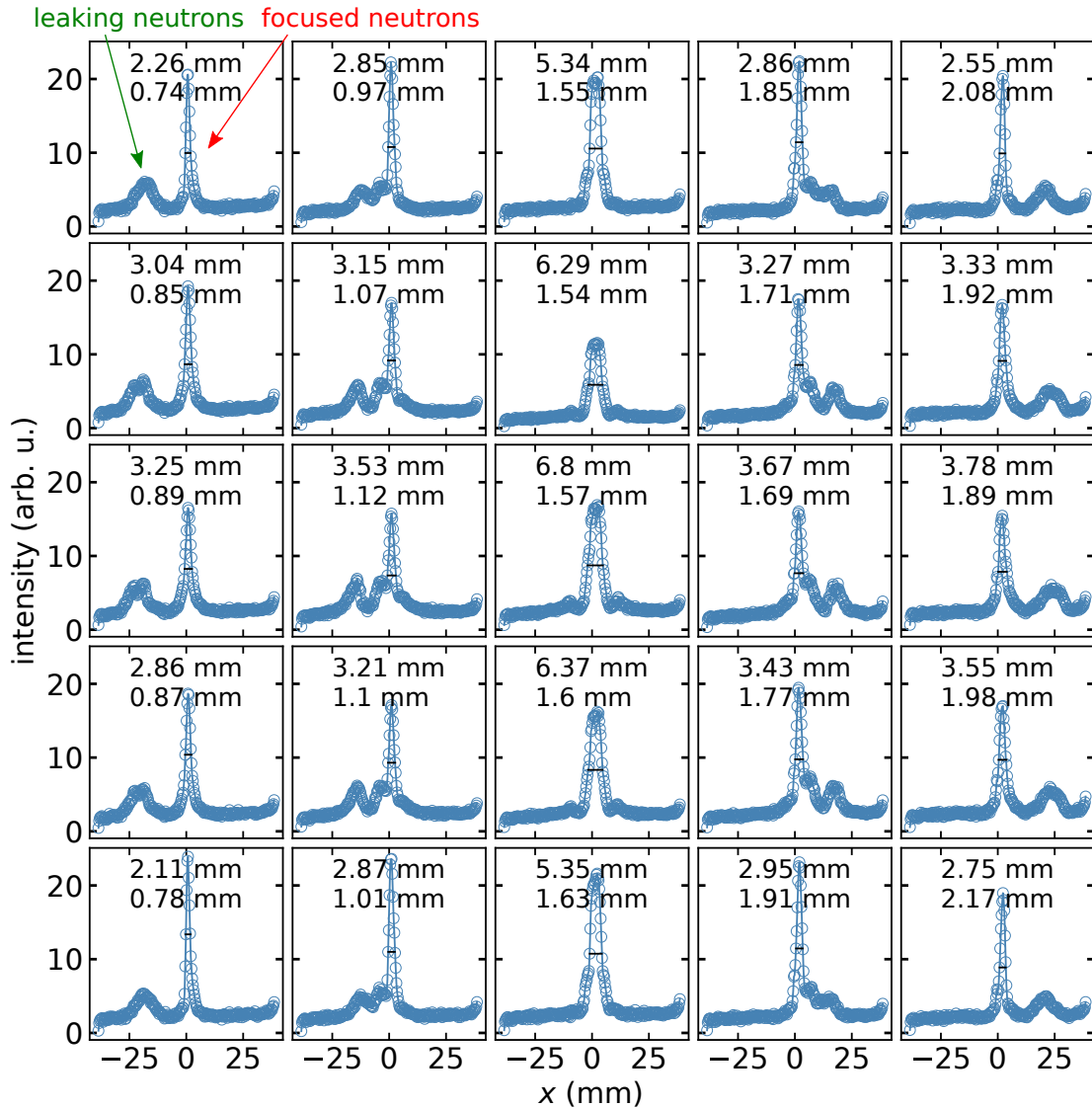


Figure 6.17: Vertically integrated intensity distributions of the data presented in Fig. 6.16. The data in each panel consists of a central peak of focused neutrons, and a diffuse region of *leaking neutrons* that either pass the **NMO** unobstructed or were doubly reflected. The **FWHM** and the position of each peak are indicated by the upper and the lower value within each panel. Notably, the position of the peaks, x_0 , exhibits only a minute change with respect to the illuminated region of the **NMO**. This observation suggests that the **NMO** is well-adjusted, and each mirror effectively provides good focusing.

6.2.2 Polarizing Elliptic NMO

In addition to the transport efficiency measurements previously conducted at MIRA-2, we utilized the superior resolution of BOA to capture the finer details of the beam after transport through the polarizing elliptic NMO. This allowed us to further explore the imaging quality of the NMO, and to image structures in one and two dimensions.

6.2.2.1 Experimental Geometry

Expanding on the initial investigation of the imaging properties at MIRA-2, a second experiment was conducted at BOA to assess the shape of the beam as imaged by the polarizing elliptic NMO. Compared to the experiment performed at MIRA-2, the CASCADE detector was replaced by a ${}^6\text{LiF}/\text{ZnS}:\text{Cu}$ -based scintillator that offers a superior resolution of $\text{FWHM} \leq 100\ \mu\text{m}$. The measurement setup and exemplary data are illustrated in Fig. 6.18. In addition to replacing the CASCADE detector with the scintillator, two notable differ-

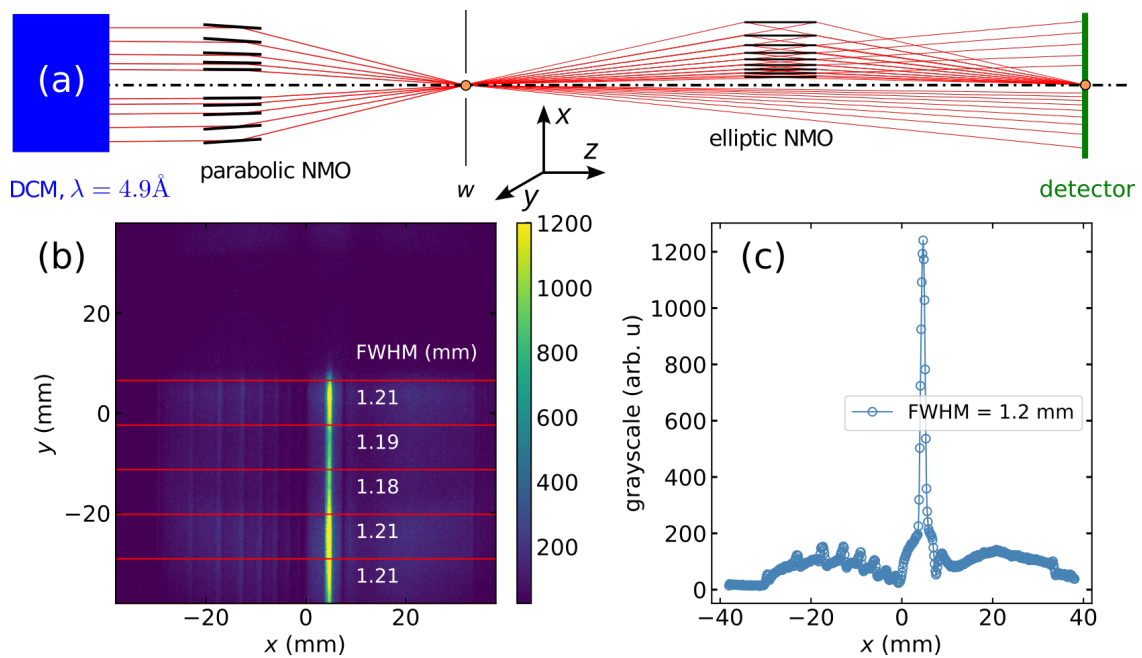


Figure 6.18: (a) Top-down view of the experimental geometry for the investigation of the elliptic polarizing NMO at BOA. Mirrors were inserted on only one side of the optical axis. The monochromatic neutron beam provided by the DCM, $\lambda = 4.5\ \text{\AA}$, was focused by the non-polarizing vertically focusing parabolic NMO onto an aperture with width, w , which was subsequently imaged by the elliptic NMO onto the detector. Both the parabolic and the elliptic NMO were positioned according to their optimum focusing conditions, with $d_{\text{parab}} = -1\ \text{cm}$, $d_{\text{ellip}} = 0\ \text{mm}$. Panel (b) shows exemplary detector data for $w = 1.0\ \text{mm}$. The data displays a sharp central peak of focused neutrons and diffuse regions of neutron leakage. Intensity texture arising from double reflections, corresponding to individual pairs of mirrors, appears left to the central peak where the NMO was equipped with mirrors. The obtained FWHM values for the central peak range from 1.18 mm to 1.21 mm for the different regions, separated by red horizontal lines. Panel (c) depicts vertically averaged detector data.

ences between the BOA experiment and the one at MIRA-2 persist. Firstly, at BOA, a parabolic NMO was utilized to illuminate the virtual source, resulting in an increased source divergence. This configuration ensures that all mirrors of the NMO can be illuminated simultaneously. Secondly, the primary focus of this experiment was to determine the shape of the imaged neutron beam. Consequently, the polarization was not maintained up to the elliptic NMO. While reducing the efficiency of transport due to the faulty polarization of half of the neutrons, this change did not alter the shape of the imaged beam. Less importantly, we utilized a double crystal monochromator to monochromatize the beam to a wavelength of 4.5 Å, as opposed to the focusing monochromator employed at MIRA.

Fig. 6.18 (b) shows exemplary detector data obtained for a virtual source with width $w = 1.0$ mm, with the vertically averaged data presented in Fig. 6.18 (c). The data exhibits a central peak of focused neutrons, accompanied by diffuse regions of neutron leakage. Texture arising from double reflections and geometric leakage between specific pairs of mirrors arises only to the left of the focused peak, where mirrors were inserted. Segmenting the detector area into stripes separated by horizontal, red lines allows us to individually determine the FWHM of the vertically averaged data for each region. These values range from 1.18 mm to 1.21 mm, which is in good agreement with the expected value for unit magnification, $\text{FWHM} = w = 1$ mm.

6.2.2.2 Evaluation of the Peak Shape

For each of the individual segments of the detector data illustrated in Fig. 6.18 (c), referred to as *top*, *upper*, *middle*, *lower*, and *bottom*, we evaluated the FWHM for various values of w . These FWHM values are presented in Fig. 6.19. For very small $w \leq 1$ mm, the FWHM deviates from w and approaches a minimum value of 0.7 mm regardless of the illuminated region. This deviation is mainly attributed to the mirror waviness or a possible misalignment of the NMO, with the resolution of the detector ≤ 0.1 mm likely playing a less relevant role. Assuming a waviness of $\eta = 2 \times 10^{-4}$ rad, we obtain a corresponding limiting FWHM of $2 \times 2.355 \times 0.6 \text{ m} \times 2 \times 10^{-4} \text{ rad} = 0.6$ mm at the focal point which is in reasonable agreement with the approached value, as illustrated in the inset. For a large range of widths $1 \text{ mm} \leq w \leq 6$ mm, the assumed one-to-one correspondence between FWHM and w aligns very well with the data before it breaks down at larger w . The discrepancy between the experimental data and the simulation is mainly attributed to the virtual source being illuminated by the parabolic NMO. For large w , this leads to an inhomogeneous intensity distribution at the first focal point, which is then imaged onto the detector. Additionally, the parabolic NMO provides a beam with limited width depending on d_{parab} , which is in qualitative agreement to the fact that the FWHM levels off at a common value of $w = 7$ mm.

Notably, the FWHM of the beam transported by the polarizing elliptic NMO does not change significantly with the vertical point of illumination. This suggests that the mirrors maintain the nominal geometry even distant from the shape-determining grooves. This observation can possibly be explained by the use double-side coated mirrors, which likely entails a compensation of surface tensions on both sides of the mirrors, thereby reducing the deformation. A more detailed discussion of this topic can be found in section 6.3.

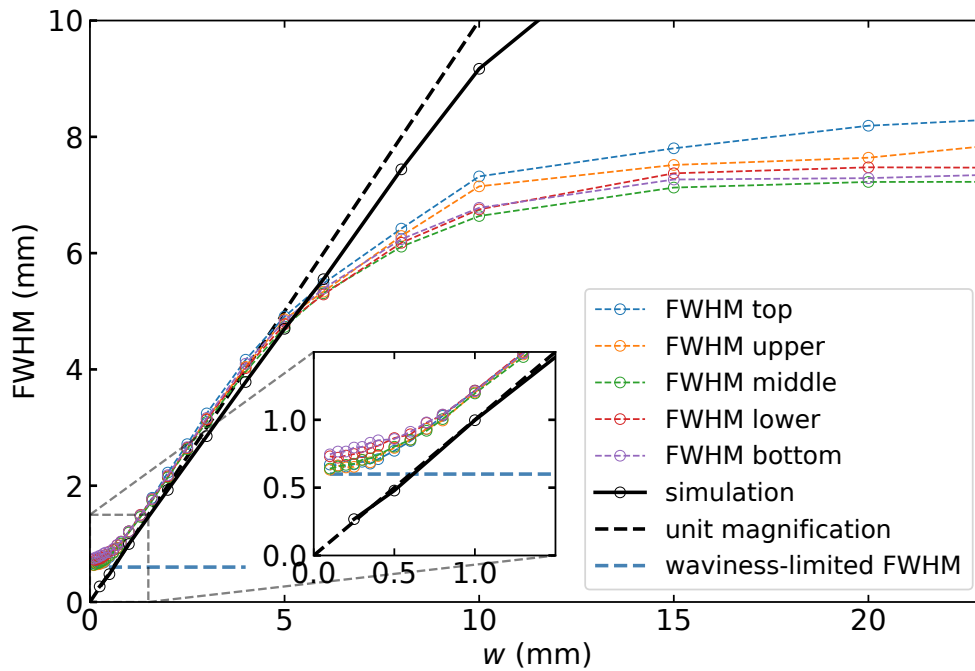


Figure 6.19: Dependence of the peak **FWHM** of the imaged neutron beam on the width of the virtual source, w , obtained for the polarizing elliptic **NMO**. The data corresponding to the various curves is obtained from the segments on the detector as illustrated in Fig. 6.18. Notably, the overall **FWHM** values do not depend on the point of illumination along the mirror, indicating that the mirrors are translationally invariant along the vertical direction. The black dashed line and the black solid lines correspond to imaging with unit magnification and a McStas simulation with unphysically high resolution, respectively.

6.2.3 Non-Polarizing Double-Planar Elliptic NMO

Similarly to the polarizing prototype, the second-generation non-polarizing elliptic **NMO** prototypes were constructed using blades of mono-crystalline silicon coated with supermirror. However, the coatings were applied only on the side closer to the optical axis. This single-sided coating is intended to enhance transport efficiency by mitigating channeling and double reflection effects illustrated in Fig. 6.9. Moreover, since this **NMO** is designed to be non-polarizing, the supermirror coatings consist of alternating layers of Ni and Ti resulting in $m = 4$ and $R_e = 82\%$.

The geometry of the overall configuration is similar to the one for the parabolic **NMO** displayed in Fig. 6.11. Focusing in two dimensions was achieved by using a double-planar design with each of the two focal points positioned at a distance $f = 675$ mm from the midpoint between the two orthogonal **NMOs**. Each mirror blade has a length of $l = 60$ mm and a height of 40 mm. Defining this midpoint to be at $z = 0$ mm, the mirrors of the horizontally focusing elliptic **NMO** span from $z_s = -61$ mm to $z_e = -1$ mm, while the mirrors of the vertically focusing counterpart range from 1 mm $\leq z \leq 61$ mm. The largest semi-minor axes for both sets of shape-determining ellipses amount to $b_0 = 20$ mm, enabling a maximum field of view of 40×40 mm². For this prototype, a partial filling of the divergence

hole was achieved by positioning equidistant mirrors close to the optical axis. Specifically, this was done if the calculated distance between adjacent mirrors was less than the sum of the substrate thickness and the space required for the fabrication of the grooves, $b_{n+1} - b_n \leq d_{\text{sub}} + d_{\text{grooves}}$, where $d_{\text{grooves}} = 0.2 \text{ mm}$. Two different substrate thicknesses were employed to ensure the stability of the outer, more strongly bent mirrors and to maximize the transport efficiency by increasing the filling ratio of the divergence hole. The outer and inner mirrors are based on substrates with $d_{\text{sub}} = 0.3 \text{ mm}$ and $d_{\text{sub}} = 0.2 \text{ mm}$, respectively.

6.2.3.1 Beam Shape

Similarly to the investigation of the transport characteristics of the first-generation polarizing elliptic NMO prototype (compare Fig. 6.19), we explored the imaging properties of the second-generation *non-polarizing vertically focusing elliptic NMO* (*npveNMO*)⁽⁴⁾. Specifically, we investigated the relationship between the width, w , of the virtual source positioned at the first focal point of the NMO and the FWHM of the beam at the second focal point after the transport. This relationship is illustrated in Fig. 6.20 for various investigated wavelengths, $2.45 \text{ \AA} \leq \lambda \leq 6.0 \text{ \AA}$. During the measurements, only the top part ($\approx 10 \text{ mm}$) of the

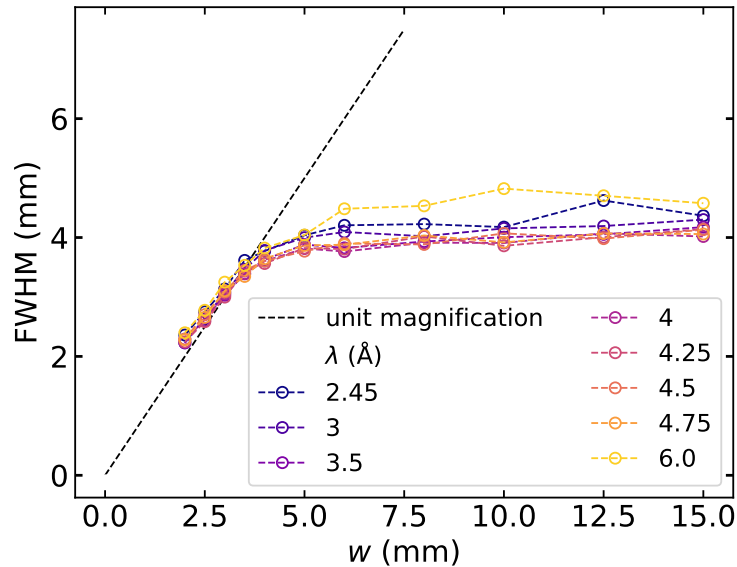


Figure 6.20: Relationship between the horizontal FWHM of the imaged beam at F_2 after transport through the rotated *npveNMO*, and the width of the virtual source at F_1 , w . Data is shown for various wavelengths of the incoming beam, λ . The measurement geometry was similar to the one for the polarizing elliptic NMO depicted in Fig. 6.18.

rotated *npveNMO* was illuminated with the rest shielded by the aperture A_2 . Limiting the points of reflection to areas close to the shape-determining grooves ensured a high imaging quality.

Notably, the observed FWHM values are in excellent agreement across all explored wavelengths, as expected when considering that the number of mirrors partaking in the imag-

⁽⁴⁾Again, the NMO originally designed to focus neutrons vertically was rotated by 90° around the optical axis, such that it focused neutrons horizontally during the experiment.

ing process should not influence the peak shape. For small widths of the virtual source, $w \leq 4$ mm, the **FWHM** of the transported beam is in excellent agreement with w , consistent with the intended imaging with unit magnification. For larger virtual sources $w \geq 4$ mm, the **FWHM** of the transported beam stabilizes at $\text{FWHM} = 4$ mm. This is attributed to the illumination of the virtual source utilizing a parabolic **NMO**, which restricts the size of the initial beam at the virtual source, as explored in more detail in section 6.2.3.3. No data was collected for smaller beam widths $w \leq 2$ mm, as this is already within the range of very small samples for neutron scattering.

6.2.3.2 One-Dimensional Imaging

In addition to examining the transport properties of elliptic **NMOs** using neutrons emitted from a simple slit-like virtual source, we conducted experiments employing more complex intensity distributions. These investigations confirmed the elliptic **NMO's** capability to effectively image various intensity distributions.

For the initial test of one-dimensional imaging, we chose a regular grid-like structure of neutron-absorbing material. The grid was fabricated with a 3D printer utilizing a borated PLA filament and was structured as follows: 0.5 mm-wide open slits are separated by 1.5 mm of filament, yielding a structure with a periodicity of 2 mm. Fig. 6.21 (a) displays an image of this structure consisting of eleven slits. To mitigate the effects associated with the previously

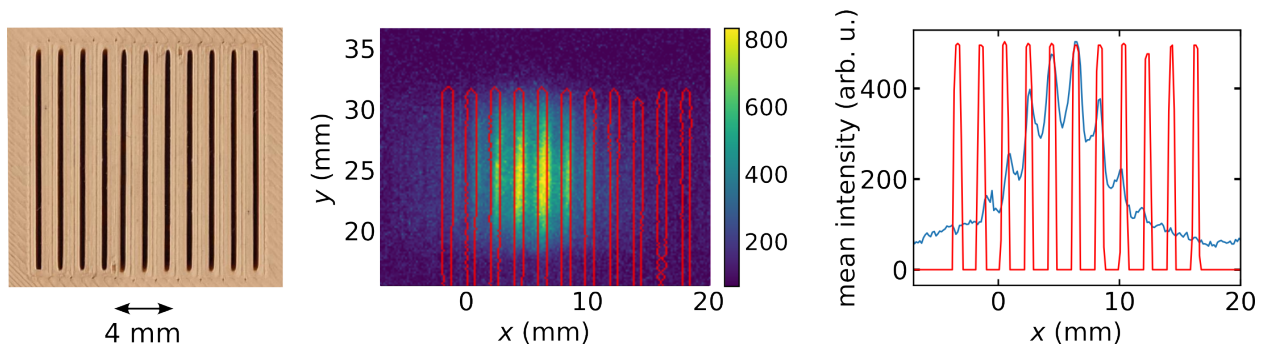


Figure 6.21: One-dimensional imaging of a grid-like intensity distribution. Panel (a) depicts the grid-like structure, positioned at F_1 of the **npveNMO**, the outline of which is highlighted in red in panel (b). The color plot illustrates the obtained spatial intensity distribution at F_2 after the transport through the elliptic **NMO**. The vertically averaged data in panel (c) distinctly reveals individual peaks of intensity, each corresponding to contributions from the respective slit.

discussed deformation of the mirrors, the entrance of the **npveNMO** was shielded such that only the top ≈ 10 mm of the mirrors were illuminated. The intensity distribution at the first focal point was determined by placing the grid structure as close to the detector as possible and recovering the **FWHM** of the resulting two-dimensional image, which is delineated in red in Fig. 6.21 (b). The acquired intensity distribution obtained at F_2 aligns closely with the outline of the imaged grid-like structure. However, the intensity significantly decreases with increasing distance from the optical axis. The vertically averaged detector image in Fig. 6.21 (b) faithfully reproduces eight out of the initial eleven slits, corresponding to an effective field of view with a width of 14 mm. The steep drop in intensity for neutrons

further from the optical axis is attributed to a combination of effects. Firstly, as derived in Eq. (5.16), the geometric losses are expected to increase linearly with increasing distance from the optical axis. Secondly, a parabolic NMO was utilized to illuminate the grid with a non-uniform spatial intensity distribution of neutrons, which even if imaged correctly falls off with increasing distance from the optical axis. Further insights into this phenomenon were provided by varying the distance between the illuminating parabolic NMO and the 3D-printed grid, as discussed in section 6.2.3.3.

6.2.3.3 Variation of d_{parab}

In the experiments reported previously, parabolic NMOs were routinely employed to condense the incident neutron beam onto a slit or grid-like structure to create a neutron distribution with a high divergence, which was subsequently imaged onto the detector by the elliptic NMO. This setup introduces a complex interplay between the maximum achievable beam size and the beam divergence, depending on the distance between the parabolic NMO and the illuminated structure. To examine the effects of varying d_{parab} , we repeated the previously discussed imaging of the one-dimensional grid, while varying the distance between the npvpNMO and the grid, as shown in Fig. 6.22 (a)⁽⁵⁾. The uncollimated beam is monochromatized by the DCM ($\lambda = 4.5 \text{ \AA}$) and focused by the npvpNMO onto the grid-like structure. The deviation between the distance from the grid to the NMO and its nominal focal length ($f = 675 \text{ mm}$), is denoted by d_{parab} . Consequently, the illuminated area, and hence the number of illuminated slits, is expected to increase with the magnitude $|d_{\text{parab}}|$. Fig. 6.22 (b) displays the detector data acquired at F_2 of the elliptic NMO displaying the imaged slits for various values of d_{parab} , separated by red lines. For $d_{\text{parab}} \leq 0 \text{ mm}$, the number of strongly illuminated slits increases from three at $d_{\text{parab}} = 0 \text{ mm}$ to eight at $d_{\text{parab}} = -200 \text{ mm}$. Conversely, for $d_{\text{parab}} \geq 0 \text{ mm}$, in addition to the observed increase in the illuminated area, a significant drop in the overall intensity of the image is apparent.

Fig. 6.22 (c) depicts simulated neutron trajectories for three different values of $d_{\text{parab}} \in \{200 \text{ mm}, 0 \text{ mm}, -200 \text{ mm}\}$. These trajectories are color-coded based on the specific slit they pass at the first focal point. The simulation illustrates how the number of illuminated and imaged slits increases for $|d_{\text{parab}}| > 0 \text{ mm}$. It also highlights the intricate relationship between the individual slit and the part of the parabolic NMO that illuminates it, which changes with the sign of d_{parab} . The correspondence between each slit's position and the divergence emitted from it also entails an interesting effect: For $d_{\text{parab}} \ll 0 \text{ mm}$, only double reflections occur at the elliptic NMO, whereas for $d_{\text{parab}} \gg 0 \text{ mm}$, geometric losses are restricted to neutrons passing between mirrors. The dilution of neutrons along the second, lateral dimension, which is neglected in the simulation, results in an additional reduction of intensity in the acquired data for $d_{\text{parab}} \gg 0 \text{ mm}$.

Overall, the imaging process was deemed successful, and the results illustrate the intricate relationship between d_{parab} , the number of illuminated slits, and the range of divergences emitted from each of those slits. This relationship needs to be taken into account when utilizing parabolic NMOs as a neutron beam condenser for imaging purposes.

⁽⁵⁾To facilitate the alignment, both devices were rotated by 90° around the optical axis such that they focused horizontally. The position of the elliptic NMO was maintained to ensure optimal imaging.

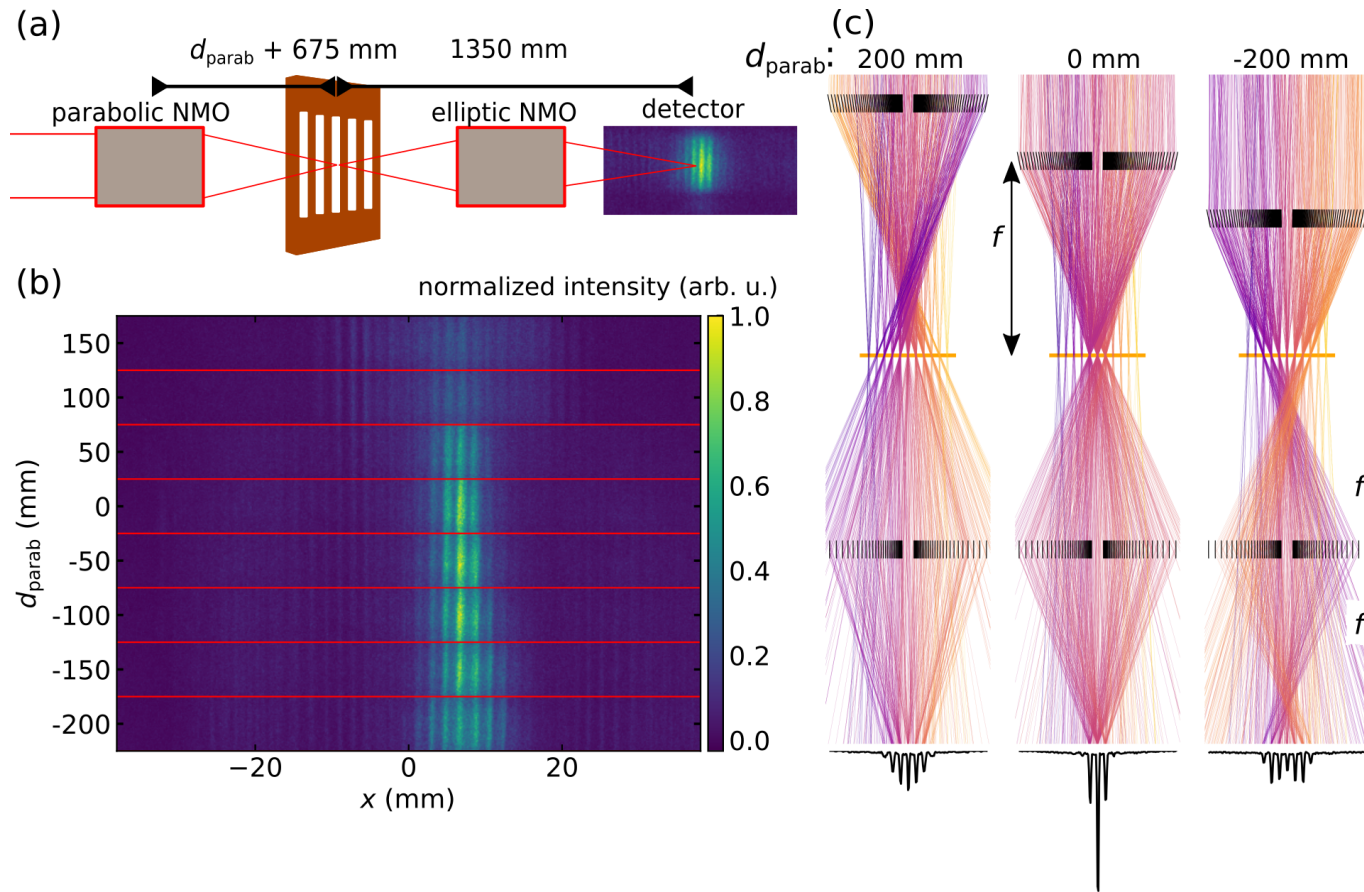


Figure 6.22: Influence of varying the distance between the parabolic NMO and an imaged grid-like structure. Panel (a) depicts a sketch of the measurement geometry: a 3D-printed grid-like structure was illuminated by the rotated non-polarizing vertically focusing parabolic NMO and imaged onto the detector by the rotated non-polarizing vertically focusing elliptic NMO. For all acquired data, the latter was arranged in its optimum focusing condition, positioned between the grid and the detector each at a distance equal to its focal length. During the measurement, the parabolic NMO was displaced to various distances, d_{parab} , from its nominal focal length. Panel (b) displays detector data for each deviation, separated by red lines. Overall, the grid-like structure is well-resolved in the detector data, with an increasing number of slits being illuminated for $d_{\text{parab}} \neq 0 \text{ mm}$. Panel (c) illustrates simulated neutron trajectories (initial divergence $\alpha_{\text{h}} = 30^\circ$) for three selected values of d_{parab} , color-coded according to the slit (orange horizontal broken line) they passed at the first focal point. The spatial intensity distribution at the detector position is depicted as black curves at the bottom of the panel, reproducing the grid-like structure.

6.2.3.4 Two-Dimensional Imaging

Evaluating the imaging capabilities of the elliptic NMOs further, we utilized two orthogonal devices to achieve two-dimensional imaging as displayed in Fig. 6.23. The common measure-

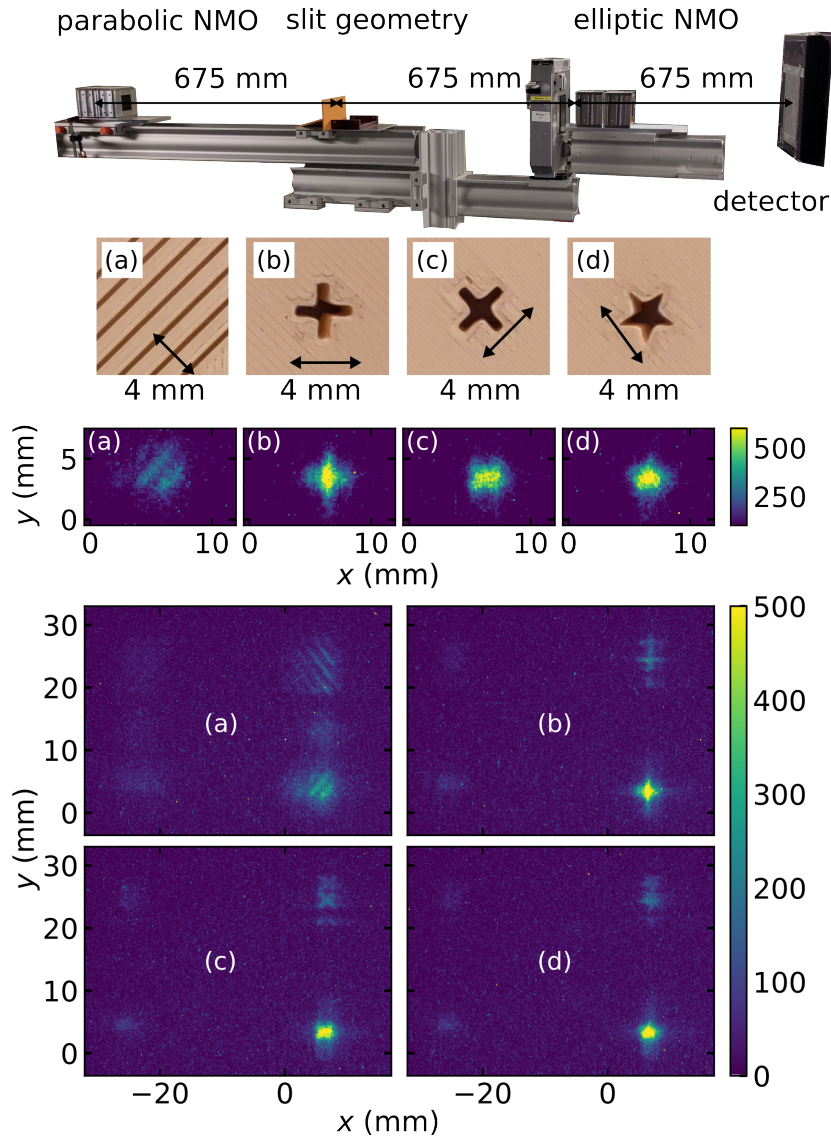


Figure 6.23: Demonstration of two-dimensional imaging using two orthogonal elliptic NMOs. A sketch of the employed measurement geometry is shown at the top, with the two parabolic NMOs illuminating a 3D-printed structure, which is then imaged by two orthogonally oriented non-polarizing elliptic NMOs. The aperture preceding the elliptic NMOs ensures that only the top left segment of each elliptic NMO contributes. (a), (b), (c), and (d) show the imaged structures and the detector data obtained at F_2 during the imaging of a 45° rotated grid, a vertically aligned cross, a 45° rotated cross, and a five-pointed star, respectively. While the bottom panels depict a large section of the detector, including contributions from leaking neutrons, the zoomed panels of the center are restricted to images corresponding to two-dimensionally redirected neutrons.

ment geometry included two parabolic NMOs illuminating the specific 3D-printed structure and the two non-polarizing elliptic NMOs imaging it onto the detector. To enhance the imaging quality and to minimize background, only the top-left corners of both the vertically and horizontally focusing elliptic NMOs were illuminated during the imaging process. This selective illumination is evident in the detector images, where distinct diffuse regions of intensity can be distinguished based on their trajectory toward the detector.

The most intense region on the bottom right corresponds to neutrons being reflected correctly at both non-polarizing elliptic NMOs, i.e., the intended image at F_2 . In contrast, neutrons arriving at the top left either interact with none of the NMOs or are doubly reflected at both. The regions at the top right and bottom left are attributed to neutrons being reflected only at the horizontally or vertically focusing elliptic NMO, respectively. This explains the mirroring of the grid-like structure (a) and the star (d) when comparing the top and bottom right intensity distributions.

Curiously, two distinct images appear when neutrons are exclusively reflected in the horizontal direction. The exact origin of these images remains inconclusive, and efforts to reproduce a similar structure within McStas simulations were unsuccessful. Most likely, these images arise from individual contributions, such as unreflected and doubly reflected neutrons, which separate vertically before arriving at the detector as seen in Fig. 6.23 (b), (c) and (d). In (a) these individual images coincidentally overlap, creating the illusion of one common grid.

Instead of accurately representing the original geometries, the region of vertically focused neutrons appears as a diffuse region lacking distinct contours. This is likely due to the improper alignment of the vertically focusing elliptic NMO, which could not be adequately adjusted without a goniometer. As a result, the quality of two-dimensional imaging is compromised significantly when compared to the horizontally reflected structures.

In conclusion, when both orthogonally oriented elliptic NMOs are properly aligned, high-quality, two-dimensional imaging of structures should be effectively achieved, constituting a part of future research.

6.3 Investigation of Mirror Deformations

To examine the observed deformation of the supermirror-coated silicon substrates and its impact on the performance of potential NMO-based systems, supplementary investigations were performed utilizing a 3D scanner. Our aim was to quantify the deformations from the nominal mirror geometry, with the intention of potentially mitigating the effects of the deformation on the performance of the NMO by adjusting the shape-determining grooves accordingly.

Determination of Mirror Deformations using a 3D-Scanner

To determine the actual geometry of the silicon substrates, and thereby quantify the extent of deviation from their nominal intended shapes, two test devices were fabricated. These devices maintained the aluminum housing of their NMO counterparts, featuring a selection of elliptic and parabolic grooves. The results of subsequent investigations carried out with an optical 3D scanner are presented here.

We explored the geometry of leftover silicon substrates featuring a length of 60 mm, a width of 40 mm, and a thickness of $d_{\text{sub}} = 0.2$ mm. These substrates were coated on one side

with a polarizing FeSi supermirror characterized by $m = 4$ and $R_e = 82\%$. The 3D-scanning process was performed using an ATOS Compact Scan/300 3D-scanner operating with optical light [183]. However, as this device cannot accurately capture reflective surfaces, a white opaque spray was applied before scanning. Following this preparation, a single capture was sufficient to digitize the geometry of each individual mirror. Fig. 6.24 showcases the test piece with the white opaque spray applied, along with a three-dimensional representation of the obtained geometry. The digitization of the entire test piece involved reconstructing

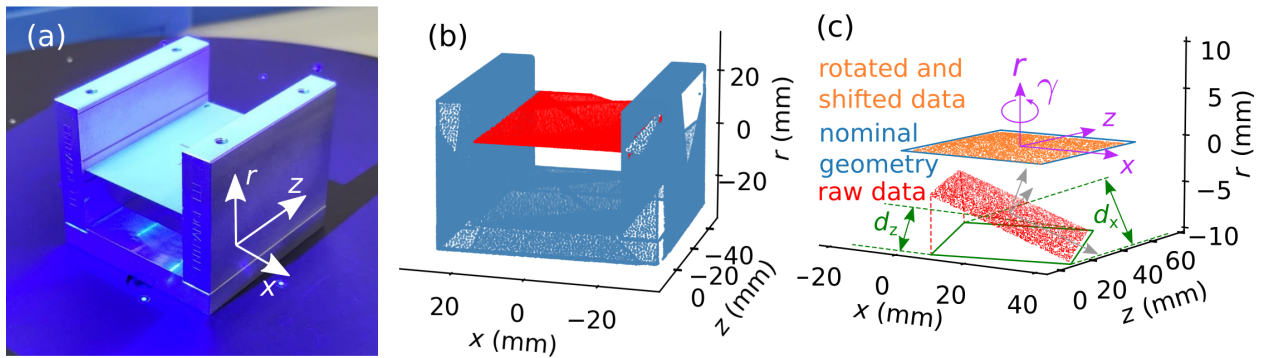


Figure 6.24: Investigation of the geometry of a Si wafer coated on the bottom side using the 3D scanner. Panel (a) depicts the test piece coated with white opaque resin, illuminated with blue light during the 3D scanning process. A few selected grooves of the elliptic and parabolic NMO prototypes were machined into the test pieces, thereby facilitating the investigation and quantification of deformations of the mirrors inserted into each of these grooves. Panel (b) illustrates the obtained 3D data represented by a point cloud, where red and blue points correspond to the mirror and the casing that houses them, respectively. Panel (c) illustrates the process of aligning the raw data to the nominal geometry. The raw measured data corresponding to the mirror (red) is rotated and shifted to agree optimally with the nominal geometry (outlined in blue). This recovered data after the alignment is illustrated in orange.

it from multiple captures obtained at various angles during a full rotation. This data was saved in the .stl format, consisting of a large number of triangles that collectively form the surface of the scanned geometry. As illustrated in Fig. 6.24 (b), only the vertices of those triangles were saved. Instances of missing data, indicated by white areas in Fig. 6.24 (b), can be attributed to insufficient coating with the opaque resin or to an insufficient range of illumination angles.

Free Mirror

To establish a baseline, we present a height profile obtained from the backside of a substrate coated with supermirror only on the bottom side, which was not supported by any shape-determining grooves; essentially a free mirror placed on a flat surface. This example will serve to briefly explore the process of data acquisition and processing.

The process of aligning the obtained data is illustrated in Fig. 6.24 (c). Following the capture and digitization of data by the 3D scanner, the resulting point cloud representing the mirror (red) is rotated around the r -axis, such that its projection into the xz -plane (delineated in green) aligns optimally with the nominal outline of the mirror (blue). This

means that x should range from $x \in [-20 \text{ mm}, 20 \text{ mm}]$, and z ranges from $z \in [1 \text{ mm}, 61 \text{ mm}]$. Assuming that the data acquired for the mirror possesses a rectangular shape, this is achieved by rotating the data around r by an angle γ until the sum of the maximum distances between any two points along x and z is minimized,

$$\gamma_{\text{opt}} = \arg \min_{\gamma} [d_z(\gamma) + d_x(\gamma)]. \quad (6.5)$$

Here, $d_x(\gamma)$ and $d_z(\gamma)$ denote the maximum distance between the two x and z coordinates of any two points, as depicted in Fig. 6.24 (c). Minimizing with respect to γ is equivalent to an alignment of the data parallel to the axes of the coordinate system. Subsequently, the data is shifted and rotated around x and z to minimize the deviation between the obtained height profile, r , and the nominal profile. It should be noted that the least squares algorithm utilized for the adjustment aims to minimize the sum of the squared distances between all corresponding points of the nominal and measured surface. Consequently, a deformed mirror will be oriented to be partially above and below the nominal profile. Since there is no absolute reference point, the discussion must be limited to relative deformations from the nominal geometry, tolerating, for example, a constant offset from 0 close to the shape-determining grooves.

In the absence of external forces on the mirror, the surface of the free mirror should resemble a plane with its surface normal oriented along r . However, the uniform tensile stress induced by the supermirror coating applied to the bottom of the mirror leads to a dome-like deformation of the substrate as illustrated in Fig. 6.25. Panel (a) illustrates the acquired and aligned height profile, showcasing almost circular contours of constant height. As depicted in panel (b), we observe a maximum relative deformation of about $\Delta r_z = 0.10 \text{ mm}$ along the z -axis for each of the investigated regions. Finally, panel (c) indicates a slightly smaller deformation of $\Delta r_x = 0.07 \text{ mm}$ along the x -axis, primarily attributed to the smaller extent of the mirror along this direction. Overall, the mirror exhibits significant deformation, in agreement with expectations arising from uniform tensile stress applied to the bottom of the substrate.

Straight Grooves

Facilitating the insertion of the mirrors into the shape-determining grooves, they are fabricated with a tolerance of 0.02 mm , i.e., mirrors with $d_{\text{sub}} = 0.2 \text{ mm}$ are supported by grooves 0.22 mm wide. To investigate the impact of this tolerance on the shape of the mirrors, the height profile of a mirror was acquired after being inserted into a straight groove. Again, disregarding any external forces, the mirror should resemble a plane with its surface normal parallel to r .

The obtained height profile and cuts along the x - and z -directions are presented in Fig. 6.26. As the scanner requires a direct line of sight between both of its cameras and the area of investigation and given that the straight grooves were machined at their original position at the vertical center of the testpiece, the long edges of the mirrors become obscured by the test piece. The available data, which covers about 30 mm of the total width of 40 mm , reveals a similar shape compared to the free mirror, although with a less pronounced deformation. In both cases, the central parts of the mirror are elevated compared to the edges. However, at the long edges of the height profile, near the shape-determining grooves, the mirror supported

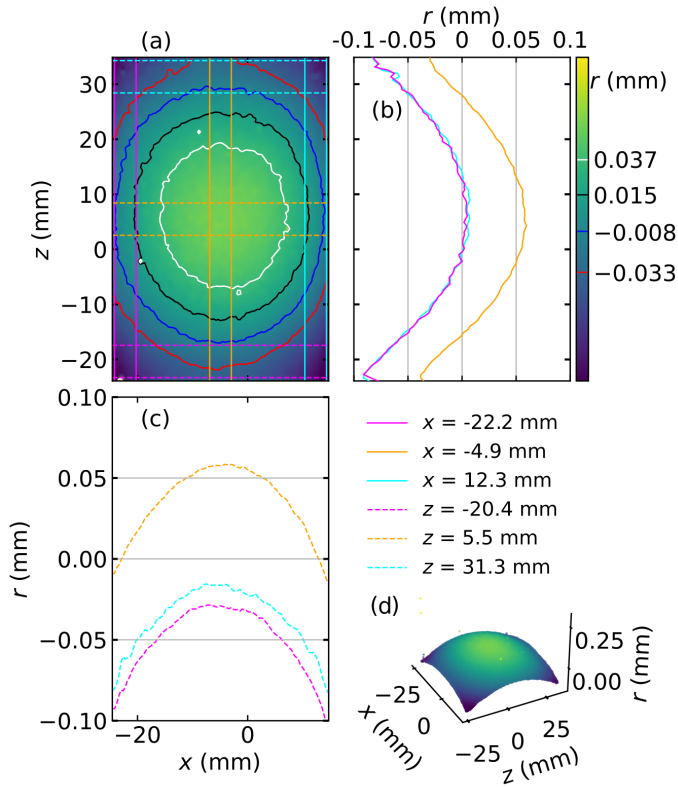


Figure 6.25: Height profile of an unsupported silicon substrate with the super mirror coating applied only on the bottom side. Panel (a) shows the aligned height profile $r(x, z)$, where z denotes the direction parallel to the long side of the mirror. Nearly circular contours of constant height are overlaid on the color plot as indicated by the color bar. Panels (b) and (c) show vertical and horizontal cuts through this height profile. The values shown are obtained by calculating the horizontal and vertical medians between the two lines of corresponding color and line style in (a). Panel (d) provides a 3D representation of the height profile (not to scale).

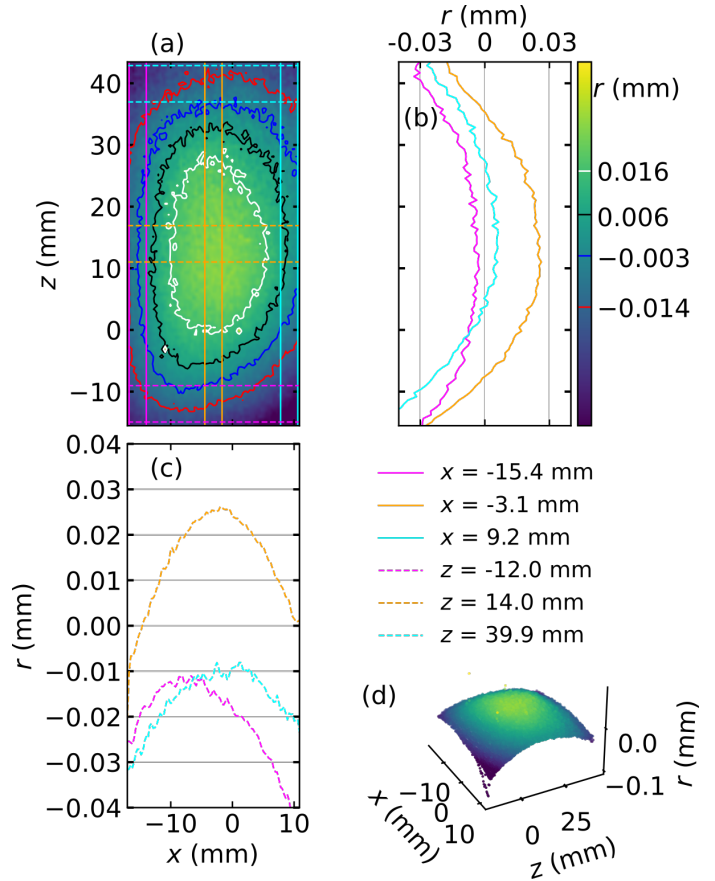


Figure 6.26: Height profile of a mirror inserted into the straight grooves of the test piece with a specified tolerance of 0.02 mm. Although the substrate is less prominently curved compared to the free mirror (compare the different ranges of r), particularly distant from the shape-determining grooves, there is still a noticeable deviation from the nominally flat geometry. For a detailed explanation of the panels, compare the analogously structured Fig. 6.25.

by the straight grooves exhibits a much smaller deformation. The pink solid line in Fig. 6.26 (b) indicates that the left side of the mirror does not curve for more than $\Delta r_z = 0.025$ mm over its complete length, which is significantly less than the almost 0.1 mm obtained for the free mirror, as illustrated by the pink solid line in Fig. 6.25 (b)⁽⁶⁾. This comparison

⁽⁶⁾Evaluating the deformation of the mirror inserted into the straight grooves was limited along the x -axis,

suggests that the elevation is well-controlled close to the grooves. Still, deformation happens due to the given tolerance of 0.02 mm and the measurement limitations, preventing us from accurately determining the mirror geometry very close to the grooves.

Parabolic Grooves

Inserting the mirror into the outermost parabolic groove with $r(z = 0 \text{ mm}) = 20 \text{ mm}$ (compare section 6.2.1) yields the height profile depicted in Fig. 6.27 (a). The parabolic shape of

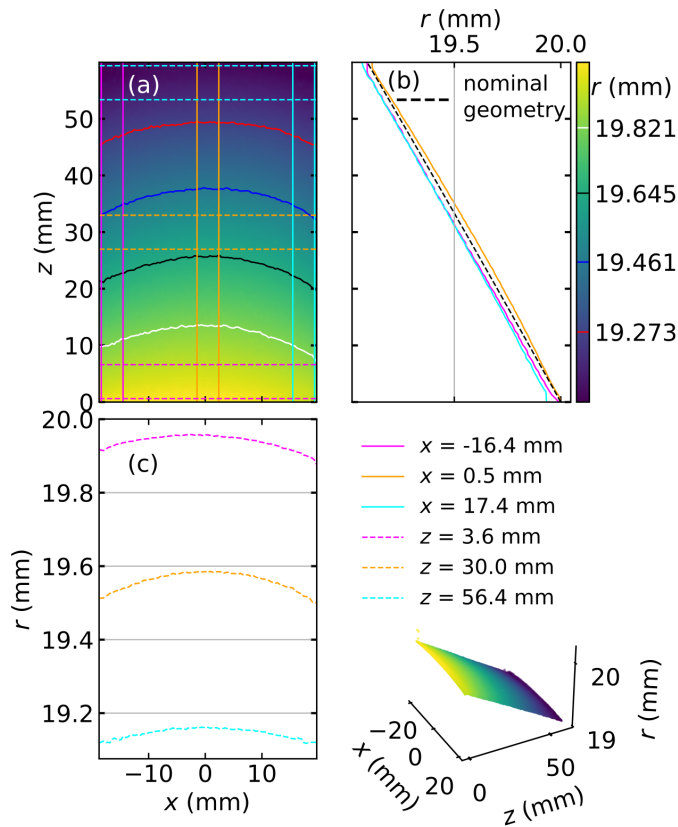


Figure 6.27: Height profile extracted from the mirror inserted into the parabolic grooves. The figure is structured analogously to Fig. 6.25

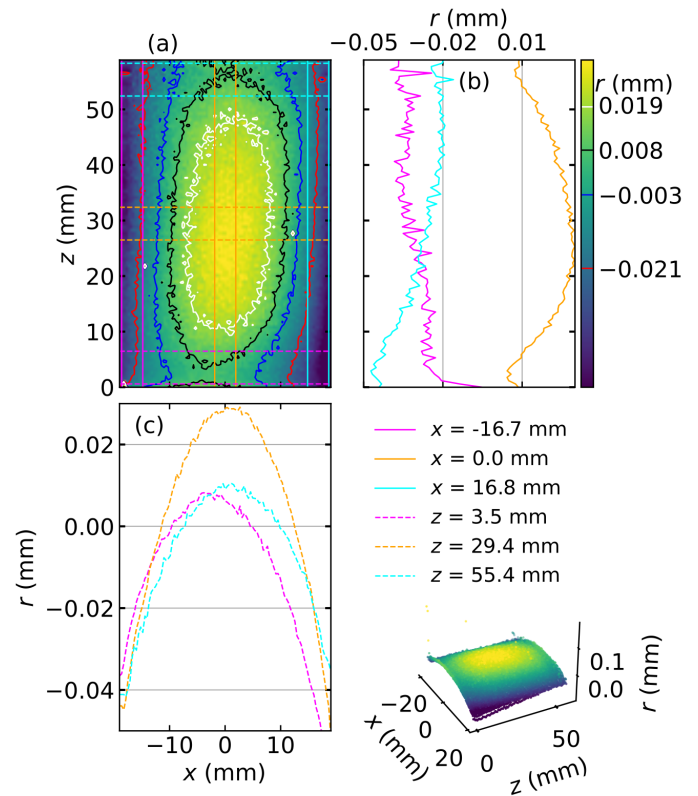


Figure 6.28: Difference between the measured and the nominal height profiles for a mirror inserted into the parabolic grooves. The figure is structured analogously to Fig. 6.25.

the reflective surface entails a nominal decrease of the distance from the optical axis, $r(z)$, with increasing z . The acquired data corresponding to the mirror was rotated and shifted to achieve an overall best fit with the nominal geometry, depicted as a broken black line in Fig. 6.27 (b). Similarly to the case of the free mirror, the tensile stress associated with the supermirror coating applied to the bottom side entails an increased curvature of those areas of the substrate that are further away from the shape-determining grooves. Fig. 6.27 (c) illustrates that the relative deformation along the x -axis amounts to approximately 0.05 mm, which is in alignment with the values obtained for the free mirror, indicating that the minute

as no data was acquired very close to the grooves.

curvature of the parabolic groove does not impact this deformation significantly.

To evaluate possible deformations along the z -axis, we subtracted the height profile of the nominal geometry from the one acquired with the 3D scanner with the result illustrated in Fig. 6.28 (a). Cuts along the z -axis through this difference are depicted in Fig. 6.28 (b) and exhibit a nearly constant offset between the nominal and the measured data close to the shape-determining grooves, indicating an absence of excess deformation. While the deformation close to the left side (pink curve) amounts to $\Delta r_z \leq 0.02$ mm, which is within the tolerance specified for the grooves, the blue curve displays a slightly more severe deformation $\Delta r_z \leq 0.03$ mm. Distant from the shape-determining grooves (orange curve), we again observe a significant deformation of the substrate exhibiting a strong curvature, which is likely responsible for the observed reduction in focusing quality and the reduction of the focal length from the nominal value.

Elliptic Grooves

In contrast to the straight and parabolic geometries, the ellipse nominally displays a significant curvature. Despite this fundamental difference, the obtained height profiles (Fig. 6.29) and especially their deviation from the nominal geometry (Fig. 6.30) yielded similar results compared to the other shapes. Once again, we observe that the grooves accurately determine the geometry of the mirrors, evident from the small relative height difference on the left side of the mirror $\Delta r_z \leq 0.02$ mm (pink curve in Fig. 6.30 (b)). However, distant from the grooves, the substrate deforms more freely ($\Delta r_z = 0.04$ mm) and exhibits a distinct excess curvature as displayed by the orange curve. Along the x -axis, the substrate exhibits its usual relative difference of about $\Delta r_x = 0.05$ mm, indicating that the increased curvature of the elliptic shape does not stabilize the mirror against these lateral deformations.

Summary of Mirror Deformations

We employed 3D scanning to evaluate the deviation of the realized mirror geometries from the nominally intended ones. For this purpose, test pieces with selected grooves were fabricated, into which the leftover mirrors were subsequently inserted. The deformation of the mirrors is attributed to the applied FeSi supermirror coatings, which induce a uniform tensile stress on the coated bottom side of the silicon substrates. As the distance to the shape-determining grooves increases, the mirrors deform more freely, and the observed deviations generally increase. The specified tolerance of the grooves (0.02 mm) is on the same scale as the observed deformations and, therefore, must always be considered when designing NMO systems.

The observed deformation of the parabolic mirrors aligns well with the neutron images presented in Chapter 5.5. We noticed better imaging quality close to the grooves, corresponding to the minor discrepancies between the nominal and observed mirror geometry. With increasing distance from the grooves, the effects observed in Fig. 6.15, such as an increase in the minimum achievable FWHM and a shift of the point of optimum focusing toward the device, are both explained by the increasing curvature of the reflecting surfaces. Verifying this result through Monte Carlo simulations is part of our future research.

During the measurements on the polarizing elliptic NMO, we demonstrated that coating the substrates on both sides significantly reduces the innate deformations, likely due to the stresses on both sides of the substrates canceling. This represents an avenue towards reducing deformations of any mirrors from their nominal geometry.

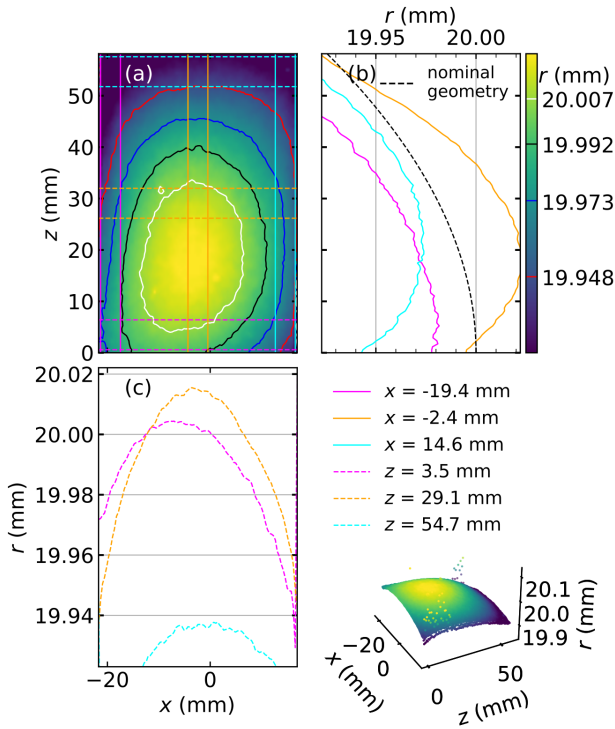


Figure 6.29: Height profile acquired for a mirror inserted into the outer elliptic groove of the test piece. The figure is structured analogously to Fig. 6.25.

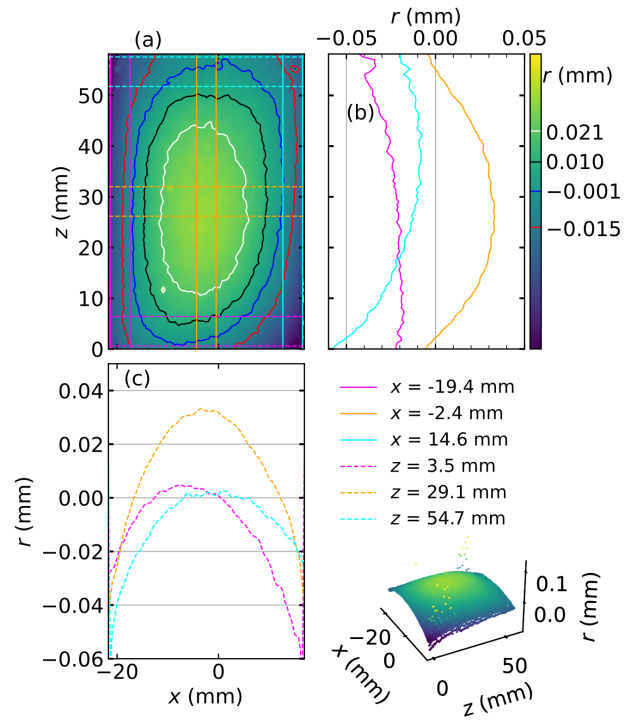


Figure 6.30: Difference between the obtained and the nominal height profile for the outer elliptic mirror. The figure is structured analogously to Fig. 6.25.

Further investigations will include determining the stress induced by supermirror coatings utilizing X-ray scattering [184]. These results will be used to perform finite element method simulations predicting the curvature of the substrates without building prototypes. Additionally, we will perform Monte Carlo simulations using the obtained deformed geometries and compare the results to the neutron measurements performed in this thesis. Finally, we will conduct an in-depth exploration of stress reduction or groove manipulation to address the deformations.

7. Applications of Nested Mirror Optics

In this chapter, we explore applications of **NMOs**, emphasizing their capability to enhance the extraction of neutrons from small sources by mitigating the effects of under-illumination associated with conventional neutron guides. The importance of such an application for high-brilliance sources alone justifies the consideration of **NMOs** when devising delivery systems for future neutron facilities. The chapter closely follows our work published in Herb et al.[19].

The calculations, simulations, and experiments presented earlier, utilizing polarizing and non-polarizing elliptic prototype **NMOs**, showcased an efficient, one- and two-dimensional imaging of neutrons between their two focal points. This indicates that an elliptic **NMO** can function as a comprehensive neutron delivery system contained within a single, compact device. To expand our examination towards longer transport distances, including losses incurred due to gravitational bending of neutron trajectories, we present the results of additional McStas simulations for planar elliptic **NMOs** in section 7.1.1.

In addition to exploring elliptic **NMOs**, we have demonstrated the complementary functionality offered by parabolic **NMOs**. They can transform a high-divergence beam emitted by a compact source into a low-divergence one, concurrent with increasing the beam size. The original phase space volume of neutrons, as extracted from the source, can be effectively recovered using a second parabolic **NMO** that refocuses the low-divergence neutrons. In section 7.1.2, we will illustrate how a system comprising two parabolic **NMOs** connected by an extended guide can circumvent gravitational limitations and achieve a reasonable brilliance transfer over substantial length scales, reaching hundreds of meters.

Furthermore, the complementary properties of elliptic and parabolic **NMOs** establish a versatile toolkit that can serve as the basis for designing a wide range of application-specific beamlines. Additionally, parabolic **NMOs** could be integrated into existing guide systems at well-established research facilities to act as a final stage for neutron delivery. For example, they could be employed to focus a beam onto a small sample inside a pressure cell. While this hybrid approach might not provide the same degree of brilliance enhancement as a fully **NMO**-based neutron extraction system, it could still result in substantial improvements in beam quality and a reduction in background at the point of focus.

7.1 Beam Extraction

The task of extracting neutron beams from a compact high-brilliance neutron source is challenging for various reasons. On the one hand, there are technological challenges. For instance, areas of increased radiation near the source necessitate a careful selection of materials and frequent replacements of neutron optical components due to radiation damage. On the other hand, there are more theoretical challenges. Optimizing the efficiency of neutron beam delivery, as characterized by its extent, divergence, and wavelength spectrum, is subject to fundamental limitations outlined in Liouville's theorem [117]. This theorem dictates that, for systems obeying Hamilton's equations of motion, the phase space density cannot increase. Ideally, the density at the sample position would match that emitted at the surface of the source. **NMOs** were developed to approach this limit in neutron extraction for a large

solid angle of transportation. Another advantage of implementing NMOs is that all sensitive optical components are positioned at a safe distance from the source and the sample. This not only mitigates some of the technological challenges but also allows for the utilization of extensive sample environments.

As discussed in section 5.2.2, under-illumination of guides can be a significant issue when extracting neutrons from compact sources. This challenge is particularly relevant for small, high-brilliance moderators like the flat, *pancake*-shaped para-hydrogen moderator at the ESS [185, 163] and *finger moderators* [186] used for compact accelerator-based neutron sources [187].

At the ESS, neutron beam optics assemblies (NBOAs) are located at a minimum distance of $d_{\text{mg}} \approx 2$ m [188] away from a flat moderator with a thickness of $t_m = 30$ mm. In comparison, the extraction guides are significantly taller, i.e., $h_g > t_m$. table 7.1 shows that, for typical NBOA parameters at the ESS, the guide stays under-illuminated even for wavelengths as short as $\lambda = 1$ Å. A significant portion of potential useful neutrons is already lost during beam extraction. These losses increase for longer wavelengths with their correspondingly larger critical angle.

As emphasized by Andersen et al. [185], “*The beam extraction efficiency suffers when the*

λ (Å)	2α (deg)	h_m (mm)	E_{eff}
0.5	0.35	46.1	0.65
1	0.69	57.7	0.52
2	1.39	80.7	0.37
4	2.78	127	0.24
6	4.16	173	0.17
10	6.93	265	0.11
15	10.40	380	0.08
20	13.68	496	0.06

Table 7.1: Vertical guide illumination losses for a typical NBOA at the ESS according to Eq. (5.7). We disregard further losses due to imperfect supermirror reflectivity and employ the following parameters for the calculation. $t_m = 30$ mm, $h_g = 34.6$ mm, $d_{\text{mg}} = 1903$ mm, and $m = 3.5$. The maximum divergence still reflected at the mirrors is determined by $2\alpha = 2\theta_{c,m}$. Illumination losses in the horizontal direction can further reduce the efficiency, albeit to a lesser extent for a moderator of assumed large width, $w_m = 200$ mm. The table is reproduced from Herb et al. [19].

source is reduced to a size similar or smaller than the opening of the neutron guide. This results in a trade-off when reducing the source size, between the resultant brightness increase and the loss of beam extraction efficiency”. In agreement with this statement, we find that the under-illumination of neutron guides introduces two distinct compromises. On the moderator side, it limits the optimization of the moderator dimensions for maximal brilliance. Ideally, the moderator’s extent should be tailored to match the size of the small samples usually investigated, providing the largest brilliance possible. On the instrumental side,

under-illumination constrains the potential of the instrument. Since it limits the transport of more divergent neutrons, an instrument designed for high resolution cannot be extended by a high-intensity option, even if that would be otherwise convenient.

The trade-off mentioned in the quote from Ref. [185] does not apply to elliptic **NMOs**. They accept a divergence determined geometrically by the ratio of their height, b_0 , to its focal length, f . When a sufficient solid angle is available for neutron extraction, elliptic **NMOs** facilitate the transport of long-wavelength neutrons to an instrument without the large efficiency losses typically associated with this process. Furthermore, considering the geometric losses derived in Eq. (5.17), the transport efficiency of **NMOs** increases with decreasing moderator size. This distinct feature of **NMOs** opens the door to design high-brilliance sources that enable fully optimized neutron delivery to even the smallest samples without dealing with the usual compromises imposed by conventional neutron extraction systems.

7.1.1 Integrated Brilliance Transfer by Elliptic NMOs

In this section, we expand our analysis of a planar elliptic **NMO** with unit magnification, serving as a fundamental solution for one-dimensional neutron extraction and transport between two focal points. Our primary objective is to investigate the impact of size-dependent effects on the transport efficiency. Again, we consider focusing only in the vertical direction, which conveniently enables us to address the influence of gravity.

The geometry of a planar elliptic **NMO** dictates the reflection kinematics during the transport of a neutron beam. When a neutron interacts with the $(n + 1)^{\text{th}}$ mirror plate (compare Fig. 5.14 for the mirror indexing conventions) it is reflected within a narrow range of angles centered approximately around $\arctan(b_n/f) \approx b_n/f$; a range which becomes narrower for smaller ratios w/f and l/f . Because the angle of reflection for a given wavelength is limited by $\theta_c(\lambda)$, the reflectivity edge of the supermirror produces a spectral cutoff for wavelengths shorter than $\lambda_{c,n}$, determined by the relation

$$b_n/f \approx m_n \kappa \lambda_{c,n}. \quad (7.1)$$

Here κ represents the wavelength-dependent critical angle of nickel, $\kappa = 0.099 \text{ deg}/\text{\AA}$. When using a common m -value, $m_n = m$, for all mirrors, this results in different $\lambda_{c,n}$ values for each of the mirrors. However, because the angles of reflection and mirror indices n are strongly correlated, it is possible to establish a common cutoff for the entire covered angular range, denoted as $\lambda_{c,n} = \lambda_c$. According to Eq. (7.1), achieving this would necessitate gradually decreasing the m -values towards the center of the **NMO**. Shaping the spectrum by employing elliptic **NMOs** might eliminate the need for auxiliary devices, such as Bragg filters or velocity selectors, to remove unwanted faster neutrons. In practice, a few specific m -values might suffice to achieve a soft cutoff, effectively preventing undesired neutrons from reaching the instrument. An interesting option suited to elliptic **NMOs** involves using band-pass supermirrors⁽¹⁾ to provide a divergent beam with a small wavelength spread and considerable flux [189], similar to the coatings found in laterally-graded parabolic guides [190]. Additionally, we showed how utilizing polarizing supermirrors for the **NMO** facilitates polarizing the beam.

⁽¹⁾These supermirrors only cover a small range of different layer thicknesses, thereby fulfilling Bragg's equation for only a limited range of wavelengths at a given angle of incidence.

Considering the relationship between the mirror indices and the angles of reflection, one can use an aperture A_2 to illuminate a selected range of mirrors, thereby defining the divergence of the beam at the sample position. If the wider angular range is not required for any applications, the NMO can be configured with correspondingly fewer mirrors. In the reported experiments, we have analyzed the imaging properties of small, planar elliptic NMOs. These devices were configured in two ways: a *half-device* with mirrors on one side of the optical axis, and a *full-device* with mirrors on both sides. In applications where a narrow beam divergence is required, such as Small Angle Neutron Scattering, the half-device configuration offers continuous coverage of the angular range, spanning from approximately $\alpha_N \approx b_N/(f - l/2)$ to $\alpha_0 \approx b_0/(f - l/2)$ ⁽²⁾. When using a full device with N additional mirrors on the other side, the range of covered angles is extended by $-\alpha_0$ to $-\alpha_N$, with a gap in between due to the divergence hole.

We will now discuss the effects of size-related factors on the brilliance transfer by utilizing simulations of a full device, equipped with $2N$ identical mirrors, single-side coated with an $m = 4.1$, $R_e = 82\%$ supermirror and possessing a thickness of $d_{\text{sub}} = 0.15$ mm. To assess the neutron transport efficiency, we calculated the partly-integrated brilliance transfer B , as defined in Eq. (6.2). Note that we consider neutrons emitted over the whole angular range between the geometric extremes, $[-\alpha_0, \alpha_0]$. This definition of the brilliance transfer as an integral quantity includes the losses associated with the divergence hole. There are several options available to achieve additional refocusing in the horizontal plane. One can utilize a double-planar device as described in section 5.6, or, for a wide moderator and not too long wavelengths, a conventional ballistic channel of vertical mirrors, for which horizontal illumination losses might still be acceptable. When considering the linearly independent components of neutron motion, the two-dimensional integrated brilliance transfer can be calculated as the product of the corresponding B -values for both dimensions lateral to the beam. Therefore, simulating a single planar elliptic NMO is sufficient.

Our primary focus lies in understanding how B changes with the size of the NMO and the neutron wavelength λ for an NMO which transports neutrons with the maximum possible divergence. To achieve this, we conducted simulations for a narrow range of wavelengths ($\pm 5\%$) around a central value λ . For each λ , we chose a corresponding value of b_0 such that the critical angle of reflection matched the geometrically-defined divergence $\alpha_0 = \theta_c$. To achieve linear size scaling of the whole NMO, we varied the focal length of the NMO, f , while keeping the ratios b_0/f and l/f , and the height of the source, $w = 6$ mm constant.

For each value of b_0 , we implemented the maximum number of mirrors for the respective wavelength. This number $2N$ is limited by requiring that the minimum distance between mirror surfaces exceeds the sum of the thickness of the substrate and the space between adjacent grooves, i.e., $d_{\text{min}} = d_{\text{sub}} + d_g$. We conservatively chose $d_g = 0.4$ mm as a technically reasonable lower limit for the space between mirrors. Considering that d_{min} is constant, the total number of mirrors $2N$ increases when scaling up the size of the NMO. The results depicted in Fig. 7.1 (a) can be explained as a combination of several effects. Firstly, the relative impact of the divergence hole becomes smaller for increasing values of f and a consequently larger number of mirrors $2N$. Secondly, geometric losses associated with neutrons being reflected twice or not at all when passing through one of the mirror channels are reduced for

⁽²⁾We note that the semi-minor axis b_N corresponds to an imaginary $(N+1)$ th mirror.

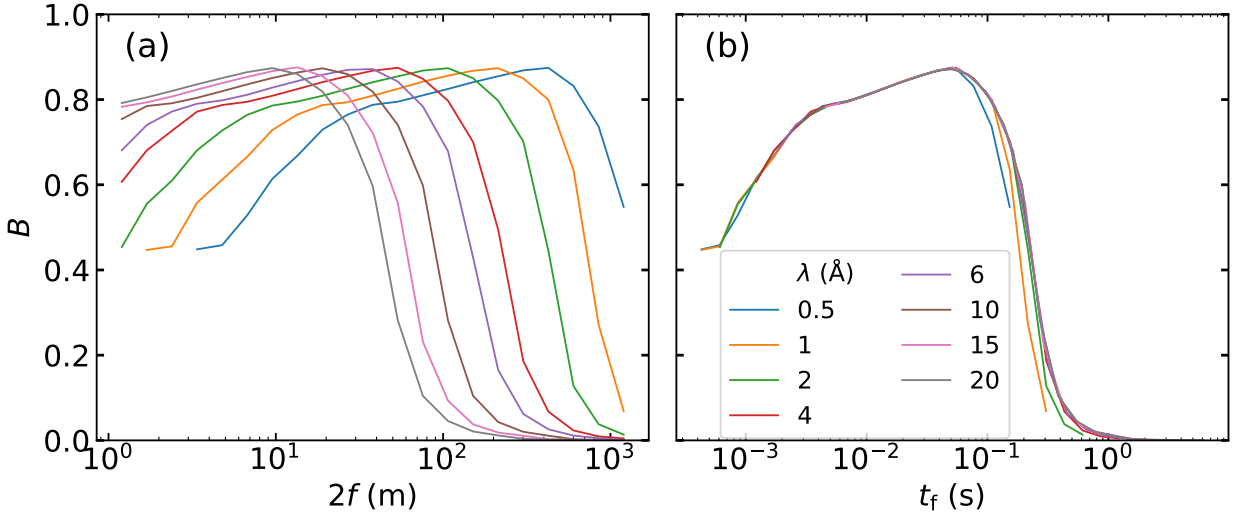


Figure 7.1: Simulated partially integrated brilliance transfer B , as defined in Eq. (6.2). A planar elliptic NMO was scaled proportionally to its focal length f . As described in the text, the following parameters remained constant: $l/f = 1/10$, $d_{\text{sub}} = 0.15$ mm, $m = 4.1$, $R_0 = 82\%$, and $w = 6$ mm. Panels (a) and (b) display the same data presented as a function of $2f$ and the time of flight t_f , respectively. The figure is reproduced from the work of Herb et al. [19].

larger NMOs. As discussed in Eq. (5.17), the magnitude of this loss, $\propto w/b_n$, decreases as the size of the NMO is scaled up while keeping the source size constant.

However, gravity disturbs the neutron trajectories, violating the assumptions upon which the NMO design is based. While it is theoretically possible to adjust the mirror distances to account for the influence of gravity, this approach only works for a small range of wavelengths and is thus considered overly restrictive. Gravity's impact on f is opposite to the effects mentioned above, ultimately limiting B to an optimal value that, for the specified assumptions, remains well above 85% across a wide range of f values. The impact of the gravity-associated effects depends on the time it takes for a neutron to travel from one focal point to the other, denoted as t_f . This time is proportional to the neutron's wavelength and the focal length of the NMO: $t_f = 2f \cdot v_n \propto 2f \cdot \lambda$. When investigating B as a function of t_f , we observe similar values across all simulated wavelengths, as illustrated in Fig. 7.1 (b).

The surprisingly small effect of gravity on B for $t_f \leq 0.05$ s can be understood by considering the symmetry of the neutron trajectories, which entails that the flight time from the source to the NMO equals the time spent between the NMO and its second focal point. As the neutron travels, it accumulates additional vertical momentum due to gravity. This results in an increase of the momentum parallel to the surface normal for reflections at the set of mirrors located below the optical axis and a reduction of this momentum for reflections above the optical axis. Consequently, the number of neutrons that are reflected at mirrors of a given m -value remains approximately constant. Moreover, given the flat reflecting surfaces, if the neutron is reflected, this additional momentum is reversed, ensuring that the imaging

condition is still fulfilled, similar to the case without the influence of gravity⁽³⁾.

The B -values for the NMO, as seen in Fig. 7.1 (a), are notably larger than those for a representative NBOA at the ESS, as given in table 7.1, despite the discussion of the NMO accounting for additional losses due to the finite mirror reflectivity. Furthermore, these loss mechanisms are expected to impact NBOAs more severely, given the increased number of required reflections compared to an NMO. By utilizing parabolic NMOs, it is feasible to double the divergence transportable in each dimension by employing a configuration consisting of two parabolic NMOs. This is achieved by halving the angle of reflection compared to a single ellipse. The following section demonstrates the suitability of this concept for long-distance neutron transport, as it is less constrained by gravitational beam bending.

7.1.2 Extraction into a Low-Divergence Beam with Parabolic NMOs

As discussed in section 5.4, an elliptic NMO with unit magnification can effectively restore the beam phase space emitted at F_1 at its second focal point, F_2 . However, for focal lengths f exceeding a few tens of meters, and for typical cold-neutron wavelengths, gravitational bending of neutron trajectories disrupts the vertical brilliance transfer of a simple elliptic NMO, as depicted in Fig. 7.1. This issue is also present in long focusing guides [191], leading to notable neutron losses and phase space distortions. Instruments with very long neutron flight paths, such as high-resolution time-of-flight (ToF) spectrometers, demand an alternative approach.

To address such applications, we propose a system that comprises two sets of parabolic NMOs connected by a long guide enabling the efficient transport of the low-divergence beam, as illustrated in Fig. 7.2 (a). The focal lengths of the two sets of parabolic NMOs, f_1 and f_2 , can be adjusted based on the specific requirements of the instrument. In this setup, the first parabolic double-planar NMO extracts the initially divergent beam from the compact moderator and transforms it into a low-divergence beam with an increased extent, adhering to Liouville's theorem. This transformation significantly reduces the number of reflections per meter within the guide and ensures that the maximum reflection angle remains well below the critical angle. Consequently, reflection losses are reduced, and the length of the guide has only a weak effect on the transported flux. At the end of the long guide, the second parabolic double-planar NMO refocuses the low-divergence onto its focal point.

We present McStas simulation results of the above-described system using example parameters not optimized for any specific purpose. The operational principle of such a configuration is depicted in Fig. 7.2. The simulation setup consists of a circular moderator with a diameter of 30 mm. This moderator provides angle- and wavelength-independent brilliance in the range of 2 Å to 8 Å and illuminates the double-planar parabolic NMO. Each set contains two subsystems, one focusing in the horizontal direction and the other along the vertical direction. The beam is transformed to low divergence by the first double-planar NMO and enters a straight guide coated with $m = 2$ supermirror. The guide measures a length of $l_g = 160$ m and has a square cross section with side lengths of 218 mm. At the end of the long guide, the second double-planar parabolic NMO refocuses the beam onto its focal point, F_2 . Both NMOs share a common focal length of 6 m measured from the midpoint between

⁽³⁾Note that the reflection process is only separated into two dimensions, one parallel and one perpendicular to gravity, for double planar devices.

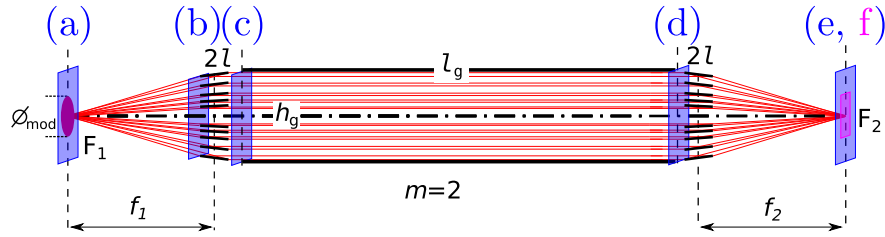


Figure 7.2: Sketch of the simulated long-distance neutron transport system based on two double-planar parabolic NMOs connected by a long straight neutron guide. The violet quadrilaterals indicate PSDs determining spatial intensity distribution during the simulations. The PSDs (a)–(e) each cover an area of $218 \times 218 \text{ mm}^2$ matching the guide. The final PSD (f) measures an area of $30 \times 30 \text{ mm}^2$ and provides a more detailed view of the focused beam. The figure is reproduced from the work of Herb et al. [19].

the parabolic NMOs to the joint focal point. These NMOs are equipped with $m = 4.1$ supermirrors, have a total length of 1.2 m, and are designed to match the cross-section of the guide. In these simulations, the substrate thickness is neglected, $d_{\text{sub}} = 0$.

Fig. 7.3 depicts simulated spatial intensity distributions at various positions of the setup shown in Fig. 7.2. The data is obtained from simulations with and without gravity, respectively. Panel (a) and (b) show the intensity distribution as emitted from the circular moderator and the homogeneous illumination of the first set of parabolic NMOs, respectively. The texture observed in the intensity distribution at the beam monitor (c), after the first double-planar NMO, results from the contributions of individual mirrors of the NMO, and the central, perpendicular stripes of lower intensity correspond to the divergence hole. Because the first planar subsystem from the source focuses horizontally, the vertical stripe is more blurred than the horizontal one. The influence of gravity on the low divergence beam entails a vertical gradient of the neutron intensity at the end of the long guide (d). The texture observed at the entrance of the guide was smoothed out along the guide. Approximately $I_f = 25\%$ of all neutrons arriving at the first NMO arrive within an area of $30 \times 30 \text{ mm}^2$ at F_2 (f). Gravity leads to a minor vertical distortion of the intensity distribution of the polychromatic beam, with its maximum found marginally below $y = 0 \text{ mm}$.

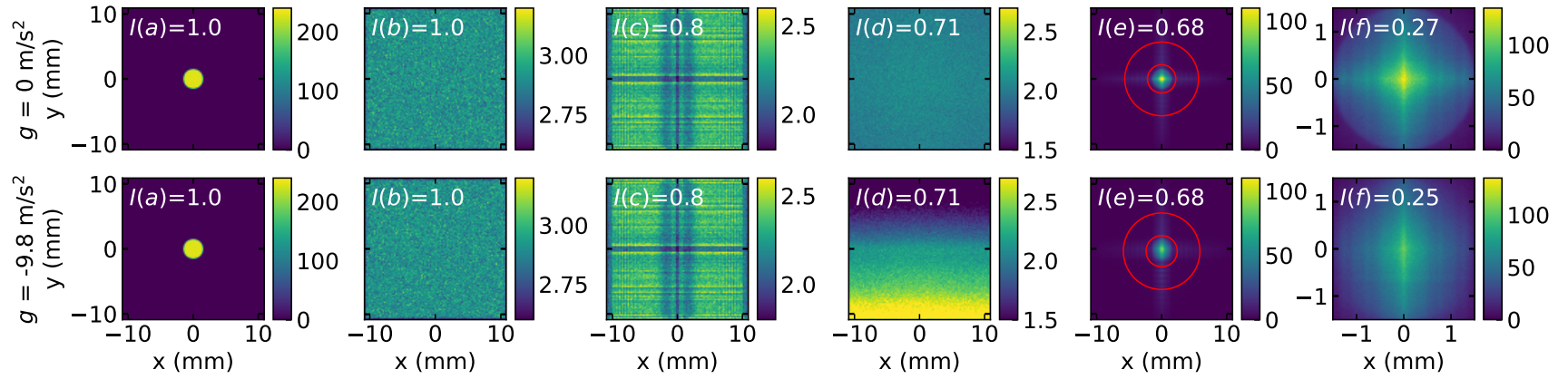


Figure 7.3: Simulated spatial intensity distributions obtained at the locations denoted in Fig. 7.2. The top and bottom rows correspond to simulations disregarding and accounting for gravity. The total intensity arriving at each PSD is denoted in white. (a) Neutrons are emitted with uniform brilliance at the circular moderator. (b) The entrance of the first set double-planar parabolic NMO is illuminated homogeneously. The intensity incident onto this monitor sets the basis for normalization $I(b) = 1.0$ (c) After passing the parabolic NMO, the neutron beam is textured due to reflections at individual mirrors. (d) At the exit of the long guide, when accounting for gravity, the low-divergence neutron beam accumulates at the bottom of the guide. (e and f) The second double-planar NMO refocuses the neutrons and recovers the initial shape of the moderator. Red circles in (e) indicate areas encompassing integrated intensities of $I_{\varnothing} = 0.3I(b)$ and $I_{\varnothing} = 0.5I(b)$, respectively. Roughly 25% of the neutrons incident on the first NMO are recaptured within the area (f) measuring $30 \times 30 \text{ mm}^2$. Figures are reproduced from the work of Herb et al. [19].

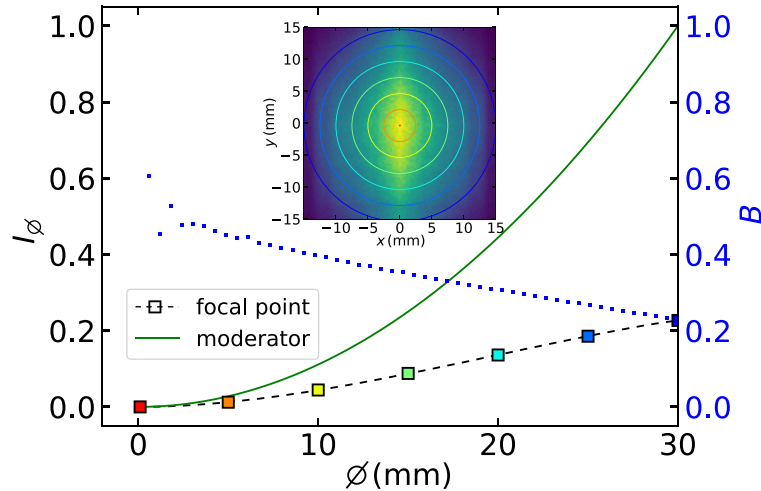


Figure 7.4: Intensity fraction and integrated brilliance transfer B , as obtained within a circular monitor at F_2 with a diameter \varnothing . The intensity data shown in the inset is reproduced from Fig. 7.3(f). For comparison, the corresponding, quadratically increasing intensity fractions at the moderator (a), with diameter 30 mm, are shown in green. Values of B shown in blue are larger than 40% for a target area of $\varnothing \leq 10$ mm and still 23% for $\varnothing = \varnothing_{\text{mod}} = 30$ mm. The colors of the circles match the colors of the data points. The figure is reproduced from Herb et al. [19].

Fig. 7.4 illustrates the relationship between the fraction of neutrons initially entering the first NMO that eventually reach a circular region at F_2 . This relationship is represented as a function of the circle's diameter, \varnothing . To illustrate, circles with diameters of 10 mm and 30 mm capture intensity fractions of $I_\varnothing = 0.045$ and $I_\varnothing = 0.23$, respectively. However, it should be noted that the integrated brilliance transfer, $B = I_\varnothing / (\varnothing / \varnothing_{\text{mod}})^2$, increases with decreasing \varnothing and reaches $\approx 50\%$ for a beam diameter of several millimeters. Importantly, our simulations already account for beam losses of around 30% due to finite supermirror reflectivity.

In summary, these results underscore the excellent performance of neutron transport, particularly when targeting small samples. Most importantly, the gravitational effects exhibit a negligible impact on the overall performance of this system consisting of compact NMOs.

When comparing the proposed system with a configuration based on elliptic NMOs, which already boasts several advantages, we can identify the following additional benefits:

- The system featuring two parabolic NMOs allows us greater flexibility when it comes to choosing the length of the straight guide section for long-distance neutron transport.
- The low beam divergence provided by the first parabolic NMO enables the use of mirrors with smaller m -values, taking advantage of a higher edge reflectivity at a reduced cost.
- The lateral extent of the neutron beam remains smaller throughout the transport in this system. Consequently, it reduces the amount of required shielding, which can be a practical advantage in experimental setups.

To avoid the direct line-of-sight from the experiment to the moderator, a vertically imaging NMO could be combined with a horizontal beam bender, which channels neutrons through multiple reflections within the empty space between curved mirror plates [192, 193]. Another approach to interrupt the line-of-sight relies on using a slightly tilted NMO. However, this approach will come at the expense of deteriorating the beam quality.

The combination of both elliptic and parabolic NMOs offers versatile configuration options for neutron beamlines. When a beamline requires the installation of choppers, utilizing elliptic NMOs can be advantageous. They have the capability to refocus the neutron beam onto the slit position of the choppers, as illustrated in Fig. 7.5 (b). For applications that require both choppers and a long neutron flight path, such as high-resolution ToF instruments, a combination of elliptic NMOs followed by a pair of parabolic NMOs connected by a long guide (as previously discussed) might be the best choice. This configuration, shown in Fig. 7.5 (c), provides the flexibility needed for such demanding experiments.

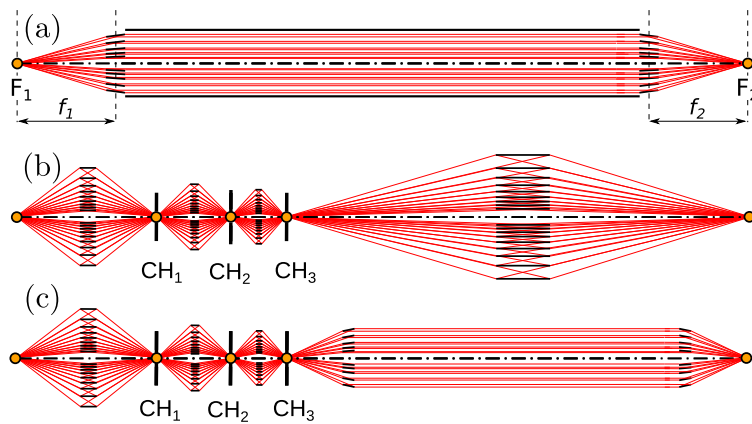


Figure 7.5: Some options for long-distance transport of neutrons from a moderator to an instrument. (a) System of two parabolic NMOs connected by a guide. Different focal lengths f_1 and f_2 may be used for non-unit magnification (see also section 7.2). (b) Elliptic NMOs provide intermediate beam images to place choppers (CH_1 - CH_3). (c) Configuration with elliptic and parabolic NMOs. Figures are reproduced from the work of Herb et al. [19].

7.2 Focusing and Magnification

Combining two parabolic NMOs with distinct focal lengths, f_1 and f_2 , provides the means to magnify neutron beams, as depicted in Fig. 7.6. This magnification can be easily derived from Eq. (5.18) as follows:

$$\begin{aligned} \frac{r_1}{f_1} = \alpha_1 = \alpha_2 = \frac{r_2}{f_2}, \\ \frac{r_2}{r_1} = \frac{f_2}{f_1}, \end{aligned} \tag{7.2}$$

where we employed the fact that the divergence of neutrons does not change within the long guide, $\alpha_1 = \alpha_2$. This neutron magnification technique might find utility in neutron imaging or microscopy [176, 194], offering an avenue to overcome the spatial resolution

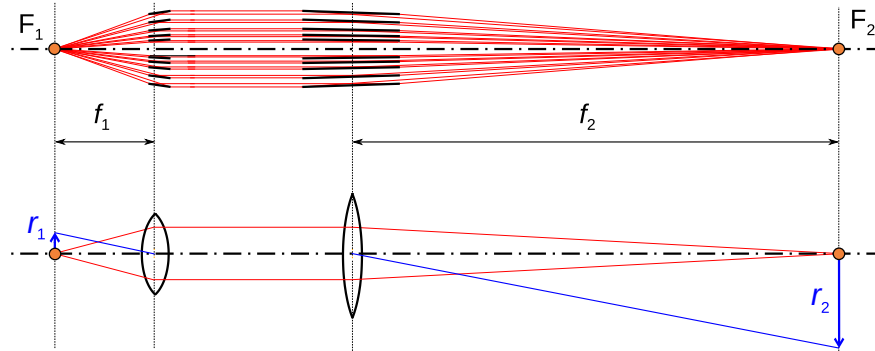


Figure 7.6: Sketch of a lens system comprised of two parabolic **NMOs**. The bottom part of the figure provides an analogy to this neutron lens system in the context of visible light optics. In both cases, the magnification is given by $M = f_2/f_1$. Figure is reproduced from Herb et al. [19].

limitations in current neutron imaging setups, which typically achieve spatial resolutions on the order of $10\ \mu\text{m}$. These limitations arise due to factors such as the resolution of neutron-sensitive scintillators and the available neutron flux at the sample position [195]. To achieve a resolution of $10\ \mu\text{m}$, considering a waviness of $\eta = 5 \times 10^{-5}$ rad for the parabolic mirrors, it would necessitate distance of $d_{\text{oss}} = 0.05$ m between the optical components (**NMO**_{micro} in table 7.2). However, for an **NMO** as small as **NMO**_{micro}, the spacing between the reflecting mirror surfaces becomes around $10\ \mu\text{m}$, which is much smaller than the typical thickness of silicon wafers. Consequently, it might be necessary to assemble the **NMO**_{micro} from stacked wafers with varying thicknesses, which would lead to exceedingly high manufacturing costs.

In summary, **NMO** lens systems configured similarly to the prototypes may not be suitable for achieving high-resolution neutron imaging. However, they could find utility in imaging at intermediate length scales, for neutron scattering experiments on small samples subjected to extreme conditions, and for adjusting the size of the beam during neutron transport.

As depicted in Fig. 7.7, varying the focal length of the second **NMO** $2\ \text{m} \leq f_2 \leq 6\ \text{m}$, generates smaller beam sizes at F_2 , with their diameters ranging from 1 cm to 3 cm. For all configurations, the diameter of the circular neutron source at F_1 , $\varnothing_{\text{mod}} = 3\ \text{cm}$, was kept constant along with the focal length of the first set of **NMOs**, $f_1 = 6\ \text{m}$. Future advancements in technology may shed light on the feasibility of developing high-performance **NMOs** for applications involving length scales on the order of micrometers.

7.3 Summary of Nested Mirror Optics

At present, the definition of neutron beams at the sample position predominantly relies on the utilization of collimators and apertures reminiscent of the principles underlying a pinhole camera, as illustrated in Fig. 7.8 (a). When the final beam-defining aperture cannot be positioned in close proximity to the sample, for example, due to the use of a bulky sample environment, the surroundings of the sample will also receive some illumination, causing a penumbra effect as indicated by the broken red line. To enhance the precision of beam definition at the sample position and to increase the flux, one potential solution involves replacing the traditional slits with elliptic or parabolic focusing guides [196], as depicted

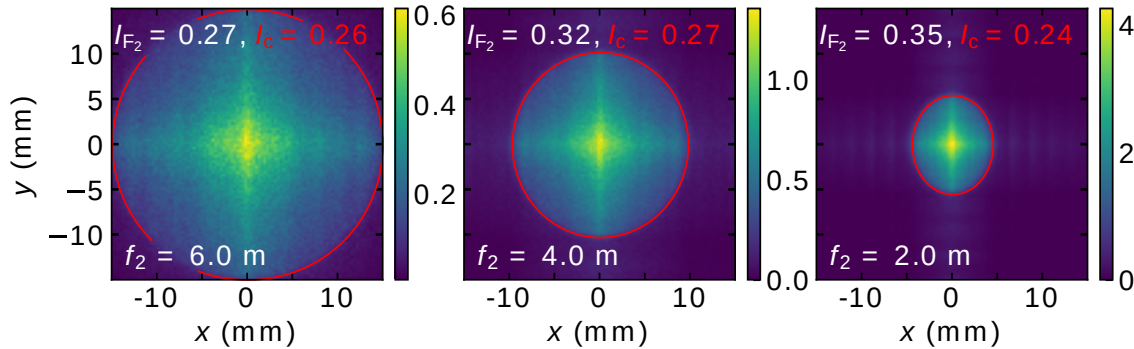


Figure 7.7: Simulated intensity distributions at F_2 of a neutron transport system as presented in Fig. 7.5 (a) (detailed discussion in section 7.1.2). The focal length of the first NMO is constant, $f_1 = 6$ m, while the focal length of the second NMO, f_2 , is adjusted within the range of 6 m to 2 m. The magnification factor is calculated as $M = f_2/f_1$. The fraction of neutrons that reach the detector area at F_2 , divided by the number of neutrons that initially enter the first NMO, is represented by I_{F_2} . The red circles encompass intensity fractions (I_c) within the plotted data. The slight deformation of the shape of the circular moderator observed for $f_2 = 2$ m is attributed to the fact that the two orthogonally oriented parabolic NMOs of the double-planar system possess slightly different focal lengths (compare Fig. 6.11 for a sketch of such a geometry). All simulations disregard the influence of gravity. Figure is reproduced from Herb et al. [19].

in Fig. 7.8 (b). A persistent challenge arises in the form of a diffuse *halo* surrounding the focused beam when the guide exit is situated at a significant distance from the sample. Furthermore, the length of the guide must exceed a certain threshold to diminish phase space inhomogeneities [196].

If sufficient space along the beam is available, a promising solution is the *Selene* setup, composed of two elliptic Montel mirrors, as suggested already in the work of Maier and Leibnitz [7] and refined by Stahn and Glavic [160]. The setup is sketched in Fig. 7.8 (c, d). Typically, this setup extracts the neutron beam from the moderator with a parabolic Montel mirror, resulting in a focused beam that is subsequently modified by a pair of elliptic Montel mirrors. This focusing system can produce beams as small as 2 mm at the sample position, preventing unwanted illumination of the surroundings. However, for larger beam sizes (approximately 10 mm), these systems span several meters in length, complicating their implementation into existing beamlines. Using a partial setup does not help, as a single Montel mirror would deflect the beam, leading to significant phase space distortion [197].

The limitations associated with slit and guide configurations can be effectively mitigated by employing NMOs. As demonstrated by the prototypes, achieving focal lengths of approximately 600 mm is straightforward, enabling the placement of the NMO at a distance of approximately 500 mm from the sample, thereby providing ample space for accommodating sample environments. Furthermore, a parabolic NMO offers a beam with a substantial divergence, determined by four times the critical angle of reflection of the outermost supermirror. For instance, an $m = 6$ supermirror can generate a beam with a divergence of nearly 4.8° for 2 \AA neutrons. At $\lambda = 0.5 \text{ \AA}$, this divergence reduces to 1.6° for $m = 8$. As discussed

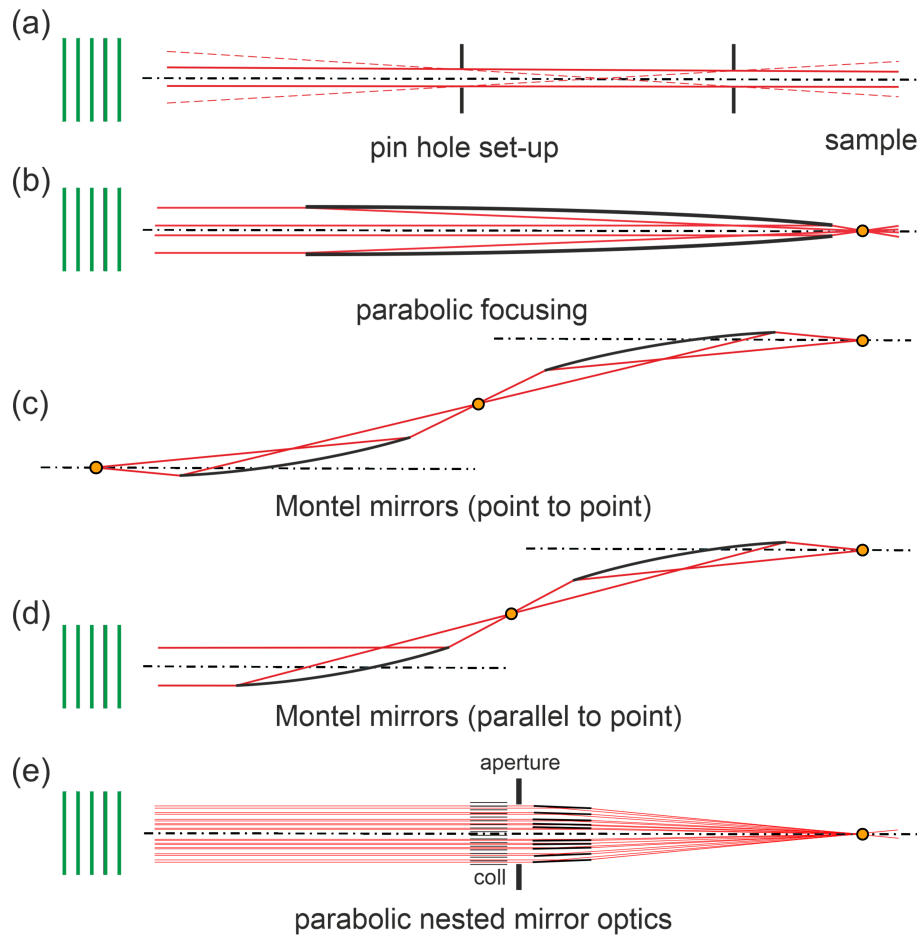


Figure 7.8: Various options for illuminating a sample with a neutron beam (only one dimension is shown). To achieve precise beam definition at the sample necessitates the placement of either slits (a) or focusing guides (b) in close proximity to the sample, which can be challenging when dealing with bulky sample environments. The *Selene*-setup incorporating elliptic (c) and/or parabolic (d) Montel mirrors, while effective, demands substantial space and introduces beam displacement from the original optical axis. In contrast, parabolic NMOs (e) offer a compact solution for precise beam definition at the sample. The figure is reproduced from the work of Herb et al. [19].

previously and shown in Fig. 7.8 (e), the divergence and the size of the beam at the sample can be adjusted by an aperture and a collimator in front of the NMO, respectively. Freely adjusting the size of the focused beam by controlling the divergence incident on the parabolic NMO requires a sophisticated setup including remotely exchangeable collimators similar to those used for parabolic guides [198]. In the case of elliptic NMOs, the footprint can be straightforwardly adjusted using a variable aperture, A_1 .

To ensure the delivery of a precisely defined beam, the mirrors must adhere to strict geometric tolerances, and the gravity-induced distortions should be minimized. Leveraging modern manufacturing techniques, the minimum achievable waviness for Montel mirrors is on the order of $\eta \simeq 4 \times 10^{-5}$ rad, resulting in an estimated beam blurring of approximately

Device	d_{os} (m)	η (10^{-4} rad)	Δw (mm)	w (mm)
Focusing guide [199]	0.5	1	0.1	1
Selene [160]	15	0.4	1.2	10
NMO _{parab}	0.6	2	0.24	6
NMO _{micro}	0.1	0.5	0.01	0.5

Table 7.2: Exemplary geometrical parameters of various focusing devices and their estimated waviness-induced blurring. The variable d_{os} represents the maximum unobstructed flight distance between a reflecting surface and the focal point/sample or between two mirrors. η denotes the waviness, and $\Delta w = 2\eta d_{\text{os}}$ and w refer to the waviness-induced blurring of the beam at sample position and the maximum achievable beam size at the sample, respectively. It has to be noted that the values provided for Δw and w are approximate, as they depend on various factors, such as the beam divergence, the neutron wavelength, and the detailed design of the specific optical components.

$\Delta w \simeq 1.2$ mm for an optics-to-sample distance of approximately $d_{\text{os}} = 15$ m (table 7.2). It should be noted that decreasing this distance can reduce the blurring, at the same time imposing limits on the maximum achievable beam size, with $w \propto d_{\text{os}}$. To compare waviness-induced blurring, we provide estimated parameters Δw and w for a short focusing guide as well [199].

Compared to a Selene setup, it appears that NMOs offer the advantage of transporting larger beam sizes over shorter distances before experiencing a significant drop in brilliance transfer. For example, the polarizing elliptic NMO investigated at MIRA transported a beam with $w \leq 6$ mm when the optics-sample distance was $d_{\text{os}} = 0.66$ m.

The non-polarizing parabolic NMO_{parab} with a focal length of 0.6 m and an assumed waviness of $\eta = 2 \times 10^{-4}$ rad would enable the definition of a focused beam with waviness-induced blurring on the order of only $\Delta w \approx 0.24$ mm (table 7.2). This is in good agreement with the experimentally obtained minimum FWHM = $2.355 \cdot 0.24$ mm ≈ 0.6 mm.

Elliptic NMOs offer additional advantages for beam transport and focusing. Firstly, they can increase the useful flux density at the sample by a factor of four compared to a setup using a single Selene guide (as seen in Fig. 7.8(c)), owing to the doubling of the achievable divergence in each dimension. Secondly, they enable a more compact beamline design. Thirdly, reflection losses are minimized as the number of reflections is halved. Lastly, the alignment of the whole NMO is as straightforward as for a single neutron guide element.

Several critical parameters must be considered when selecting the optimal optical device for neutron extraction and refocusing onto a sample. These include the sizes and shapes of the source and the sample, the distance between them, and the available lateral space. As discussed, NMOs require less space along the optical axis for a given beam size at the sample position, w . Additionally, the efficiency of NMOs tends to increase as w decreases. Consequently, elliptic NMOs are an excellent choice for the extraction and transport of neutrons when dealing with a compact source with a diameter $\varnothing \leq 10$ mm and a relatively short distance between the source and sample position, up to 20 m.

When dealing with a compact source and a distance between the source and the sample amounting to a few tens of meters, a Selene-type setup also images the whole source. This configuration can potentially mitigate the effects of gravity, thanks to shorter paths of unobstructed flight between reflections. Here, one needs to consider the required maximum divergence and the divergence hole, the supermirror-coated area, and the feasibility of the mirror systems. When transporting the same total divergence, the reflecting surfaces of Selene guides are typically illuminated at larger incident angles compared to the mirrors of a corresponding NMO. This introduces a trade-off in fabrication costs. On the one hand, an NMO necessitates a larger coated area to effectively transport the same phase space volume. On the other hand, it requires a lower m -value for most of the mirrors, which reduces the costs per coating and increases their reflectivity.

If the extent of the source is large enough that illumination losses are not a significant concern, an ordinary neutron guide may still offer competitiveness, primarily in terms of the transferred flux. However, NMOs maintain their superiority in preserving the phase space emitted by the source, as explored in detail in section 5.4.

In cases where the vertical and horizontal extents of the source significantly differ, various conceptually different optical systems might be effectively combined to achieve neutron transport in two dimensions. For instance, one could use a ballistic neutron guide for beam transport in one dimension and employ an NMO for refocusing a narrow source along the other dimension.

NMOs may also offer an efficient means to focus neutron beams for prompt gamma activation analysis (PGAA). Because the NMO can be placed far away from the sample, neutron captures occurring in the NMO can be shielded very efficiently, thus reducing background.

The reported experimental results, obtained with a small prototype elliptic NMO equipped with polarizing $m = 4.1$ supermirrors, have demonstrated a high figure of merit for imaging of 72%. Additionally, we demonstrate the imaging capabilities of elliptic NMOs for sub-millimeter beams in one and two dimensions. Future experiments on larger NMOs will demonstrate their capabilities for the extraction of sources with some cm diameters.

NMOs are well-suited to extracting neutrons from a small moderator. In the standard technique, which uses neutron guides, illumination losses increase with the neutron wavelength and scale inversely with the moderator size. NMOs can, by design, provide a high extraction efficiency, even for large wavelengths and especially for small beam sizes. As such, their natural field of application is in the development of delivery systems for the extraction of cold neutrons from compact, high-brilliance sources, like the flat para-hydrogen moderator at the ESS [185, 163] or tube-like moderators proposed for future accelerator-based neutron sources [137, 11]. NMOs are a viable alternative to non-linearly tapered neutron guides, and Montel mirrors at such sources.

In summary, for delivering neutrons to scattering instruments, NMOs offer a distinct advantage over contemporary neutron guides. NMOs enable the precise selection and matching of the phase space to meet the specific requirements of individual experiments. The imaging properties of elliptic NMOs contribute to a clean spatial definition of the beam, eliminating the penumbra effect observed behind neutron guides and apertures. The beam spectrum transported by an NMO can be adjusted precisely through its geometry and the chosen supermirror m -values. The well-defined angles of reflection in NMOs result in a short-wavelength

cut-off, contrasting with neutron guides that transport faster neutrons, often necessitating additional devices for spectral cleaning. The flexibility to adjust the beam divergence remotely through the control of apertures enables the optimization of the signal-to-background ratio. This is particularly valuable when operating an instrument in high-resolution or high-intensity mode or when aligning the beam with the acceptance of a sample environment. Notably, the placement of apertures far from the experiment minimizes associated backgrounds. This configuration also provides ample space for accommodating advanced sample environments.

NMOs are also simpler to install than neutron guides. Their neutron extraction performance increases with **NMO** size and, hence, with distance to the source (up to distances exceeding several tens of meters, at which point neutron trajectories are appreciably curved by gravity). Increased distance from the source provides the additional benefit that irradiation damage to and activation of the optics are strongly reduced, the latter of which also implies that **NMOs** can be easily accessed and exchanged to accommodate varying needs of beamlines. From a technological point of view, the complexity of producing **NMOs** is comparable to the manufacture of neutron benders [192], which are frequently used to place instruments out of the direct line-of-sight of a neutron source.

Parabolic **NMOs** can be used in a variety of ways. Their complementary neutron transport and focusing capabilities enable the configuration of entire beamlines for dedicated purposes and are especially suitable for satisfying instrument needs. Long beam lines, which transport neutrons over more than 100 m, as well as small optical setups for focusing existing beams onto tiny samples, are possible.

Owing to their superior large-wavelength extraction capability, **NMOs** will be an asset for future sources of very-cold neutrons (VCN), for which new moderator materials are being studied (see, e.g., Ref. [200, 201]). Higher neutron intensities at larger wavelengths would, for different classes of scattering instruments, lead to significant gains of performance [202]. Experiments in fundamental physics, including in-beam searches for a non-vanishing neutron electric dipole moment [203] and searches for a baryon-number violation by neutron oscillations to antineutrons or sterile neutrons [204], would also profit. **NMOs** could be employed in such dedicated, large-scale projects, but also in general-purpose fundamental-physics beamlines, such as ANNI at the ESS [205], or at in-beam sources of ultracold neutrons [206, 207].

Conclusion and Outlook

In this thesis, we explored the overarching topic of neutron scattering with our main focus turned toward two subjects. On the one hand, we utilized the versatile technique of triple-axis neutron spectroscopy to examine a phonon softening phenomenon in the rare earth vanadate LuVO_3 , specifically in the transversal acoustic TA1 phonon mode. On the other hand, we assessed the performance of novel NMO prototypes using analytic calculations, McStas simulations, and neutron imaging techniques. The presented results demonstrate their promising characteristics for neutron extraction, transport, and focusing and suggest their compatibility with the contemporary landscape of neutron optics.

Phonon softening in LuVO_3

Utilizing inelastic triple-axis neutron scattering, we explored a softening in the transversal acoustic TA1 phonon branch of a single crystal of LuVO_3 . A reduction in the energy of the phonon mode occurs when cooling the compound below a temperature of $T_{\text{SO}_2} = 82.5 \text{ K}$, concomitant with a structural phase transition from a monoclinic $P2_1b$ to an orthorhombic $Pbnm$ structure. At the zone boundary, $\vec{Q} = (0, -0.5, 4)$ r.l.u., the phonon energy exhibited a discontinuous relative reduction of 3%, corresponding to an absolute value of 0.3 meV. This subtle yet significant softening was consistently observed across various instruments and beamtimes. However, the effect could not be observed near the Γ -point at the zone center, likely due to limitations of the instrumental resolution. Assuming a sinusoidal dispersion relation, we expect the relative softening of the phonon mode to remain constant for all \vec{Q} , suggesting challenges in resolving this phenomenon with increasing distance from the zone boundary where the energy is reduced. An alternative explanation not explored further involves a *zone boundary soft acoustic mode*. No significant change in the phonon linewidth was detected within the resolution of our triple-axis neutron measurements, contradicting the idea of a coupling of the phonon to another excitation.

The observed softening of TA1 was discussed within the context of elastic anomalies during structural phase transitions, hinting at a potential improper ferroelastic transition. Remarkably, no softening was observed along other directions in reciprocal space, highlighting the unique symmetry of the coupling strain.

Looking ahead, supersonic measurements can be performed to directly determine relative changes in the elastic constants. However, a quantitative comparison is unlikely to be fruitful due to the significant difference in the probing frequencies. Additionally, determining the order of the phase transition could be achieved through high-precision heat capacity measurements. For a closer examination of the softening near the zone center, where the absolute energy differences are smaller, neutron resonant spin-echo methods with superior energy resolution are suggested. This approach further promises to yield insights into the phonon linewidth behavior around the phase transition.

Building upon the presented study, subjecting the crystal to external uniaxial stress using a bellow-driven in-situ pressure cell might yield valuable insights into the lattice dynamics in response to stress applied along different directions. Furthermore, exploring the effects

of hydrostatic pressure and monitoring the phonon dispersion and the lattice constants in proximity to the transition holds potential interest.

Exploring the temperature hysteresis of the investigations presented here and the proposed experiments could provide valuable information about the processes involved in the phase transition. Finally, simulation-assisted theoretical investigations are suggested, considering various couplings between the TA1 phonon mode and other excitations, focusing on understanding the connection between the anomalous behavior of the phonon dispersion and alterations in orbital- and spin ordering.

Evaluation of Nested Mirror Optics

In the second part of the thesis, we explored the novel [nested mirror optics \(NMO\)](#) with a focus on expanding the current toolkit of neutron optics and, ultimately, improving the quality of neutron scattering experiments.

As a starting point, we discussed challenges associated with under-illuminating a long guide during neutron extraction from a compact source. While elliptic or ballistic neutron guides facilitate the transport between two points, they still suffer from under-illumination and significantly distort the phase space volume of the transported neutron beam. We utilized analytic calculations, numerical approximations, and Monte Carlo methods to comprehensively evaluate these aberrations, where we improved the precision of previous results. While under-illumination reduces the available neutron flux at the sample positions, the aberrations of the phase space complicate the extraction of the double-differential cross-section from the obtained data, rendering both undesirable effects.

Following this introduction, the concept of an [NMO](#) was introduced as a solution to reduce phase space aberrations by limiting the points of reflection to a confined region along the optical axis and nesting additional reflecting surfaces laterally to improve the angular acceptance of the device. The phase space-preserving nature of [NMOs](#) was validated through Monte Carlo simulations. This work also provides a detailed methodology for determining the reflecting surfaces and estimating the geometric losses associated with [NMOs](#). Finally, we presented the designed McStas simulation component, which enables Monte Carlo simulations of double-planar [NMO](#) geometries.

Beyond the theoretical and simulation-based evaluation, various elliptic and parabolic [NMO](#) prototypes were commissioned and investigated with neutrons. We utilized a CASCADE detector to determine the efficiency of transport of the polarizing elliptic [NMO](#) at MIRA-2 and a neutron imaging setup at BOA to investigate the beam shape provided by the parabolic and elliptic [NMOs](#). The efficiency of transport for the polarizing elliptic [NMO](#) prototype was determined to be above 72 %, in good agreement with the performed simulations and the analytic calculations of the geometric losses.

The imaging capabilities of the elliptic [NMOs](#) were initially confirmed by demonstrating that, when correctly aligned, the width of the transported neutron beam at the second focal point precisely matches the width of the intensity distribution at the first focal point. Imaging of a one-dimensional grid-like structure was similarly successful. Additionally, successful imaging of simple two-dimensional intensity distributions was accomplished despite a minor misalignment of the vertically focusing [NMO](#), which resulted from the absence of a goniometer during the measurement.

While investigating the novel **NMO** prototypes, we repeatedly encountered a minor deformation of the reflective surfaces, likely due to tensile stress induced by the applied supermirror coatings. Besides resulting in decreasing focusing quality reflected by an increased **FWHM**, the excessively curved substrates entailed a reduction of the effective focal length from its nominal value by up to 25 mm, depending on the point of illumination. We began quantifying this deformation through 3D scanning to gain additional insights into the behavior of the substrates when inserted into differently shaped grooves. Ultimately, the deformations should be mitigated by reducing the stress on the substrates, for example, by coating the mirrors from both sides, by utilizing thicker substrates, or by adjusting the nominal geometries to account for the expected deformations.

Various applications of parabolic and elliptic **NMOs** or combinations thereof were presented. Whereas an elliptic **NMO** is limited in its ability to transport neutrons over extended distances due to gravity, the combination of two double-planar **NMOs** facilitates an efficient long-distance neutron transport through a straight guide connecting both. Using parabolic **NMOs** with different focal lengths offers additional flexibility to control the extent of the beam at the sample position. This guide system holds potential utility for instruments dealing with samples of widely varying sizes.

In summary, **NMOs** can potentially advance neutron transport, especially in the context of compact high-brilliance sources. The here-presented findings open avenues for further practical applications and optimizations of **NMOs**. Future work should involve i) a repetition of the imaging investigations addressing alignment challenges, ii) refining mirror and coating designs to mitigate substrate deformation, and iii) exploring additional scenarios to validate the versatility and robustness of larger **NMOs** by simulation and experiment. These experimental scenarios include neutron time-of-flight experiments, triple-axis scattering, and neutron resonance spin-echo experiments. Finally, investigating the potential of **NMOs** in various neutron imaging setups and considering advancements in the extraction of neutrons from cold compact sources are believed to be among the most promising applications of **NMOs**.

Acronyms

AIC Akaike information criterion.

BZ Brillouin zone.

CCD charge-coupled device.

DCM double crystal monochromator.

DDCS double differential cross section.

FWHM full width at half maximum.

ILL Institut Laue-Langevin.

NMO nested mirror optics.

npveNMO non-polarizing vertically focusing elliptic NMO.

npvpNMO non-polarizing vertically focusing parabolic NMO.

OO orbital order.

PDF probability density function.

pdNMO parabolic de-focusing nested mirror optics.

pfNMO parabolic focusing nested mirror optics.

PG pyrolytic graphite.

phpNMO polarizing horizontally focusing parabolic NMO.

PSD position-sensitive detector.

REV rare-earth vanadates.

SO spin order.

TAS triple-axis spectroscopy.

Bibliography

- [1] S. Miyasaka, Y. Okimoto, M. Iwama, and Y. Tokura. Spin-orbital phase diagram of perovskite-type RVO_3 ($R = \text{rare-earth ion or Y}$). *Physical Review B*, 68(10):100406, September 2003. ISSN 0163-1829, 1095-3795. doi:[10.1103/PhysRevB.68.100406](https://doi.org/10.1103/PhysRevB.68.100406). 1, 29, 32
- [2] M. Skoulatos, S. Toth, B. Roessli, M. Enderle, K. Habicht, D. Sheptyakov, A. Cervellino, P. G. Freeman, M. Reehuis, A. Stunault, G. J. McIntyre, L. D. Tung, C. Marjerson, E. Pomjakushina, P. J. Brown, D. I. Khomskii, Ch. Rüegg, A. Kreyssig, A. I. Goldman, and J. P. Goff. Jahn-Teller versus quantum effects in the spin-orbital material LuVO_3 . *Physical Review B*, 91(16):161104, April 2015. ISSN 1098-0121, 1550-235X. doi:[10.1103/PhysRevB.91.161104](https://doi.org/10.1103/PhysRevB.91.161104). 1, 29, 31, 33, 34, 35, 44, 52
- [3] V. M. Goldschmidt. Die Gesetze der Krystallochemie. *Naturwissenschaften*, 14(21):477–485, May 1926. ISSN 1432-1904. doi:[10.1007/BF01507527](https://doi.org/10.1007/BF01507527). 1, 28
- [4] John B. Goodenough. An interpretation of the magnetic properties of the perovskite-type mixed crystals $\text{La}_{1-x}\text{Sr}_x\text{CoO}_3$. *Journal of Physics and Chemistry of Solids*, 6(2):287–297, August 1958. ISSN 0022-3697. doi:[10.1016/0022-3697\(58\)90107-0](https://doi.org/10.1016/0022-3697(58)90107-0). 1
- [5] G. Khaliullin. Order from disorder: Quantum spin gap in magnon spectra of LaTiO_3 . *Physical Review B*, 64(21):212405, November 2001. ISSN 0163-1829, 1095-3795. doi:[10.1103/PhysRevB.64.212405](https://doi.org/10.1103/PhysRevB.64.212405). 1
- [6] Michael A. Carpenter and Ekhard K.H. Salje. Elastic anomalies in minerals due to structural phase transitions. *European Journal of Mineralogy*, 10(4):693–812, July 1998. doi:[10.1127/ejm/10/4/0693](https://doi.org/10.1127/ejm/10/4/0693). 1, 44, 45, 46, 47, 48, 49, 50
- [7] H. Maier-Leibnitz and T. Springer. The use of neutron optical devices on beam-hole experiments on beam-hole experiments. *Journal of Nuclear Energy. Parts A/B. Reactor Science and Technology*, 17(4):217 – 225, 1963. ISSN 0368-3230. doi:[https://doi.org/10.1016/0368-3230\(63\)90022-3](https://doi.org/10.1016/0368-3230(63)90022-3). 2, 58, 60, 62, 134
- [8] F. Mezei. Novel polarized neutron devices: supermirror and spin component amplifier. *Communications on Physics*, 1:81–85, 1976. 2, 61
- [9] J.M. Carpenter and D.F.R. Mildner. Neutron guide tube gain for a remote finite source. *Nuclear Instruments and Methods in Physics Research*, 196(2-3):341–348, May 1982. ISSN 01675087. doi:[10.1016/0029-554X\(82\)90097-0](https://doi.org/10.1016/0029-554X(82)90097-0). 2, 63
- [10] Ken Holst Andersen, Mads Bertelsen, Luca Zanini, Esben Bryndt Klinkby, Troels Schönfeldt, Phillip Martin Bentley, and Jan Saroun. Optimization of moderators and beam extraction at the ESS. *Journal of Applied Crystallography*, 51(2):264–281, April 2018. ISSN 1600-5767. doi:[10.1107/S1600576718002406](https://doi.org/10.1107/S1600576718002406). 2

- [11] T. Gutberlet, U. Rucker, P. Zakalek, T. Cronert, J. Voigt, J. Baggemann, P.-E. Doege, E. Mauerhofer, S. Böhm, J.P. Dabruck, R. Nabbi, M. Butzek, M. Klaus, C. Lange, and T. Brückel. The Jülich high brilliance neutron source project – Improving access to neutrons. *Physica B: Condensed Matter*, 570:345–348, 2019. ISSN 0921-4526. doi:<https://doi.org/10.1016/j.physb.2018.01.019>. 2, 137
- [12] T. Gutberlet, U. Rucker, E. Mauerhofer, P. Zakalek, T. Cronert, J. Voigt, J. Baggemann, J. Li, P. Doege, S. Böhm, M. Rimpler, O. Felden, R. Gebel, O. Meusel, H. Podlech, W. Barth, and T. Brückel. Sustainable neutrons for today and tomorrow—The Jülich High Brilliance neutron Source project. *Neutron News*, 31(2-4):37–43, October 2020. ISSN 1044-8632. doi:[10.1080/10448632.2020.1819132](https://doi.org/10.1080/10448632.2020.1819132). 2, 63
- [13] Hans Wolter. Spiegelsysteme streifenden Einfalls als abbildende Optiken für Röntgenstrahlen. *Annalen der Physik*, 445(1-2):94–114, 1952. ISSN 1521-3889. doi:<https://doi.org/10.1002/andp.19524450108>. 2
- [14] M. Friedmann and H. Rauch. Neutron focusing by a curved sollar collimator system. *Nuclear Instruments and Methods*, 86(1):55–59, September 1970. ISSN 0029-554X. doi:[10.1016/0029-554X\(70\)90035-2](https://doi.org/10.1016/0029-554X(70)90035-2). 2
- [15] D. F. R. Mildner. The neutron microguide as a probe for materials analysis. *Nuclear Instruments and Methods in Physics Research Section A: Accelerators, Spectrometers, Detectors and Associated Equipment*, 299(1):416–419, December 1990. ISSN 0168-9002. doi:[10.1016/0168-9002\(90\)90816-O](https://doi.org/10.1016/0168-9002(90)90816-O). 2
- [16] B. Alefeld, L. Dohmen, D. Richter, and Th. Brückel. X-ray space technology for focusing small-angle neutron scattering and neutron reflectometry. *Physica B: Condensed Matter*, 283(4):330–332, June 2000. ISSN 0921-4526. doi:[10.1016/S0921-4526\(00\)00325-2](https://doi.org/10.1016/S0921-4526(00)00325-2). 2
- [17] Mark R Daymond and Michael W Johnson. An experimental test of a neutron silicon lens. *Nuclear Instruments and Methods in Physics Research Section A: Accelerators, Spectrometers, Detectors and Associated Equipment*, 485(3):606–614, June 2002. ISSN 0168-9002. doi:[10.1016/S0168-9002\(01\)02132-5](https://doi.org/10.1016/S0168-9002(01)02132-5). 2
- [18] Roland Bartmann, Nicolas Behr, André Hilger, and Thomas Krist. New solid state lens for reflective neutron focusing. *Nuclear Instruments and Methods in Physics Research Section A: Accelerators, Spectrometers, Detectors and Associated Equipment*, 634(1, Supplement):S104–S107, April 2011. ISSN 0168-9002. doi:[10.1016/j.nima.2010.05.040](https://doi.org/10.1016/j.nima.2010.05.040). 2
- [19] Christoph Herb, Oliver Zimmer, Robert Georgii, and Peter Böni. Nested mirror optics for neutron extraction, transport, and focusing. *Nuclear Instruments and Methods in Physics Research Section A: Accelerators, Spectrometers, Detectors and Associated Equipment*, 1040:167154, October 2022. ISSN 0168-9002. doi:[10.1016/j.nima.2022.167154](https://doi.org/10.1016/j.nima.2022.167154). 2, 63, 65, 71, 75, 78, 82, 85, 86, 88, 89, 90, 91, 96, 97, 123, 124, 127, 129, 130, 131, 132, 133, 134, 135

- [20] J. Chadwick. Possible Existence of a Neutron. *Nature*, 129(3252):312–312, February 1932. ISSN 1476-4687. doi:[10.1038/129312a0](https://doi.org/10.1038/129312a0). Number: 3252 Publisher: Nature Publishing Group. 5, 20
- [21] Hartmut Abele. The neutron. Its properties and basic interactions. *Progress in Particle and Nuclear Physics*, 60(1):1–81, January 2008. ISSN 0146-6410. doi:[10.1016/j.pnpnp.2007.05.002](https://doi.org/10.1016/j.pnpnp.2007.05.002). 5
- [22] J. Baumann, R. Gähler, J. Kalus, and W. Mampe. Experimental limit for the charge of the free neutron. *Physical Review D: Particles and Fields*, 37(11):3107–3112, June 1988. doi:[10.1103/PhysRevD.37.3107](https://doi.org/10.1103/PhysRevD.37.3107). Number of pages: 0 Publisher: American Physical Society. 5
- [23] Eite Tiesinga, Peter J. Mohr, David B. Newell, and Barry N. Taylor. CODATA recommended values of the fundamental physical constants: 2018*. *Journal of Physical and Chemical Reference Data*, 50(3):033105, September 2021. ISSN 0047-2689. doi:[10.1063/5.0064853](https://doi.org/10.1063/5.0064853). 5, 8
- [24] R. L. Workman and Others. Review of particle physics. *PTEP*, 2022:083C01, 2022. doi:[10.1093/ptep/ptac097](https://doi.org/10.1093/ptep/ptac097). tex.collaboration: Particle Data Group. 5, 55
- [25] C. Abel, S. Afach, N. J. Ayres, C. A. Baker, G. Ban, G. Bison, K. Bodek, V. Bondar, M. Burghoff, E. Chanel, Z. Chowdhuri, P.-J. Chiu, B. Clement, C. B. Crawford, M. Daum, S. Emmenegger, L. Ferraris-Bouchez, M. Fertl, P. Flaux, B. Franke, A. Fratangelo, P. Geltenbort, K. Green, W. C. Griffith, M. van der Grinten, Z. D. Grujić, P. G. Harris, L. Hayen, W. Heil, R. Henneck, V. Hélaine, N. Hild, Z. Hodge, M. Horras, P. Iaydjiev, S. N. Ivanov, M. Kasprzak, Y. Kermaidic, K. Kirch, A. Knecht, P. Knowles, H.-C. Koch, P. A. Koss, S. Komposch, A. Kozela, A. Kraft, J. Kempel, M. Kuźniak, B. Lauss, T. Lefort, Y. Lemièrre, A. Leredde, P. Mohanmurthy, A. Mtchedlishvili, M. Musgrave, O. Naviliat-Cuncic, D. Pais, F. M. Piegsa, E. Pierre, G. Pignol, C. Plonka-Spehr, P. N. Prashanth, G. Quémener, M. Rawlik, D. Rebreyend, I. Rienäcker, D. Ries, S. Rocchia, G. Rogel, D. Rozpedzik, A. Schnabel, P. Schmidt-Wellenburg, N. Severijns, D. Shiers, R. Tavakoli Dinani, J. A. Thorne, R. Viot, J. Voigt, A. Weis, E. Wursten, G. Wyszynski, J. Zejma, J. Zenner, and G. Zsigmond. Measurement of the Permanent Electric Dipole Moment of the Neutron. *Physical Review Letters*, 124(8):081803, February 2020. ISSN 0031-9007, 1079-7114. doi:[10.1103/PhysRevLett.124.081803](https://doi.org/10.1103/PhysRevLett.124.081803). 5
- [26] TUM. Secondary sources for neutrons and positrons. <https://www.frm2.tum.de/en/frm2/the-neutron-source/neutrons/secondary-sources/>. Accessed: 2023-09-06. 6
- [27] U. Rucker, T. Cronert, J. Voigt, J. P. Dabruck, P.-E. Doege, J. Ulrich, R. Nabbi, Y. Beßler, M. Butzek, M. Büscher, C. Lange, M. Klaus, T. Gutberlet, and T. Brückel. The Jülich high-brilliance neutron source project. *The European Physical Journal Plus*, 131(1):19, January 2016. ISSN 2190-5444. doi:[10.1140/epjp/i2016-16019-5](https://doi.org/10.1140/epjp/i2016-16019-5). Number: 1 Publisher: Springer Berlin Heidelberg. 7, 63

- [28] G. L. Squires. Nuclear scattering by crystals. In *Introduction to the theory of thermal neutron scattering*, pages 25–60. Cambridge University Press, Cambridge, 3 edition, 2012. doi:[10.1017/CBO9781139107808.004](https://doi.org/10.1017/CBO9781139107808.004). 7, 9, 11, 12, 13, 14
- [29] N. E. Holden. Neutron capture cross section standards for BNL 325, Fourth Edition. Technical Report BNL-NCS-51388, Brookhaven National Lab. (BNL), Upton, NY (United States), January 1981. 7
- [30] Lukas Beddrich. *Consequences of lattice dimensionality in solid state magnetism*. PhD thesis, TUM School of Natural Sciences, Garching, 2023. 9
- [31] Paul Adrien Maurice Dirac and Niels Henrik David Bohr. The quantum theory of the emission and absorption of radiation. *Proceedings of the Royal Society of London. Series A, Containing Papers of a Mathematical and Physical Character*, 114(767):243–265, January 1927. doi:[10.1098/rspa.1927.0039](https://doi.org/10.1098/rspa.1927.0039). Publisher: Royal Society. 9
- [32] Enrico Fermi. *Nuclear Physics*. Chicago: University of Chicago Press, Chicago, 1950. 9
- [33] Enrico Fermi and others. Motion of neutrons in hydrogenous substances. *Ricerca Scientifica*, 7(2):13–52, 1936. 10, 59
- [34] Javier Dawidowski, José Rolando Granada, Javier Roberto Santisteban, Florencia Cantargi, and Luis Alberto Rodríguez Palomino. Appendix - Neutron Scattering Lengths and Cross Sections. In Felix Fernandez-Alonso and David L. Price, editors, *Experimental Methods in the Physical Sciences*, volume 44 of *Neutron Scattering – Fundamentals*, pages 471–528. Academic Press, January 2013. doi:[10.1016/B978-0-12-398374-9.09989-7](https://doi.org/10.1016/B978-0-12-398374-9.09989-7). 12, 60
- [35] Siegfried Hunklinger. *Festkörperphysik*, volume 3. Oldenbourg Wissenschaftsverlag GmbH, München, 2011. ISBN 978-3486705478. 12, 13, 39, 43, 45, 46, 47, 51
- [36] Igor A. Zaliznyak and John M. Tranquada. Neutron Scattering and Its Application to Strongly Correlated Systems. In *Strongly Correlated Systems*, pages 205–235. Springer, Berlin, Heidelberg, 2015. doi:[10.1007/978-3-662-44133-6_7](https://doi.org/10.1007/978-3-662-44133-6_7). 13
- [37] Bertram N. Brockhouse. Slow neutron spectroscopy and the grand atlas of the physical world. *Reviews of Modern Physics*, 67(4):735–751, October 1995. ISSN 0034-6861, 1539-0756. doi:[10.1103/RevModPhys.67.735](https://doi.org/10.1103/RevModPhys.67.735). 15
- [38] THE NOBEL PRIZE. Presentation speech by Professor Carl Nordling of the royal swedish academy of sciences. <https://www.nobelprize.org/prizes/physics/1994/ceremony-speech/>, 1994. Accessed: 2024-01-28. 15
- [39] Gen Shirane, Stephen M. Shapiro, and John M. Tranquada. *Neutron Scattering with a Triple-Axis Spectrometer: Basic Techniques*. Cambridge University Press, 2002. doi:[10.1017/CBO9780511534881](https://doi.org/10.1017/CBO9780511534881). 15, 18, 19

- [40] William Henry Bragg and William Lawrence Bragg. The reflection of X-rays by crystals. *Proceedings of the Royal Society of London. Series A, Containing Papers of a Mathematical and Physical Character*, 88(605):428–438, 1913. doi:[10.1098/rspa.1913.0040](https://doi.org/10.1098/rspa.1913.0040). 16
- [41] S. A. Werner and Anthony Arrott. Propagation of Bragg-Reflected Neutrons in Large Mosaic Crystals and the Efficiency of Monochromators. *Physical Review*, 140(2A):A675–A686, October 1965. ISSN 0031-899X. doi:[10.1103/PhysRev.140.A675](https://doi.org/10.1103/PhysRev.140.A675). 16
- [42] V. F. Sears. Theory of neutron diffraction in mosaic crystals. *Acta Crystallographica Section A*, 33(3):373–381, 1977. ISSN 1600-5724. doi:[10.1107/S0567739477001016](https://doi.org/10.1107/S0567739477001016). 16
- [43] V. F. Sears. Bragg Reflection in Mosaic Crystals. I. General Solution of the Darwin Equations. *Acta Crystallographica Section A Foundations of Crystallography*, 53(1):35–45, January 1997. ISSN 0108-7673. doi:[10.1107/S0108767396009804](https://doi.org/10.1107/S0108767396009804). 16
- [44] T. Riste and K. Otnes. Oriented graphite as a neutron monochromator. *Nuclear Instruments and Methods*, 75(2):197–202, November 1969. ISSN 0029-554X. doi:[10.1016/0029-554X\(69\)90594-1](https://doi.org/10.1016/0029-554X(69)90594-1). 16
- [45] Rasmus Toft-Petersen, Robert Georgii, Michael Schneider, Naomi Nishiki, and Peter Böni. Characterization of pyrolytic graphite with cold neutrons. *Nuclear Instruments and Methods in Physics Research Section A: Accelerators, Spectrometers, Detectors and Associated Equipment*, 977:164341, October 2020. ISSN 0168-9002. doi:[10.1016/j.nima.2020.164341](https://doi.org/10.1016/j.nima.2020.164341). 16
- [46] A. K. Freund. Single-crystal diamond: a potential gem in neutron instrumentation. *Journal of Applied Crystallography*, 42(1):36–42, February 2009. ISSN 0021-8898. doi:[10.1107/S0021889808039125](https://doi.org/10.1107/S0021889808039125). Number: 1 Publisher: International Union of Crystallography. 16
- [47] S. Stoupin, T. Krawczyk, J. P. C. Ruff, K. D. Finkelstein, H. H. Lee, and R. Huang. Performance of CVD Diamond Single Crystals as Side-bounce Monochromators in the Laue Geometry at High Photon Energies. page 060019, 2019. doi:[10.1063/1.5084650](https://doi.org/10.1063/1.5084650). arXiv:1806.02226 [physics]. 16
- [48] J. Witz. Focusing monochromators. *Acta Crystallographica Section A*, 25(1):30–42, 1969. ISSN 1600-5724. doi:[10.1107/S0567739469000052](https://doi.org/10.1107/S0567739469000052). 17
- [49] Markos Skoulatos, Klaus Habicht, and Klaus Lieutenant. Improving energy resolution on neutron monochromator arrays. *Journal of Physics: Conference Series*, 340:012019, February 2012. ISSN 1742-6588, 1742-6596. doi:[10.1088/1742-6596/340/1/012019](https://doi.org/10.1088/1742-6596/340/1/012019). 17
- [50] Tobias Weber. *Dynamics at the Orbital Ordering Phase Transition in MgV_2O_4 and at the Ferromagnetic Phase Transition in $MnSi$* . PhD thesis, Fakultät für Physik der Technischen Universität München, Munich, August 2017. 18, 53

- [51] M. D. Lumsden, J. L. Robertson, and M. Yethiraj. UB matrix implementation for inelastic neutron scattering experiments. *Journal of Applied Crystallography*, 38(3): 405–411, June 2005. ISSN 0021-8898. doi:[10.1107/S0021889805004875](https://doi.org/10.1107/S0021889805004875). Number: 3 Publisher: International Union of Crystallography. 18
- [52] G. Shirane and V. J. Minkiewicz. Pyrolytic graphite as a high efficiency filter for 13–15 meV neutrons. *Nuclear Instruments and Methods*, 89:109–110, December 1970. ISSN 0029-554X. doi:[10.1016/0029-554X\(70\)90812-8](https://doi.org/10.1016/0029-554X(70)90812-8). 18
- [53] K. C. Rule, F. Darmann, T. Oste, D. Bartlett, F. Franceschini, A. Berry, A. McGregor, A. Ogrin, T. Ersez, A. Kafes, S. Pangelis, S. Danilkin, A. P. J. Stampfl, and S. R. Olsen. Recent enhancements and performance gains from upgrades to ANSTO’s thermal neutron instrument TAIPAN and the triple-axis and Be-filter spectrometers. *Nuclear Instruments and Methods in Physics Research Section A: Accelerators, Spectrometers, Detectors and Associated Equipment*, 901:140–149, September 2018. ISSN 0168-9002. doi:[10.1016/j.nima.2018.05.056](https://doi.org/10.1016/j.nima.2018.05.056). 18
- [54] Walter Soller. A New Precision X-ray Spectrometer. *Physical Review*, 24(2):158–167, August 1924. ISSN 0031-899X. doi:[10.1103/PhysRev.24.158](https://doi.org/10.1103/PhysRev.24.158). 18
- [55] C J Carlile, P D Hey, and B Mack. High-efficiency Soller slit collimators for thermal neutrons. *Journal of Physics E: Scientific Instruments*, 10(5):543–546, May 1977. ISSN 0022-3735. doi:[10.1088/0022-3735/10/5/035](https://doi.org/10.1088/0022-3735/10/5/035). 18
- [56] L. D. Cussen, P. Høghøj, and I. S. Anderson. Neutron collimator with rectangular beam profile. *Nuclear Instruments and Methods in Physics Research Section A: Accelerators, Spectrometers, Detectors and Associated Equipment*, 460(2):374–380, March 2001. ISSN 0168-9002. doi:[10.1016/S0168-9002\(00\)01077-9](https://doi.org/10.1016/S0168-9002(00)01077-9). 18
- [57] P. F. Rago, R. C. Barrall, and T. G. Carter. Sensitive fast neutron monitor using fission-foil Lexan detectors. *Health Phys.*, v. 26, no. 1, pp. 102-104, January 1974. Institution: Stanford Univ., CA. 19
- [58] TW Crane and MP Baker. Neutron detectors. *Passive Nondestructive Assay of Nuclear Materials*, 13:1–28, 1991. Publisher: no. NUREG/CR-5550 in United States Nuclear Regulatory Commission. 19
- [59] R. Georgii, T. Weber, G. Brandl, M. Skoulatos, M. Janoschek, S. Mühlbauer, C. Pfeleiderer, and P. Böni. The multi-purpose three-axis spectrometer (TAS) MIRA at FRM II. *Nuclear Instruments and Methods in Physics Research Section A: Accelerators, Spectrometers, Detectors and Associated Equipment*, 881:60 – 64, 2018. ISSN 0168-9002. doi:<https://doi.org/10.1016/j.nima.2017.09.063>. 19, 86, 94
- [60] M. Köhli, M. Klein, F. Allmendinger, A.-K. Perrevoort, T. Schröder, N. Martin, C. J. Schmidt, and U. Schmidt. CASCADE - a multi-layer Boron-10 neutron detection system. *Journal of Physics: Conference Series*, 746:012003, September 2016. doi:[10.1088/1742-6596/746/1/012003](https://doi.org/10.1088/1742-6596/746/1/012003). Publisher: IOP Publishing. 19

- [61] U. Stuhr, B. Roessli, S. Gvasaliya, H. M. Rønnow, U. Filges, D. Graf, A. Bollhalder, D. Hohl, R. Bürge, M. Schild, L. Holitzner, C. Kaegi, P. Keller, and T. Mühlebach. The thermal triple-axis-spectrometer EIGER at the continuous spallation source SINQ. *Nuclear Instruments and Methods in Physics Research Section A: Accelerators, Spectrometers, Detectors and Associated Equipment*, 853:16–19, May 2017. ISSN 0168-9002. doi:[10.1016/j.nima.2017.02.003](https://doi.org/10.1016/j.nima.2017.02.003). 19
- [62] Oleg Sobolev and Jitae T. Park. PUMA: Thermal three axes spectrometer. *Journal of large-scale research facilities JLSRF*, 1:A13–A13, August 2015. ISSN 2364-091X. doi:[10.17815/jlsrf-1-36](https://doi.org/10.17815/jlsrf-1-36). 20
- [63] J.S. Brenizer. A review of significant advances in neutron imaging from conception to the present. *Physics Procedia*, 43:10–20, 2013. ISSN 1875-3892. doi:<https://doi.org/10.1016/j.phpro.2013.03.002>. 20
- [64] Eberhard H. Lehmann, P. Vontobel, G. Frei, and C. Brönnimann. Neutron imaging—detector options and practical results. *Nuclear Instruments and Methods in Physics Research Section A: Accelerators, Spectrometers, Detectors and Associated Equipment*, 531(1):228–237, September 2004. ISSN 0168-9002. doi:[10.1016/j.nima.2004.06.010](https://doi.org/10.1016/j.nima.2004.06.010). 20, 21
- [65] Hartmut Kallmann. Neutron radiography. *Research; a journal of science and its applications*, 1(6):254–260, 1948. 20
- [66] Kallmann Hartmut and Kuhn Ernst. Photographic detection of slowly moving neutrons, 1940. US Patent 2,186,757. 20
- [67] Tobias Neuwirth, Bernhard Walfort, Simon Sebold, and Michael Schulz. Light Yield Response of Neutron Scintillation Screens to Sudden Flux Changes. *Journal of Imaging*, 6(12):134, December 2020. ISSN 2313-433X. doi:[10.3390/jimaging6120134](https://doi.org/10.3390/jimaging6120134). 20, 22
- [68] Nobuo Niimura, Yuuko Karasawa, Kenji Takahashi, and Hiroki Saito. Method for forming neutron images, 1998. US Patent 5,852,301. 20
- [69] Daniel S. Hussey, Jacob M. LaManna, Elias Baltic, and David L. Jacobson. Neutron imaging detector with 2 μm spatial resolution based on event reconstruction of neutron capture in gadolinium oxysulfide scintillators. *Nuclear Instruments and Methods in Physics Research Section A: Accelerators, Spectrometers, Detectors and Associated Equipment*, 866:9–12, September 2017. ISSN 0168-9002. doi:[10.1016/j.nima.2017.05.035](https://doi.org/10.1016/j.nima.2017.05.035). 21
- [70] Jiri Stepanek. Emission spectra of Gadolinium-158. *Medical Physics*, 30(1):41–43, 2003. ISSN 2473-4209. doi:[10.1118/1.1528176](https://doi.org/10.1118/1.1528176). 21
- [71] Christian Tötze, Ingo Manke, André Hilger, Gerard Choinka, Nikolay Kardjilov, Tobias Arlt, Henning Markötter, Alexander Schröder, Klaus Wippermann, Detlef Stolten, Christoph Hartnig, Phillip Krüger, Robert Kuhn, and John Banhart. Large area high

- resolution neutron imaging detector for fuel cell research. *Journal of Power Sources*, 196(10):4631–4637, May 2011. ISSN 0378-7753. doi:[10.1016/j.jpowsour.2011.01.049](https://doi.org/10.1016/j.jpowsour.2011.01.049). 21
- [72] Helena Pleinert, Eberhard Lehmann, and Sonja Körner. Design of a new CCD-camera neutron radiography detector. *Nuclear Instruments and Methods in Physics Research Section A: Accelerators, Spectrometers, Detectors and Associated Equipment*, 399(2): 382–390, November 1997. ISSN 0168-9002. doi:[10.1016/S0168-9002\(97\)00944-3](https://doi.org/10.1016/S0168-9002(97)00944-3). 22
- [73] M. Morgano, S. Peetermans, E.H. Lehmann, T. Panzner, and U. Filges. Neutron imaging options at the BOA beamline at Paul Scherrer Institut. *Nuclear Instruments and Methods in Physics Research Section A: Accelerators, Spectrometers, Detectors and Associated Equipment*, 754:46–56, August 2014. ISSN 01689002. doi:[10.1016/j.nima.2014.03.055](https://doi.org/10.1016/j.nima.2014.03.055). 25, 99
- [74] Padma Kanya Radhakrishnan. *Electronic properties of rare earth vanadate heterostructures*. PhD, Max-Planck-Institut für Festkörperforschung Universität Stuttgart, Stuttgart, 2022. 27
- [75] Eva Benckiser. *Optical Spectroscopy of Orbital and Magnetic Excitations in Vanadates and Cuprates*. PhD, Universität zu Köln, Köln, 2007. 27, 29, 35
- [76] John B. Goodenough and J.-S. Zhou. Orbital ordering in orthorhombic perovskites. *Journal of Materials Chemistry*, 17(23):2394, 2007. ISSN 0959-9428, 1364-5501. doi:[10.1039/b701805c](https://doi.org/10.1039/b701805c). 27, 28, 31
- [77] T. Mizokawa, D. I. Khomskii, and G. A. Sawatzky. Interplay between orbital ordering and lattice distortions in LaMnO_3 , YVO_3 , and YTiO_3 . *Physical Review B*, 60(10): 7309–7313, September 1999. doi:[10.1103/PhysRevB.60.7309](https://doi.org/10.1103/PhysRevB.60.7309). Publisher: American Physical Society. 27, 29, 30, 31
- [78] B Souvignier, H Wondratschek, M I Aroyo, G Chapuis, and A M Glazer. 1.4. Space groups and their descriptions. doi:[10.1107/97809553602060000922](https://doi.org/10.1107/97809553602060000922). 27
- [79] M. J. Martínez-Lope, J. A. Alonso, M. Retuerto, and M. T. Fernández-Díaz. Evolution of the Crystal Structure of RVO_3 (R = La, Ce, Pr, Nd, Tb, Ho, Er, Tm, Yb, Lu, Y) Perovskites from Neutron Powder Diffraction Data. *Inorganic Chemistry*, 47(7): 2634–2640, April 2008. ISSN 0020-1669. doi:[10.1021/ic701969q](https://doi.org/10.1021/ic701969q). Publisher: American Chemical Society. 27, 29
- [80] H. L. Yakel. On the structures of some compounds of the perovskite type. *Acta Crystallographica*, 8(7):394–398, July 1955. ISSN 0365-110X. doi:[10.1107/S0365110X55001291](https://doi.org/10.1107/S0365110X55001291). 27
- [81] Félix Bertaut and Francis Forrat. Sur les déformations dans les pérovskites à base de terres rares et d'éléments de transition trivalents. *Journal de Physique et le Radium*, 17(2):129–131, 1956. ISSN 0368-3842. doi:[10.1051/jphysrad:01956001702012900](https://doi.org/10.1051/jphysrad:01956001702012900). 27

- [82] M. O’Keeffe and B. G. Hyde. Some structures topologically related to cubic perovskite (E21), ReO_3 (D09) and Cu_3Au (L12). *Acta Crystallographica Section B: Structural Crystallography and Crystal Chemistry*, 33(12):3802–3813, December 1977. ISSN 0567-7408. doi:[10.1107/S0567740877012114](https://doi.org/10.1107/S0567740877012114). 27, 29
- [83] A. Vailionis, H. Boschker, W. Siemons, E. P. Houwman, D. H. A. Blank, G. Rijnders, and G. Koster. Misfit strain accommodation in epitaxial ABO_3 perovskites: Lattice rotations and lattice modulations. *Physical Review B*, 83(6):064101, February 2011. ISSN 1098-0121, 1550-235X. doi:[10.1103/PhysRevB.83.064101](https://doi.org/10.1103/PhysRevB.83.064101). 28
- [84] R. D. Shannon and C. T. Prewitt. Revised values of effective ionic radii. *Acta Crystallographica Section B*, 26(7):1046–1048, 1970. ISSN 1600-5740. doi:[10.1107/S0567740870003576](https://doi.org/10.1107/S0567740870003576). 28
- [85] Robert D Shannon. Revised effective ionic radii and systematic studies of interatomic distances in halides and chalcogenides. *Acta Cryst. A*, 32(5):751–767, 1976. doi:<https://doi-org/10.1107/S0567739476001551>. 28, 29
- [86] V. L. Miller and S. C. Tidrow. Review: New simple material model versus Goldschmidt’s tolerance factor formalism. *Ferroelectrics*, 503(1):149–162, October 2016. ISSN 0015-0193, 1563-5112. doi:[10.1080/00150193.2016.1215750](https://doi.org/10.1080/00150193.2016.1215750). 28
- [87] Imperial College. Database of Ionic Radii. <http://abulafia.mt.ic.ac.uk/shannon/>. Accessed: 2024-01-28. 29
- [88] Y. Q. Jia. Crystal radii and effective ionic radii of the rare earth ions. *Journal of Solid State Chemistry*, 95(1):184–187, November 1991. ISSN 0022-4596. doi:[10.1016/0022-4596\(91\)90388-X](https://doi.org/10.1016/0022-4596(91)90388-X). 29
- [89] Ulrich Müller. *Anorganische Strukturchemie*. Vieweg+Teubner, Wiesbaden, 6 edition, 2008. ISBN 978-3-8348-0626-0 978-3-8348-9545-5. doi:[10.1007/978-3-8348-9545-5](https://doi.org/10.1007/978-3-8348-9545-5). 29
- [90] Adolfo Avella, Andrzej M. Oleś, and Peter Horsch. Defect-Induced Orbital Polarization and Collapse of Orbital Order in Doped Vanadium Perovskites. *Physical Review Letters*, 122(12):127206, March 2019. ISSN 0031-9007, 1079-7114. doi:[10.1103/PhysRevLett.122.127206](https://doi.org/10.1103/PhysRevLett.122.127206). 29
- [91] G. R. Blake, T. T. M. Palstra, Y. Ren, A. A. Nugroho, and A. A. Menovsky. Transition between Orbital Orderings in YVO_3 . *Physical Review Letters*, 87(24):245501, November 2001. ISSN 0031-9007, 1079-7114. doi:[10.1103/PhysRevLett.87.245501](https://doi.org/10.1103/PhysRevLett.87.245501). 29
- [92] Zhong Fang and Naoto Nagaosa. Quantum Versus Jahn-Teller Orbital Physics in YVO_3 and LaVO_3 . *Physical Review Letters*, 93(17):176404, October 2004. ISSN 0031-9007, 1079-7114. doi:[10.1103/PhysRevLett.93.176404](https://doi.org/10.1103/PhysRevLett.93.176404). 29, 35, 44
- [93] J. Fujioka, T. Yasue, S. Miyasaka, Y. Yamasaki, T. Arima, H. Sagayama, T. Inami, K. Ishii, and Y. Tokura. Critical competition between two distinct orbital-spin ordered states in perovskite vanadates. *Physical Review B*, 82(14):144425, October 2010. ISSN 1098-0121, 1550-235X. doi:[10.1103/PhysRevB.82.144425](https://doi.org/10.1103/PhysRevB.82.144425). 29

- [94] A. Muñoz, J. A. Alonso, M. T. Casais, M. J. Martínez-Lope, J. L. Martínez, and M. T. Fernández-Díaz. Thermal Evolution of the Crystallographic and Magnetic Structure in LuVO_3 : A Neutron Diffraction Study. *Chemistry of Materials*, 16(8):1544–1550, April 2004. ISSN 0897-4756, 1520-5002. doi:[10.1021/cm035314a](https://doi.org/10.1021/cm035314a). 29, 35
- [95] Benoit Roberge, Serge Jandl, Agung A. Nugroho, Thomas T. M. Palstra, Le D. Tung, and Geetha Balakrishnan. Study of phase coexistence in YVO_3 and LaVO_3 . *Journal of Raman Spectroscopy*, 46(11):1157–1160, 2015. ISSN 1097-4555. doi:[10.1002/jrs.4735](https://doi.org/10.1002/jrs.4735). 29
- [96] Kliment I Kugel' and D I Khomskii. The jahn-teller effect and magnetism: transition metal compounds. *Soviet Physics Uspekhi*, 25(4):231, apr 1982. doi:[10.1070/PU1982v025n04ABEH004537](https://doi.org/10.1070/PU1982v025n04ABEH004537). 29, 30, 31
- [97] A. A. Tsvetkov, F. P. Mena, P. H. M. Van Loosdrecht, D. Van Der Marel, Y. Ren, A. A. Nugroho, A. A. Menovsky, I. S. Elfimov, and G. A. Sawatzky. Structural, electronic, and magneto-optical properties of YVO_3 . *Physical Review B*, 69(7):075110, February 2004. ISSN 1098-0121, 1550-235X. doi:[10.1103/PhysRevB.69.075110](https://doi.org/10.1103/PhysRevB.69.075110). 29
- [98] H. A. Jahn, E. Teller, and Frederick George Donnan. Stability of polyatomic molecules in degenerate electronic states - I—Orbital degeneracy. *Proceedings of the Royal Society of London. Series A - Mathematical and Physical Sciences*, 161(905):220–235, January 1997. doi:[10.1098/rspa.1937.0142](https://doi.org/10.1098/rspa.1937.0142). Publisher: Royal Society. 29
- [99] M. Reehuis, C. Ulrich, K. Prokeš, S. Mat'aš, J. Fujioka, S. Miyasaka, Y. Tokura, and B. Keimer. Structural and magnetic phase transitions of the orthovanadates RVO_3 ($\text{R} = \text{Dy}, \text{Ho}, \text{Er}$) as seen via neutron diffraction. *Physical Review B*, 83(6):064404, February 2011. ISSN 1098-0121, 1550-235X. doi:[10.1103/PhysRevB.83.064404](https://doi.org/10.1103/PhysRevB.83.064404). 31, 33
- [100] Giniyat Khaliullin. Orbital order and fluctuations in mott insulators. *Progress of Theoretical Physics Supplement*, 160:155–202, June 2005. ISSN 0375-9687. doi:[10.1143/PTPS.160.155](https://doi.org/10.1143/PTPS.160.155). 34
- [101] C. Ulrich, G. Khaliullin, J. Sirker, M. Reehuis, M. Ohl, S. Miyasaka, Y. Tokura, and B. Keimer. Magnetic Neutron Scattering Study of YVO_3 : Evidence for an Orbital Peierls State. *Physical Review Letters*, 91(25):257202, December 2003. ISSN 0031-9007, 1079-7114. doi:[10.1103/PhysRevLett.91.257202](https://doi.org/10.1103/PhysRevLett.91.257202). 34, 44
- [102] Vladimir I. Anisimov, F. Aryasetiawan, and A. I. Lichtenstein. First-principles calculations of the electronic structure and spectra of strongly correlated systems: the LDA+ U method. *Journal of Physics: Condensed Matter*, 9(4):767, January 1997. ISSN 0953-8984. doi:[10.1088/0953-8984/9/4/002](https://doi.org/10.1088/0953-8984/9/4/002). 35
- [103] L.D. Tung, J. Schefer, M.R. Lees, G. Balakrishnan, and D.McK. Paul. Magnetic properties of a LuVO_3 single crystal studied by magnetometry, heat capacity and neutron diffraction. *Journal of Science: Advanced Materials and Devices*, 1(2):174–178, June 2016. ISSN 24682179. doi:[10.1016/j.jsamd.2016.06.013](https://doi.org/10.1016/j.jsamd.2016.06.013). 36

- [104] J. Friedrich. Methods for Bulk Growth of Inorganic Crystals: Crystal Growth. In *Reference Module in Materials Science and Materials Engineering*. Elsevier, January 2016. ISBN 978-0-12-803581-8. doi:[10.1016/B978-0-12-803581-8.01010-9](https://doi.org/10.1016/B978-0-12-803581-8.01010-9). 36
- [105] L. D. Tung, M. R. Lees, G. Balakrishnan, and D. McK. Paul. Magnetization reversal in orthovanadate RVO_3 compounds ($R = \text{La, Nd, Sm, Gd, Er, and Y}$): Inhomogeneities caused by defects in the orbital sector of quasi-one-dimensional orbital systems. *Physical Review B*, 75(10):104404, March 2007. doi:[10.1103/PhysRevB.75.104404](https://doi.org/10.1103/PhysRevB.75.104404). Publisher: American Physical Society. 36
- [106] Yoyo Hinuma, Giovanni Pizzi, Yu Kumagai, Fumiyasu Oba, and Isao Tanaka. Band structure diagram paths based on crystallography. *Computational Materials Science*, 128:140–184, February 2017. ISSN 0927-0256. doi:[10.1016/j.commatsci.2016.10.015](https://doi.org/10.1016/j.commatsci.2016.10.015). 37
- [107] M. J. Cooper and R. Nathans. The resolution function in neutron diffractometry. I. The resolution function of a neutron diffractometer and its application to phonon measurements. *Acta Crystallographica*, 23(3):357–367, 1967. ISSN 0365-110X. doi:[10.1107/S0365110X67002816](https://doi.org/10.1107/S0365110X67002816). 37, 38, 72
- [108] M. Popovici. On the resolution of slow-neutron spectrometers. IV. The triple-axis spectrometer resolution function, spatial effects included. *Acta Crystallographica Section A*, 31(4):507–513, July 1975. ISSN 0567-7394. doi:[10.1107/S0567739475001088](https://doi.org/10.1107/S0567739475001088). 37, 72
- [109] Hirotogu Akaike. Information Theory and an Extension of the Maximum Likelihood Principle. In Emanuel Parzen, Kunio Tanabe, and Genshiro Kitagawa, editors, *Selected Papers of Hirotogu Akaike*, Springer Series in Statistics, pages 199–213. Springer, New York, NY, 1998. ISBN 978-1-4612-1694-0. doi:[10.1007/978-1-4612-1694-0_15](https://doi.org/10.1007/978-1-4612-1694-0_15). 38
- [110] Hirotogu Akaike. A new look at the statistical model identification. *IEEE transactions on automatic control*, 19(6):716–723, 1974. Publisher: Ieee. 38
- [111] G. Shirane, J. D. Axe, J. Harada, and J. P. Remeika. Soft Ferroelectric Modes in Lead Titanate. *Physical Review B*, 2(1):155–159, July 1970. doi:[10.1103/PhysRevB.2.155](https://doi.org/10.1103/PhysRevB.2.155). Publisher: American Physical Society. 43
- [112] Jiawang Hong, Alessandro Stroppa, Jorge Íñiguez, Silvia Picozzi, and David Vanderbilt. Spin-phonon coupling effects in transition-metal perovskites: A DFT + U and hybrid-functional study. *Physical Review B*, 85(5):054417, February 2012. doi:[10.1103/PhysRevB.85.054417](https://doi.org/10.1103/PhysRevB.85.054417). Publisher: American Physical Society. 44
- [113] Michael A. Carpenter, Ekhard K.H. Salje, and Ann Graeme-Barber. Spontaneous strain as a determinant of thermodynamic properties for phase transitions in minerals. *European Journal of Mineralogy*, 10(4):621–691, July 1998. ISSN 0935-1221. doi:[10.1127/ejm/10/4/0621](https://doi.org/10.1127/ejm/10/4/0621). 44

- [114] Isao Suzuki, Orson L. Anderson, and Yoshio Sumino. Elastic properties of a single-crystal forsterite Mg_2SiO_4 , up to 1,200 K. *Physics and Chemistry of Minerals*, 10(1): 38–46, January 1983. ISSN 1432-2021. doi:[10.1007/BF01204324](https://doi.org/10.1007/BF01204324). 46, 51
- [115] Woldemar Voigt. *Lehrbuch der Kristallphysik (mit Ausschluss der Kristalloptik)*. Leipzig, Berlin, B.G. Teubner, 1910. ISBN 978-3-663-15316-0. doi:[10.1007/978-3-663-15884-4](https://doi.org/10.1007/978-3-663-15884-4). 47
- [116] J.F. Nye. *Physical properties of crystals.*, volume 1. Oxford University Press, Oxford, 1985. ISBN 978-0-1985-1165-6. 47
- [117] L. D. Landau and E. M. Lifshitz. *Statistical Physics - 3rd Edition*, volume 1. Elsevier, 3 edition, 1951. ISBN 978-0-7506-3372-7. 47, 123
- [118] L. Landau. The Theory of Phase Transitions. *Nature*, 138(3498):840–841, November 1936. ISSN 1476-4687. doi:[10.1038/138840a0](https://doi.org/10.1038/138840a0). Number: 3498 Publisher: Nature Publishing Group. 47
- [119] B. Kressdorf, T. Meyer, M. Ten Brink, C. Seick, S. Melles, N. Ottinger, T. Titze, H. Meer, A. Weisser, J. Hoffmann, S. Mathias, H. Ulrichs, D. Steil, M. Seibt, P. E. Blöchl, and C. Jooss. Orbital-order phase transition in $\text{Pr}_{1-x}\text{Ca}_x\text{MnO}_3$ probed by photovoltaics. *Physical Review B*, 103(23):235122, June 2021. ISSN 2469-9950, 2469-9969. doi:[10.1103/PhysRevB.103.235122](https://doi.org/10.1103/PhysRevB.103.235122). 50
- [120] T. Weber, B. Roessli, C. Stock, T. Keller, K. Schmalzl, F. Bourdarot, R. Georgii, R. A. Ewings, R. S. Perry, and P. Böni. Transverse acoustic phonon anomalies at intermediate wave vectors in MgV_2O_4 . *Physical Review B*, 96(18):184301, November 2017. ISSN 2469-9950, 2469-9969. doi:[10.1103/PhysRevB.96.184301](https://doi.org/10.1103/PhysRevB.96.184301). 52
- [121] Martin T. Dove. *Introduction to lattice dynamics*. Number 4 in Cambridge topics in mineral physics and chemistry. Cambridge University Press, Cambridge ; New York, 1993. ISBN 978-0-521-39293-8. 53
- [122] S. Waffenschmidt, C. Pfeiderer, and H. v. Löhneysen. Critical Behavior of the Conductivity of Si:P at the Metal-Insulator Transition under Uniaxial Stress. *Physical Review Letters*, 83(15):3005–3008, October 1999. doi:[10.1103/PhysRevLett.83.3005](https://doi.org/10.1103/PhysRevLett.83.3005). 53
- [123] C. Pfeiderer, E. Bedin, and B. Salce. He activated loading device for low temperature uniaxial and anvil cell pressure experiments. *Review of Scientific Instruments*, 68(8): 3120–3124, August 1997. ISSN 0034-6748. doi:[10.1063/1.1148254](https://doi.org/10.1063/1.1148254). 53
- [124] G. Gamow and Ernest Rutherford. Mass defect curve and nuclear constitution. *Proceedings of the Royal Society of London. Series A, Containing Papers of a Mathematical and Physical Character*, 126(803):632–644, March 1930. doi:[10.1098/rspa.1930.0032](https://doi.org/10.1098/rspa.1930.0032). 55

- [125] C. F. v. Weizsäcker. Zur Theorie der Kernmassen. *Zeitschrift für Physik*, 96(7):431–458, July 1935. ISSN 0044-3328. doi:[10.1007/BF01337700](https://doi.org/10.1007/BF01337700). 55
- [126] J. M. Carpenter and C.-K. Loong. *Elements of Slow-Neutron Scattering: Basics, Techniques, and Applications*. Cambridge University Press, 1 edition, September 2015. ISBN 978-1-139-02931-5 978-0-521-85781-9. doi:[10.1017/CBO9781139029315](https://doi.org/10.1017/CBO9781139029315). 55, 56
- [127] Nadia Fomin, Jason Fry, Robert W. Pattie, and Geoffrey L. Greene. Fundamental neutron physics at spallation sources. *Annual Review of Nuclear and Particle Science*, 72(1):151–176, 2022. doi:[10.1146/annurev-nucl-121521-051029](https://doi.org/10.1146/annurev-nucl-121521-051029). 56
- [128] Bruce M. Foreman, Walter M. Gibson, Richard A. Glass, and Glenn T. Seaborg. Spallation-fission competition in heavy-element reactions: Th232+He4 and U233+d. *Physical Review*, 116(2):382–392, October 1959. doi:[10.1103/PhysRev.116.382](https://doi.org/10.1103/PhysRev.116.382). 56
- [129] S Kaminskas. SNS mercury target design optimization. *Journal of Physics: Conference Series*, 1021(1):012052, May 2018. doi:[10.1088/1742-6596/1021/1/012052](https://doi.org/10.1088/1742-6596/1021/1/012052). 56
- [130] V. Weisskopf. Statistics and Nuclear Reactions. *Physical Review*, 52(4):295–303, August 1937. ISSN 0031-899X. doi:[10.1103/PhysRev.52.295](https://doi.org/10.1103/PhysRev.52.295). 56
- [131] John M. Carpenter. Pulsed spallation neutron sources for slow neutron scattering. *Nuclear Instruments and Methods*, 145(1):91–113, August 1977. ISSN 0029-554X. doi:[10.1016/0029-554X\(77\)90560-2](https://doi.org/10.1016/0029-554X(77)90560-2). 56
- [132] William P. Swanson. Calculation of Neutron Yields Released by Electrons Incident on Selected Materials. *Health Physics*, 35(2):353, August 1978. ISSN 0017-9078. 56
- [133] Andrew Taylor, Mike Dunne, Steve Bennington, Stuart Ansell, Ian Gardner, Peter Norreys, Tim Broome, David Findlay, and Richard Nelves. A Route to the Brightest Possible Neutron Source? *Science*, 315(5815):1092–1095, February 2007. doi:[10.1126/science.1127185](https://doi.org/10.1126/science.1127185). 56
- [134] J. Alvarez, J. Fernández-Tobias, K. Mima, S. Nakai, S. Kar, Y. Kato, and J. M. Perlado. Laser Driven Neutron Sources: Characteristics, Applications and Prospects. *Physics Procedia*, 60:29–38, January 2014. ISSN 1875-3892. doi:[10.1016/j.phpro.2014.11.006](https://doi.org/10.1016/j.phpro.2014.11.006). 56
- [135] Vojtěch Horný, Sophia N. Chen, Xavier Davoine, Vincent Lelasseux, Laurent Gremillet, and Julien Fuchs. High-flux neutron generation by laser-accelerated ions from single- and double-layer targets. *Scientific Reports*, 12(1):19767, November 2022. ISSN 2045-2322. doi:[10.1038/s41598-022-24155-z](https://doi.org/10.1038/s41598-022-24155-z). 56
- [136] D. Habs, S. Gasilov, C. Lang, P. G. Thirolf, M. Jentschel, R. Diehl, C. Schroer, C. P. J. Barty, and N. V. Zamfir. Intense, brilliant micro γ -beams in nuclear physics and applications. In *Harnessing Relativistic Plasma Waves as Novel Radiation Sources from Terahertz to X-Rays and Beyond II*, volume 8075, pages 35–47. SPIE, May 2011. doi:[10.1117/12.891512](https://doi.org/10.1117/12.891512). 56

- [137] D. Habs, M. Gross, P. G. Thirolf, and P. Böni. Neutron halo isomers in stable nuclei and their possible application for the production of low energy, pulsed, polarized neutron beams of high intensity and high brilliance. *Applied Physics B*, 103(2):485–499, May 2011. ISSN 1432-0649. doi:[10.1007/s00340-010-4276-3](https://doi.org/10.1007/s00340-010-4276-3). 56, 137
- [138] Paul Bolton, Katia Parodi, and Jörg Schreiber. *Applications of laser-driven particle acceleration*. CRC Press, Boca Raton, FL, USA, 1 edition, 2018. ISBN 978-0-4294-4510-1. doi:[10.1201/9780429445101](https://doi.org/10.1201/9780429445101). 57
- [139] M. J. Mühlbauer, T. Bücherl, M. Kellermeier, M. Knapp, M. Makowska, M. Schulz, S. Zimmnik, and H. Ehrenberg. Neutron imaging with fission and thermal neutrons at NECTAR at MLZ. *Physica B: Condensed Matter*, 551:359–363, December 2018. ISSN 0921-4526. doi:[10.1016/j.physb.2017.11.088](https://doi.org/10.1016/j.physb.2017.11.088). 56
- [140] Franz M. Wagner, Peter Kneschaurek, Anton Kastenmüller, Birgit Loeper-Kabasakal, Severin Kampfer, Harald Breitzkreutz, Wolfgang Waschkowski, Michael Molls, and Winfried Petry. The Munich Fission Neutron Therapy Facility MEDAPP at the research reactor FRM II. *Strahlentherapie Und Onkologie: Organ Der Deutschen Rontgengesellschaft ... [et Al]*, 184(12):643–646, December 2008. ISSN 0179-7158. doi:[10.1007/s00066-008-1878-3](https://doi.org/10.1007/s00066-008-1878-3). 56
- [141] Konstantin Gordon, Igor Gulidov, Timur Fatkhudinov, Sergey Koryakin, and Andrey Kaprin. Fast and Furious: Fast Neutron Therapy in Cancer Treatment. *International Journal of Particle Therapy*, 9(2):59–69, August 2022. ISSN 2331-5180. doi:[10.14338/IJPT-22-00017](https://doi.org/10.14338/IJPT-22-00017). 56
- [142] Naohiko Otuka, Tsuneo Nakagawa, and Keiichi Shibata. Uranium-235 Neutron Capture Cross Section at keV Energies. *Journal of Nuclear Science and Technology*, 44(6): 815–818, June 2007. ISSN 0022-3131, 1881-1248. doi:[10.1080/18811248.2007.9711318](https://doi.org/10.1080/18811248.2007.9711318). 56
- [143] Phillip M. Rinard. Neutron interactions with matter. 1997. 57
- [144] Vladimir Hutanu, A Röhrmoser, C Müller, M Fuss, A Pichlmaier, M Meven, L Peters, and G Roth. Hot neutrons and their applications at FRM II reactor. In *European research reactor conference*, 2021. Number: FZJ-2021-05248 tex.organization: Streumethoden. 57
- [145] Werner Gaubatz and Klaus Gobrecht. The FRM-II cold neutron source. *Physica B: Condensed Matter*, 276-278:104–105, March 2000. ISSN 0921-4526. doi:[10.1016/S0921-4526\(99\)01260-0](https://doi.org/10.1016/S0921-4526(99)01260-0). 57
- [146] H. Aschauer, A. Fleischmann, C. Schanzer, and E. Steichele. Neutron guides at the FRM-II. *Physica B: Condensed Matter*, 283(4):323–329, June 2000. ISSN 0921-4526. doi:[10.1016/S0921-4526\(00\)00324-0](https://doi.org/10.1016/S0921-4526(00)00324-0). 57

- [147] E. Fermi, W.H. Zinn, Los Alamos National Laboratory, and U. S. Atomic Energy Commission. *Reflection of Neutrons on Mirrors*. United States. Atomic Energy Commission. MDDC. Manhattan District, 1946. 58
- [148] M. L. Goldberger and Frederick Seitz. Theory of the Refraction and the Diffraction of Neutrons by Crystals. *Physical Review*, 71(5):294–310, March 1947. doi:[10.1103/PhysRev.71.294](https://doi.org/10.1103/PhysRev.71.294). 58
- [149] V. F. Sears. Fundamental aspects of neutron optics. *Physics Reports*, 82(1):1–29, February 1982. ISSN 0370-1573. doi:[10.1016/0370-1573\(82\)90151-X](https://doi.org/10.1016/0370-1573(82)90151-X). 59
- [150] D. A. Kirschner and D. L. D. Caspar. Comparative Diffraction Studies on Myelin Membranes*. *Annals of the New York Academy of Sciences*, 195(1):309–320, 1972. ISSN 1749-6632. doi:[10.1111/j.1749-6632.1972.tb54811.x](https://doi.org/10.1111/j.1749-6632.1972.tb54811.x). 61
- [151] VF Turchin. Diffraction of slow neutrons by stratified systems. *Soviet Atomic Energy*, 22(2):124–125, 1967. doi:[10.1007/BF01246267](https://doi.org/10.1007/BF01246267). 61
- [152] F. Mezei and P. A. Dagliesh. Corrigendum and first experimental evidence on neutron supermirrors. *Communications on Physics*, 2:41–43, 1977. 61
- [153] J. B. Hayter and H. A. Mook. Discrete thin-film multilayer design for X-ray and neutron supermirrors. *Journal of Applied Crystallography*, 22(1):35–41, February 1989. doi:[10.1107/S0021889888010003](https://doi.org/10.1107/S0021889888010003). 61
- [154] C. Schanzer, M. Schneider, and P. Böni. Neutron Optics: Towards Applications for Hot Neutrons. *Journal of Physics: Conference Series*, 746(1):012024, 2016. doi:[10.1088/1742-6596/746/1/012024](https://doi.org/10.1088/1742-6596/746/1/012024). 61
- [155] W. Wagner, G.S. Bauer, J. Duppich, S. Janssen, E. Lehmann, M. Lüthy, and H. Spitzer. Flux Measurements at the New Swiss Spallation Neutron Source SINQ. *Journal of Neutron Research*, 6(4):249–278, 1998. doi:[10.1080/10238169808200039](https://doi.org/10.1080/10238169808200039). 61
- [156] O. Schaerpf. Comparison of theoretical and experimental behaviour of supermirrors and discussion of limitations. *Physica B: Condensed Matter*, 156-157:631–638, January 1989. ISSN 09214526. doi:[10.1016/0921-4526\(89\)90750-3](https://doi.org/10.1016/0921-4526(89)90750-3). 62
- [157] T. Krist and F. Mezei. Neutron optical developments at HMI Berlin. *Proceedings of ICANS-XVIII*, pages 149 – 155, 2007. 62
- [158] S. Masalovich. Analysis and design of multilayer structures for neutron monochromators and supermirrors. *Nuclear Instruments and Methods in Physics Research Section A: Accelerators, Spectrometers, Detectors and Associated Equipment*, 722:71–81, September 2013. ISSN 01689002. doi:[10.1016/j.nima.2013.04.051](https://doi.org/10.1016/j.nima.2013.04.051). 62
- [159] Christine Klauser, Ryan Bergmann, Uwe Filges, and Jochen Stahn. A Selene Guide for AMOR. *Journal of Physics: Conference Series*, 1021:012024, May 2018. ISSN 1742-6588, 1742-6596. doi:[10.1088/1742-6596/1021/1/012024](https://doi.org/10.1088/1742-6596/1021/1/012024). 62

- [160] J. Stahn and A. Glavic. Focusing neutron reflectometry: Implementation and experience on the TOF-reflectometer Amor. *Nuclear Instruments and Methods in Physics Research Section A: Accelerators, Spectrometers, Detectors and Associated Equipment*, 821:44–54, June 2016. ISSN 0168-9002. doi:[10.1016/j.nima.2016.03.007](https://doi.org/10.1016/j.nima.2016.03.007). 62, 134, 136
- [161] P Zakalek, T Cronert, J Baggemann, P-E Doege, M Rimmler, J Voigt, E Mauerhofer, U Rucker, T Gutberlet, H Podlech, O Meusel, M Schwarz, J Li, S Böhm, and Th Brückel. High-Brilliance Neutron Source Project. *Journal of Physics: Conference Series*, 1401(1):012010, January 2020. ISSN 1742-6588, 1742-6596. doi:[10.1088/1742-6596/1401/1/012010](https://doi.org/10.1088/1742-6596/1401/1/012010). 63
- [162] C Schanzer, P Böni, and M Schneider. High performance supermirrors on metallic substrates. In *Journal of physics: Conference series*, volume 251, page 012082. IOP Publishing, 2010. Issue: 1. 64
- [163] L. Zanini, K.H. Andersen, K. Batkov, E.B. Klinkby, F. Mezei, T. Schönfeldt, and A. Takibayev. Design of the cold and thermal neutron moderators for the European Spallation Source. *Nuclear Instruments and Methods in Physics Research Section A: Accelerators, Spectrometers, Detectors and Associated Equipment*, 925:33–52, 2019. ISSN 0168-9002. doi:<https://doi.org/10.1016/j.nima.2019.01.003>. 64, 124, 137
- [164] Christian Schanzer, Peter Böni, Uwe Filges, and Thomas Hils. Advanced geometries for ballistic neutron guides. *Nuclear Instruments and Methods in Physics Research Section A: Accelerators, Spectrometers, Detectors and Associated Equipment*, 529(1): 63 – 68, 2004. ISSN 0168-9002. doi:<https://doi.org/10.1016/j.nima.2004.04.178>. 64
- [165] H. Häse, A. Knöpfler, K. Fiederer, U. Schmidt, D. Dubbers, and W. Kaiser. A long ballistic supermirror guide for cold neutrons at ILL. *Nuclear Instruments and Methods in Physics Research Section A: Accelerators, Spectrometers, Detectors and Associated Equipment*, 485(3):453–457, June 2002. ISSN 01689002. doi:[10.1016/S0168-9002\(01\)02105-2](https://doi.org/10.1016/S0168-9002(01)02105-2). 64
- [166] C. Zendler, D. Martin Rodriguez, and P. M. Bentley. Generic guide concepts for the European Spallation Source. *Nuclear Instruments and Methods in Physics Research Section A: Accelerators, Spectrometers, Detectors and Associated Equipment*, 803:89 – 99, 2015. ISSN 0168-9002. doi:<https://doi.org/10.1016/j.nima.2015.09.035>. 64
- [167] G. Brandl, R. Georgii, S. R. Dunsiger, V. Tsurkan, A. Loidl, T. Adams, C. Pfeleiderer, and P. Böni. Compact turnkey focussing neutron guide system for inelastic scattering investigations. *Applied Physics Letters*, 107(25):253505, 2015. doi:[10.1063/1.4938503](https://doi.org/10.1063/1.4938503). 64
- [168] Ursula Benggaard Hansen, Mads Bertelsen, Erik Bergbäck Knudsen, and Kim Lefmann. Simulation of waviness in neutron guides. *Journal of Neutron Research*, 18(2-3):45–59, January 2015. ISSN 1023-8166. doi:[10.3233/JNR-150023](https://doi.org/10.3233/JNR-150023). 64

- [169] L. D. Cussen, D. Nekrassov, C. Zandler, and K. Lieutenant. Multiple reflections in elliptic neutron guide tubes. *Nuclear Instruments and Methods in Physics Research Section A: Accelerators, Spectrometers, Detectors and Associated Equipment*, 705:121–131, 2013. ISSN 0168-9002. doi:<https://doi.org/10.1016/j.nima.2012.11.183>. 65
- [170] Phillip M. Bentley, Shane J. Kennedy, Ken H. Andersen, Damián Martín Rodríguez, and David F. R. Mildner. Correction of optical aberrations in elliptic neutron guides. *Nuclear Instruments and Methods in Physics Research Section A: Accelerators, Spectrometers, Detectors and Associated Equipment*, 693:268 – 275, 2012. ISSN 0168-9002. doi:<https://doi.org/10.1016/j.nima.2012.07.002>. 65
- [171] Wolfram Research Inc. Mathematica, Version 13.3. <https://www.wolfram.com/mathematica>. Accessed: 2024-01-28. 70, 179, 181
- [172] Peter Kjær Willendrup and Kim Lefmann. McStas (i): Introduction, use, and basic principles for ray-tracing simulations. *Journal of Neutron Research*, 22(1):1–16, January 2020. ISSN 1023-8166. doi:[10.3233/JNR-190108](https://doi.org/10.3233/JNR-190108). 71, 82, 94
- [173] Tobias Weber, Robert Georgii, and Peter Böni. Takin: An open-source software for experiment planning, visualisation, and data analysis. *SoftwareX*, 5:121–126, January 2016. ISSN 2352-7110. doi:[10.1016/j.softx.2016.06.002](https://doi.org/10.1016/j.softx.2016.06.002). Publisher: Elsevier. 72
- [174] Oliver Zimmer. *Multi-mirror imaging optics for low-loss transport of divergent neutron beams and tailored wavelength spectra*. 2016. doi:[10.48550/arXiv.1611.07353](https://doi.org/10.48550/arXiv.1611.07353). 74, 75, 189
- [175] Nikolay Kardjilov, Peter Böni, André Hilger, Markus Strobl, and Wolfgang Treimer. Characterization of a focusing parabolic guide using neutron radiography method. *Nuclear Instruments and Methods in Physics Research Section A: Accelerators, Spectrometers, Detectors and Associated Equipment*, 542(1):248–252, April 2005. ISSN 0168-9002. doi:[10.1016/j.nima.2005.01.108](https://doi.org/10.1016/j.nima.2005.01.108). 79
- [176] B. Khaykovich, M. V. Gubarev, Y. Bagdasarova, B. D. Ramsey, and D. E. Moncton. From x-ray telescopes to neutron scattering: Using axisymmetric mirrors to focus a neutron beam. *Nuclear Instruments and Methods in Physics Research Section A: Accelerators, Spectrometers, Detectors and Associated Equipment*, 631(1):98–104, March 2011. ISSN 0168-9002. doi:[10.1016/j.nima.2010.11.110](https://doi.org/10.1016/j.nima.2010.11.110). 81, 83, 132
- [177] B. Khaykovich, S. Romaine, A. Ames, R. Bruni, H. A. Ambaye, A. Glavic, V. Lauter, and D. Engelhaupt. Fabrication and testing of high-performance all-metal neutron guides and axisymmetric mirrors by electrochemical replication. *MRS Advances*, 5 (29-30):1513–1528, June 2020. ISSN 2059-8521. doi:[10.1557/adv.2020.142](https://doi.org/10.1557/adv.2020.142). 81
- [178] Huarui Wu, Yang Yang, Daniel S. Hussey, Zhiyuan Wang, Kun Song, Zhong Zhang, Zhanshan Wang, Zhe Wang, and Xuewu Wang. Study of a nested neutron-focusing supermirror system for small-angle neutron scattering. *Nuclear Instruments and Methods in Physics Research Section A: Accelerators, Spectrometers, De-*

- tectors and Associated Equipment*, 940:380–386, October 2019. ISSN 0168-9002. doi:[10.1016/j.nima.2019.06.054](https://doi.org/10.1016/j.nima.2019.06.054). 81
- [179] Huarui Wu, Zhiyuan Wang, Yao Zhang, Wenbo Mo, Pulin Bai, Kun Song, Zhong Zhang, Zhanshan Wang, Daniel S. Hussey, Yun Liu, Zhe Wang, and Xuewu Wang. Demonstration of small-angle neutron scattering measurements with a nested neutron-focusing supermirror assembly. *Nuclear Instruments and Methods in Physics Research Section A: Accelerators, Spectrometers, Detectors and Associated Equipment*, 972:164072, August 2020. ISSN 0168-9002. doi:[10.1016/j.nima.2020.164072](https://doi.org/10.1016/j.nima.2020.164072). 81
- [180] McStas homepage. https://www.mcstas.org/download/components/3.4/contrib/FlatEllipse_finite_mirror.html. Accessed: 2024-01-12. 83
- [181] M. Köhli, F. Allmendinger, W. Häußler, T. Schröder, M. Klein, M. Meven, and U. Schmidt. Efficiency and spatial resolution of the CASCADE thermal neutron detector. *Nuclear Instruments and Methods in Physics Research Section A: Accelerators, Spectrometers, Detectors and Associated Equipment*, 828:242–249, August 2016. ISSN 01689002. doi:[10.1016/j.nima.2016.05.014](https://doi.org/10.1016/j.nima.2016.05.014). 87, 89
- [182] O Ruediger, J Stickforth, and G Lohrke. Boral-a shielding material for thermal neutrons. *Technische Mitteilungen Krupp (West Germany) Divided into Tech. Mitt. Krupp, Forschungsber. and Tech. Mitt. Krupp, Werksber.*, 19, 1961. Publisher: Fried. Krupp WIDIA-Fabrik, Essen. 99
- [183] ATOS Compact Scan. <https://www.gom.com/en/products/3d-scanning/atos-compact-scan>. Accessed: 2024-01-28. 116
- [184] M E* Fitzpatrick, A T Fry, P* Holdway, F A Kandil, J* Shackleton, and L Suominen. Determination of residual stresses by x-ray diffraction. <http://eprintspublications.npl.co.uk/2391/>, September 2005. Accessed: 28.01.2024. 121
- [185] Ken Holst Andersen, Mads Bertelsen, Luca Zanini, Esben Bryndt Klinkby, Troels Schönfeldt, Phillip Martin Bentley, and Jan Saroun. Optimization of moderators and beam extraction at the ESS. *Journal of Applied Crystallography*, 51(2):264–281, April 2018. doi:[10.1107/S1600576718002406](https://doi.org/10.1107/S1600576718002406). 124, 125, 137
- [186] T Cronert, J P Dabruck, P E Doege, Y Bessler, M Klaus, M Hofmann, P Zakalek, U Rücker, C Lange, M Butzek, W Hansen, R Nabbi, and T Brückel. High brilliant thermal and cold moderator for the HBS neutron source project Jülich. *Journal of Physics: Conference Series*, 746:012036, September 2016. ISSN 1742-6588, 1742-6596. doi:[10.1088/1742-6596/746/1/012036](https://doi.org/10.1088/1742-6596/746/1/012036). 124
- [187] John M. Carpenter. The development of compact neutron sources. *Nature Reviews Physics*, 1(3):177–179, March 2019. ISSN 2522-5820. doi:[10.1038/s42254-019-0024-8](https://doi.org/10.1038/s42254-019-0024-8). Number: 3 Publisher: Nature Publishing Group. 124

- [188] Troels Schönfeldt, K. Batkov, Esben Bryndt Klinkby, Bent Lauritzen, F. Mezei, E. Pitcher, A. Takibayev, Peter Kjær Willendrup, and L. Zanini. Optimization of cold neutron beam extraction at ESS. 2013. 11th International Topical Meeting on Nuclear Applications of Accelerators, ACCAPP ; Conference date: 05-08-2013 Through 08-08-2013. [124](#)
- [189] Oliver Zimmer. Imaging nested-mirror assemblies – A new generation of neutron delivery systems? *Journal of Neutron Research*, 20:91–98, 2018. ISSN 1477-2655. doi:[10.3233/JNR-190101](#). Publisher: IOS Press. [125](#)
- [190] M. Schneider, J. Stahn, and P. Böni. Focusing of cold neutrons: Performance of a laterally graded and parabolically bent multilayer. *Nuclear Instruments and Methods in Physics Research Section A: Accelerators, Spectrometers, Detectors and Associated Equipment*, 610(2):530–533, November 2009. ISSN 0168-9002. doi:[10.1016/j.nima.2009.08.047](#). [125](#)
- [191] S. Weichselbaumer, G. Brandl, R. Georgii, J. Stahn, T. Panzner, and P. Böni. Tailoring phase-space in neutron beam extraction. *Nuclear Instruments and Methods in Physics Research Section A: Accelerators, Spectrometers, Detectors and Associated Equipment*, 793:75–80, 2015. ISSN 0168-9002. doi:<https://doi.org/10.1016/j.nima.2015.05.003>. [128](#)
- [192] O. Schaerpf. Properties of beam bender type neutron polarizers using supermirrors. *Physica B: Condensed Matter*, 156-157:639 – 646, 1989. ISSN 0921-4526. doi:[https://doi.org/10.1016/0921-4526\(89\)90751-5](https://doi.org/10.1016/0921-4526(89)90751-5). [132](#), [138](#)
- [193] B. Alefeld, J. Christ, W. Schmatz, D. Kukla, and R. Scherm. Neutronenleiter : ein Bericht über den derzeitigen Stand der Entwicklung. Technical Report FZJ-2017-03252, Kernforschungsanlage Jülich, Verlag, 1965. [132](#)
- [194] Pau Jorba, Michael Schulz, Daniel S. Hussey, Muhammad Abir, Marc Seifert, Vladimir Tsurkan, Alois Loidl, Christian Pfeiderer, and Boris Khaykovich. High-resolution neutron depolarization microscopy of the ferromagnetic transitions in Ni₃Al and HgCr₂Se₄ under pressure. *arXiv:1812.00864 [cond-mat]*, December 2018. doi:[10.1016/j.jmmm.2018.11.086](#). arXiv: 1812.00864. [132](#)
- [195] Pavel Trtik, Jan Hovind, Christian Grünzweig, Alex Bollhalder, Vincent Thominet, Christian David, Anders Kaestner, and Eberhard H. Lehmann. Improving the Spatial Resolution of Neutron Imaging at Paul Scherrer Institut – The Neutron Microscope Project. *Physics Procedia*, 69:169–176, January 2015. ISSN 1875-3892. doi:[10.1016/j.phpro.2015.07.024](#). [133](#)
- [196] Peter Böni. High intensity neutron beams for small samples. *Journal of Physics: Conference Series*, 502:012047, April 2014. doi:[10.1088/1742-6596/502/1/012047](#). [133](#), [134](#)
- [197] J. Stahn, T. Panzner, U. Filges, C. Marcelot, and P. Böni. Study on a focusing, low-background neutron delivery system. *Nuclear Instruments and*

- Methods in Physics Research Section A: Accelerators, Spectrometers, Detectors and Associated Equipment*, 634(1, Supplement):S12–S16, 2011. ISSN 0168-9002. doi:<https://doi.org/10.1016/j.nima.2010.06.221>. 134
- [198] Christian Schanzer, Michael Schneider, Uwe Filges, and Peter Böni. Variable focusing system for neutrons. *Journal of Physics: Conference Series*, 1021:012023, May 2018. doi:[10.1088/1742-6596/1021/1/012023](https://doi.org/10.1088/1742-6596/1021/1/012023). 135
- [199] T Hils, P Boeni, and J Stahn. Focusing parabolic guide for very small samples. *Physica B: Condensed Matter*, 350(1):166–168, July 2004. ISSN 0921-4526. doi:[10.1016/j.physb.2004.04.020](https://doi.org/10.1016/j.physb.2004.04.020). 136
- [200] Oliver Zimmer. Neutron conversion and cascaded cooling in paramagnetic systems for a high-flux source of very cold neutrons. *Physical Review C*, 93(3):035503, March 2016. doi:[10.1103/PhysRevC.93.035503](https://doi.org/10.1103/PhysRevC.93.035503). 138
- [201] Oliver Zimmer, Thierry Bigault, Skyler Degenkolb, Christoph Herb, Thomas Neulinger, Nicola Rizzi, Valentina Santoro, Alan Takibayev, Richard Wagner, and Luca Zanini. In-beam superfluid-helium ultracold neutron source for the ESS. *Journal of Neutron Research*, 24(2):95–110, January 2022. ISSN 1023-8166. doi:[10.3233/JNR-220045](https://doi.org/10.3233/JNR-220045). 138
- [202] B. J. Micklich and John M. Carpenter. Proceedings of the Workshop on Applications of a Very Cold Neutron Source. In *ANL-05/42*, 2005. 138
- [203] Florian M. Piegsa. New concept for a neutron electric dipole moment search using a pulsed beam. *Physical Review C*, 88(4):045502, October 2013. doi:[10.1103/PhysRevC.88.045502](https://doi.org/10.1103/PhysRevC.88.045502). 138
- [204] A. Addazi, K. Anderson, S. Ansell, K. S. Babu, J. L. Barrow, D. V. Baxter, P. M. Bentley, Z. Berezhiani, R. Bevilacqua, R. Biondi, C. Bohm, G. Brooijmans, L. J. Brousard, J. Cedercäll, C. Crawford, P. S. B. Dev, D. D. DiJulio, A. D. Dolgov, K. Dunne, P. Fierlinger, M. R. Fitzsimmons, A. Fomin, M. J. Frost, S. Gardiner, S. Gardner, A. Galindo-Uribarri, P. Geltenbort, S. Girmohanta, P. Golubev, E. Golubeva, G. L. Greene, T. Greenshaw, V. Gudkov, R. Hall-Wilton, L. Heilbronn, J. Herrero-Garcia, A. Holley, G. Ichikawa, T. M. Ito, E. Iverson, T. Johansson, L. Jönsson, Y.-J. Jwa, Y. Kamyshev, K. Kanaki, E. Kearns, Z. Kokai, B. Kerbikov, M. Kitaguchi, T. Kittelmann, E. Klinkby, A. Kobakhidze, L. W. Koerner, B. Kopeliovich, A. Kozela, V. Kudryavtsev, A. Kupsc, Y. T. Lee, M. Lindroos, J. Makkinje, J. I. Marquez, B. Meirose, T. M. Miller, D. Milstead, R. N. Mohapatra, T. Morishima, G. Muhrer, H. P. Mumm, K. Nagamoto, A. Nepomuceno, F. Nesti, V. V. Nesvizhevsky, T. Nilsson, A. Oskarsson, E. Paryev, R. W. Pattie, S. Penttil, H. Perrey, Y. N. Pokotilovski, I. Potashnikov, K. Ramic, C. Redding, J.-M. Richard, D. Ries, E. Rinaldi, N. Rizzi, N. Rossi, A. Ruggles, B. Rybolt, V. Santoro, U. Sarkar, A. Saunders, G. Senjanovic, A. P. Serebrov, H. M. Shimizu, R. Shrock, S. Silverstein, D. Silvermyr, W. M. Snow, A. Takibayev, I. Tkachev, L. Townsend, A. Tureanu, L. Varriano, A. Vainshtein, J. de Vries, R. Wagner, R. Woracek, Y. Yamagata, S. Yiu, A. R. Young, L. Zanini, Z. Zhang,

- and O. Zimmer. New high-sensitivity searches for neutrons converting into antineutrons and/or sterile neutrons at the HIBEAM/NNBAR experiment at the European Spallation Source. *Journal of Physics G: Nuclear and Particle Physics*, 48(7):070501, June 2021. ISSN 0954-3899. doi:[10.1088/1361-6471/abf429](https://doi.org/10.1088/1361-6471/abf429). 138
- [205] Torsten Soldner, Hartmut Abele, Gertrud Konrad, Bastian Märkisch, Florian M. Piegsa, Ulrich Schmidt, Camille Theroine, and Pablo Torres Sánchez. ANNI – A pulsed cold neutron beam facility for particle physics at the ESS. *EPJ Web of Conferences*, 219:10003, 2019. ISSN 2100-014X. doi:[10.1051/epjconf/201921910003](https://doi.org/10.1051/epjconf/201921910003). 138
- [206] J. M. Pendlebury and G. L. Greene. Considerations for an Intense Source of Ultracold Neutrons at the European Long Pulse Spallation Source. *Physics Procedia*, 51:78–84, January 2014. ISSN 1875-3892. doi:[10.1016/j.phpro.2013.12.018](https://doi.org/10.1016/j.phpro.2013.12.018). 138
- [207] Oliver Zimmer, Florian M. Piegsa, and Sergey N. Ivanov. Superthermal Source of Ultracold Neutrons for Fundamental Physics Experiments. *Physical Review Letters*, 107(13):134801, September 2011. doi:[10.1103/PhysRevLett.107.134801](https://doi.org/10.1103/PhysRevLett.107.134801). 138

Acknowledgments

At the end of the thesis, I now have the enormous pleasure of expressing gratitude towards all the great people who contributed to the successful completion of this thesis in a more or less direct way:

- My primary supervisor, Prof. Dr. Peter Böni: Without you and your invaluable guidance, this project would not have been possible. Even during the troubling times of the COVID-19 outbreak, you were always available for a quick virtual chat or a lengthy conversation. For this, for the innumerable discussions on neutron optics, and for your help with my general development as a physicist, I am deeply grateful.
- My second supervisor, Dr. Robert Georgii: You always had an open ear for my problems, cleared bureaucratic boundaries where you could, and supported my endeavors with helpful discussions. You have been a valuable mentor on the journey toward this thesis.
- Dr. Markos Skoulatos: You introduced me to the wonderful world of rare-earth vanadates. Your guidance, companionship, cooking at various beamtimes, humor, and interest in puzzles and gears were greatly appreciated. You made this work significantly more enjoyable.
- My mentor, Dr. Peter Link: Thank you for critically discussing neutron optical systems with me and for the general advice you were always happy to provide.
- Prof. Dr. Oliver Zimmer: Thank you for the countless hours discussing NMOs, for your assistance with acquiring, evaluating, and most importantly, discussing the data; and for teaching me how to think about scans you want to present in a paper when things look grim at the beamline. It was always a pleasure working with you.
- Dr. Richard Wagner: I fondly look back on our late-night discussions at BOA. You taught me to be a bit more stoic. Thank you for comparing your simulation results to mine.
- Dr. Tobias Weber: I am indebted to you for conceiving and conducting the experiments regarding LuVO_3 presented here and for our discussions regarding the topic. I greatly appreciate your help with some obscure aspects of McStas and your general input on the thesis.
- Dr. Lukas Beddrich: Thank you for lending me your mental machete when I could not even see the forest. Your dedication as a physicist was truly inspiring. You are a friend and a mentor to me.
- Dr. Tobias Neuwirth and Simon Sebold: Although I was not part of the “Kaffeerunde” as of late, I still have fond memories of sharing mate tee with you before COVID struck. Thank you for 3D-printing the neutron-absorbing structures for me.

- Dr. Matteo Busi: Thank you for your assistance at BOA, where we assessed the performance of NMO focusing (We still need to go rock climbing near PSI).
- The FRM-II/Mira Team, Dr. Alexander Book, Dr. Henrik Gabold, Ran Tang, Jonathan Frank, Martin Hertwig, Johanna Jochum: All of you enriched the past few years of my life and made the time memorable, for which I am forever grateful.
- My climbing companions and internet friends: You helped me preserve my sanity during the trying times that come up when writing a thesis.
- My parents: Without your unwavering support, it is safe to say, that this thesis would not have been possible. You always believed in me, even (especially) when I did not. Thank you so much for letting me choose my own path and having my back!
- Finally, my partner, Dr. Elisabeth Hirmer: I don't even know where to begin. In the swirl of emotions that is thesis writing (for me), you were the calm at the center of the storm. Your companionship, humor, and positive attitude have helped me tremendously. You were always there to cheer me up, to go climbing with me, and of course to prevent me from succumbing to the hermit lifestyle.

Thank you for everything!

List of Publications

- **Nested mirror optics for neutron extraction, transport, and focusing**
Christoph Herb, Oliver Zimmer, Robert Georgii, and Peter Böni.
Nuclear Instruments and Methods in Physics Research Section A: Accelerators, Spectrometers, Detectors and Associated Equipment, **1040**, 167154, October 2022.
doi:10.1016/j.nima.2022.167154.
- **In-beam superfluid-helium ultracold neutron source for the ESS**
Oliver Zimmer, Thierry Bigault, Skyler Degenkolb, Christoph Herb, Thomas Neulinger, Nicola Rizzi, Valentina Santoro, Alan Takibayev, Richard Wagner, and Luca Zanini.
Journal of Neutron Research, **24**, 95-110, January 2022.
doi:10.3233/JNR-220045.
- **Mushroom: an indirect-geometry spectrometer for FRM II**
Mushroom Geometry
Ran Tang, Jörg Voigt, Christoph Herb, and Robert Georgii.
submitted to JINST.
- **Investigation of Nested Mirror Optics using High-Resolution Imaging**
Christoph Herb, Oliver Zimmer, Richard Wagner, Robert Georgii, Peter Böni.
In preparation.
- Conference contributions
 - MLZ User Meetings
 - ICNS 2022
 - ECNS 2023
 - Workshop on Neutron Delivery Systems 2023

Appendix A: Inelastic TAS Data Obtained for LuVO_3

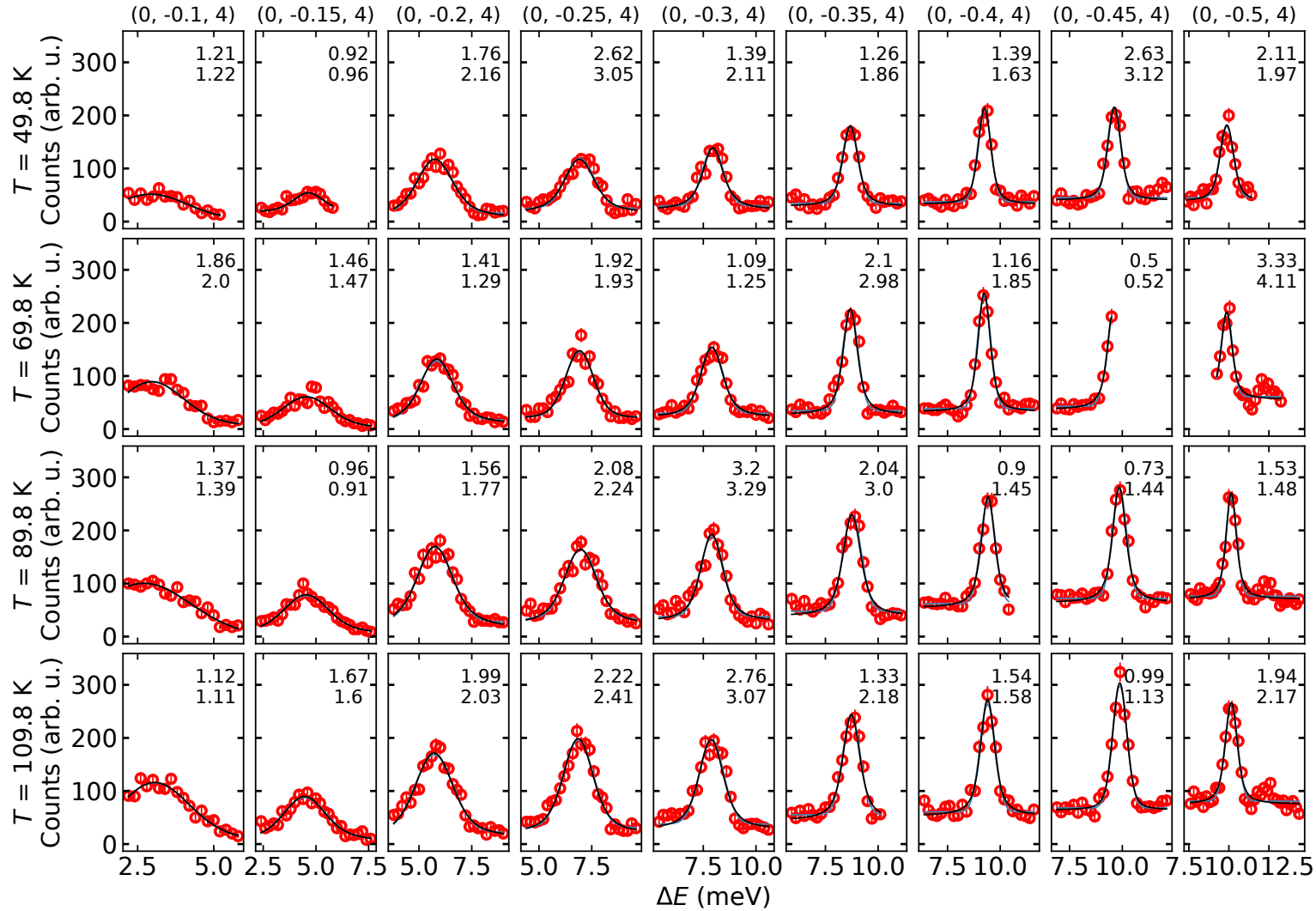


Figure A.1: Inelastic neutron scattering data investigating the dispersion of the transversal TA1 phonon branch in LuVO_3 at four different temperatures measured at EIGER in 2016. Gaussian and Voigtian fits to the data are shown in blue and black, respectively. The reduced chi-square values corresponding to the Gaussian and Voigt fits are depicted as each panel's upper and lower numbers.

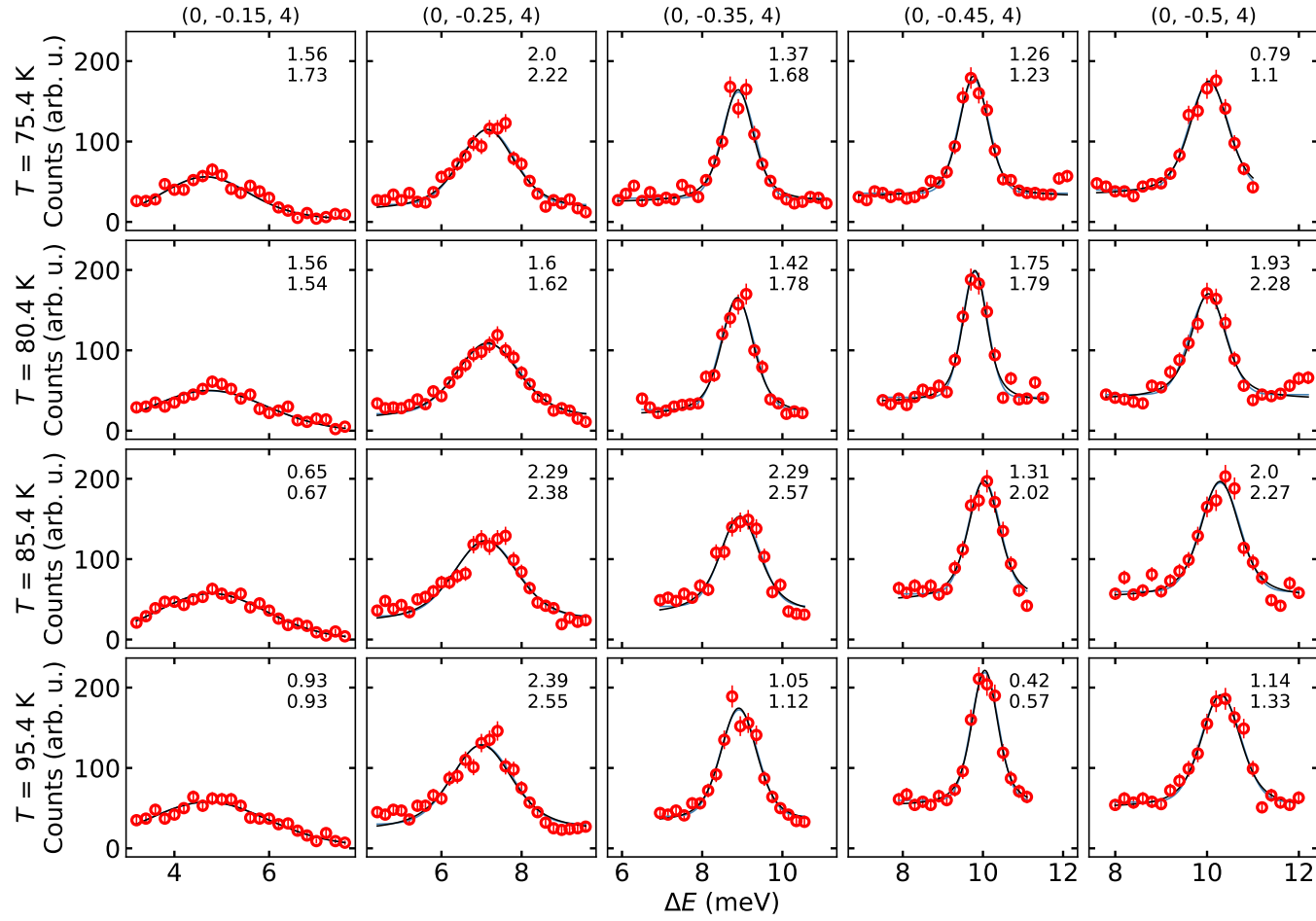


Figure A.2: Inelastic neutron scattering data investigating the dispersion of the transversal TA1 phonon branch in LuVO₃ at four different temperatures obtained at EIGER in 2017. Gaussian and Voigt fits to the data are shown in blue and black, respectively. The reduced chi-square values corresponding to the Gaussian and Voigt fits are shown as each panel's upper and lower numbers.

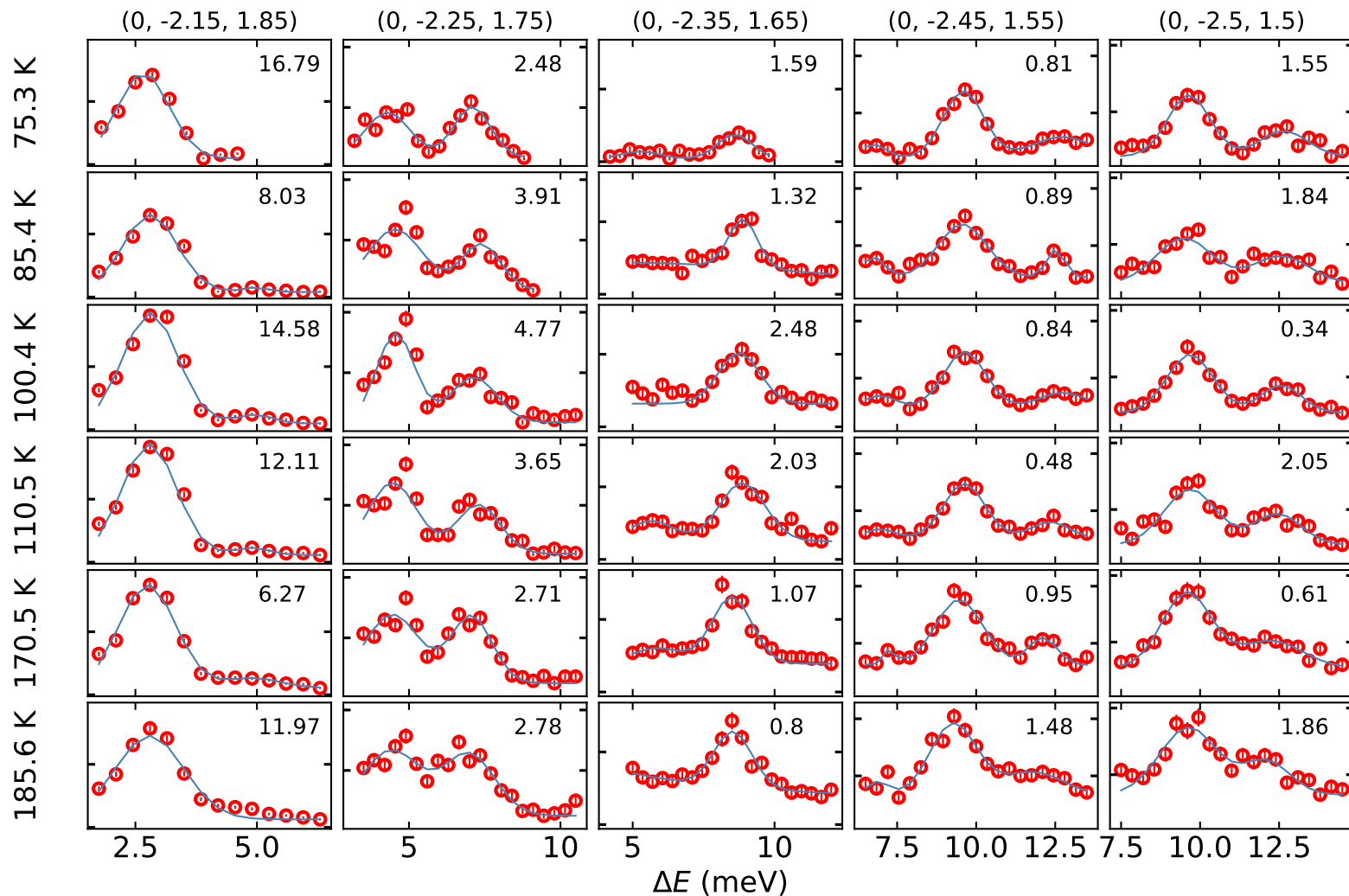


Figure A.3: Inelastic neutron scattering data investigating a transversal and a longitudinal phonon branch in LuVO_3 at six different temperatures and five Q positions obtained at EIGER in 2017. Fits comprising the sum of multiple Gaussian components and a constant background are shown in blue. The reduced chi-square values corresponding to the Gaussian fits are shown in each panel.

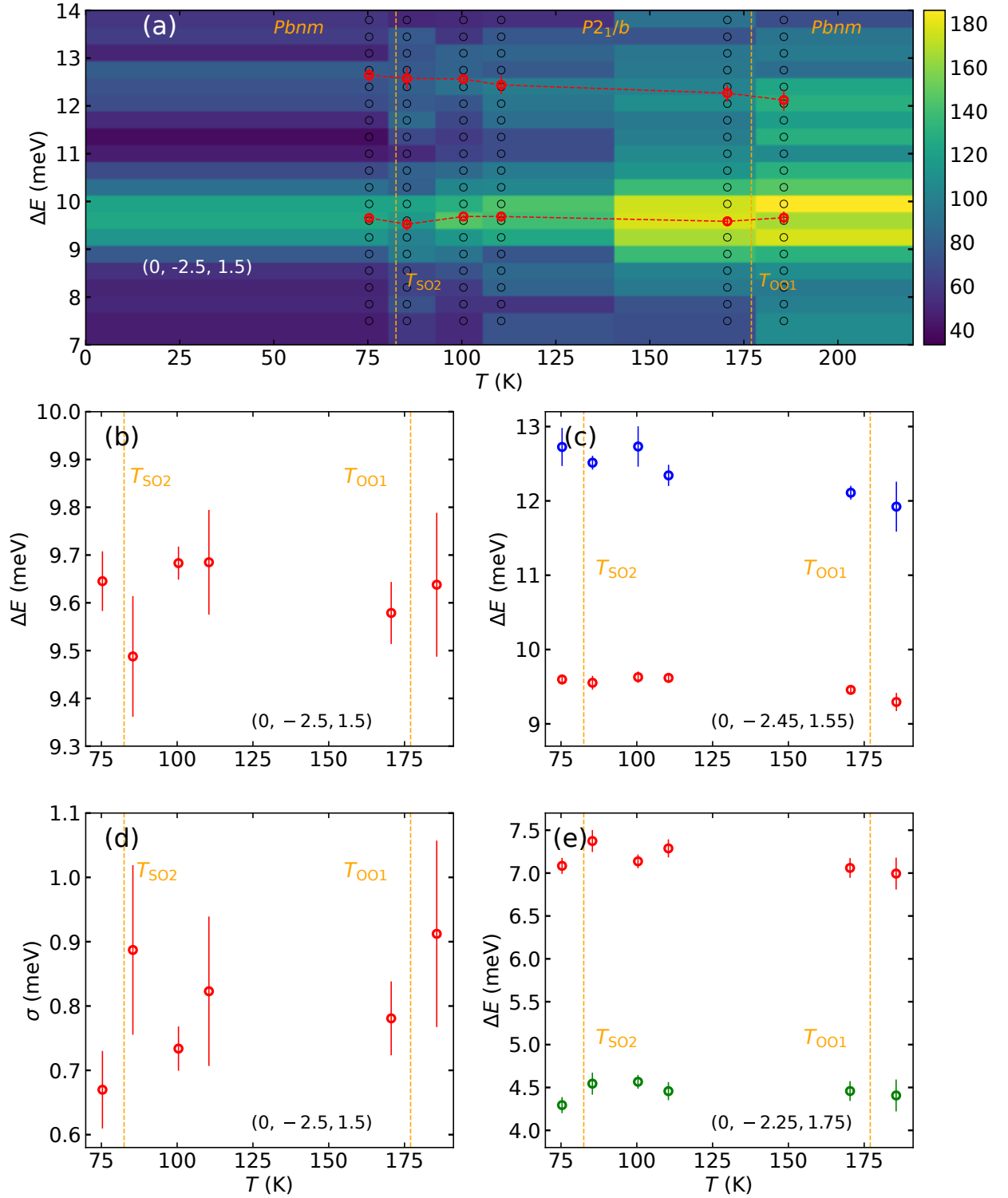


Figure A.4: Temperature dependence of phonon energy and linewidths obtained at different Q -points around $Q = (0, -2.5, 1.5)$. (a), (b) and (d) show a color plot of the raw data, the energy transfer, and the width of the peaks at $Q = (0, -2.5, 1.5)$, respectively. The colorplot in (a) shows the neutron intensity per 10 min normalized to a common monitor as a function of both the applied temperature and the energy transfer at the sample. Additionally, the acoustic and the optical phonon energy transfers are indicated by broken red lines (error bars correspond to the uncertainties of the fits). No significant change in phonon energy can be observed at T_{OO2} for any modes investigated.

Appendix B: Derivation of Snell's law

We here examine the situation of a neutron with kinetic energy $T = \frac{\hbar^2 k^2}{2m_n}$ transitioning between regions with different neutron potentials V_1 and V_2 . The results derived from this discussion were employed to simulate the kinematics of refraction and reflection at silicon-air interfaces. Additionally, we obtain Snell's law in the process.

At any interface, the total energy, i.e., the sum of kinetic and potential energy $E_i = T_i + V_i$, has to be preserved. Additionally, the component of momentum perpendicular to the surface normal (parallel to the surface) has to remain constant due to the symmetry of the interface, $k_{1\perp} = k_{2\perp}$. A sketch of the behavior at the interface is shown in Fig. B.1. We observe that

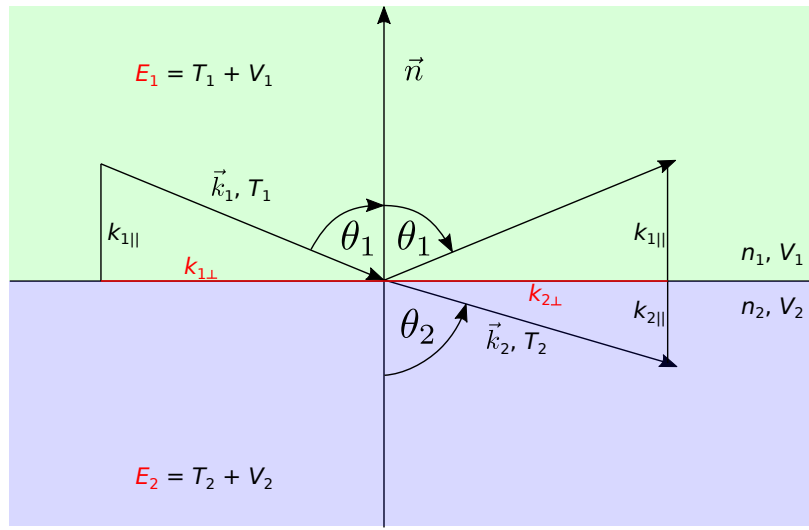


Figure B.1: Behavior of a neutron at material interfaces with different neutron potentials V_i . The total energy of the neutron, comprising kinetic and potential energy, $E_i = T_i + V_i$, as well as the component of momentum perpendicular to the surface normal, k_{\perp} , are preserved at the interface. Both constants are highlighted in red.

$k_i^2 = k_{i\perp}^2 + k_{i\parallel}^2$, and utilize $T_i = \frac{k_i^2 \hbar^2}{2m_n}$ to calculate

$$\begin{aligned}
 E_1 &= E_2, \\
 \frac{(k_{1\parallel}^2 + k_{1\perp}^2)\hbar^2}{2m_n} + V_1 &= \frac{(k_{2\parallel}^2 + k_{2\perp}^2)\hbar^2}{2m_n} + V_2, \\
 \frac{k_{1\parallel}^2 \hbar^2}{2m_n} + V_1 &= \frac{k_{2\parallel}^2 \hbar^2}{2m_n} + V_2,
 \end{aligned} \tag{B.1}$$

where the last equality was derived using $k_{1\perp} = k_{2\perp}$. Solving for the momentum parallel to the surface normal, $k_{2\parallel}^2$, yields

$$k_{2\parallel}^2 = k_{1\parallel}^2 + \frac{2m_n(V_1 - V_2)}{\hbar^2}. \tag{B.2}$$

For $V_1 > V_2$, the resulting increase in momentum perpendicular to the surface leads to a refraction of the neutron towards the surface normal. As per intuition, for $V_1 = V_2$, the trajectory of the neutron remains undisturbed.

Two cases have to be discriminated if $V_2 < V_1$. Firstly, if $\frac{k_{1\parallel}^2 \hbar^2}{2m_n} > V_1 - V_2$, the neutron is refracted away from the surface normal. Otherwise, the equation can not be solved, and instead of being refracted, the neutron is totally reflected at the surface. All performed McStas simulations account for neutron refraction and reflection according to the above formalism.

For completeness, a refactoring of the given equations in terms of Snell's law is given, including a derivation of the critical angle in terms of the neutron Fermi pseudopotential. We begin by expressing the component of momentum parallel to the surface in terms of the angle to the surface normal θ_i :

$$\begin{aligned} k_1 \sin \theta_1 &= k_{1\perp} = k_{2\perp} = k_2 \sin \theta_2, \\ \left(\frac{(E - V_1)2m_n}{\hbar^2} \right)^{\frac{1}{2}} \sin \theta_1 &= \left(\frac{(E - V_2)2m_n}{\hbar^2} \right)^{\frac{1}{2}} \sin \theta_2, \\ \sin \theta_1 \left(\frac{E - V_1}{E} \right)^{\frac{1}{2}} &= \sin \theta_2 \left(\frac{E - V_2}{E} \right)^{\frac{1}{2}} \equiv \sin \theta_1 n_1 = \sin \theta_2 n_2. \end{aligned} \quad (\text{B.3})$$

A comparison of the latter equation to Snell's law allows the extraction of the indices of refraction,

$$n_i = \left(1 - \frac{V_i}{E} \right)^{\frac{1}{2}}. \quad (\text{B.4})$$

For an interface between vacuum, $n_1 = 1$, and a material with neutron potential V_2 , we calculate the critical angle to the surface normal $\theta_{c,n}$ as follows,

$$\sin \theta_{c,n} = n_2 = \left(1 - \frac{V_2}{E} \right)^{\frac{1}{2}} = \left(1 - \frac{V_2 \lambda^2 2m_n}{\hbar^2 4\pi^2} \right)^{\frac{1}{2}} \quad (\text{B.5})$$

Considering that $\theta_c = \pi - \theta_{c,n}$ ⁽¹⁾ and inserting in the Fermi pseudopotential as a function of the bound coherent scattering length and the density, one obtains the well-known expression for the critical angle

$$\sin^2 \theta_c = \lambda^2 \frac{V_2 2m_n}{\hbar^2 4\pi^2} = \lambda^2 \frac{\sum_j b_{\text{coh},j} \rho_{n,j}}{\pi}. \quad (\text{B.6})$$

Finally, the indices of refraction can be expressed in terms of b_{coh} and ρ or the critical angle,

$$n_i = \left(1 - \lambda^2 \frac{V_i 2m_n}{\hbar^2 4\pi^2} \right)^{\frac{1}{2}} = \left(1 - \lambda^2 \frac{\sum_j b_{\text{coh},j} \rho_{n,j}}{\pi} \right)^{\frac{1}{2}} = (1 - \sin^2 \theta_c)^{\frac{1}{2}}. \quad (\text{B.7})$$

⁽¹⁾The critical angle, θ_c , is measured between the surface of the interface and the critical trajectory of the neutron, different from the angle between the surface normal and the critical trajectory, $\theta_{c,n}$.

Appendix C: Derivation of Geometric Aberrations in Elliptic Guides

Within this section, we derive a more precise approximation for the geometric aberrations of neutrons reflected in a long elliptic guide. We first obtain an analytic value of r_2 as a function of r_1 , z , b , and f before expanding the result in terms of $\frac{f-z}{f+z} - 1$ around a value of 0, which corresponds to $z = 0$. The extensive calculations were performed with the help of Mathematica [171].

We describe the two-dimensional situation in terms of a coordinate system, where the first coordinate, z , is aligned parallel to the optical axis and the one perpendicular to it is denoted by r . Using this geometry, the outline of an ellipse centered around $z = 0$ is implicitly defined by,

$$0 = r^2 - b^2 \frac{f^2 + b^2 - z^2}{f^2 + b^2}, \quad (\text{C.1})$$

where f and b denote the focal length and the semi-minor axis of the ellipse, respectively ($a^2 = f^2 + b^2$). The surface normal of the ellipse is given by:

$$\vec{n} = \begin{bmatrix} z b^2 \\ r(f^2 + b^2) \end{bmatrix}. \quad (\text{C.2})$$

A neutron is emitted above the first focal point at $z = -f$, $r = r_1$. With the reflection occurring at z , $r = r_r$, the trajectory of the incident neutron is described by,

$$\vec{t}_i = \begin{bmatrix} -f \\ r_1 \end{bmatrix} + \lambda_i \begin{bmatrix} z + f \\ r_r - r_1 \end{bmatrix} = \begin{bmatrix} -f \\ r_1 \end{bmatrix} + \lambda_i \vec{v}_i, \quad (\text{C.3})$$

which yields the trajectory of the reflected neutron:

$$\vec{t}_r = \begin{bmatrix} z \\ r_r \end{bmatrix} + \lambda_r \left(\vec{v}_i - 2 \frac{\vec{n} (\vec{v}_i \cdot \vec{n})}{|\vec{n}|^2} \right). \quad (\text{C.4})$$

Here, we used the fact that a vector \vec{v}_i reflected at a surface with normal vector \vec{n} has a direction:

$$\vec{v}_r = \vec{v}_i - 2 \frac{\vec{n} (\vec{v}_i \cdot \vec{n})}{|\vec{n}|^2}. \quad (\text{C.5})$$

Equating the z -coordinate in Eq. (C.4) with the position of the second focal point $z = f$, we utilize the computer algebra system Mathematica [171] to derive the r -coordinate at F_2 ,

$$r_2(r_1, z) = \frac{r_1(f+z)(b^2 + f(f-z))^2}{2br_1z(b^2 + f^2)\sqrt{\frac{b^2+f^2-z^2}{b^2+f^2}} + 2b^2(f^3 - fz^2) + b^4(f-z) + f^2(f-z)(f+z)^2}. \quad (\text{C.6})$$

This analytic expression can be Taylor expanded in terms of $\frac{f-z}{f+z}$ around 1, corresponding to $z = 0$, up to first order, we finally obtain

$$\begin{aligned} r_2(r_1, z) &\approx r_1 + r_1 \left(\frac{f-z}{f+z} - 1 \right) \frac{(f^2 - b^2 + b r_1)}{b^2 + f^2} + \mathcal{O} \left(\left(\frac{f-z}{f+z} - 1 \right)^2 \right) \dots \\ &= r_1 \left(\frac{b^2 + f^2 - (f^2 - b^2 + b r_1)}{b^2 + f^2} + \frac{f-z}{f+z} \cdot \frac{f^2 - b^2 + b r_1}{b^2 + f^2} \right) + \mathcal{O} \left(\left(\frac{f-z}{f+z} - 1 \right)^2 \right) \dots \end{aligned} \quad (\text{C.7})$$

The series expansion was performed by utilizing:

$$\frac{\partial g(z)}{\partial \frac{f-z}{f+z}} = \left(\frac{\partial \frac{f-z}{f+z}}{\partial z} \right)^{-1} \frac{\partial g(z)}{\partial z} = -\frac{(f+z)^2}{2f} \frac{\partial g(z)}{\partial z} \quad (\text{C.8})$$

It is easily seen that for $f \gg b$, Eq. (C.7) can be approximated by:

$$r_2(r_1, z) \approx r_1 \frac{f-z}{f+z}, \quad (\text{C.9})$$

typically valid for elliptic guides. The improvement of Eq. (C.7) compared to Eq. (C.9) might enable the utilization during the evaluation of long elliptic guide systems.

Appendix D: Analytic Derivation of $p_{R_2}(r_2)$ at the Second Focal Point of an Elliptic Guide

Here, we present the analytic calculation of the intensity distribution at the second focal spot after reflection by a long elliptic guide. Parts of the derivation were performed utilizing Mathematica [171].

Using the simple approximation given in Eq. (5.8),

$$r_2 = r_1 \frac{f - z}{f + z}, \quad (\text{D.1})$$

the distance to the optical axis at F_2 depends only on z , f , and the distance at F_1 , r_1 . To perform the calculations, z and r_1 are assumed to be independent and uniformly distributed with the following [probability density functions \(PDFs\)](#),

$$\begin{aligned} p_Z(z) &= 1/l \text{ for } z \in [-l/2, l/2], \\ p_{R_1}(r_1) &= 1/h \text{ for } r_1 \in [-h/2, h/2]. \end{aligned} \quad (\text{D.2})$$

The [PDFs](#) can be interpreted as two intensity distributions of neutrons normalized to 1. While p_{R_1} describes the spatial intensity distribution of neutrons at the first focal point as a function of r_1 , $p_Z(z)$ describes the density of neutrons impinging on the elliptic mirror surface as a function of the point of reflection, z . For a source possessing a rectangular spatial intensity distribution, the assumption of a uniform [PDF](#) in r_1 is reasonable. However, one expects $p_Z(z)$ to decrease with increasing distance from the source or equivalently, z . The validity of this necessary simplification is discussed in the [appendix E](#) in more detail. Under the assumption that both variables are independent, which is reasonable in the case of $h \ll b \ll f$, we use the joint probability distribution of both variables, $p_Z(z) \cdot p_{R_1}(r_1) = \frac{1}{hl}$, and Eq. (C.9) to calculate the [PDF](#) of r_2 following the standard approach,

$$p_{R_2}(r_2) = \int_{-\frac{h}{2}}^{\frac{h}{2}} \int_{-\frac{l}{2}}^{\frac{l}{2}} \frac{\delta\left(r_2 - r_1 \frac{f-z}{f+z}\right)}{h l} dz dr_1, \quad (\text{D.3})$$

where δ denotes the Dirac delta function. To evaluate the integral over dz , we utilize the following property of the Dirac delta

$$\delta(g(z)) = \sum_i \frac{\delta(z - z_i)}{|g'(z_i)|}, \quad (\text{D.4})$$

where the sum extends over all roots, z_i , of the function $g(z)$ and $g'(z_i) = \left. \frac{d}{dz} g(z) \right|_{z=z_i}$. Since $g(z) = r_2 - r_1 \frac{f-z}{f+z}$ has only one root for a given r_2 and r_1 , we can integrate in dz after calculating

$$g'(z) = \frac{2fr_1}{(f+z)^2} \quad (\text{D.5})$$

and

$$z = f \frac{r_1 - r_2}{r_1 + r_2} \quad (\text{D.6})$$

finally resulting in

$$p_{R_2}(r_2) = \begin{cases} \int_{-\frac{h}{2}}^{\frac{h}{2}} \frac{2 \left| \frac{fr_1}{(r_1+r_2)^2} \right|}{hl} dr_1 & \text{for } \left[r_2 \frac{f-l/2}{f+l/2} \leq r_1 \leq r_2 \frac{f+l/2}{f-l/2} \right] \\ 0 & \text{else} \end{cases} \quad (\text{D.7})$$

We now discern four cases depending on the value of r_2 . Assuming it to be positive, the lower limit of integration for r_1 can be calculated as $r_{1, \min} = r_2 \frac{f-l/2}{f+l/2}$, which corresponds to a reflection at the entrance of the guide. Accordingly, the upper limit occurs for reflection at the end of the guide and amounts to $r_{1, \max} = r_2 \frac{f+l/2}{f-l/2}$. Another two cases have to be discerned depending on the ratio of this upper limit and the extent of the source, h .

Altogether, the four cases concerning r_2 are the following

$$p_{R_2}(r_2) = \begin{cases} \int_{r_2 \frac{f-l/2}{f+l/2}}^{\frac{h}{2}} \frac{2 \left| \frac{fr_1}{(r_1+r_2)^2} \right|}{hl} dr_1 & \text{for } \overbrace{\left[\frac{h}{2} \leq r_2 \frac{f+l/2}{f-l/2} \right]}^{r_2 > 0} \\ \int_{r_2 \frac{f-l/2}{f+l/2}}^{r_2 \frac{f+l/2}{f-l/2}} \frac{2 \left| \frac{fr_1}{(r_1+r_2)^2} \right|}{hl} dr_1 & \text{for } \left[0 \leq r_2 \frac{f+l/2}{f-l/2} \leq \frac{h}{2} \right] \\ \int_{r_2 \frac{f+l/2}{f-l/2}}^{r_2 \frac{f-l/2}{f+l/2}} \frac{2 \left| \frac{fr_1}{(r_1+r_2)^2} \right|}{hl} dr_1 & \text{for } \overbrace{\left[-\frac{h}{2} \leq r_2 \frac{f+l/2}{f-l/2} \leq 0 \right]}^{r_2 < 0} \\ \int_{-\frac{h}{2}}^{r_2 \frac{f-l/2}{f+l/2}} \frac{2 \left| \frac{fr_1}{(r_1+r_2)^2} \right|}{hl} dr_1 & \text{for } \left[r_2 \frac{f+l/2}{f-l/2} \leq -\frac{h}{2} \right] \end{cases} \quad (\text{D.8})$$

Evaluating the integral for strictly positive values of r_1 (and r_2) yields,

$$\int \frac{2fr_1}{hl(r_1+r_2)^2} dr_1 = \frac{2f \left(\frac{r_2}{r_1+r_2} + \log(r_1+r_2) \right)}{hl} + C, \quad (\text{D.9})$$

with \log denoting the natural logarithm and C being the constant of integration. Carefully handling the individual limits of integration results in the following PDF for r_2 ,

$$p_{R_2}(r_2) = \begin{cases} \frac{2f}{hl} \left[\frac{2r_2}{2r_2-h} - \frac{1}{4} (2 + l/f) + \ln \left(\frac{(r_2-h/2)(2f+l)}{4fr_2} \right) \right] & \text{for } \left[-\frac{h}{2} \frac{f+l/2}{f-l/2} \leq r_2 \leq -\frac{h}{2} \frac{f-l/2}{f+l/2} \right] \\ \frac{2f}{hl} \left[-\frac{l}{2f} + \ln \left(\frac{f+l/2}{f-l/2} \right) \right] & \text{for } \left[-\frac{h}{2} \frac{f-l/2}{f+l/2} \leq r_2 \leq \frac{h}{2} \frac{f-l/2}{f+l/2} \right] \\ \frac{2f}{hl} \left[\frac{2r_2}{2r_2+h} - \frac{1}{4} (2 + l/f) + \ln \left(\frac{(r_2+h/2)(2f+l)}{4fr_2} \right) \right] & \text{for } \left[\frac{h}{2} \frac{f-l/2}{f+l/2} \leq r_2 \leq \frac{h}{2} \frac{f+l/2}{f-l/2} \right] \\ 0 & \text{else.} \end{cases} \quad (\text{D.10})$$

It is readily seen, that the distribution is symmetric with respect to $r_2 = 0$ as is expected due to the initial distribution also being symmetric in r_1 . Furthermore, the function is continuous at $r_2 = \pm \frac{h}{2} \frac{f-l/2}{f+l/2}$ and integrates to 1, validating the calculation. The central part of the PDF is surprisingly constant. The width of this region of constant density increases with decreasing l in agreement with the geometric consideration outlined in Fig. 5.6.

Appendix E: Derivation of $p_Z(z)$ for Straight and Elliptic Guides

We here assess the assumption used in appendix D, that the points of reflections, z , are distributed uniformly over the length of the mirror.

As a starting point, the PDF of neutrons arriving at a straight reflecting surface will be calculated. Assuming a uniform distribution of neutrons in angles

$$p_\alpha(\alpha) = \frac{1}{\alpha_{\max} - \alpha_{\min}} \text{ for } \alpha \in [\alpha_{\min}, \alpha_{\max}], \quad (\text{E.1})$$

and the neutron to be emitted from the optical axis at $z = -f$, we can calculate the point of reflection to be

$$z = \frac{b}{\tan \alpha} - f, \quad (\text{E.2})$$

where b denotes the constant distance between the optical axis and the reflective mirror surface. This allows us to determine the PDF of neutrons as a function of z to be

$$\begin{aligned} p_Z(z) &= \int_{\alpha_{\min}}^{\alpha_{\max}} p_\alpha(\alpha) \delta \left(z - \left(\frac{b}{\tan \alpha} - f \right) \right) d\alpha \\ &= \frac{1}{\alpha_{\max} - \alpha_{\min}} \int_{\alpha_{\min}}^{\alpha_{\max}} \left| \frac{\sin^2 \alpha}{b} \right| \delta \left(\alpha - \arctan \left(\frac{b}{f+z} \right) \right) d\alpha \\ &= \begin{cases} \frac{1}{\arctan(\frac{b}{f-l/2}) - \arctan(\frac{b}{f+l/2})} \frac{b}{b^2 + (f+z)^2} & \text{for } z \in [-l/2, l/2] \\ 0 & \text{else} \end{cases} \end{aligned} \quad (\text{E.3})$$

where the first term is constant and is concerned with the normalization of the integral only. The second, z -dependent term decreases for increasing z , which is due to the two effects mentioned in the main text. Firstly, the distance from the source to the point of reflection increases with z reducing the incident intensity appropriately, $I_z \propto 1/d_s$. Secondly, the angle of incidence also decreases with increasing z , now distributing the already smaller neutron flux over a larger area, thus reducing the flux arriving at the mirror further, $I_z \propto \sin \alpha$. Calculating the intensity according to the above consideration yields a qualitative agreement with the more formal calculation resulting in Eq. (E.3),

$$\begin{aligned} I_z &\propto I_0 \frac{\sin \alpha}{d_s} \\ &= I_0 \frac{b}{d_s^2} = I_0 \frac{b}{b^2 + (f+z)^2}, \end{aligned} \quad (\text{E.4})$$

thus validating both. Here, we used $\sin \alpha = b/d_s$ and $d_s^2 = b^2 + (f+z)^2$.

In comparison to the flat guide, the two effects described above have opposing influence on $p_Z(z)$ for an elliptic guide. For increasing z , the distance to the reflecting surface again

increases. However, now the angle between the incident neutron and the surface also increases due to the shape of the ellipse, hence diminishing the overall influence of z on the density of neutrons arriving at the reflecting surface compared to a flat guide. p_Z being independent of z up to a higher order in z would validate the initial assumption of the intensity being uniformly distributed on the mirror.

To determine the true PDF of neutrons in z arriving at the mirror, we use a description of the ellipse in a polar coordinate system, with its origin coinciding with the first focal point, where the neutrons are emitted under an angle α . This angle equals the polar angle, θ , determining the elliptic shape together with the distance from the first focal point according to

$$r(\theta) = \frac{b^2}{a - f \cos \theta} \quad (\text{E.5})$$

where $a = (b^2 + f^2)^{\frac{1}{2}}$. As usual, b and f denote the semi-major and semi-minor axes, and the focal length of the ellipse, respectively. From this, the probability of a neutron arriving at $z_f := z + f = \frac{b^2 \cos \alpha}{a - f \cos \alpha}$ can be calculated by transforming the distribution of a neutron being emitted under an initial angle α ,

$$p_\alpha(\alpha) = \frac{1}{\alpha_{\max} - \alpha_{\min}} \text{ for } \alpha \in [\alpha_{\min}, \alpha_{\max}] \quad (\text{E.6})$$

$$p_{Z_f}(z_f) = \frac{1}{\alpha_{\max} - \alpha_{\min}} \int_{\alpha_{\min}}^{\alpha_{\max}} \delta \left(z_f - \frac{b^2 \cos \alpha}{a - f \cos \alpha} \right) d\alpha. \quad (\text{E.7})$$

Employing the relation Eq. (D.4), this integral can be expressed as

$$p_{Z_f}(z_f) = \frac{1}{\alpha_{\max} - \alpha_{\min}} \int_{\alpha_{\min}}^{\alpha_{\max}} \frac{\delta \left(\alpha - \arccos \left(\frac{z_f a}{b^2 + f z_f} \right) \right)}{\left| \frac{b^2 a^2 \sin \alpha}{(a - f \cos^2 \alpha)^2} \right|} d\alpha \quad (\text{E.8})$$

and evaluated to be

$$p_{Z_f}(z_f) = \frac{1}{\alpha_{\max} - \alpha_{\min}} \frac{ab}{(b^2 + f z_f)^2} \left(\frac{(b^2 + f z_f)^2}{b^2 + (2f - z_f)z_f} \right)^{\frac{1}{2}}, \quad (\text{E.9})$$

$$p_Z(z) = \frac{1}{\alpha_{\max} - \alpha_{\min}} \frac{ab}{(b^2 + f(z + f))^2} \left(\frac{(b^2 + f(f + z))^2}{b^2 + (2f - (z + f))(z + f)} \right)^{\frac{1}{2}}.$$

In the final step, we shifted the coordinate system back from the polar one centered around F_1 to the one centered around the semi-minor axis, $z_f = z + f$. This adjustment allows for better comparability to the previous results. For $z = 0$ one obtains accordingly

$$\frac{1}{\alpha_{\max} - \alpha_{\min}} \frac{b}{b^2 + f^2} \quad (\text{E.10})$$

which is in agreement with the value obtained at $z = 0$ for the straight mirror.

While Eq. (E.9) evidently still depends on the point of reflection z , we can perform a series expansion in z around $z = 0$ to determine the leading order term and compare it to the one obtained from the expression calculated for a flat mirror. For the flat mirror we obtain,

$$p_Z(z)_{\text{flat}} \approx \frac{b}{(b^2 + f^2)(\alpha_{\text{max}} - \alpha_{\text{min}})} - \frac{2bf}{(b^2 + f^2)^2(\alpha_{\text{max}} - \alpha_{\text{min}})}z + \mathcal{O}(z^2), \quad (\text{E.11})$$

while the series expansion for the PDF of the elliptic mirror around $z = 0$ yields

$$p_Z(z)_{\text{ell}} \approx \frac{b}{(b^2 + f^2)(\alpha_{\text{max}} - \alpha_{\text{min}})} - \frac{bf}{(b^2 + f^2)^2(\alpha_{\text{max}} - \alpha_{\text{min}})}z + \mathcal{O}(z^2). \quad (\text{E.12})$$

Both expansions are in agreement regarding the constant term and the sign of the linear term being negative, indicating that $p_Z(z)$ decreases with increasing z , as expected. The magnitude of the linear term shows that this dependence is twice as fast in the case of the flat mirror. This is attributed to the discussed observation that the angle of incidence of the neutrons decreases with z for the flat mirror, while it increases in an elliptic geometry⁽¹⁾.

However, despite the effect being of reduced importance for the elliptic mirror, $p_Z(z)$ is not uniform as originally assumed. In the case of short mirrors, say $l/f = 1/20$, the effect is small, but when describing long, elliptic mirrors, one is required to take it into account to obtain the correct $p_{R_2}(r_2)$, which shall be evaluated in appendix F.

Until now, we have not considered the influence of r_1 , due to not being able to solve the arising second integral in r_1 analytically. Despite this limitation, one can still use numerical integration methods to recover a $p_Z(z)$, which also considers the density of neutrons in r_1 . Starting at the following expression,

$$p_Z(z) = \int_{\alpha_{\text{min}}}^{\alpha_{\text{max}}} \int_{r_{1,\text{min}}}^{r_{1,\text{max}}} p_{R_1}(r_1) p_{\alpha}(\alpha) \delta(z - z(r_1, \alpha)) \, d\alpha dr_1, \quad (\text{E.13})$$

where $z(r_1, \alpha)$ denotes a function returning the z -coordinate of the point of reflection for a given initial angle α and the deviation from the optical axis r_1 . For a value of z , one calculates the minimum and maximum value of α to be

$$\begin{aligned} \alpha_{\text{min}} &= \alpha(z, r_1 = +h/2) = \arctan \left(\frac{b\sqrt{\frac{b^2+f^2-z^2}{b^2+f^2}} - h/2}{f+z} \right) \\ \alpha_{\text{max}} &= \alpha(z, r_1 = -h/2) = \arctan \left(\frac{b\sqrt{\frac{b^2+f^2-z^2}{b^2+f^2}} + h/2}{f-z} \right). \end{aligned} \quad (\text{E.14})$$

The limits of integration in r_1 will be accounted for by the δ -distribution. The joint probability of r_1 and α is uniform and can be calculated by integrating both variables within their limits over 1 as,

$$p_{R_1}(r_1) p_{\alpha}(\alpha) = 1/A, \quad \text{with } A = \int_{\alpha_{\text{min}}}^{\alpha_{\text{max}}} \int_{r_{1,\text{min}}}^{r_{1,\text{max}}} d\alpha dr_1 \quad (\text{E.15})$$

⁽¹⁾It should be noted that for the elliptic geometry, the illuminated segment of the mirror corresponding to an interval dz also increases with $|z|$ due to the increasing angle between the mirrors and the optical axis along z .

Using Eq. (D.4), one arrives at the following integral:

$$p_Z(z) = \int_{\alpha_{\min}}^{\alpha_{\max}} \int_{r_{1,\min}}^{r_{1,\max}} 1/A \frac{\delta(r_1 - r_1(z, \alpha))}{\left| \frac{dz(r_1, \alpha)}{dr_1} \right|} dr_1 d\alpha. \quad (\text{E.16})$$

To calculate the derivative, we start with the following equation describing the intersection of the neutron trajectory with the elliptic mirror,

$$b \left(\frac{f^2 + b^2 - z^2}{f^2 + b^2} \right)^{\frac{1}{2}} = r_1 + (f + z) \tan \alpha \quad (\text{E.17})$$

where the left side represents the r -coordinate of an elliptic mirror centered around $z = 0$ and the right side describes the r -coordinate of a neutron being emitted from $z = -f$ with an offset r_1 under an angle α to the optical axis. Eq. (E.17) can be solved for either of its three unknowns with respect to the other two. We need $z(r_1, \alpha)$ for the derivative with respect to z and $r_1(z, \alpha)$ for the δ -distribution.

$$r_1(z, \alpha) = b \left(\frac{(b^2 + f^2 - z^2)}{b^2 + f^2} \right)^{\frac{1}{2}} - \tan(\alpha)(f + z) \quad (\text{E.18})$$

$$\left(\frac{dz}{dr_1} \right)^{-1} = \frac{2(\tan^2(\alpha)(b^2 + f^2) + b^2)}{(b^2 + f^2) \left(-2 \tan(\alpha) - \frac{2b^2(f \tan(\alpha) + r_1)}{\sqrt{b^2(b^2 + f^2)(b^2 \tan^2(\alpha) + b^2 - 2f r_1 \tan(\alpha) - r_1^2)}} \right)}$$

Evaluating the derivative at $r_1(z, \alpha)$ yields a complex equation, which cannot be integrated analytically in α with the available CAS, necessitating numerical integration.

$$p_Z(z) = \int_{\alpha_{\min}}^{\alpha_{\max}} \frac{1}{A} \left| \frac{dz(r_1, \alpha)}{dr_1} \right|^{-1} \Bigg|_{r_1=r_1(z, \alpha)} d\alpha \quad (\text{E.19})$$

Due to the integrand's smooth nature, a simple trapezoidal integration algorithm suffices for the numerical integration.

Appendix F: Numerical Approximation of $p_{R_2}(r_2)$ at the Second Focal Point of an Elliptic Guide

To determine a more realistic intensity distribution at the second focal point as a function of the distance to the optical axis, r_2 , we start by writing out the final expression for the neutron density at the second focal point,

$$p_{R_2}(r_2) = \int_{z_{\min}}^{z_{\max}} \int_{r_{1,\min}}^{r_{1,\max}} p_Z(z) p_{R_1}(r_1) \delta(r_2 - r_2(r_1, z)) dr_1 dz, \quad (\text{F.1})$$

where r_2 denotes the distance of the neutron from the second focal point. r_1 and z describe the distance of the neutron at the first focal point and z denotes the z -coordinate of the point of reflection and $p_Z(z)$ and p_{R_1} denote the respective probability functions normalized to 1. Finally, the function $r_2(r_1, z)$ relates the three magnitudes as shown in Eq. (C.6). Due to r_2 and r_1 sharing signs, we here only evaluate the integral for $r_2 \geq 0$, with the calculation for $r_2 \leq 0$ being analogous.

The limits of integration in z are themselves limited by the entrance and the exit of the elliptic guide, i.e., $z_{\min} \geq -l/2$ and $z_{\max} \leq l/2$. At the same time, not all values of z are geometrically allowed for a certain r_2 . When dealing with large values of r_2 , e.g., $r_2 \geq w/2$, all neutrons reaching that r_2 must be reflected in the first half of the ellipse, $z \leq 0$. However, arbitrarily small values of r_2 can be realized for all points of reflection by choosing an appropriately small r_1 . Considering both arguments, the limits in z are as follows: $z_{\min} = -l/2$ and $z_{\max} = \min[l/2, z(r_2, r_1 = h/2)]$, where $\min[\]$ yields the smallest of its arguments and $z(r_2, h/2)$ returns the z -coordinate of the point of reflection connecting $r_1 = h/2$ and r_2 . Due to the sheer number of appearances of z in $r_2(r_1, z)$ (Eq. (F.3)) the employed CAS was not able to return $z(r_2, h/2)$ analytically. Instead, the approximation for r_2 (Eq. (5.8)) was solved for z , which then served as a starting point for a Newton-Raphson algorithm yielding a numerical solution for z with a relative precision of 1×10^{-8} .

The limits of integration in r_1 are geometrically confined by $-h/2 \leq r_1 \leq h/2$, with h denoting the height of the source. Additionally, there exists a limit for r_1 given by the chosen r_2 , similar to the one discussed before, yielding $r_{1,\max} = \min[h/2, r_1(r_2, z = l/2)]$ and $r_{1,\min} = \max[0, r_1(r_2, z = -l/2)]$. However, the δ -distribution in the integrand always yields a value for r_1 , which is in agreement with those limits.

The probability density function of r_1 is given by $p_{R_1}(r_1) = 1/h$ for $r_1 \in [-h/2, h/2]$. The derivation of $p_Z(z)$ was presented in appendix E. The values of $p_Z(z)$ were calculated numerically and tabulated for the numerical integration.

Finally, the δ distribution in the integrand is transformed according to Eq. (D.4), to be

$$\delta(r_2 - r_2(r_1, z)) = \frac{\delta(r_1 - r_1(r_2, z))}{\left| \frac{dr_2(r_1, z)}{dr_1} \right|}, \quad (\text{F.2})$$

with

$$r_2(r_1, z) = \frac{r_1(f+z)(b^2+f(f-z))^2}{2br_1z(b^2+f^2)\sqrt{\frac{b^2+f^2-z^2}{b^2+f^2}} + 2b^2(f^3-fz^2) + b^4(f-z) + f^2(f-z)(f+z)^2} \quad (\text{F.3})$$

and its derivative being calculated to

$$\frac{dr_2(r_1, z)}{dr_1} = \frac{(f-z)(f+z)(b^2+f(f-z))^2(b^2+f(f+z))^2}{\left(2br_1z(b^2+f^2)\sqrt{\frac{b^2+f^2-z^2}{b^2+f^2}} + 2b^2(f^3-fz^2) + b^4(f-z) + f^2(f-z)(f+z)^2\right)^2}. \quad (\text{F.4})$$

By solving Eq. (F.3) for r_1 ,

$$r_1(r_2, z) = \frac{r_2(f-z)(b^2+f^2+fz)^2}{-2br_2z(f^2+b^2)\sqrt{\frac{b^2+f^2-z^2}{b^2+f^2}} + 2b^2f^3 - 2b^2fz^2 + b^4f + b^4z - f^3z^2 + f^2z^3 - f^4z + f^5} \quad (\text{F.5})$$

one obtains all the pieces necessary to perform the integration numerically:

$$p_{R_2}(r_2) = \int_{-l/2}^{\min[l/2, z(r_2, h/2)]} \left[p_Z(z) p_{R_1}(r_1) \left| \frac{dr_2(r_1, z)}{dr_1} \right|^{-1} \right]_{r_1=r_1(r_2, z)} dz. \quad (\text{F.6})$$

Due to the smooth nature of the integrand, equidistant values of z in combination with a simple numerical integration method based on the trapezoidal rule, e.g., the *trapz*-function from the NumPy package in Python, allow for a quick evaluation of the integral. Calculating Eq. (F.6) for uniformly distributed values of r_2 results in the data shown in Fig. 5.10.

Appendix G: Design of Elliptic NMOs

A more general version of the recipe for the construction of elliptic NMOs given in [174] shall here be discussed for geometries not centered around the semi-minor axes of the shape-determining ellipses, which in the case of one very distant focal point also can be used for an approximation of a parabolic NMO.

For the purpose of illustration, two exemplary elliptic mirrors are sketched in Fig. G.1. Initially, a point on the outermost mirror has to be determined by the maximum angle of reflection allowed by the combination of minimum neutron wavelength, λ , and maximum possible m -value. Assuming the height of the source to be negligible, this point can be calculated to be,

$$\begin{aligned} z_p &= z_s \\ r_p &= \tan(0.00173 \text{ m } \lambda/\text{\AA})(z_s - F_1) \end{aligned} \quad (\text{G.1})$$

After the point on the outermost mirror is calculated as shown above or chosen in accordance with other parameters, the two focal points F_1 and F_2 have to be determined. For the here shown calculations, we orient the coordinate systems such that the z -coordinate coincides with the optical axis connecting the two points. In this geometry, it is useful to represent elliptic (or parabolic) mirror surfaces as follows

$$r^2 = k_1 + k_2 z + k_3 z^2, \quad (\text{G.2})$$

for which the k -values can be determined by starting from the general form of the ellipse centered around $z_0 = \frac{F_1 + F_2}{2}$:

$$\frac{(z - z_0)^2}{a^2} + \frac{r^2}{a^2 - f^2} = 1. \quad (\text{G.3})$$

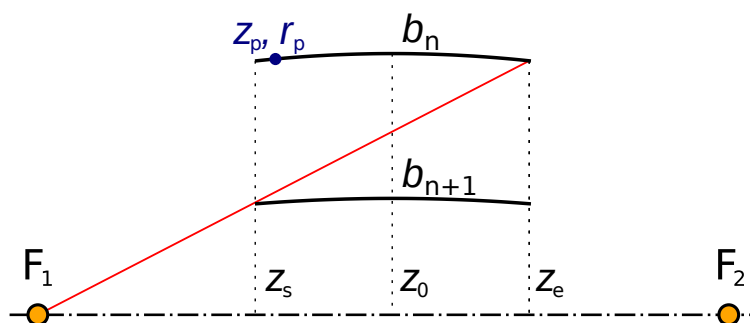


Figure G.1: Schematics of the determination of an elliptic nested geometry. A point on the elliptic surface (z_p, r_p) in combination with the z -coordinates of the two focal points F_1 and F_2 , and the entrance and the exit of the NMO, z_s, z_e , is sufficient to fully determine the nested geometry.

Here, f denotes the focal length of the ellipse, $f = \frac{F_1 - F_2}{2}$. Considering the point on the mirror surface allows the calculation of the semi-major axis,

$$a = \left(\frac{[(z_p - z_0)^2 + r_p^2 + f^2] + \left([(z_p - z_0)^2 + r_p^2 + f^2]^2 - 4(z_p - z_0)^2 f^2 \right)^{\frac{1}{2}}}{2} \right)^{\frac{1}{2}} \quad (\text{G.4})$$

which then allows to calculate all k -values for Eq. (G.2):

$$\begin{aligned} k_3 &= \frac{f^2}{a^2} - 1 \\ k_2 &= -2z_0 k_3 \\ k_1 &= z_0^2 k_3 + (a^2 - f^2). \end{aligned} \quad (\text{G.5})$$

This allows us to determine the distance of a mirror from the optical axis at the exit of the NMO, $r_n(z_e)$, and connect it with F_1 , as indicated by a red line in Fig. G.1. Using the theorem of intersecting lines, we can determine a point on the adjacent inner mirror to be located at the following coordinates,

$$\begin{aligned} z_{n+1} &= z_s \\ r_{n+1} &= r_n(z_e) \frac{z_s - F_1}{z_e - F_1}, \end{aligned} \quad (\text{G.6})$$

which in turn enables calculating the next set of k -values allowing to repeat the above process until a satisfactory number of mirrors is reached or until the spacing between individual mirrors subceeds the minimum distance, which can still be fabricated.

The total number of mirrors, N , needed to transport an angular range from α_{\min} to α_{\max} using a symmetric elliptic nested mirror geometry can be approximated by the following considerations. Assuming a focal length, f , and a common length of the mirrors, l , the point determining the outermost mirror is given by,

$$\begin{aligned} z_0 &= -l/2 \\ r_0 &= (f - l/2) \tan \alpha_{\max}, \end{aligned} \quad (\text{G.7})$$

which, in the case of $f \gg l$, allows to approximate the corresponding semi-minor axis to be $b_0 \approx f \alpha_{\max}$. Considering Fig. 5.14 and Eq. (G.6), it is evident that the semi-minor axis of the adjacent inner mirror is smaller by a factor of $b_{n+1} = b_n \frac{f-l/2}{f+l/2}$. Since this factor remains constant for each pair of mirrors, the semi-minor axis of the N -th mirror is approximately,

$$b_N = b_0 \left(\frac{f - l/2}{f + l/2} \right)^N, \quad (\text{G.8})$$

which can, in the case of $f \gg l$, be simplified to

$$b_N \approx b_0 \left(1 - \frac{l}{f} \right)^N \quad (\text{G.9})$$

where $b_N = (f + l/2) \tan \alpha_{\min}$. The number of required mirrors is then expressed as,

$$N = \frac{\ln\left(\frac{b_N}{b_0}\right)}{\ln\left(1 - \frac{l}{f}\right)} \approx \frac{\ln\left(\frac{\alpha_{\min}}{\alpha_{\max}}\right)}{\ln\left(1 - \frac{l}{f}\right)} \approx \ln\left(\frac{\alpha_{\max}}{\alpha_{\min}}\right) \frac{f}{l}. \quad (\text{G.10})$$

The number of required mirrors thus scales with the logarithm of the angular range and linearly with the ratio of focal length to mirror length. Interestingly, the total coated area required to transport a certain angular range stays constant under variations of l , as the area per individual mirror scales as $\propto l$, whereas the number of mirrors scales reciprocally to l . This finding typically favors small l , which ensures better imaging quality, albeit more complex to fabricate.

When designing a parabolic **NMO**, one can resort to the here presented recipe with one of the focal points located very far from the optical axis. However, one must balance numerical errors, which carry more impact for large values of f , with the errors associated with choosing a finite distance between the focal points. Instead, one can perform an analogous calculation for a *truly* parabolic mirror shape, which is not shown here.